REPORT DOCUMENTATION PAGE

1a. REPORT SECURITY CLASSIFICATION	1b. RESTRICTIVE MARKINGS
Unclassified	

2a. SECURITY CLASSIFICATION AUTHORITY	3. DISTRIBUTION/AVAILABILITY OF REPORT
	Unlimited Approved for public release, distribution unlimited
2b. DECLASSIFICATION/DOWNGRADING SCHEDULE	

4. PERFORMING ORGANIZATION REPORT NUMBER(S)	5. MONITORING ORGANIZATION REPORT NUMBER(S)
C463-3	AFOSR-TR-96 0299

6a. NAME OF PERFORMING ORGANIZATION	6b. OFFICE SYMBOL (If applicable)	7a. NA
Northwestern University		esearch

6c. ADDRESS (City, State and ZIP Code)	7b. ADDRESS (City, State and ZIP Code)
Evanston, IL 60208	Bolling AFB, DC 20332

8a. NAME OF FUNDING/SPONSORING ORGANIZATION	8b. OFFICE SYMBOL (If applicable)	9. PROCUREMENT INSTRUMENT IDENTIFICATION NUMBER
AFOSR/NA Bolling AFB DC 20332-6448	NA	Grant No. F49620-92-J-0423/P1

8c. ADDRESS (City, State and ZIP Code)

AFOSR/NA
Bolling AFB DC 20332-6448

10. SOURCE OF FUNDING NOS.

PROGRAM ELEMENT NO.	PROJECT NO.	TASK NO.	WORK UNIT NO.

11. TITLE (Include Security Classification) Characterization of Deformation & Damage in Brittle Matrix Composite Materials

12. PERSONAL AUTHOR(S)
I. M. Daniel

13a. TYPE OF REPORT	13b. TIME COVERED	14. DATE OF REPORT (Yr., Mo., Day)	15. PAGE COUNT
Final	FROM 8/1/92 TO 1/31/96	1996/05/10	147

16. SUPPLEMENTARY NOTATION

17. COSATI CODES			18. SUBJECT TERMS (Continue on reverse if necessary and identify by block number)
FIELD	GROUP	SUB. GR.	Composite Materials; Micromechanics; Failure Mechanisms; Brittle Matrix Composites; Ceramic Composites; Acoustic Emission; Constitutive Modeling

19. ABSTRACT (Continue on reverse if necessary and identify by block number)

The objective of this investigation is to study deformation and failure of brittle-matrix composite materials. Unidirectional and crossply continuous-fiber ceramic-matrix composites were investigated under uniaxial loading. Failure mechanisms and their development were studied in real time under the microscope and also by means of ultrasonic and acoustic emission techniques. All observations and measurements were correlated with the macroscopic stress-strain behavior of the material and compared with predictions of analytical models. A new model was developed for correlation of failure micromechanisms and macroscopic response of the material.

19960624 316

20. DISTRIBUTION/AVAILABILITY OF ABSTRACT	21. ABSTRACT SECURITY CLASSIFICATION
UNCLASSIFIED/UNLIMITED ☒ SAME AS RPT. ☐ DTIC USERS ☐	Unclassified

22a. NAME OF RESPONSIBLE INDIVIDUAL	22b. TELEPHONE NUMBER (Include Area Code)	22c. OFFICE SYMBOL
DR WALTER JONES	202-767-0460	NA

DD FORM 1473, 83 APR   EDITION OF 1 JAN 73 IS OBSOLETE.

DISCLAIMER NOTICE
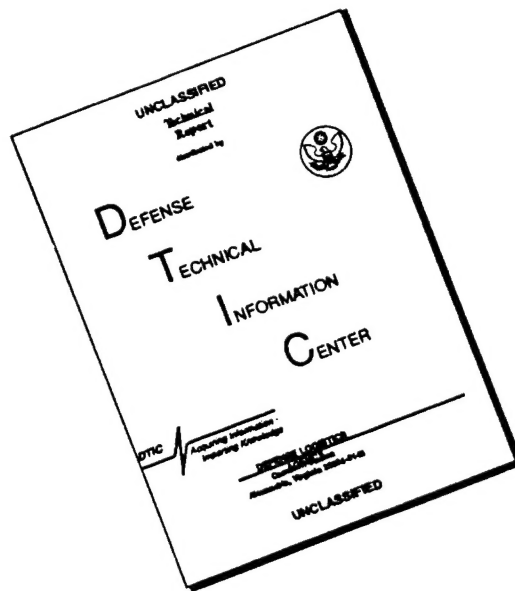
THIS DOCUMENT IS BEST QUALITY AVAILABLE. THE COPY FURNISHED TO DTIC CONTAINED A SIGNIFICANT NUMBER OF PAGES WHICH DO NOT REPRODUCE LEGIBLY.

Foreword

This is the Final Report on project "Characterization of Deformation and Damage in Brittle-Matrix Composite Materials," prepared by Northwestern University for the Air Force Office of Scientific Research (AFOSR) under Grant No. F 49620-92-J-0423/P1. The work described in this report was conducted in the period August 1, 1992 to January 31, 1996. Dr. Walter F. Jones is the AFOSR project manager. Professors I. M. Daniel and J. D. Achenbach are co-principal investigators. Contributors to the program include Drs. H. S. Choi, H. J. Chun, C. L. Tsai and S. C. Wooh, and Mr. J. J. Luo.

Northwestern University

I. M. Daniel
Professor
Theoretical and Applied Mechanics

CHARACTERIZATION OF DEFORMATION AND DAMAGE IN BRITTLE-MATRIX COMPOSITE MATERIALS

1. INTRODUCTION

The behavior of brittle-matrix composite materials is intimately related to the deformation and failure micromechanisms including their exact sequence and interaction. These in turn are related to the properties of the constituents, matrix, fiber and interface/interphase, as well as the processing residual stresses.

The micromechanics of stress transfer and fracture of brittle matrix composites has been studied experimentally and analytically by many investigators [1-17]. Under longitudinal tension damage initiates with the development of multiple matrix cracking, since the failure strain of the matrix is lower than that of the fiber. This is accompanied by partial debonding at the fiber-matrix interface and fiber fractures, which strongly depend on the properties of the interface. Most studies to date deal with longitudinal behavior of the unidirectional composite. Very few studies deal with behavior under transverse loading [10, 11, 18-20]. Although the various failure mechanisms are known and understood their relative magnitudes, exact sequence and interaction and quantitative effect on the overall macroscopic behavior vary from case to case. The various analytical models proposed to date are deficient or incomplete or lack experimental substantiation.

The objective of this investigation was to study the deformation and failure of brittle-matrix composite materials. Unidirectional and cross-ply continuous-fiber ceramic-matrix composites under uniaxial tension were investigated experimentally and analytically. The various tasks of this study are described below.

2. EXPERIMENTAL STUDIES of UNIDIRECTIONAL COMPOSITE UNDER LONGITUDINAL TENSION [10-14, 21-24]

2.1 Macroscopic Characterization

The material investigated is a unidirectional SiC/CAS, calcium aluminosilicate glass ceramic (CAS, Corning Glass Works) reinforced with

continuous silicon carbide fibers (Nicalon, Nippon Carbon Co.). A typical transverse section of this material is shown in Fig. 1. Properties of the constituents are tabulated in Table 1.

Longitudinal, transverse and shear tests were conducted to characterize the macroscopic response of the composite material and determine its macroscopic mechanical properties. Typical stress-strain curves to failure in the longitudinal and transverse directions are shown in Fig. 2. The Difference between the ultimate properties in the two directions is extreme. Additional tests were conducted to determine the coefficients of thermal expansion. Results are tabulated in Table 2.

The characteristic features of the longitudinal stress-strain curve are illustrated in Fig. 3. The material initially behaves linearly elastically up to the proportional limit (point A). This is followed by a nonlinear region with decreasing stiffness up to the "bend over" point B. Then, follow a region BC of stabilized stiffness reduction rate (or sometimes a plateau), another region CD of increasing tangential stiffness (strain hardening), and the terminal quasi-linear region DE. These characteristic features are obviously related to the microscopic failure mechanisms that develop during loading.

2.2   Microscopic Observations [10-14]

Failure mechanisms were studied by testing and observing specimens under the microscope (Fig. 4). The damage development scenario, observed directly in part and inferred in part, consists of the following (Fig. 5):

1. Matrix crack initiation

2. Crack propagation and fiber/matrix debonding

3. Crack saturation

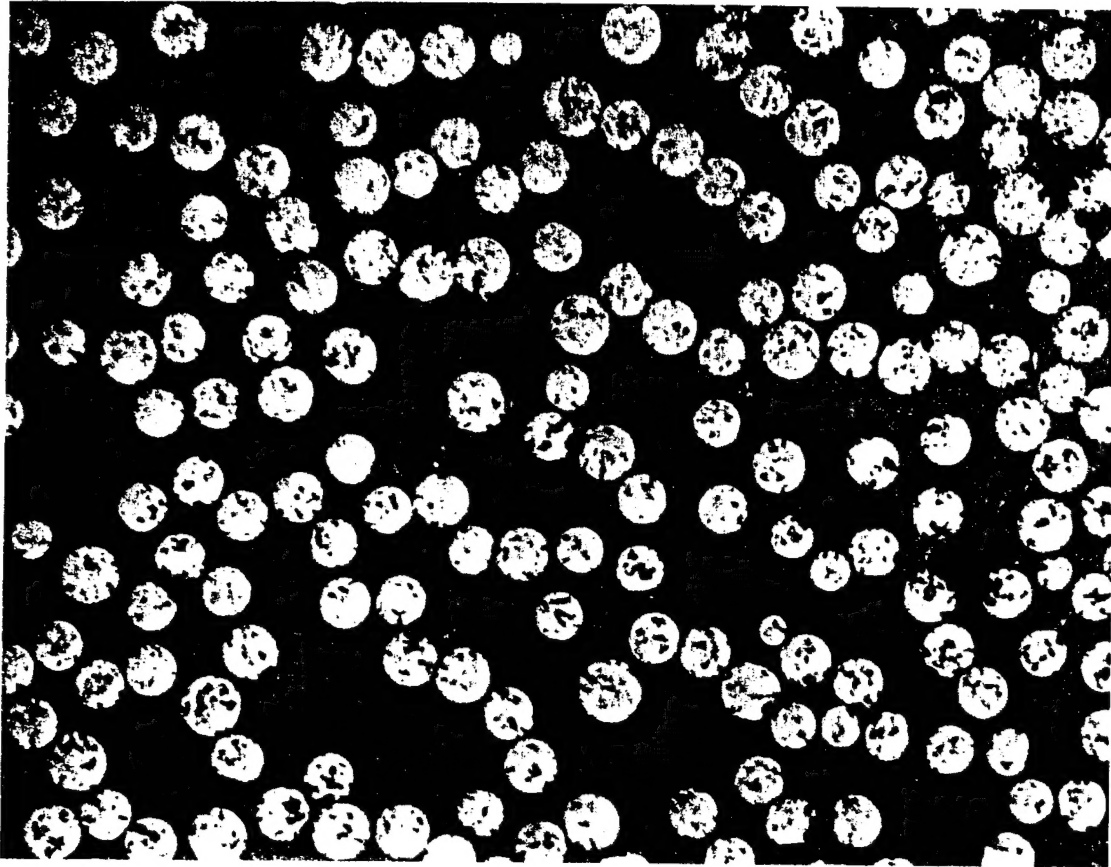4. Fiber fractures

5. Ultimate failure

Fig. 1   Photomicrograph of a Typical Transverse Section of Unidirectional
SiC/CAS Composite
(Fiber diameter: range 8-20 μm, average 15 μm)

Table 1. Constituent Material Properties

Property	CAS Matrix[1]	SiC Fiber[2]
Maximum Use Temperature, °C (°F)	1350 (2460)	1300 (2370)
Fiber Diameter (μm)	-	15
Density (g/cm^3)	2.8	2.6
Coefficient of Thermal Expansion, 10^{-6}/°C (10^{-6}/°F)	5.0 (2.8)	3.2 (1.8) - 4.9 (2.7)
Elastic Modulus, GPa (10^6 psi)	98 (14.2)	170 (24.6)
Tensile Strength, MPa (ksi)	124 (18) (flexural	1930 (280)

[1] Larsen and Adams (1989)

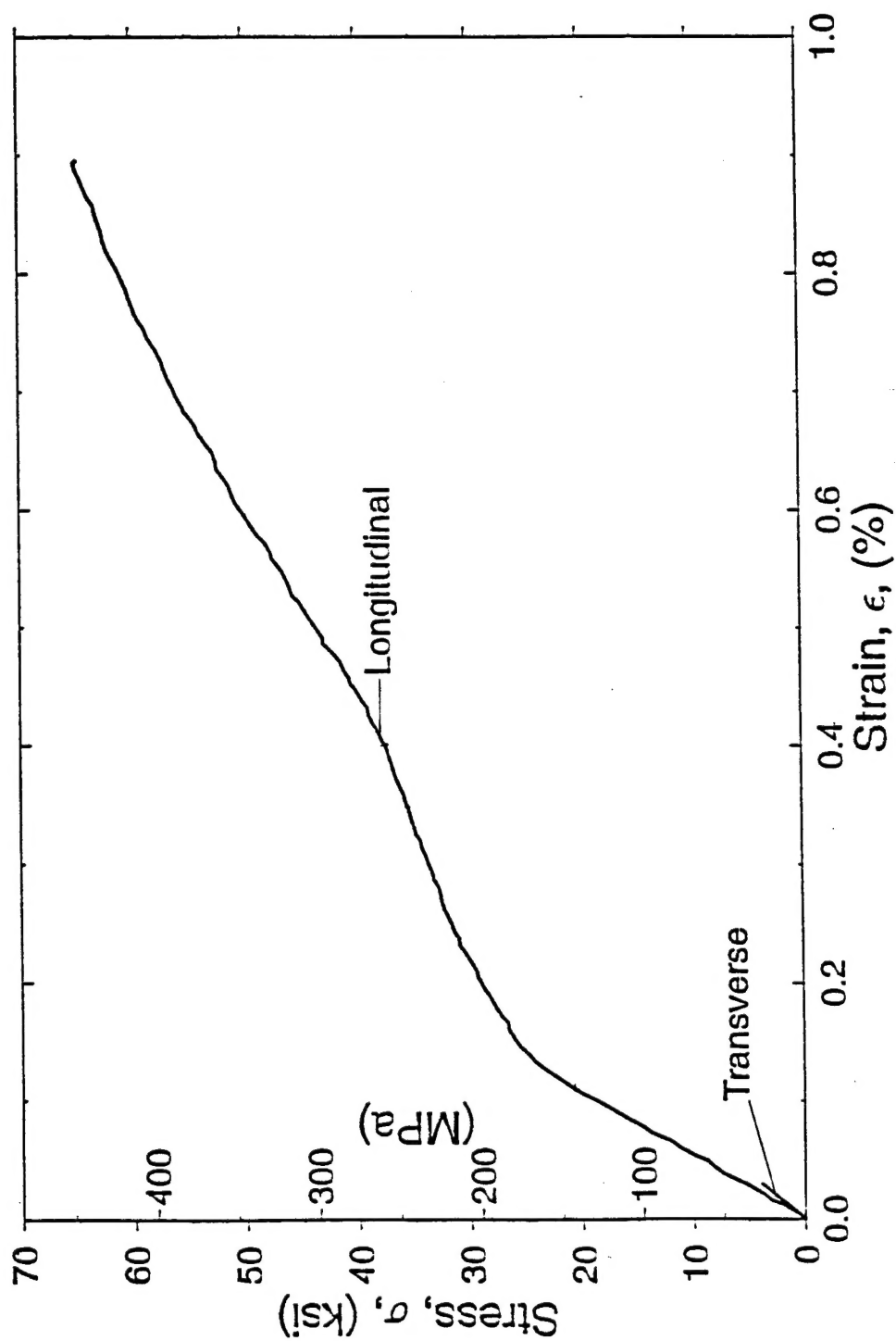[2] Prewo and Brennan (1982), Daniel et al. (1989)

4

Fig. 2 Stress-Strain Curves to Failure of Unidirectional SiC/CAS Composite under Longitudinal and Transverse Tension

Table 2. Measured Properties of SiC/CAS Unidirectional Composite

Property	Value
Fiber Volume Ratio, V_f	0.39
Ply Thickness, t, mm (in.)	0.38 (0.015)
Longitudinal Modulus, E_1, GPa (Msi)	127 (18.4)
Transverse Modulus, E_2, GPa (Msi)	112 (16.2)
In-plane Shear Modulus, G_{12}, GPa (Msi)	52 (7.5)
Out-of-plane Shear Modulus, G_{23}, GPa (Msi)	32 (4.7)
Major Poisson's Ratio, ν_{12}	0.18
Longitudinal Tensile Strength, F_{1t}, MPa (ksi)	448 (65)
Transverse Tensile Strength, F_{2t}, MPa (ksi)	28 (4)
Longitudinal Ultimate Tensile Strain, ε^u_{1t}	9×10^{-3}
Transverse Ultimate Tensile Strain, ε^u_{2t}	2.5×10^{-4}
Longitudinal Coefficient of Thermal Expansion, α_1, $\mu\varepsilon/°K$ ($\mu\varepsilon/°F$)	4.05 (2.25)
Transverse Coefficient of Thermal Expansion, α_2, $\mu\varepsilon/°K$ ($\mu\varepsilon/°F$)	4.23 (2.35)
Out-of-plane Coefficient of Thermal Expansion, α_3, $\mu\varepsilon/°K$ ($\mu\varepsilon/°F$)	4.32 (2.40)
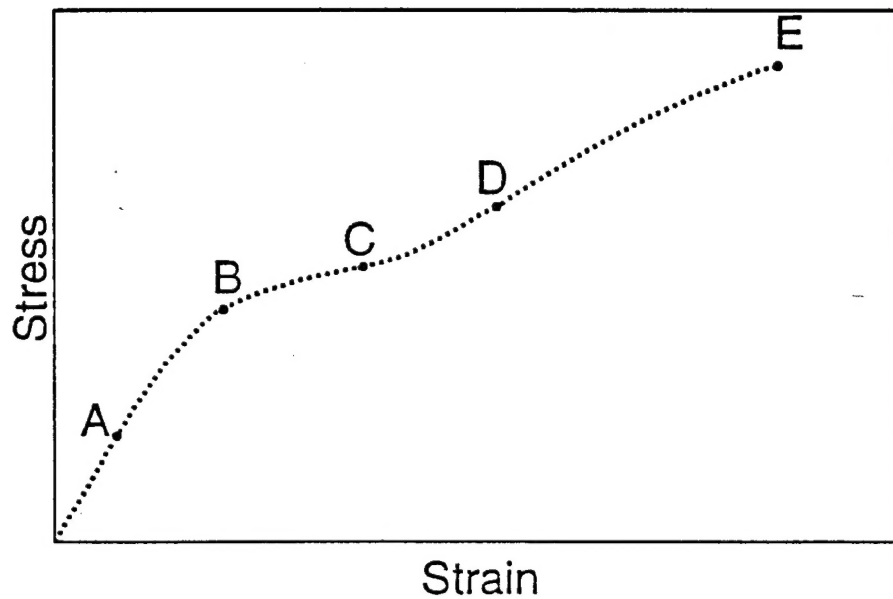
A: Proportional limit
B: Bend-over point
BC: Plateau or low tangential stiffness region
CD: Region of increasing tangential stiffness
DE: Terminal region

Fig. 3 Stress-Strain Curve of Unidirectional SiC/CAS Composite under Longitudinal Tension
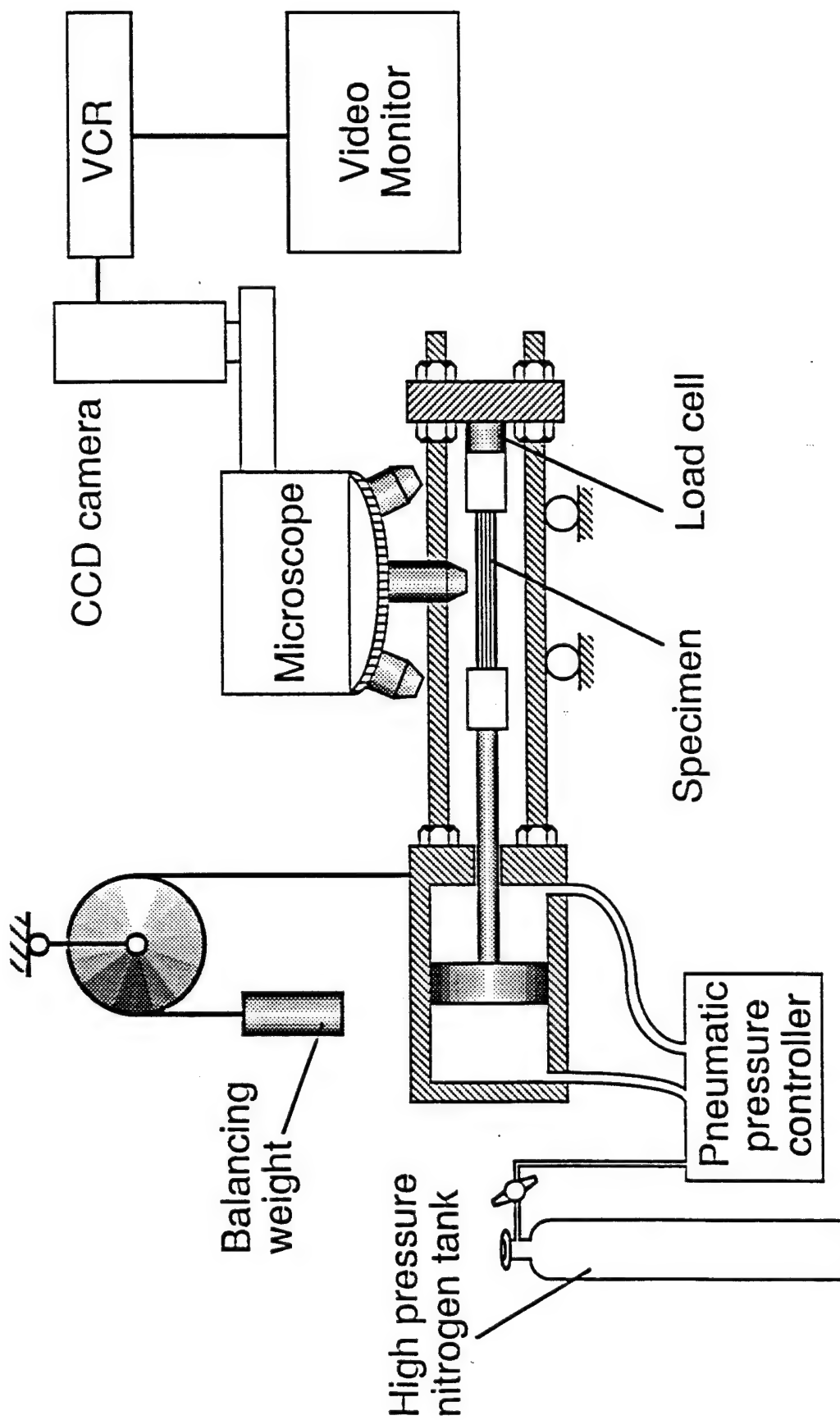
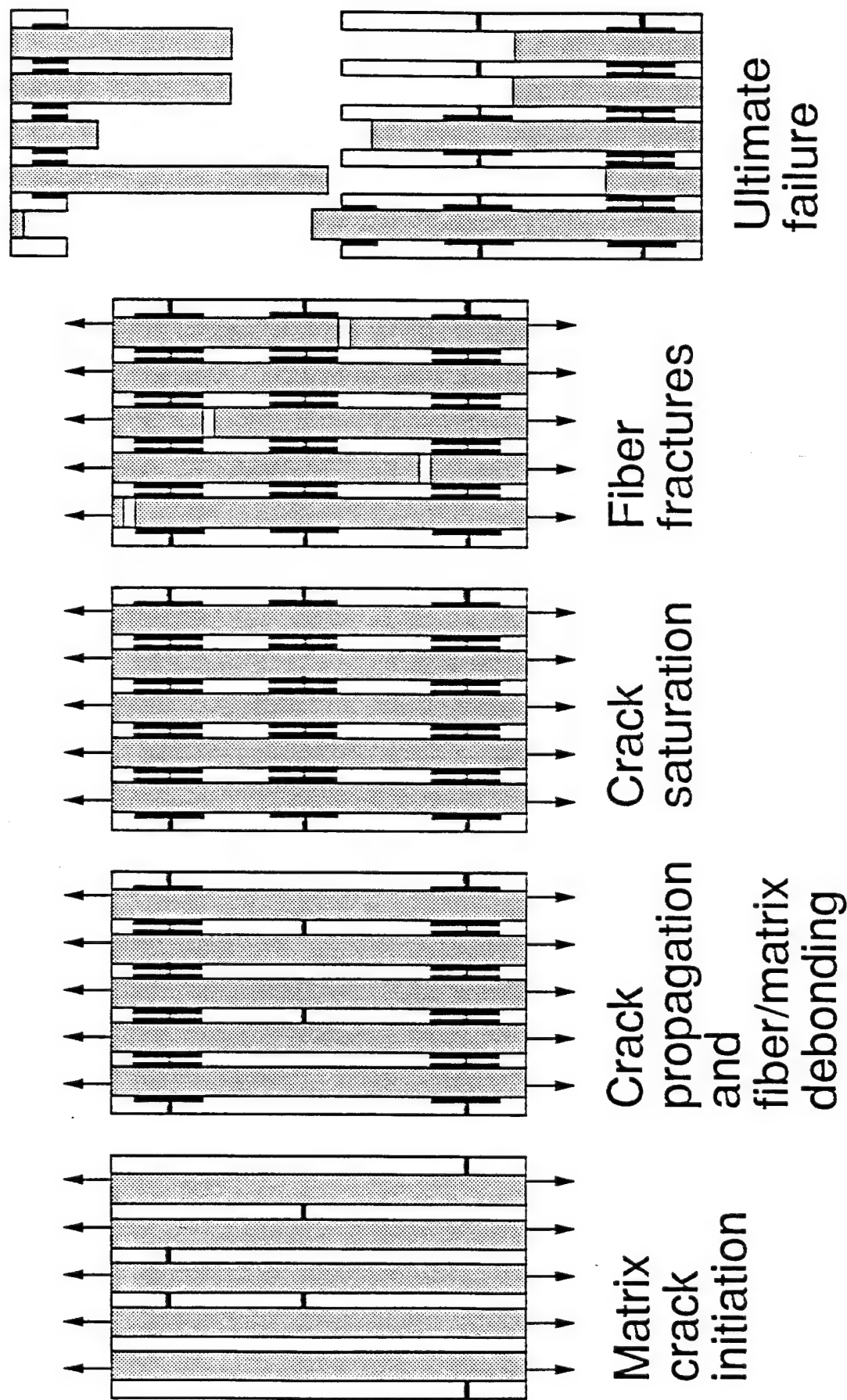Fig. 4 Setup for Real-Time Observation of Failure Mechanisms

Fig. 5 Damage Development in Unidirectional SiC/CAS Composite under Longitudinal Tension

Ultimate failure

Fiber fractures

Crack saturation

Crack propagation and fiber/matrix debonding
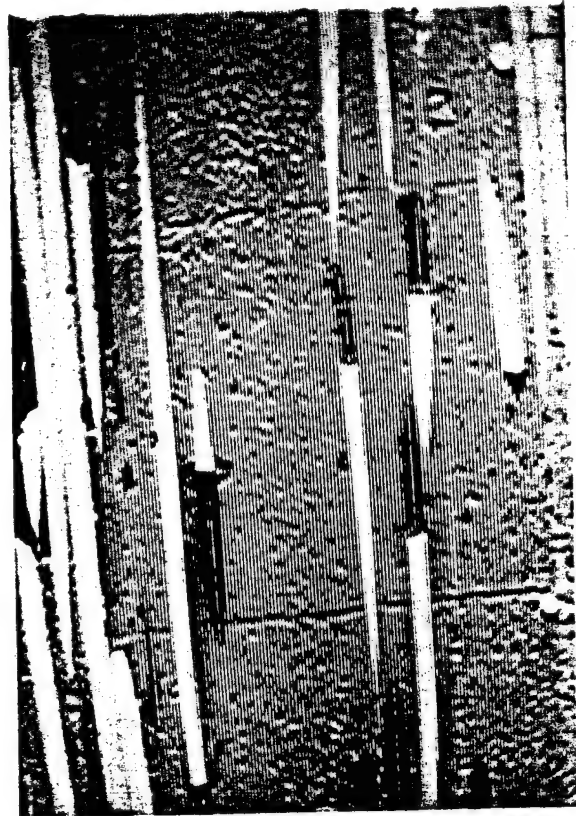
Matrix crack initiation

9

Matrix cracking was observed directly and recorded during loading (Fig. 6). Matrix crack density is plotted versus average strain and compared with the stress-strain curve in Fig. 7. This plot shows that matrix cracking starts very close to the proportional limit and its density varies nearly linearly with applied average strain up to a saturation level. This occurs at a strain of approximately 0.35 to 0.40% and usually corresponds to a minimum crack spacing of seven to ten fiber diameters.

Fiber/matrix debonding is very difficult to observe directly. Indirect evidence of debonding, through ultrasonic and acoustic emission measurements, will be discussed below. Whenever fiber fractures were observed, they always occurred at some distance from the matrix cracks and most likely at the end of the debonded region (Fig. 8). This is further illustrated by the SEM fractograph of a failure surface (Fig. 9).

2.3 Ultrasonic Investigations (21-23]

Ultrasonic techniques were developed for real-time monitoring of damage evolution in a unidirectional ceramic matrix composite under longitudinal tensile loading. A schematic diagram of the testing system used is shown in Fig. 10. A pair of transducers is mounted in contact with the specimen and the through-transmission signals are monitored during loading. Two types of transducers were used, longitudinal (compression) wave and shear wave transducers. Wavespeeds and attenuation corresponding to longitudinal and shear waves across the thickness (3-direction) of the specimen were determined and correlated with the macroscopic stress-strain behavior.
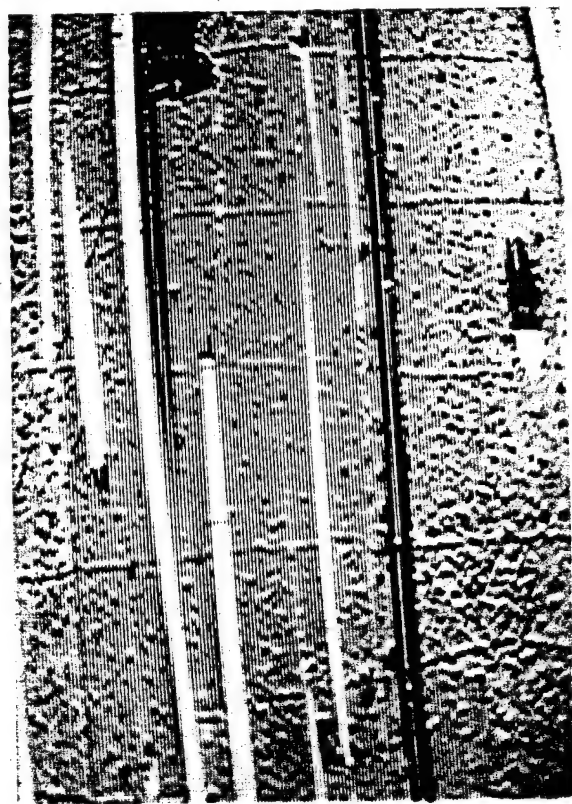
The change in attenuation of the longitudinal and shear waves, polarized in the parallel to the fiber direction, as a function of applied average strain is shown in Figs. 11 and 12 and compared with the corresponding stress-strain curve. Considering the previous microscopic observations of damage development, it
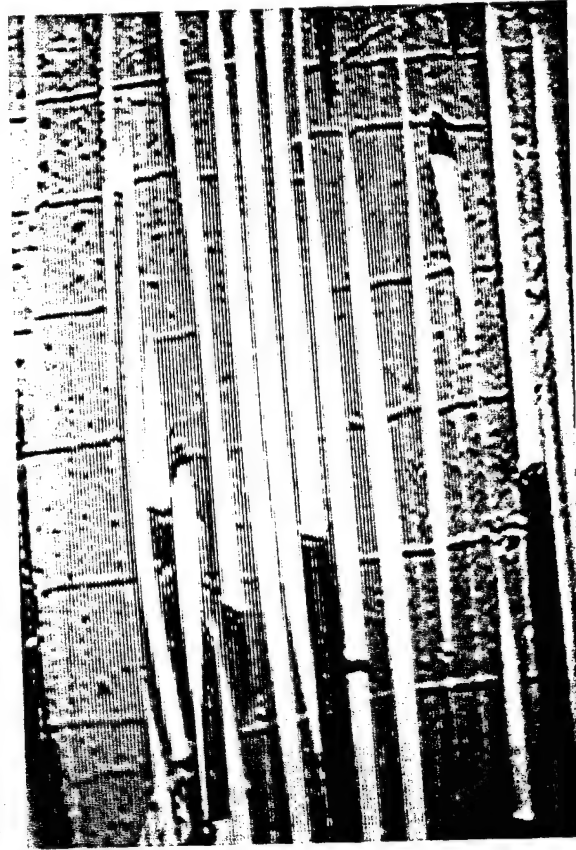
10
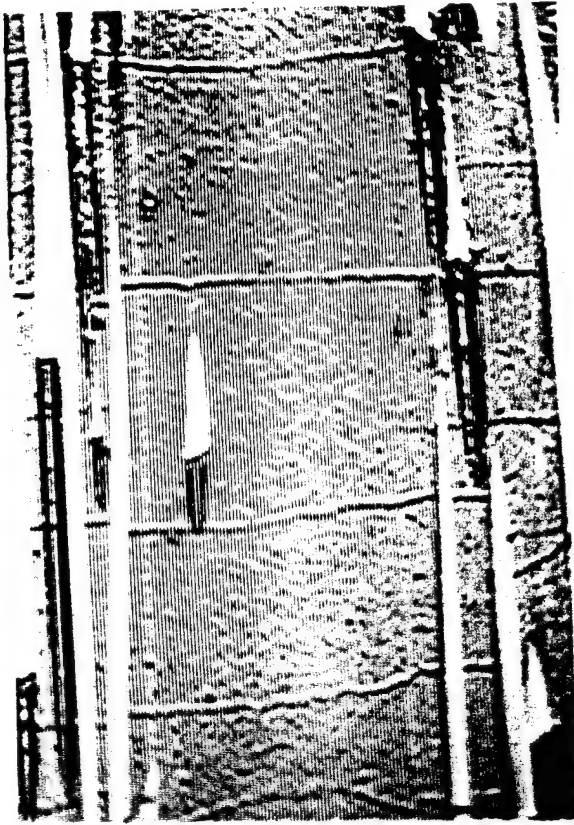
Fig. 6 Multiplication of Transverse Matrix Cracking in Unidirectional SiC/CAS Composite Under Longitudinal Tension. (a) σ = 25.7ksi, ϵ = 0.15%, (b) σ = 28.3ksi, ϵ = 0.23% (c) σ = 32.3ksi, ϵ = 0.31% (d) σ = 57.2ksi, ϵ = 0.68%.

11
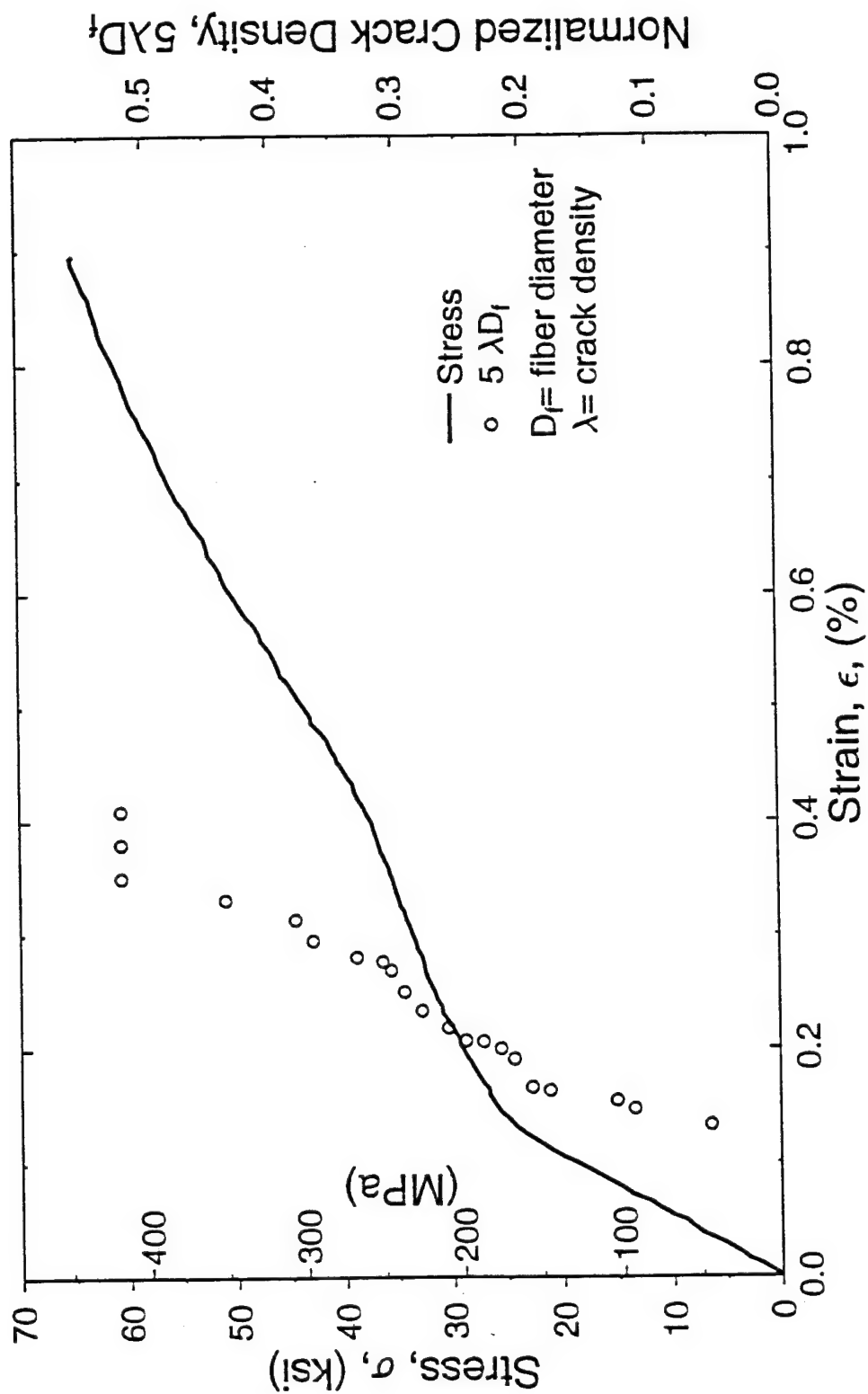
Fig. 7 Stress and Matrix Crack Density versus Strain in Unidirectional SiC/CAS Composite under Longitudinal Tension

TYPICAL FIBER BREAKS
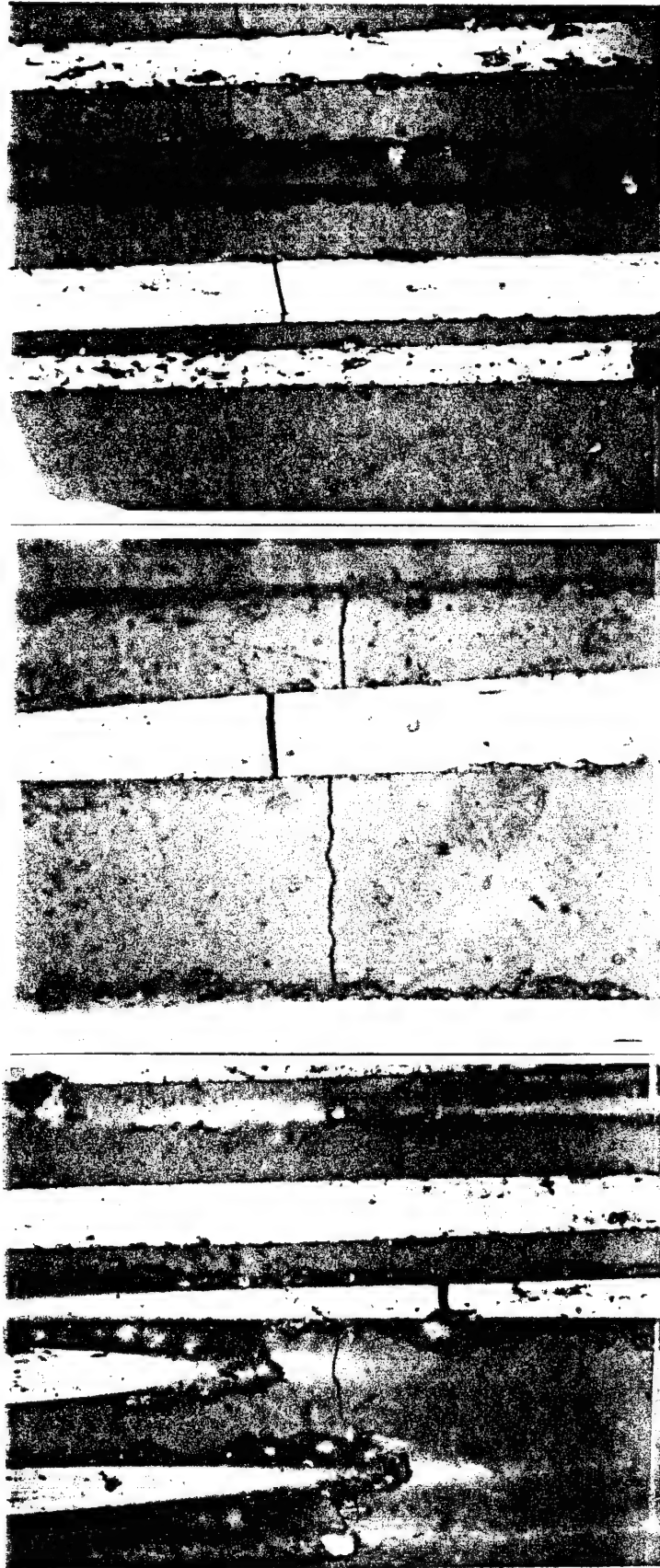
Fig. 8   Typical Fiber Fractures Near Matrix Cracks with Fiber–Matrix Debonding

13

Fig. 9   SEM Fractograph of Failure Surface under Longitudinal
Tension Illustrating Fiber Breaks and Pullout.

14

Fig. 10 Schematic of Ultrasonic System

15

Fig. 11 Change in Attenuation of Longitudinal Waves due to Induced Damage during Loading and Associated Stress-Strain Curve

Fig. 12 Change in Attenuation of Shear Wave due to Induced Damage during Loading and Associated Stress-Strain Curve

seems that the attenuation and wavespeed of the longitudinal wave are particularly sensitive to matrix cracking and relatively insensitive to fiber-matrix debonding. On the other hand, the attenuation and wavespeed of the t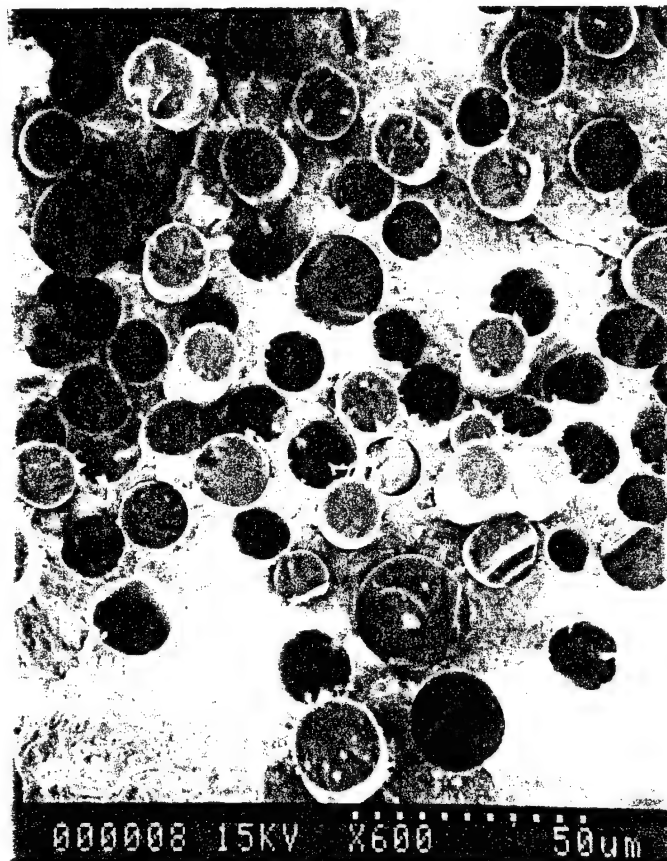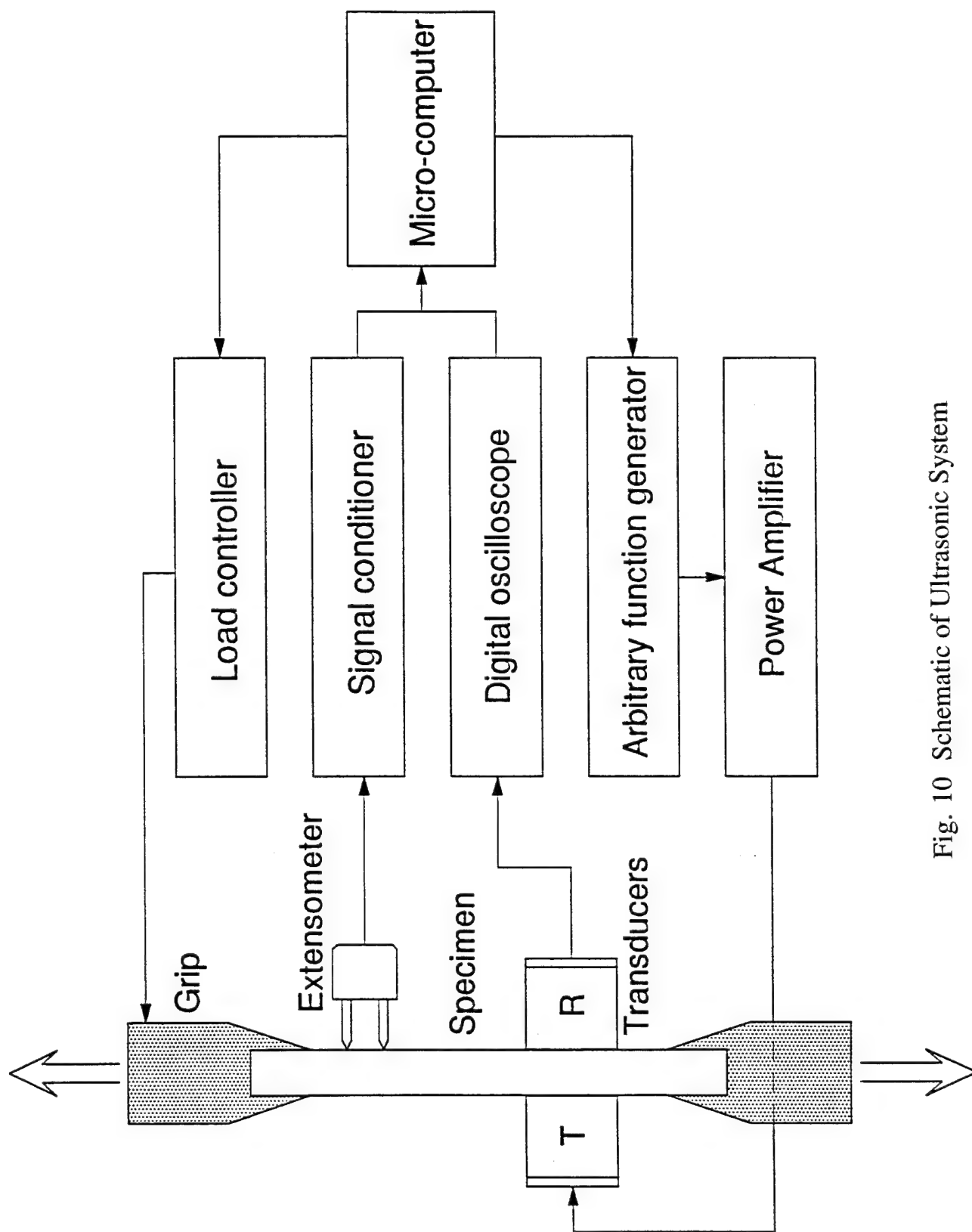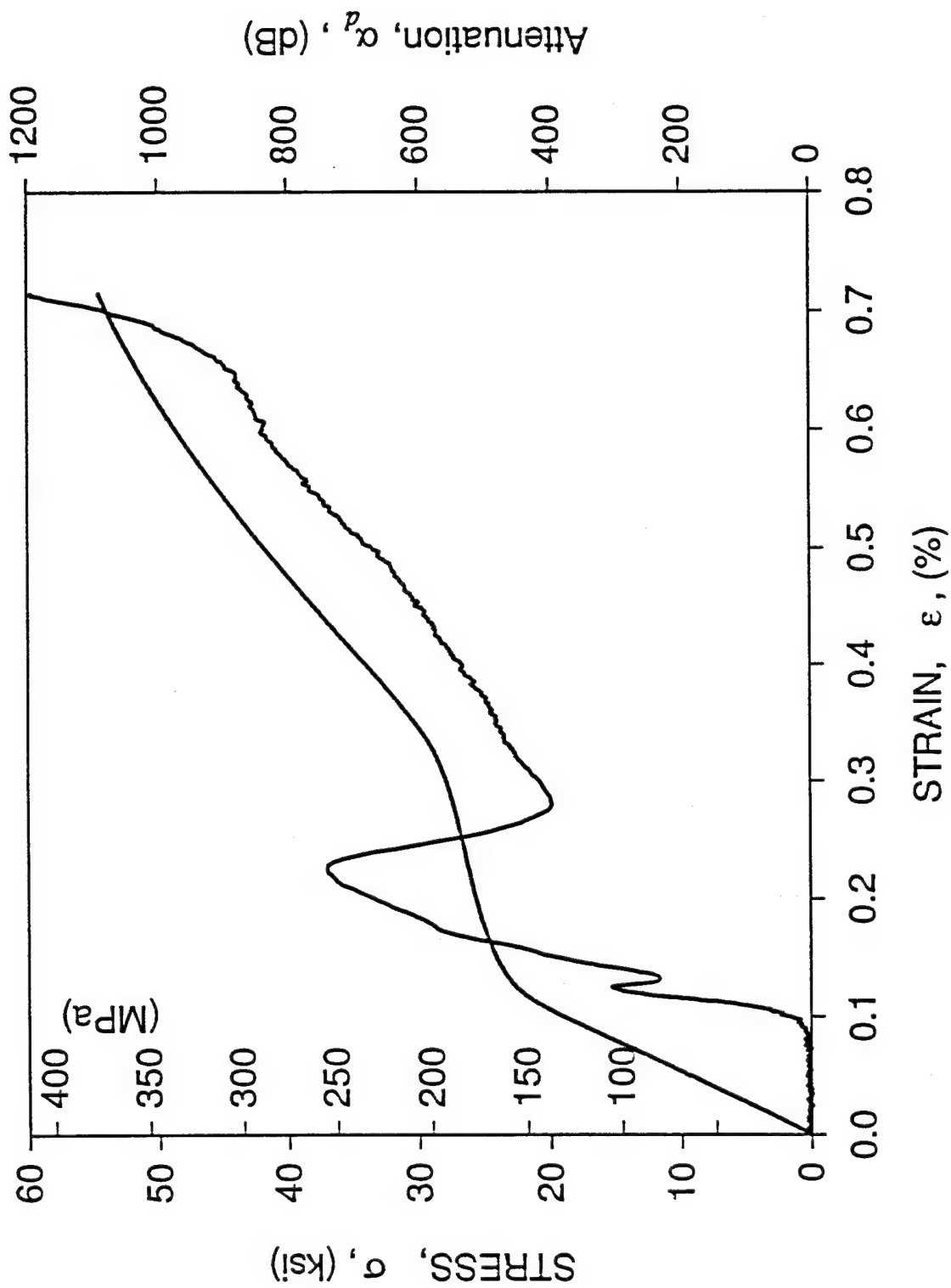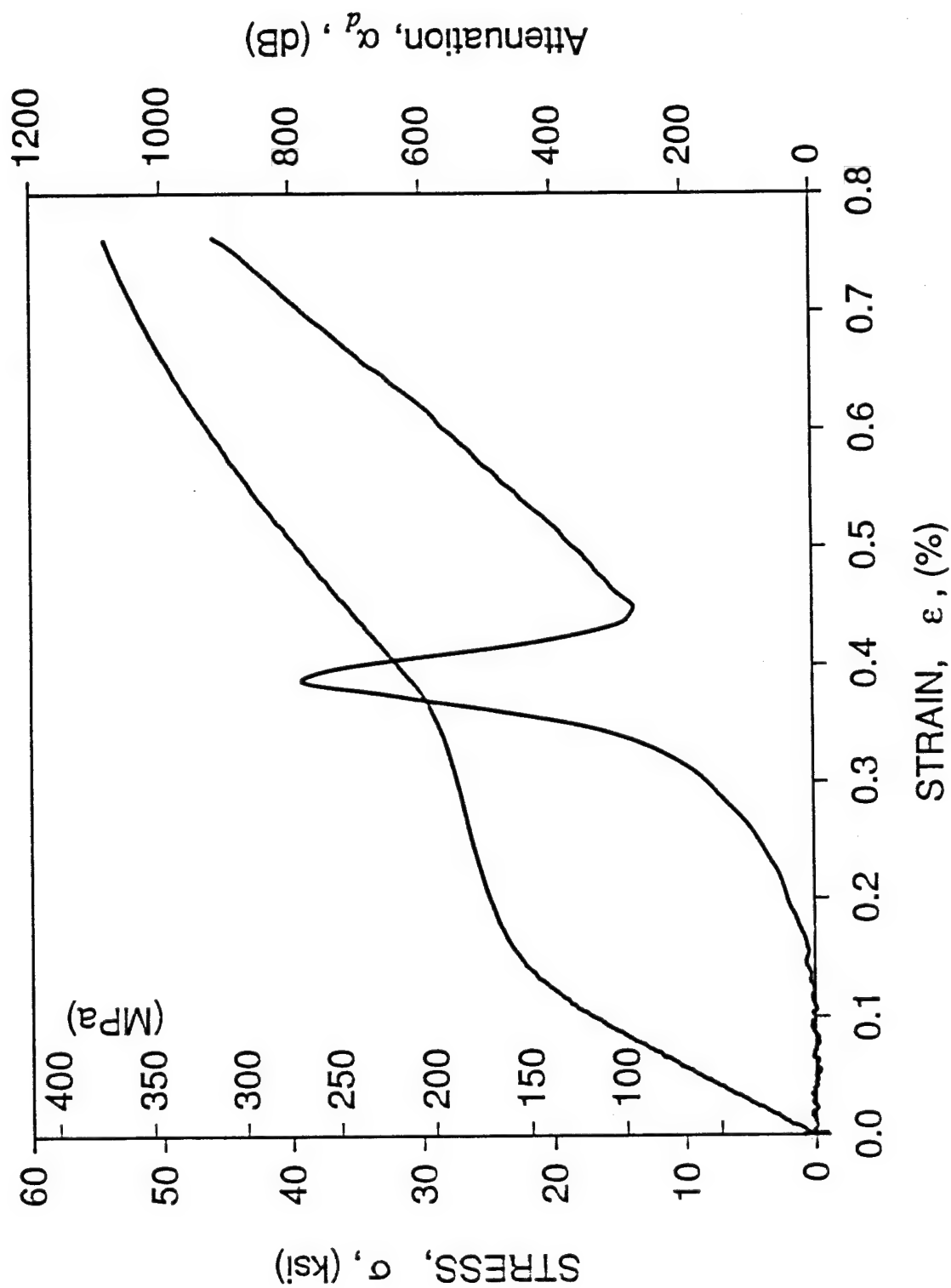ransverse (shear) wave seem to be most sensitive to fiber-matrix debonding. All ultrasonic measures (attenuation and wavespeeds of longitudinal and shear waves) seem to respond to the last stage of damage development consisting primarily of fiber fractures.

The attenuation and wavespeed of transverse shear waves, polarized in the normal to the fiber direction, were also measured and used to evaluate the extent of fiber-matrix debonding. The varying transverse shear modulus G_{23} can be determined from the measured wavespeed of the shear wave during the entire process of loading. In addition to the wavespeed the attenuation of the wave was measured and plotted in normalized form versus applied strain along with the stress-strain curve (Fig. 13). It is clear that the normalized signal loss starts at the point of matrix crack initiation and continuous at some moderate rate up to the strain hardening region. At that point, believed to be the region of extensive fiber-matrix debonding, the attenuation rate of the shear wave increases abruptly.

2.4 Acoustic Emission Study of Failure Mechanisms [24]

Acoustic emission techniques were used to monitor damage mechanisms and evolution in a unidirectional SiC/CAS ceramic composite under monotonic longitudinal tensile loading. In addition to the monotonic loading, loading/unloading tests were performed.

Three major types of damage were investigated; transverse matrix cracking, fiber-matrix interfacial debonding, and fiber fractures. Acoustic emission events were monitored in real time during loading and unloading and they were correlated with the corresponding stress-strain curves and microscopically recorded damage mechanisms.
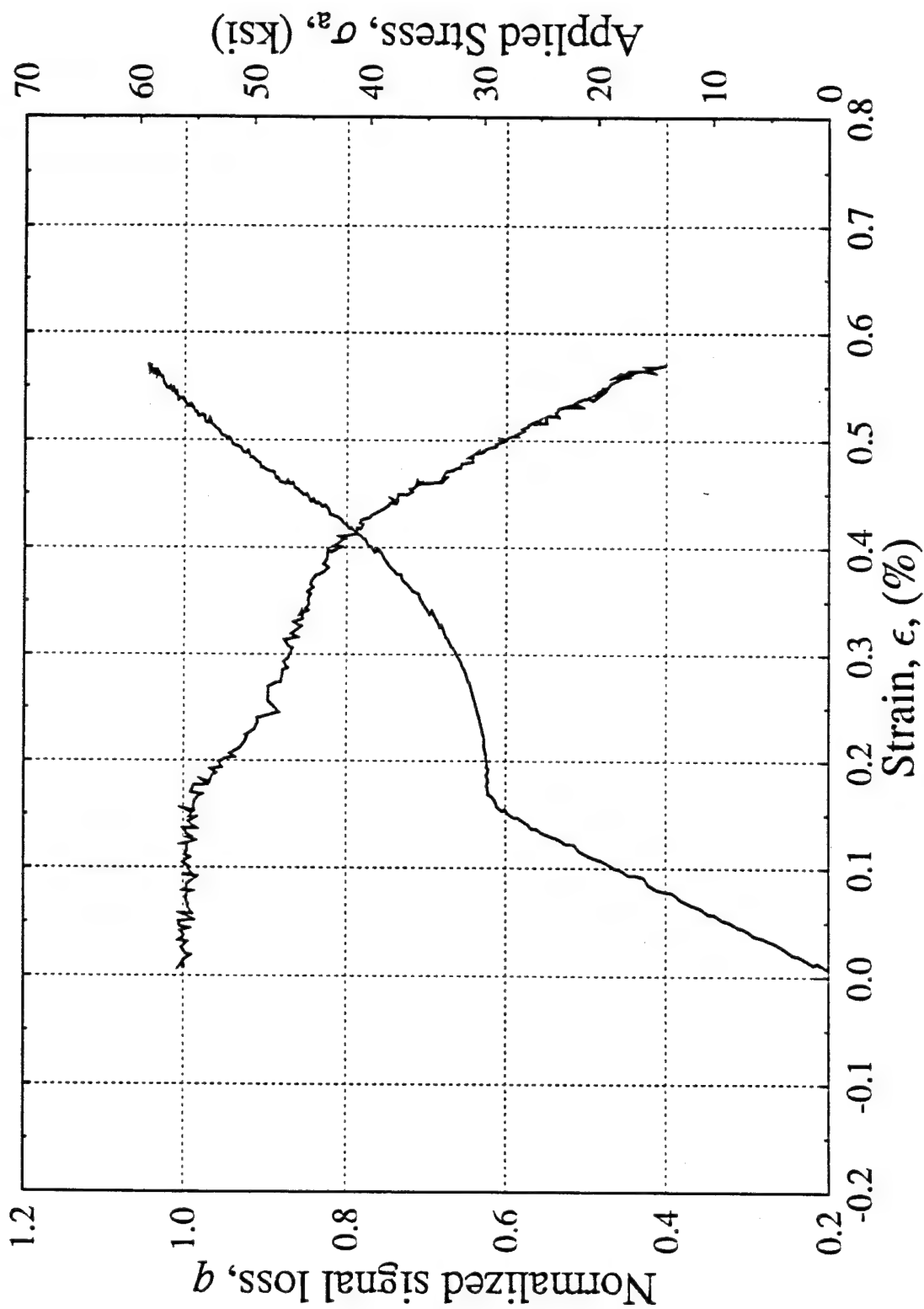
18

Fig. 13 Change in Normalized Signal Loss due to Induced Damage during Loading with Superimposed Stress-Strain Curve

The test setup is shown in Fig. 14. The cumulative acoustic emission counts are plotted versus strain and compared with the stress-strain curve in Fig. 15. The onset of AE corresponds to the proportional limit of the material. The cumulative AE output increases linearly with applied strain up to the strain hardening region, which corresponds to extensive fiber-matrix debonding. At that point, the cumulative AE rate increases abruptly for some time and then it drops to a lower rate up to ultimate failure. The cumulative AE counts were also compared with matrix crack density measurements (Fig. 16). The correspondence of the various features of the stress-strain, crack density and AE curves and their physical significance are illustrated in Fig. 17.

The amplitude distribution of AE events and its relationship to the failure mechanisms were investigated. The variation of cumulative AE counts of various amplitude ranges with applied strain is shown in Figs. 18 and 19, and histograms of AE events of various amplitude ranges are shown in Fig. 20. It can be deduced that high amplitude signals correspond to matrix cracking in region ABC and level off at matrix crack saturation. It can also be deduced that the extensive debonding activity in region CD produces medium to lower amplitude signals.

Several loading/unloading tests were conducted as shown in Fig. 21. Upon reloading, the material follows the stress-strain curve obtained under monotonic loading. This shows that the loading-unloading process does not introduce any additional damage. Stress and cumulative AE counts versus strain for some loading-unloading loops are shown in Figs. 22-24. These records show that AE increases up to the peak applied strain and no AE activity exists during unloading. Furthermore, upon reloading during the following loop, no significant AE output is produced until the previous peak strain has been exceeded, i.e., the material shows the Kaiser effect. This behavior continues for successive loading-unloading loops up to the strain level corresponding to strain hardening or matrix crack saturation or
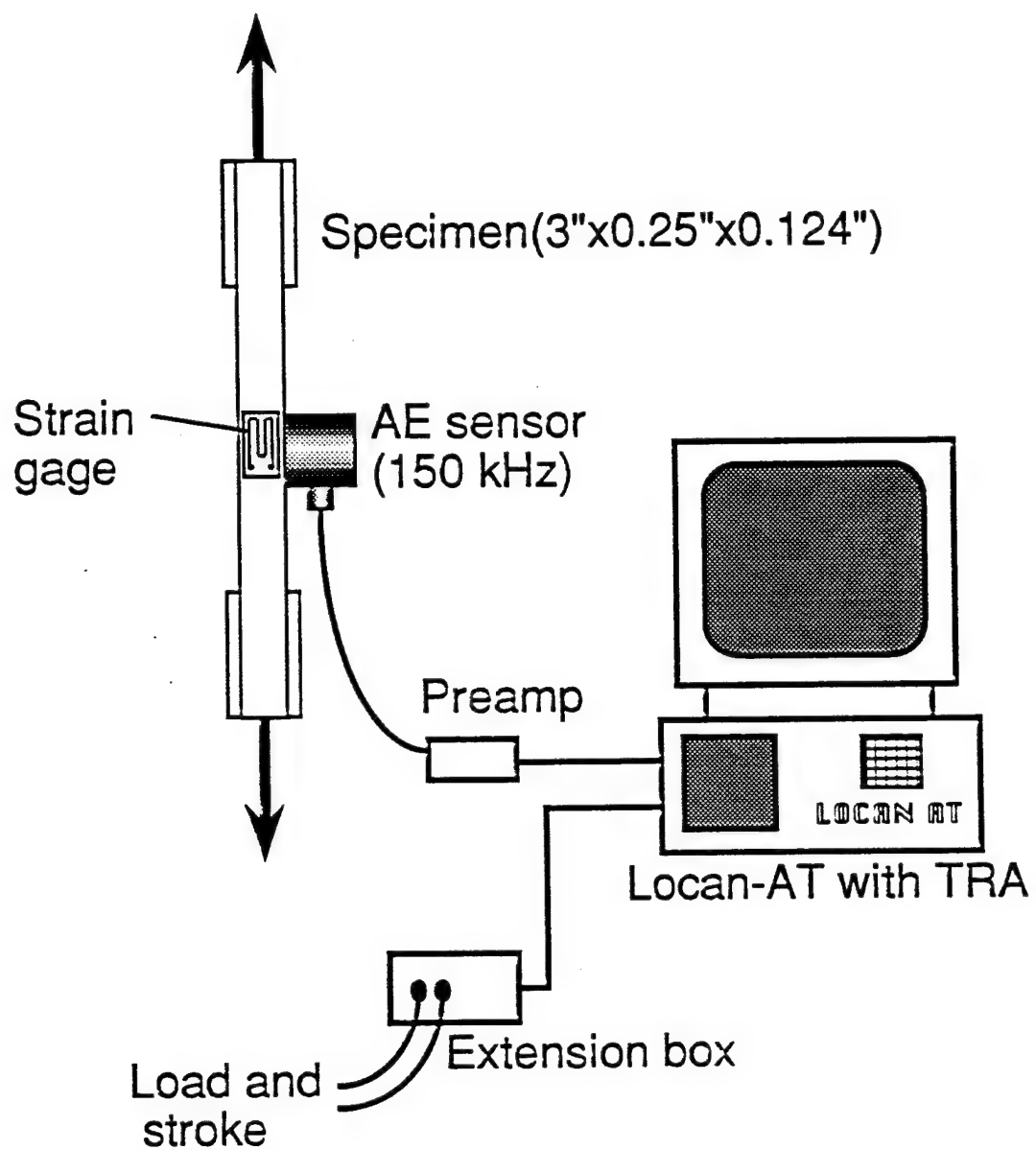
Fig. 14   Setup for Acoustic Emission Test
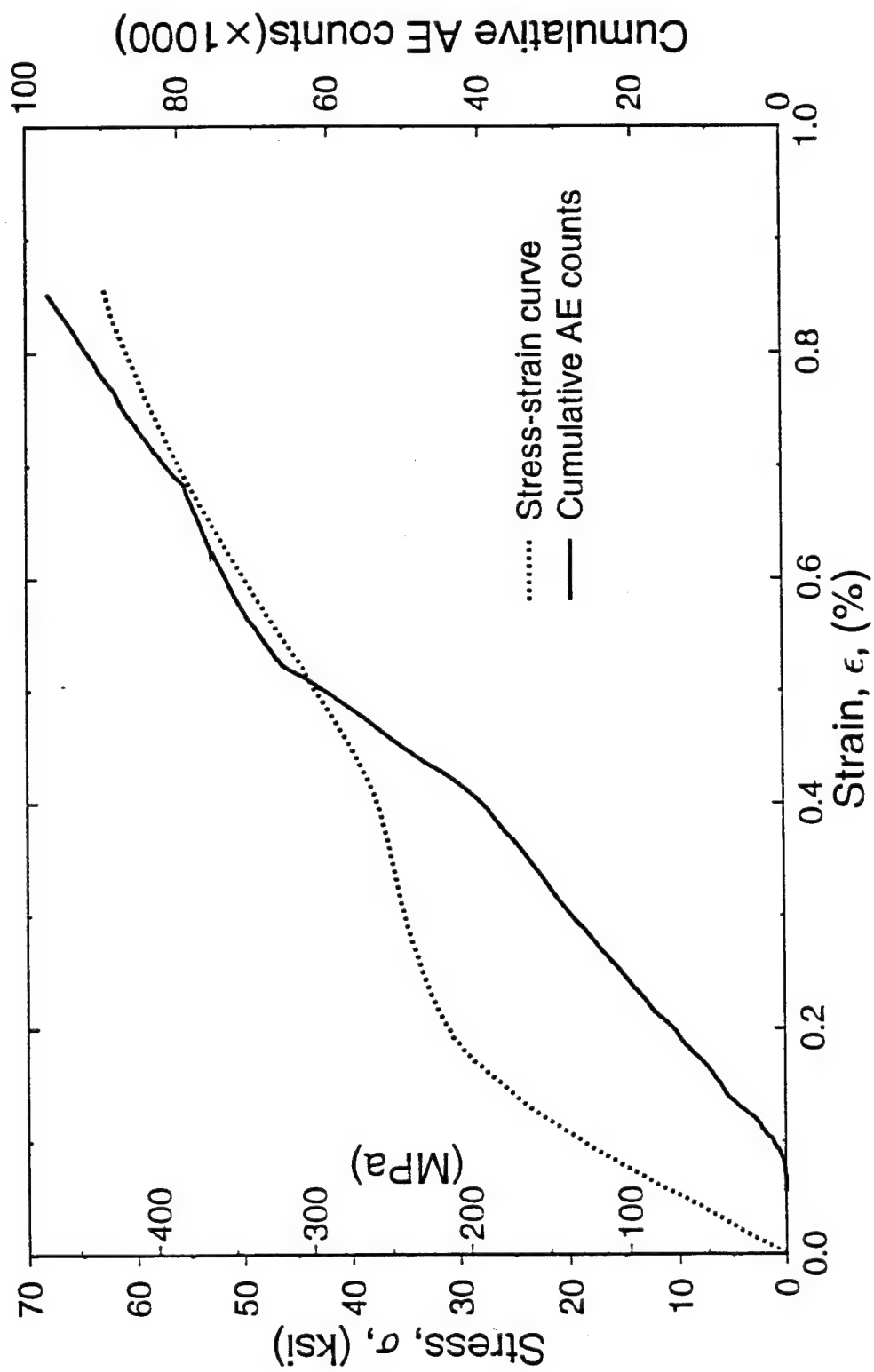
Fig. 15 Stress and Cumulative AE Counts versus Strain for Unidirectional SiC/CAS Composite under Longitudinal Tension
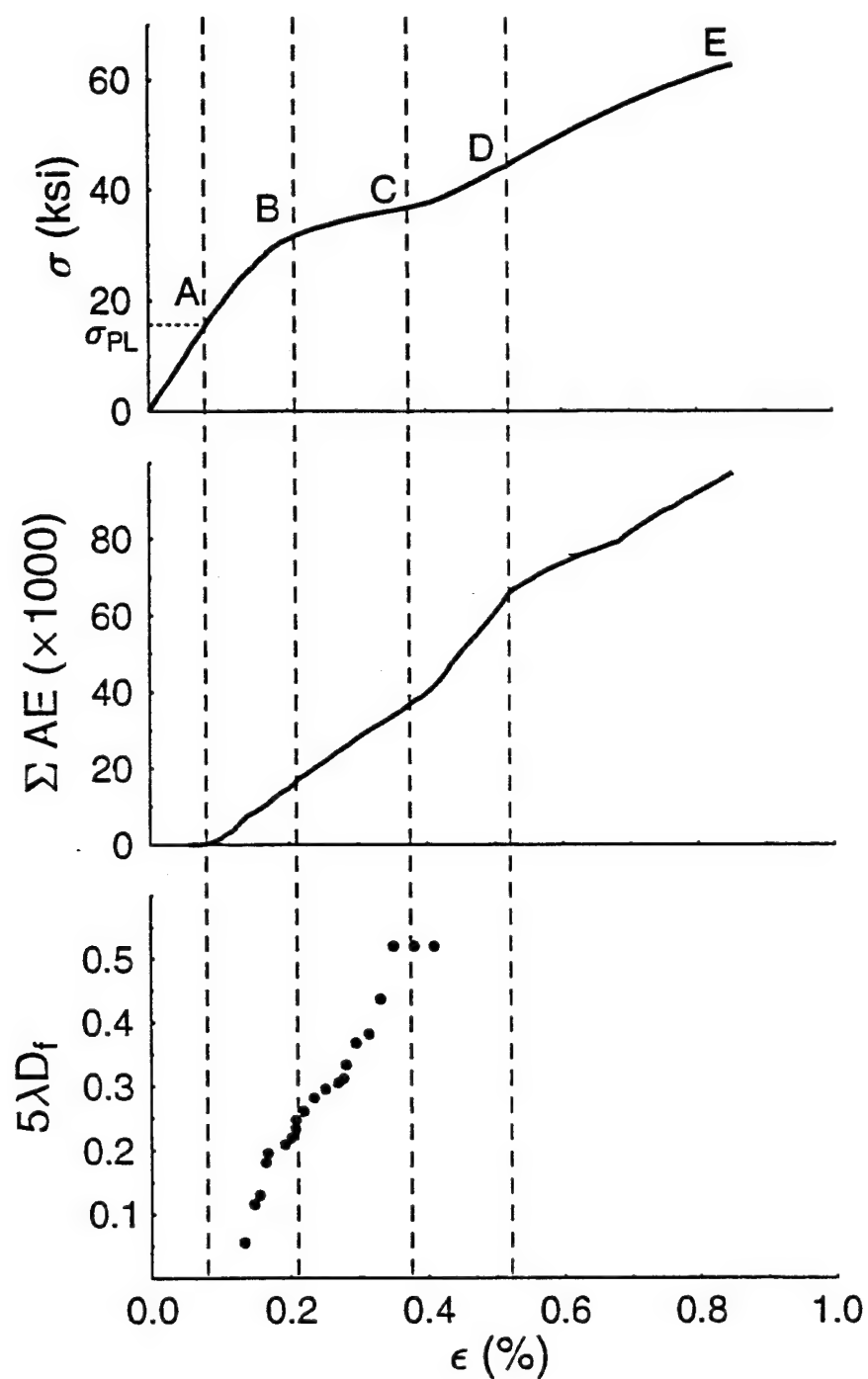
Fig. 16   Stress, Cumulative AE Counts, and Matrix Crack Density versus Strain
for Unidirectional SiC/CAS Composite under Longitudinal Tension
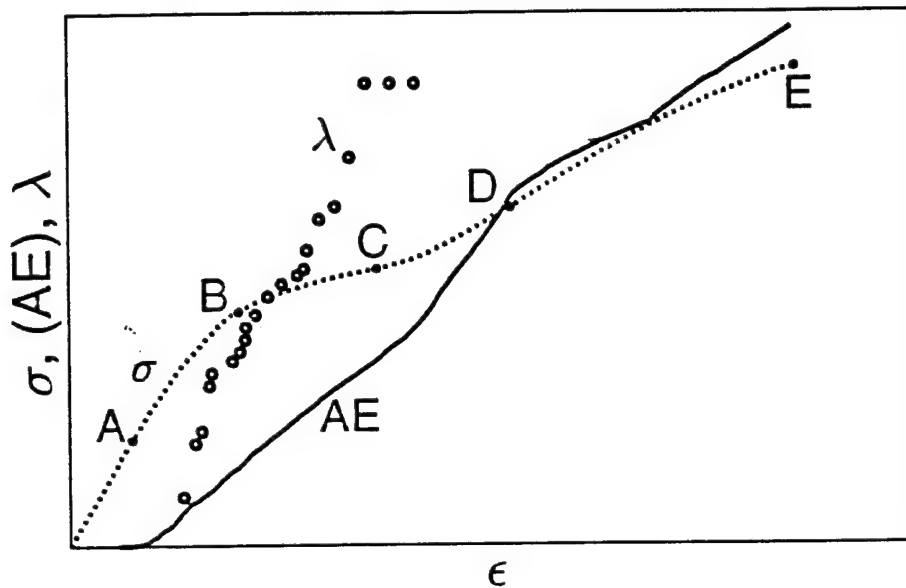
A: Proportional limit
                AE initiation
                Crack initiation

AB: Slight stiffness reduction (nonlinear behavior)
                Constant rate AE
                Crack extension (continuous cracks)

BC: Plateau or low tangential stiffness region
                Crack multiplication
                Fiber/matrix debonding
                Continued constant AE rate

C: Crack saturation
                Increased AE rate
                (for low and moderate amplitudes)

CD: Region of increasing tangential stiffness
                High rate AE (low to intermediate amplitude)
                Fiber/matrix debonding/sliding

DE: Terminal region
                Fiber fracture and pullout
                Reduced AE rate

Fig. 17   Correspondence of Features and Physical Significance of
Stress-Strain, Crack Density and AE Curves
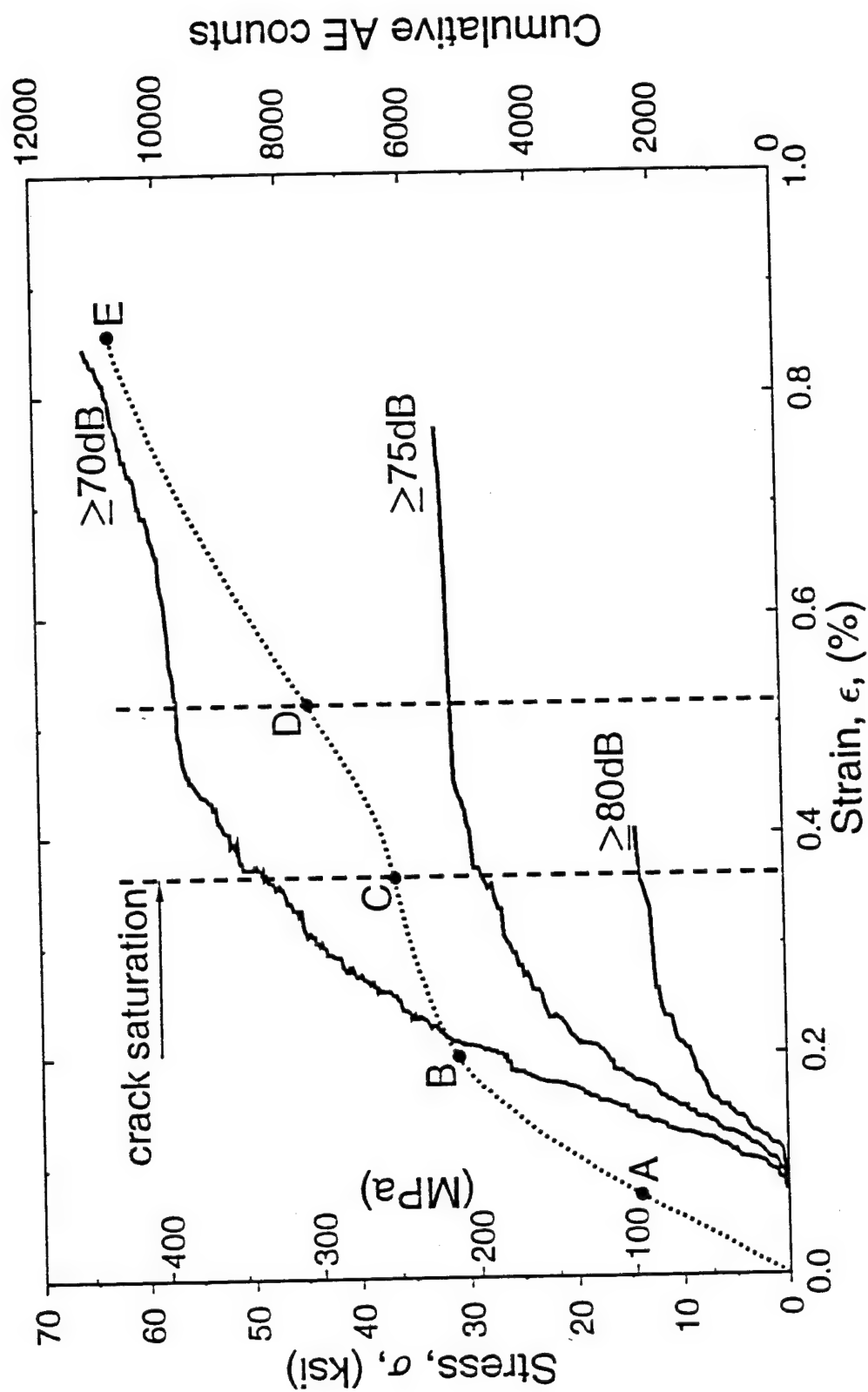
Fig. 18   Cumulative AE Counts for High Amplitude Thresholds versus   Strain for a Unidirectional SiC/CAS Composite under Longitudinal Tension
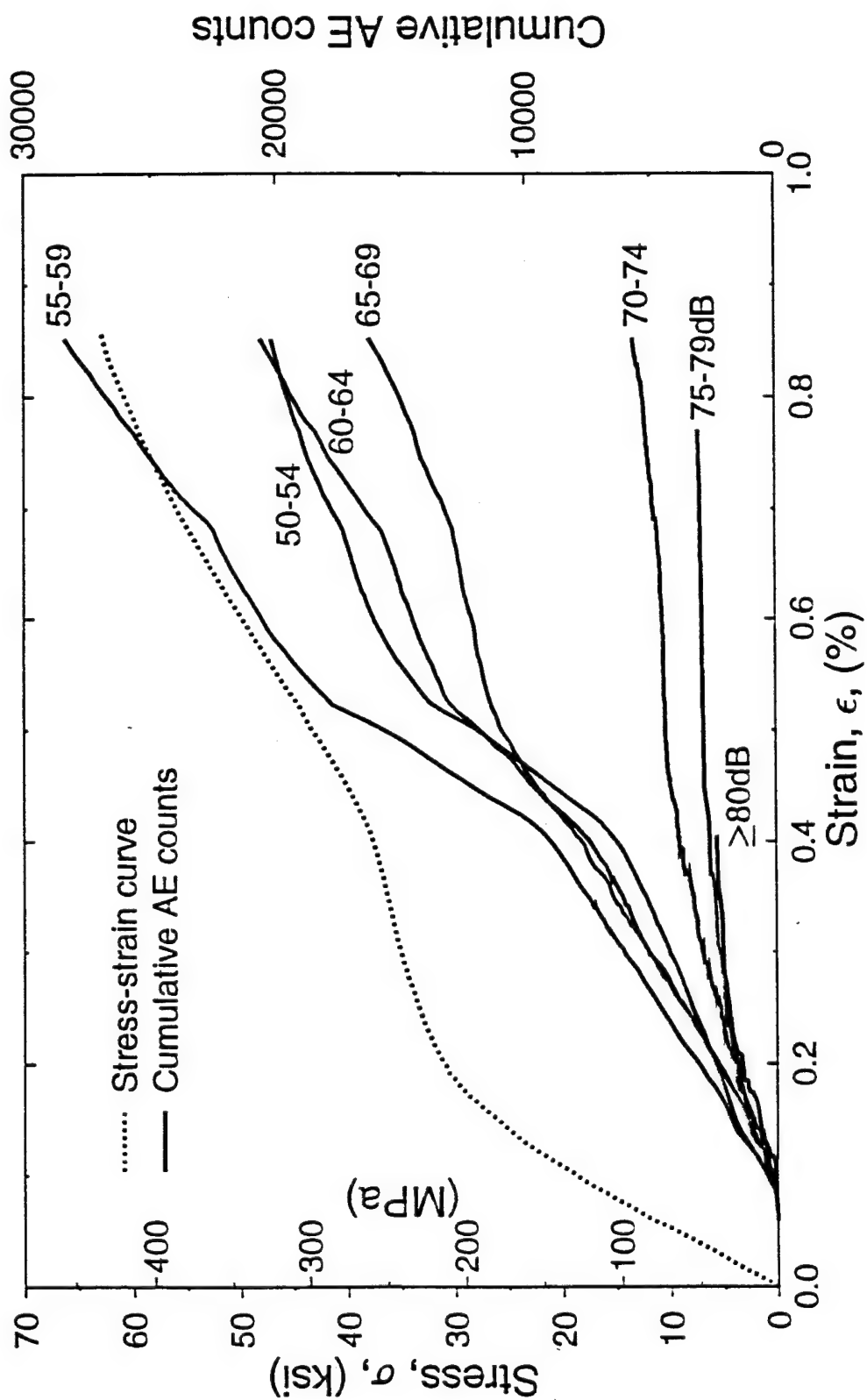
Fig. 19   Cumulative AE Counts of Various Amplitude Ranges for a
Unidirectional SiC/CAS Composite under Longitudinal Tension
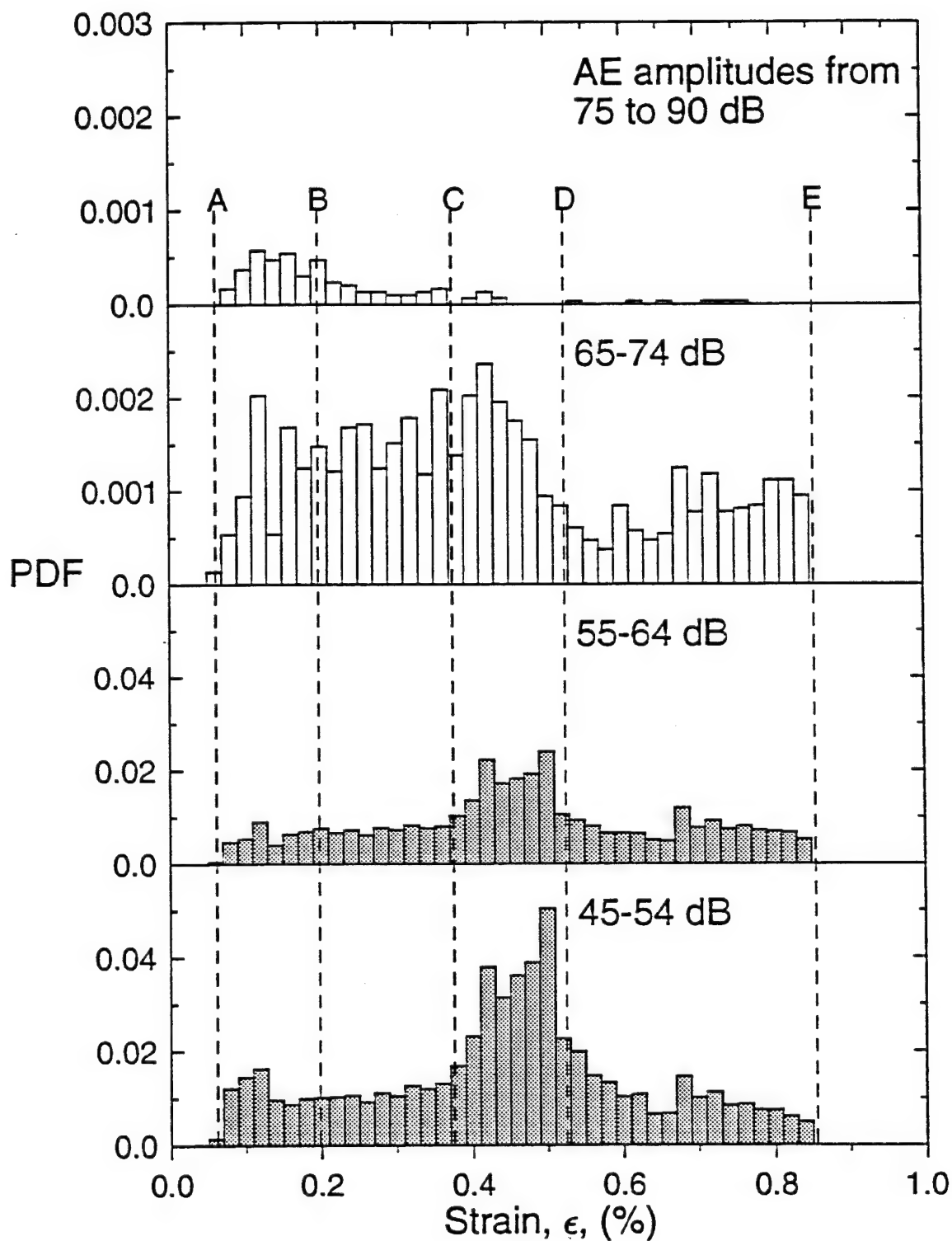
Fig. 20   Histogram of AE Events for Various Amplitude Ranges
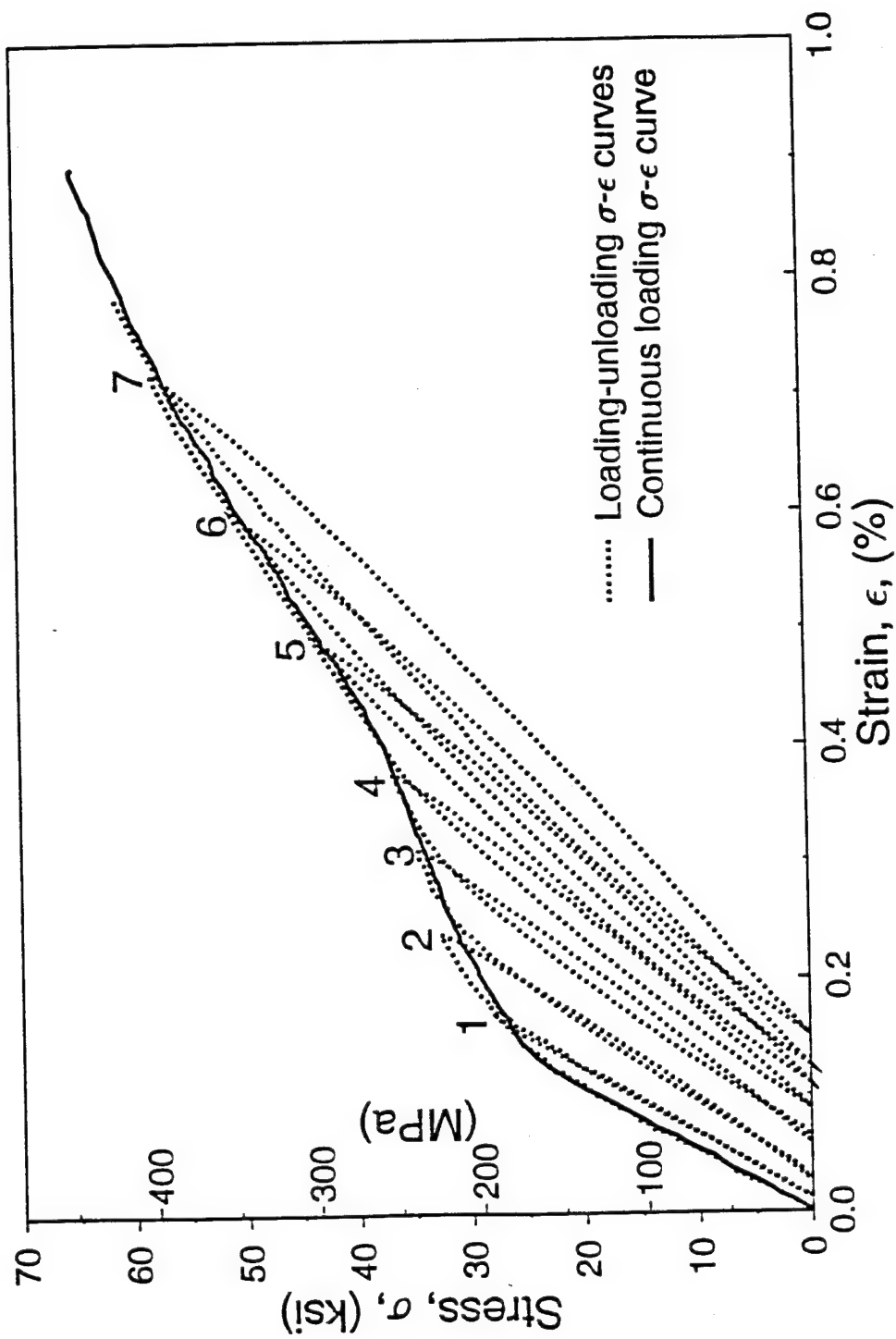
Fig. 21 Continuous Loading and Loading-Unloading Stress-Strain Curves for Unidirectional SiC/CAS Composite under Uniaxial Tension

Fig. 22 Stress and Cumulative AE Counts versus Strain for Loading and
Unloading of Unidirectional SiC/CAS Composite under
Longitudinal Tension (Loop 1)

Fig. 23   Stress and Cumulative AE Counts versus Strain for Loading and
Unloading of Unidirectional SiC/CAS Composite under
Longitudinal Tension (Loop 2)

Fig. 24 Stress and Cumulative AE Counts versus Strain for Loading and Unloading of Unidirectional SiC/CAS Composite under Longitudinal Tension (Loop 5)

31

extensive fiber-matrix debonding (region CD). When the corresponding strain level (approximately 0.5%) is reached during a loading-unloading loop (loop 6) an abrupt change in AE rate occurs (Figs. 25, 26). Furthermore, upon unloading additional AE output is recorded which is convincing proof of debonding and frictional sliding. The combined loading-unloading stress-strain loops and corresponding AE output are shown in Fig. 27. The above observations show that most of the debonding and sliding occur after matrix crack saturation.

3. ANALYTICAL STUDIES OF UNIDIRECTIONAL COMPOSITE

3.1 Shear Lab Model for Longitudinal Tension [12, 13, 14]

A modified shear lag analysis started earlier was further extended and refined. It is based on a cylindrical composite element containing a central fiber and two transverse matrix cracks. The basic assumptions of this analysis are that (1) the fiber and matrix are bonded initially and even after multiple matrix cracking, (2) the axial load carried by the matrix is proportional to the difference in average axial displacements of the matrix and fiber, (3) the variation of the shear stress in the radial direction is linear in the fiber and inverse quadratic in the matrix, and (4) the influence of radial displacements in matrix and fiber are neglected. The stress level at crack initiation is given by

$$\sigma_a = \frac{E_1}{E_m} (F_{mt} - \sigma_{rm}) \tag{1}$$

where

σ_a = applied stress in composite

σ_{rm} = residual axial stress in matrix

F_{mt} = matrix tensile strength

E_m = matrix modulus

E_1 = initial longitudinal modulus of composite ($E_f V_f + E_m V_m$)

E_f = fiber modulus

V_f, V_m = fiber and matrix volume ratios, respectively

32
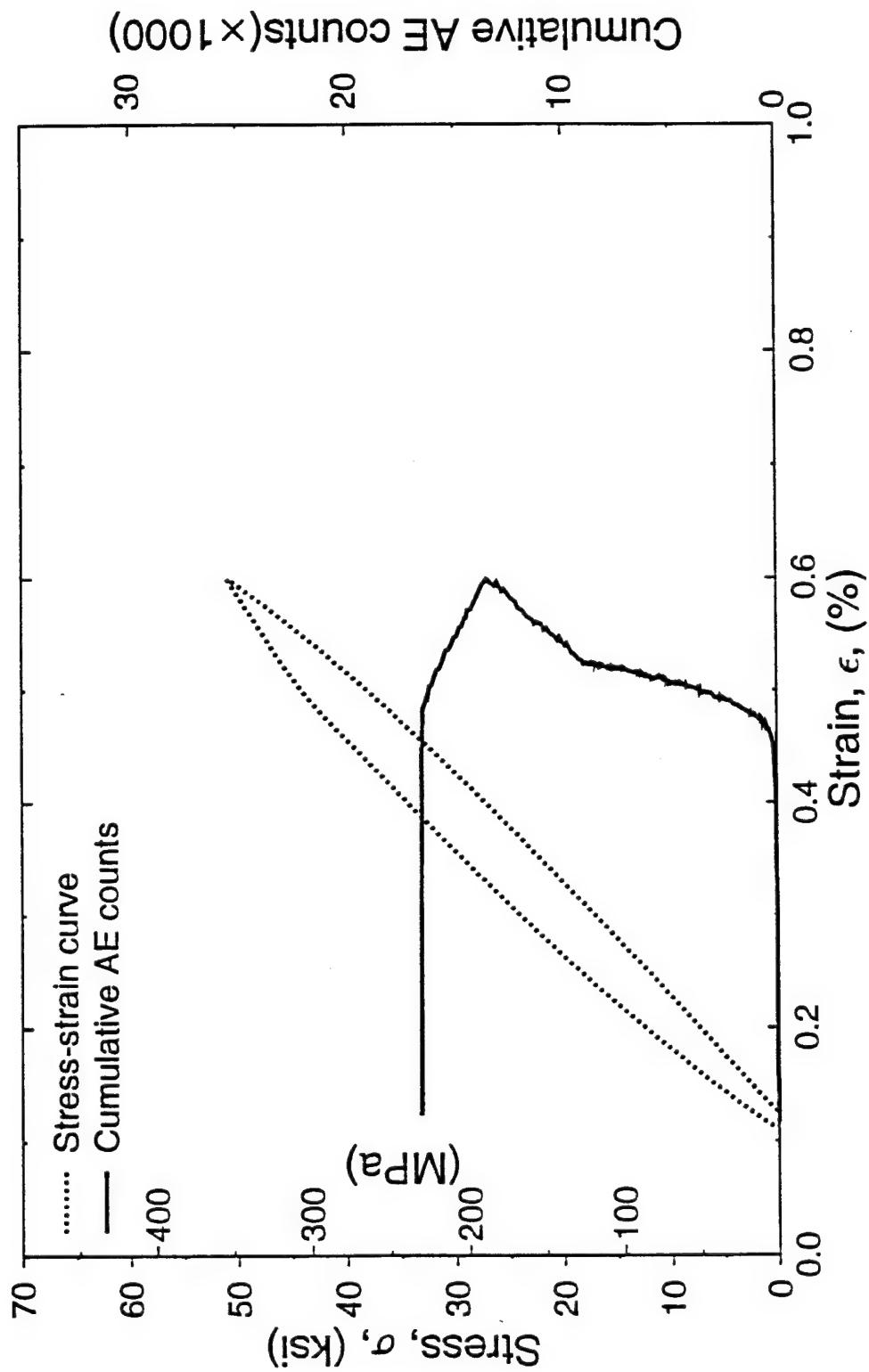
Fig. 25   Stress and Cumulative AE Counts versus Strain for Loading and
Unloading of Unidirectional SiC/CAS Composite under
Longitudinal Tension (Loop 6)
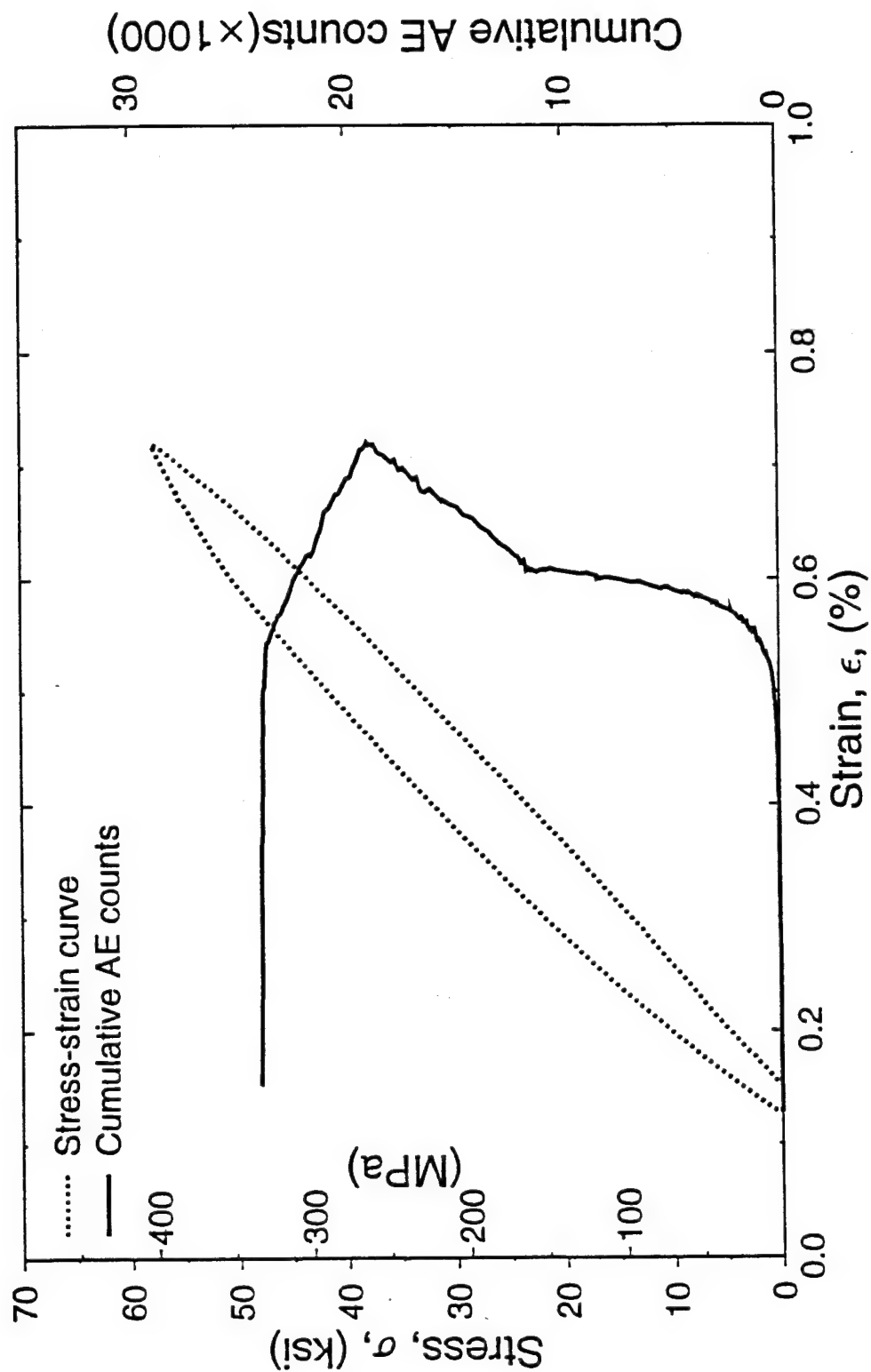
Fig. 26 Stress and Cumulative AE Counts versus Strain for Loading and Unloading of Unidirectional SiC/CAS Composite under Longitudinal Tension (Loop 7)

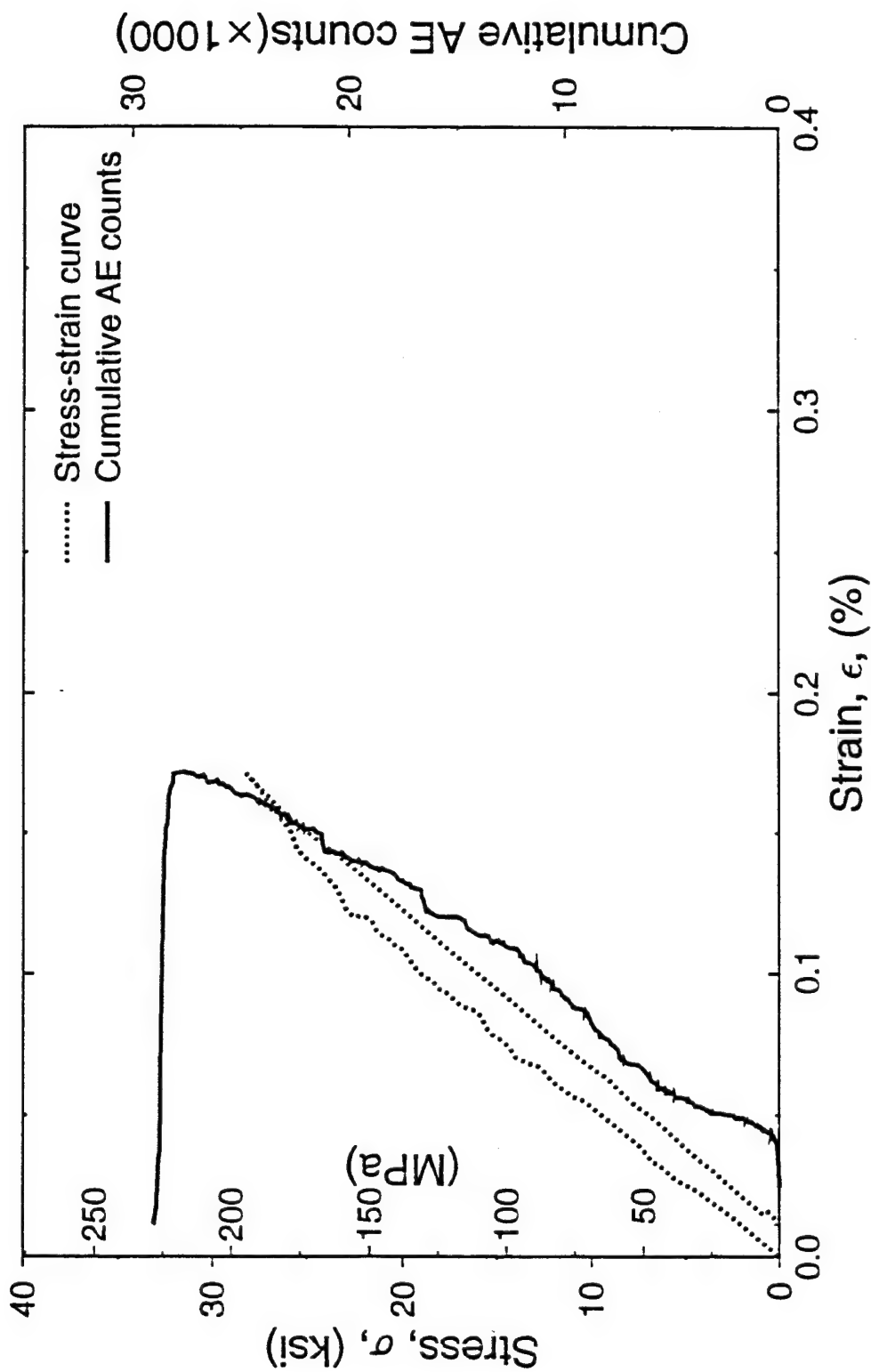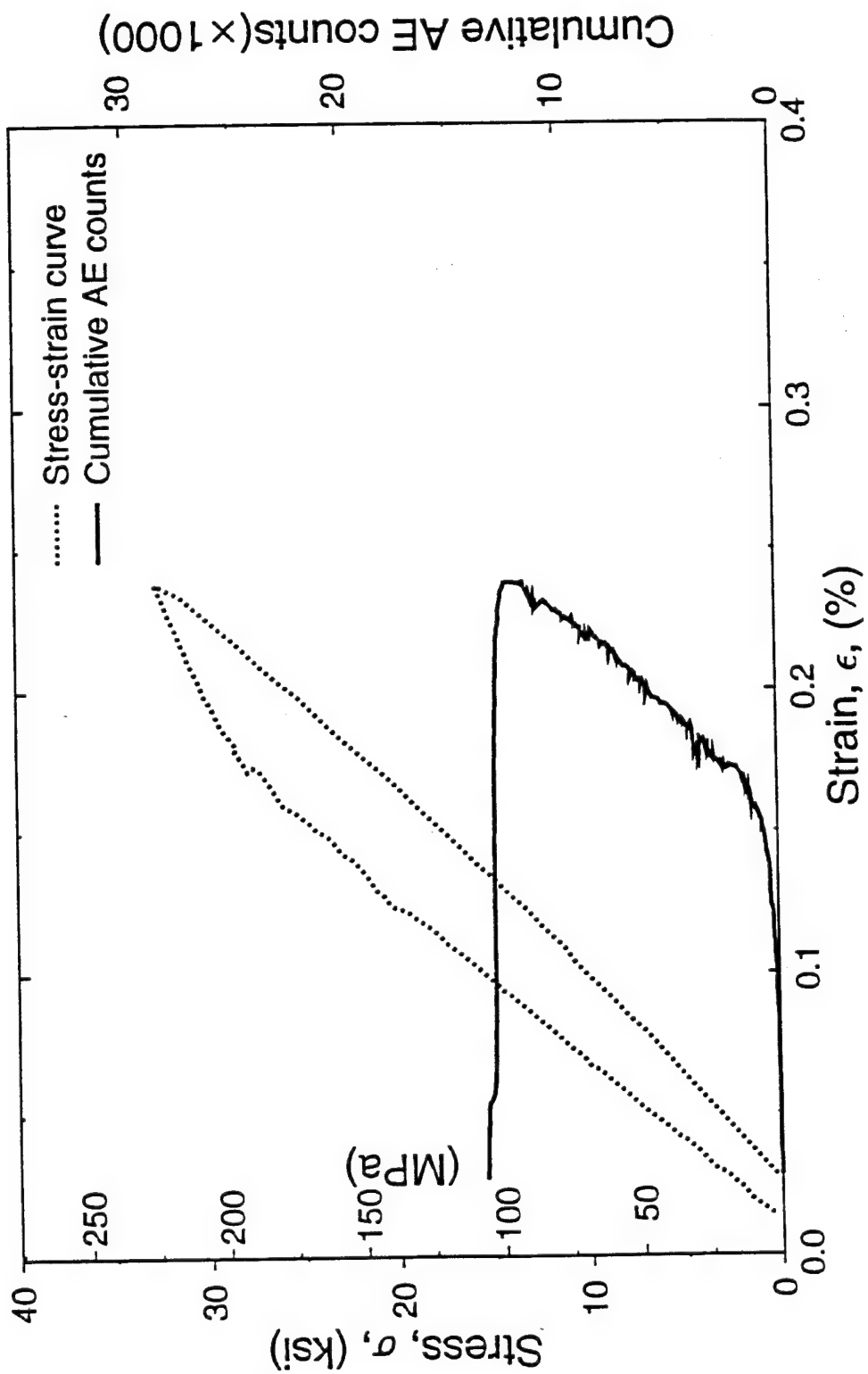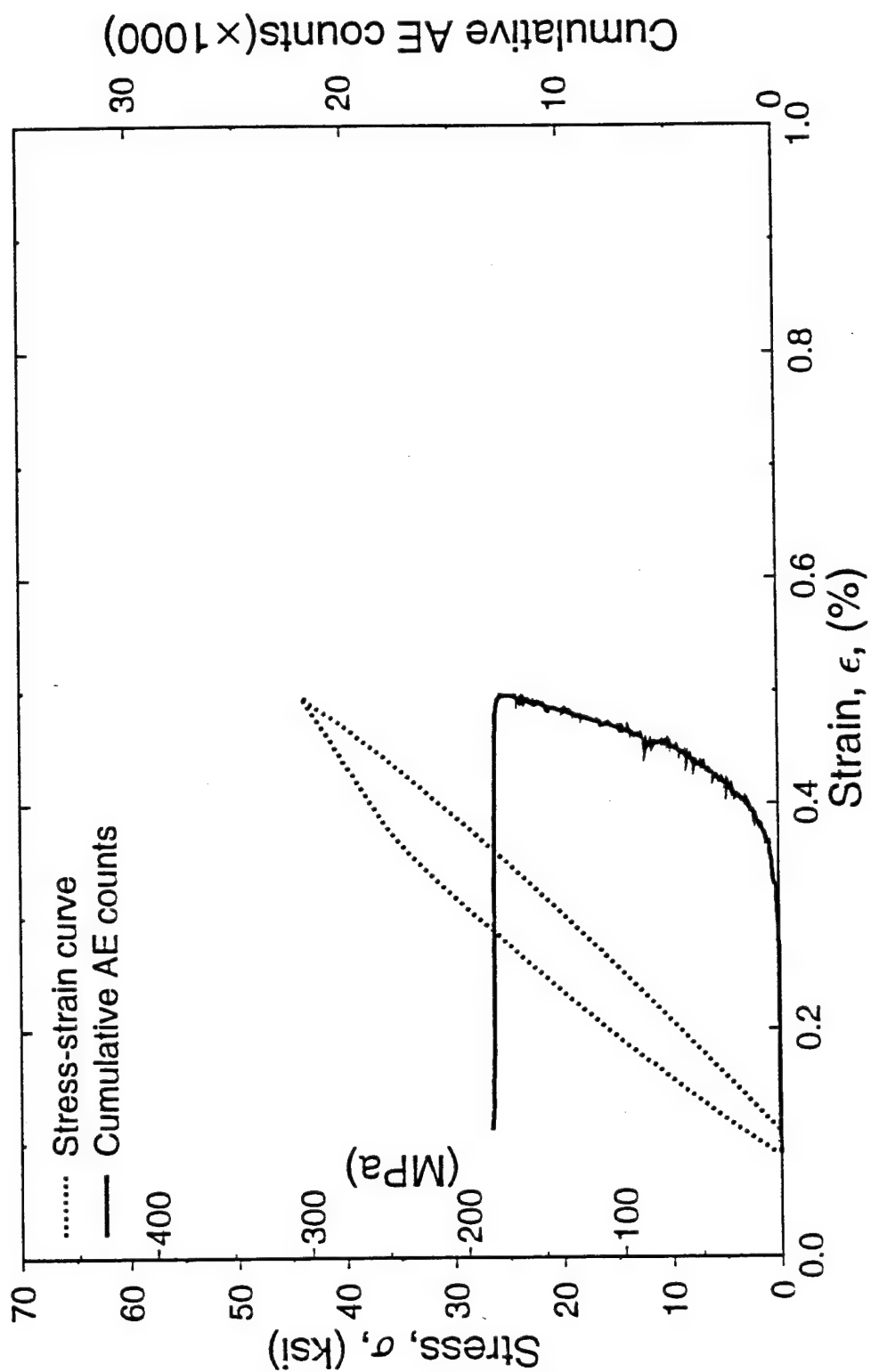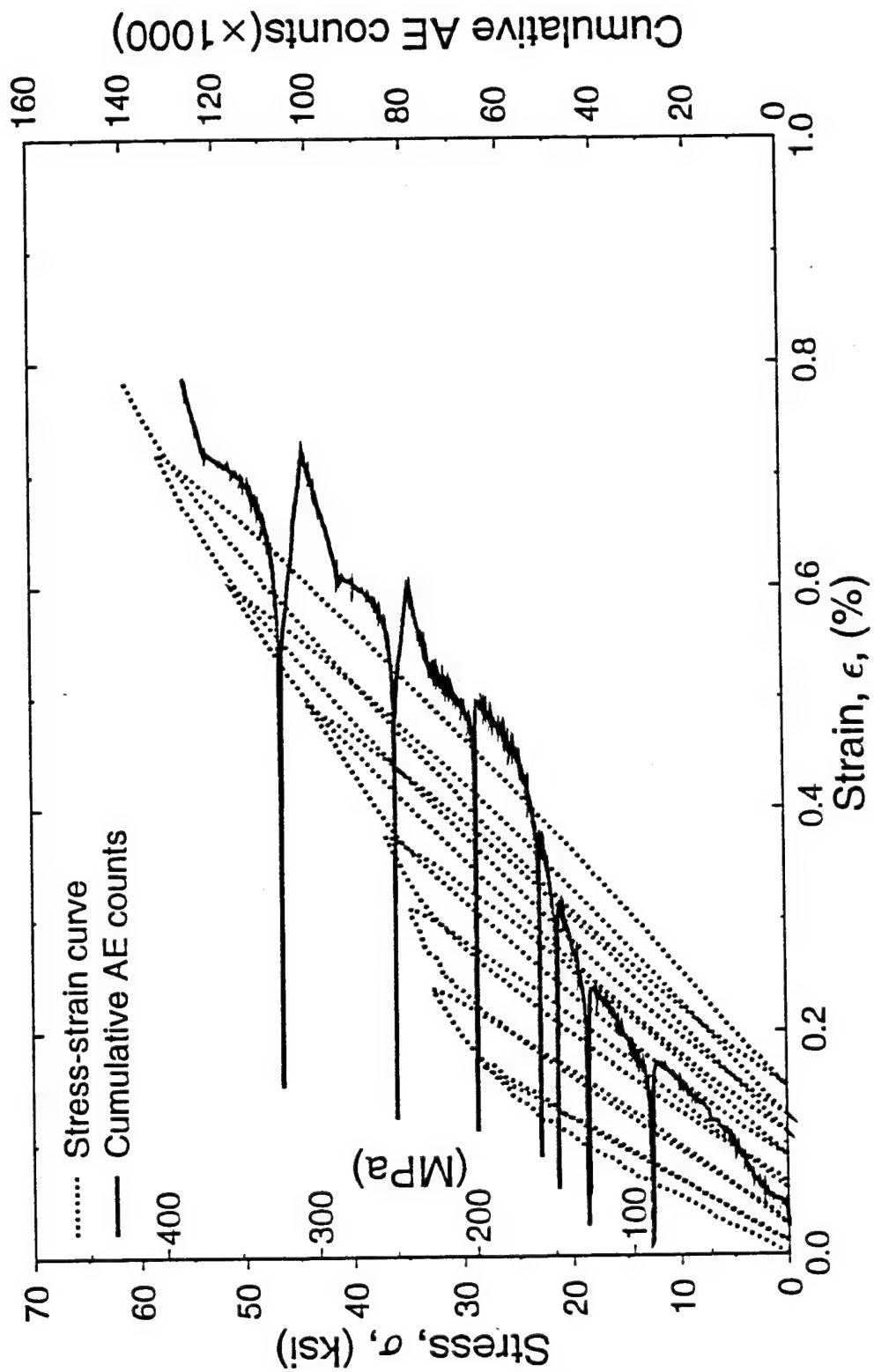Fig. 27   Stress and Cumulative AE Counts versus Strain for Loading and
Unloading of Unidirectional SiC/CAS Composite under
Longitudinal Tension

Thus, matrix cracking in the composite depends on the matrix tensile strength and the processing residual stresses. The average residual stresses in the fiber and matrix can be determined from the following equilibrium and continuity conditions (Fig. 28):

$$\sigma_{rm} V_m + \sigma_{rf} V_f = 0 \tag{2}$$

$$\frac{\sigma_{rf}}{E_f} - \frac{\sigma_{rm}}{E_m} = (\alpha_m - \alpha_f) \Delta T \tag{3}$$

For

$$\Delta T \quad = \quad - 1000° \, C$$

$$\alpha_m \quad = \quad 5.0 \times 10^{-6}/° \, C$$

$$\alpha_f \quad = \quad 4.0 \times 10^{-6}/° \, C$$

$$E_m \quad = \quad 98 \, GPa$$

$$E_f \quad = \quad 170 \, GPa$$

$$v_m \quad = \quad 0.2$$

$$v_f \quad = \quad 0.2$$

$$\sigma_{rm} \quad = \quad 52 \, MPa \, (7.5 \, ksi)$$

The matrix strength F_{mt} that controls matrix cracking in the composite is the "in-situ" strength which is different from the one measured in the bulk material. The in-situ matrix strength is best determined by recording the applied axial (longitudinal) stress in the composite at crack initiation, σ_{ci}, and using eq. (1). Thus, for $\sigma_a = \sigma_{ci} = 100 \, MPa$, $\sigma_{rm} = 52 \, MPa$, $E_m = 98 \, GPa$ and $E_1 = 127 \, GPa$,

$$F_{mt} \quad = \quad \frac{E_m}{E_1} \sigma_{ci} + \sigma_{rm} \quad = \quad 129 \, MPa \, (18.7 \, ksi)$$

After crack initiation, microcracks propagate and combine to form a pattern of continuous transverse cracks with an average crack spacing l (Fig. 29). The analytical model in question gives the local stress distributions between two matrix

36
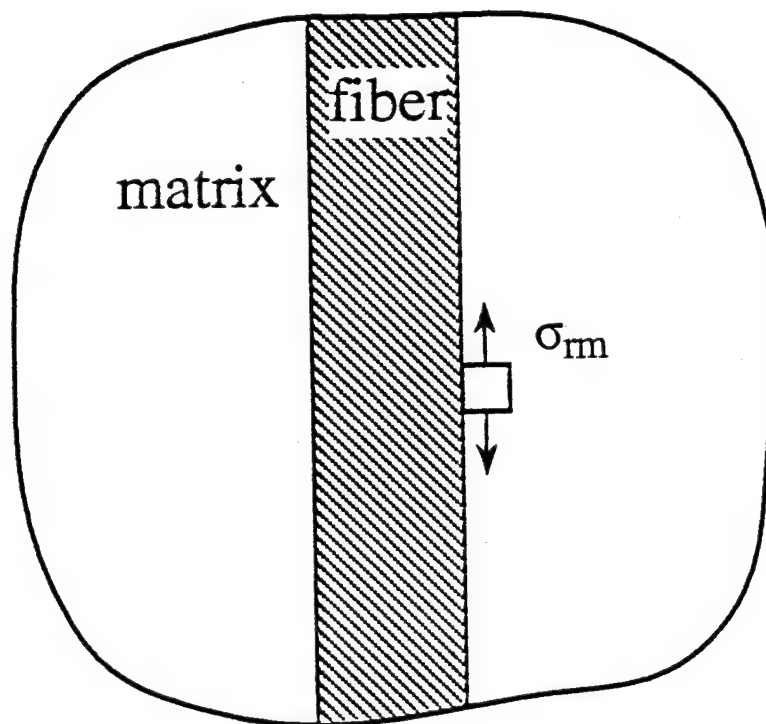
Fig. 28 Axial Residual Stress in the Matrix
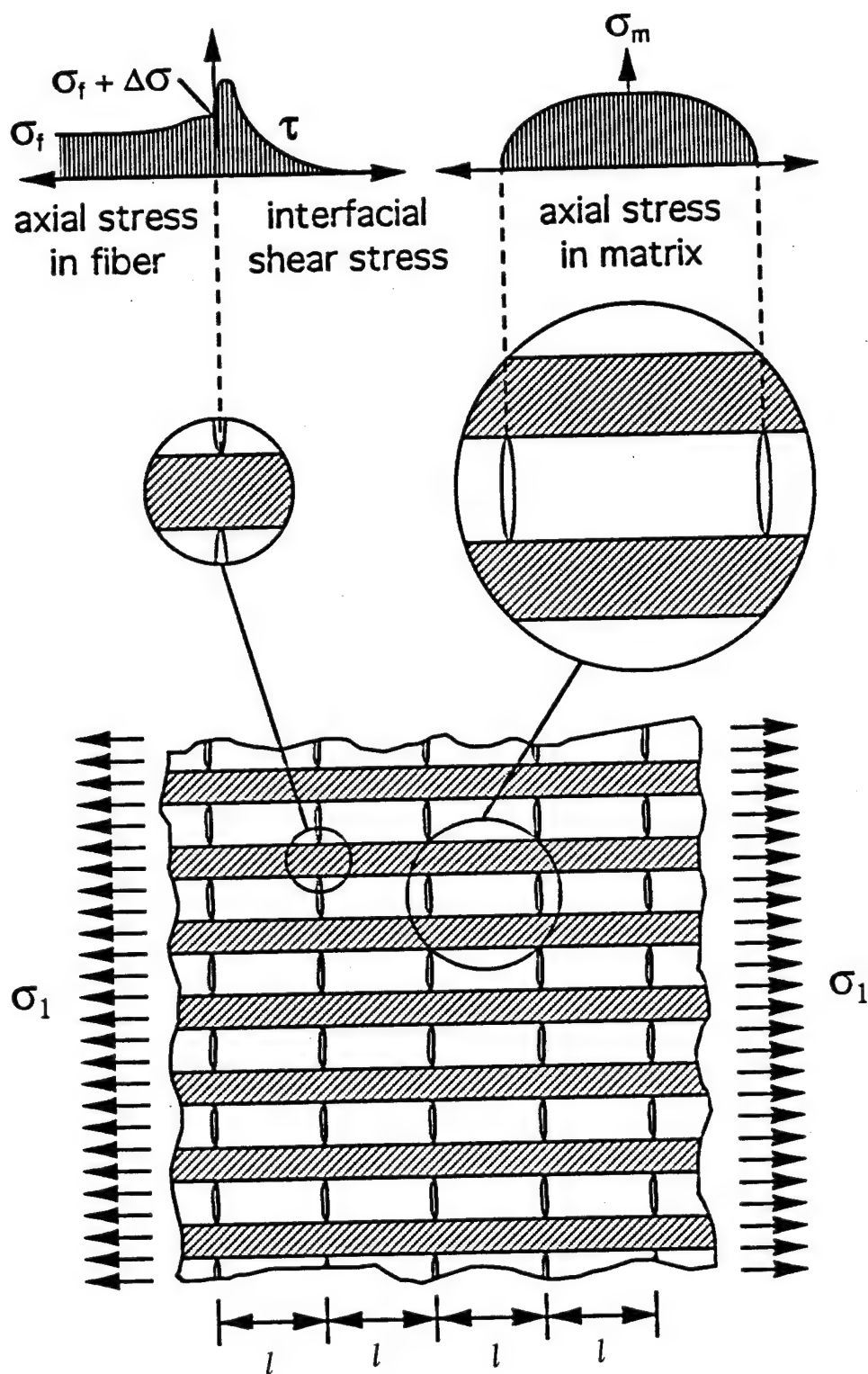
Fig. 29 Matrix Cracking and Local Stress Distributions in
Unidirectional Brittle Matrix Composite under Longitudinal Tension

cracks [12 - 14]. Closed form expressions were given for the distributions of the axial stress in the matrix and fiber and the interfacial shear stress:

$$\sigma_{mx} = \left(\frac{E_m \, \sigma_a}{E_1} + \sigma_{rm}\right) \left(1 - \frac{\cosh\left(\frac{\alpha l}{2} - \alpha x\right)}{\cosh\left(\frac{\alpha l}{2}\right)}\right) \tag{4}$$

$$\sigma_{fx} = \frac{E_f}{E_1} \left(1 + \frac{E_m \, V_m}{E_f \, V_f} \frac{\cosh\left(\frac{\alpha l}{2} - \alpha x\right)}{\cosh\left(\frac{\alpha l}{2}\right)}\right) \sigma_a + \left(1 - \frac{\cosh\left(\frac{\alpha l}{2} - \alpha x\right)}{\cosh\left(\frac{\alpha l}{2}\right)}\right) \sigma_{rf} \tag{5}$$

$$\tau_i(x) = \frac{\alpha r_f \, V_m}{2 V_f} \left(\frac{E_m \, \sigma_a}{E_1} + \sigma_{rm}\right) \frac{\sinh\left(\frac{\alpha l}{2} - \alpha x\right)}{\cosh\left(\frac{\alpha l}{2}\right)} \tag{6}$$

where

σ_{mx} = average axial stress in matrix

σ_{fx} = average axial stress in fiber

τ_i = interfacial shear stress

x = axial coordinate measured from crack face

l = crack spacing

$$\alpha^2 = \frac{2}{A r_f} \cdot \frac{E_1}{E_f \, E_m \, V_m}$$

$$A = \frac{r_f}{4 G_f} + \frac{1}{G_m} \left[\frac{2}{3} \cdot \frac{V_f(r_f - r_m)}{(1 - V_f)^2} \left(4 + \frac{r_f}{r_m} + V_f\right) + \frac{r_f(1 + V_f)}{1 - V_f}\right]$$

G_f, G_m = fiber and matrix shear moduli, respectively

r_f, r_m = fiber and matrix radii in model, respectively

39

Crack spacing prior to any significant debonding could be obtained by setting

$\sigma_m = F_{mt}$ at $x = l/2$ in eq. (4):

$$l = \frac{2}{\alpha} \cosh^{-1} \frac{E_m \sigma_a + E_1 \sigma_{rm}}{E_m \sigma_a + E_1 (\sigma_{rm} - F_{mt})} \qquad (7)$$

The next failure mechanism accompanying or following matrix cracking is interfacial debonding (Fig. 30). A debond initiation criterion can be expressed in terms of a critical strain energy at the intersection of the matrix crack and the fiber or a "nominal" interfacial shear strength F_{is}. The latter may not correspond to an actual shear stress because of the singularity of the stress but it can be correlated to a similarly measured property. e.g., by means of pullout or pushout tests. Debond initiation then, could be predicted by setting the interfacial shear stress τ_i at $x = 0$ in eq. (6) to F_{is}:

$$\tau_i (0) = \frac{\alpha r_f}{2} \frac{V_m}{V_f} \left(\frac{E_m \sigma_a}{E_1} + \sigma_{rm} \right) \tanh \frac{\alpha l}{2} = F_{is} \qquad (8)$$

where

$\tau_i (0)$ = maximum interfacial shear stress (at $x = 0$)

F_{is} = interfacial shear strength

The corresponding crack spacing at debond initiation is calculated as

$$l_{di} = \frac{2}{\alpha} \tanh^{-1} \left[\frac{F_{is}}{\frac{\alpha r_f}{2} \left(\frac{V_m}{V_f} \right) \left(\frac{E_m}{E_1} \sigma_a + \sigma_{rm} \right)} \right] \qquad (9)$$

40
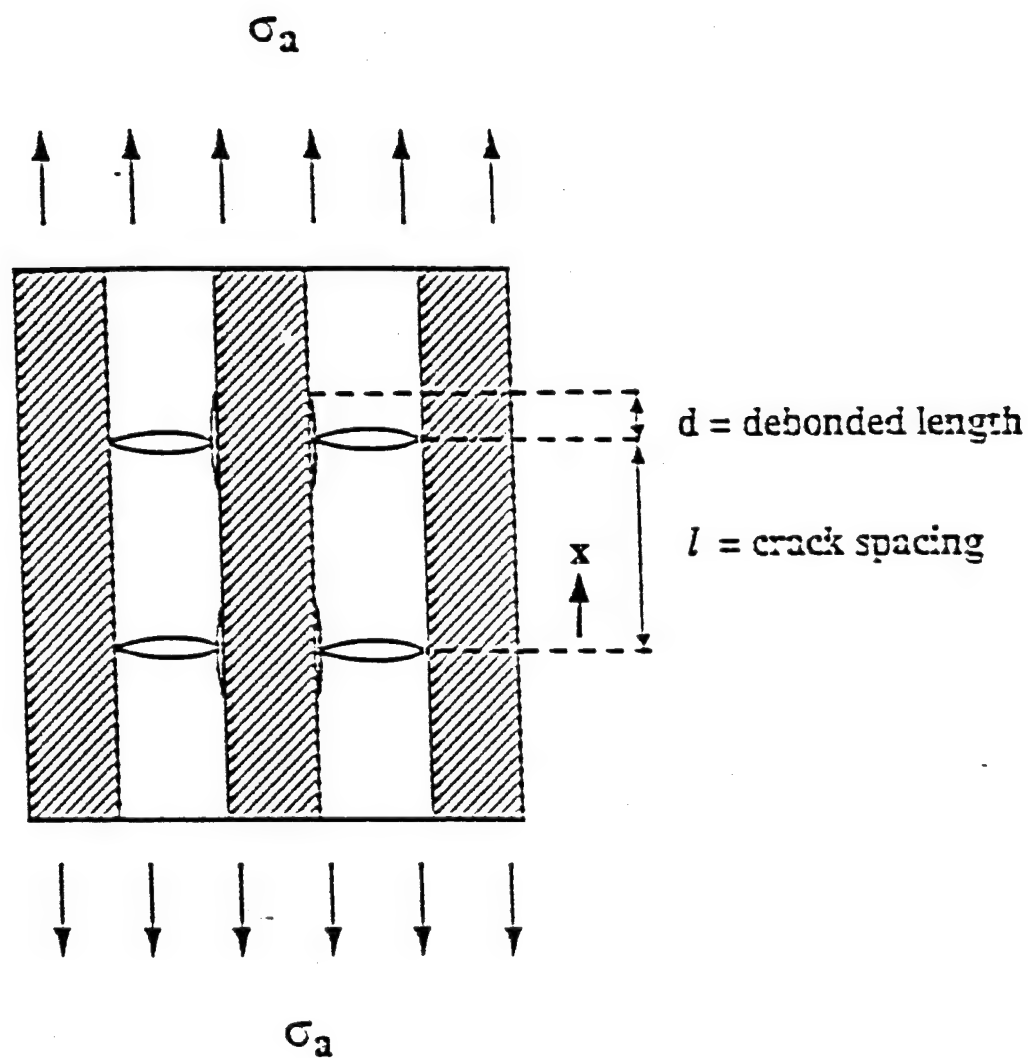
Fig. 30   Matrix Cracking and Debonding in Unidirectional
Composite under Longitudinal Tensile Loading

Stress distributions following debonding have been proposed for the bonded and unbonded regions including the effects of residual stresses and interfacial friction as illustrated in Fig. 31. In the debonded area $(0 \leq x < d)$

$$\sigma_{mx} = \frac{2V_f \tau_f x}{V_m r_f} \tag{10}$$

$$\sigma_{fx} = \frac{\sigma_a}{V_f} - \frac{2\tau_f x}{r_f} \tag{11}$$

$$\tau_i = \tau_f \tag{12}$$

where τ_f = interfacial frictional stress

In the bonded area $(d \leq x \leq l - d)$

$$\sigma_{mx} = \left(\frac{E_m}{E_1} \sigma_a + \sigma_{rm}\right) + \left(\frac{2V_f \tau_f d}{V_m r_f} - \frac{E_m}{E_1} \sigma_a - \sigma_{rm}\right) \frac{\cosh \alpha(l/2 - x)}{\cosh \alpha(l/2 - d)} \tag{13}$$

$$\sigma_{fx} = \left(\frac{E_f}{E_1} \sigma_a + \sigma_{rf}\right) + \left(\frac{E_m V_m}{E_1 V_f} \sigma_a - \sigma_{rf} - \frac{2\tau_f d}{r_f}\right) \frac{\cosh \alpha(l/2 - x)}{\cosh \alpha(l/2 - d)} \tag{14}$$

$$\tau_i = \frac{\alpha r_f V_m}{2V_f} \left[\frac{E_m}{E_1} \sigma_a + \sigma_{rm} - \frac{2V_f \tau_f d}{V_m r_f}\right] \frac{\sinh \alpha(l/2 - x)}{\cosh \alpha(l/2 - d)} \tag{15}$$

The extent of debonding can be calculated by setting

$$\tau_i (d) = F_{is} \qquad (\text{at } x = d) \tag{16}$$

An explicit relation for the debond length d is obtained by neglecting friction:

$$d = \frac{1}{2}\left[l - \frac{1}{\alpha} \log \frac{1 + \xi}{1 - \xi}\right] \tag{17}$$

where

$$\xi = \frac{2F_{is}}{\alpha r_f} \frac{V_f}{V_m} \frac{E_1}{E_m \sigma_a + E_1 \sigma_{rm}}$$

42
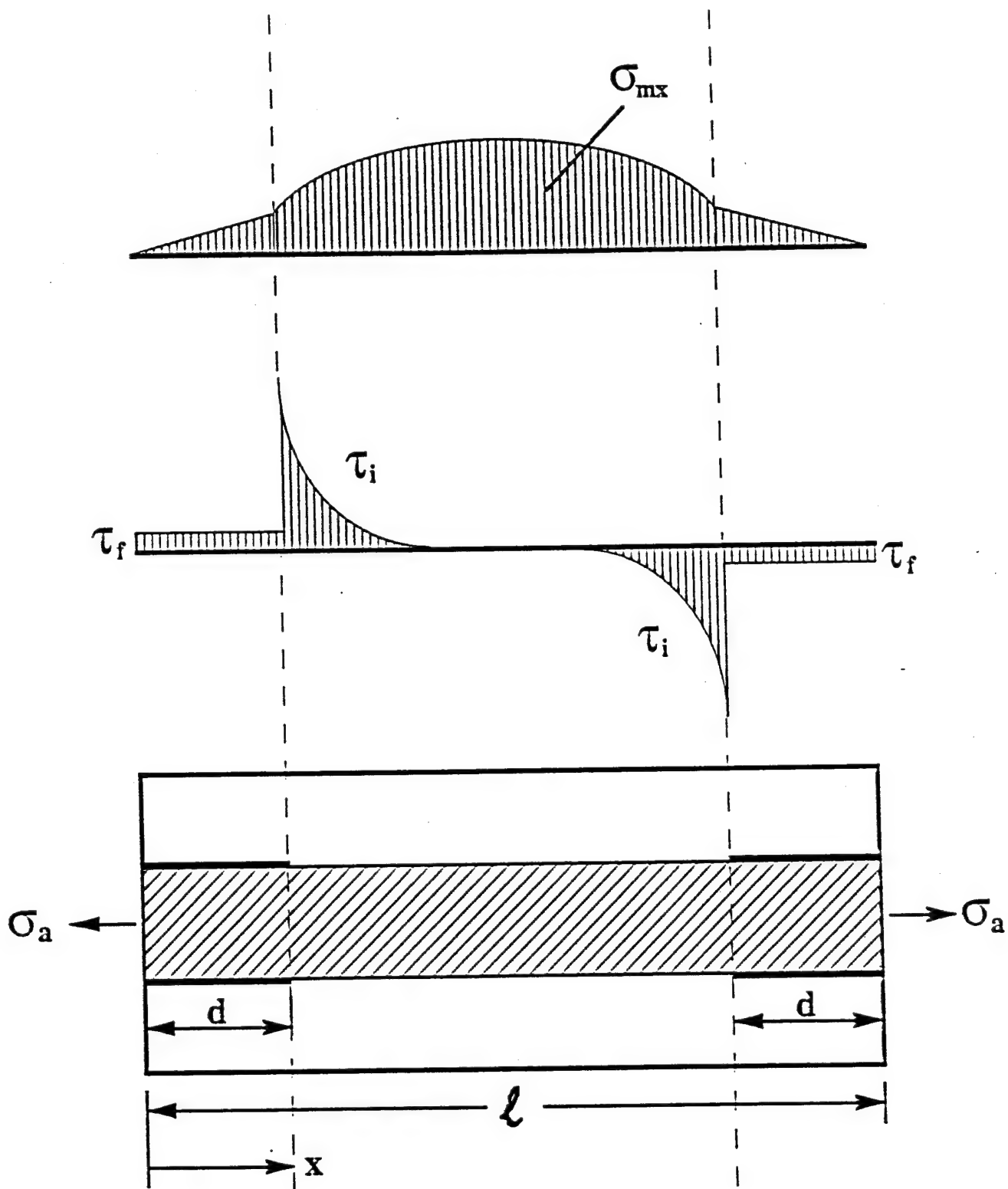
Fig. 31   Axial Matrix Stress and Interfacial Shear Stress
Distributions in Cracked and Partially Debonded Composite Element

The interfacial shear strength which controls debonding is difficult to determine. A determination of this strength has been proposed in relation to the matrix tensile strength by assuming debonding starts at matrix crack saturation, i.e.,

$$l_{di} \cong l_{min}$$

$$\frac{F_{is}}{F_{mt}} = \frac{V_m}{V_f} \cdot \frac{ar_f}{2} \coth \frac{\alpha l_{min}}{4} \tag{18}$$

For the available material properties it is found that

$$F_{is} = 179 \text{ MPa } (26.0 \text{ ksi})$$

which can be compared with microindentation test results for the same material [25].

$$F_{is} = 248 \text{ MPa } (36 \text{ ksi})$$

The longitudinal stress-strain behavior of the material was predicted based on the shear lag model discussed and using the material properties obtained. The result is shown in Fig. 32 where it is compared with the measured stress-strain curve [22]. The agreement between the predicted and measured curves is good, at least up to the point of debond initiation. The deviation may be due in part to the fact that fiber fracture was not included in the analysis.

3.2 Interfacial Debonding and Transverse Shear Modulus

An attempt was made to calculate the transverse shear modulus G_{23} throughout the loading history based on Eshelby's equivalent inclusion method and utilizing the debond length result from the shear lag model discussed before [26-28, 23]. For perfect bonding between fibers and matrix the transverse shear modulus is predicted as:

$$\frac{G_{23}^0}{G_m} = \frac{G_m(1 - V_f) + G_{23f}(3 - 4v_m + V_f)}{G_m[1 + (3 - 4v_m)V_f] + G_{23f}(3 - 4v_m)(1 - V_f)} \tag{19}$$
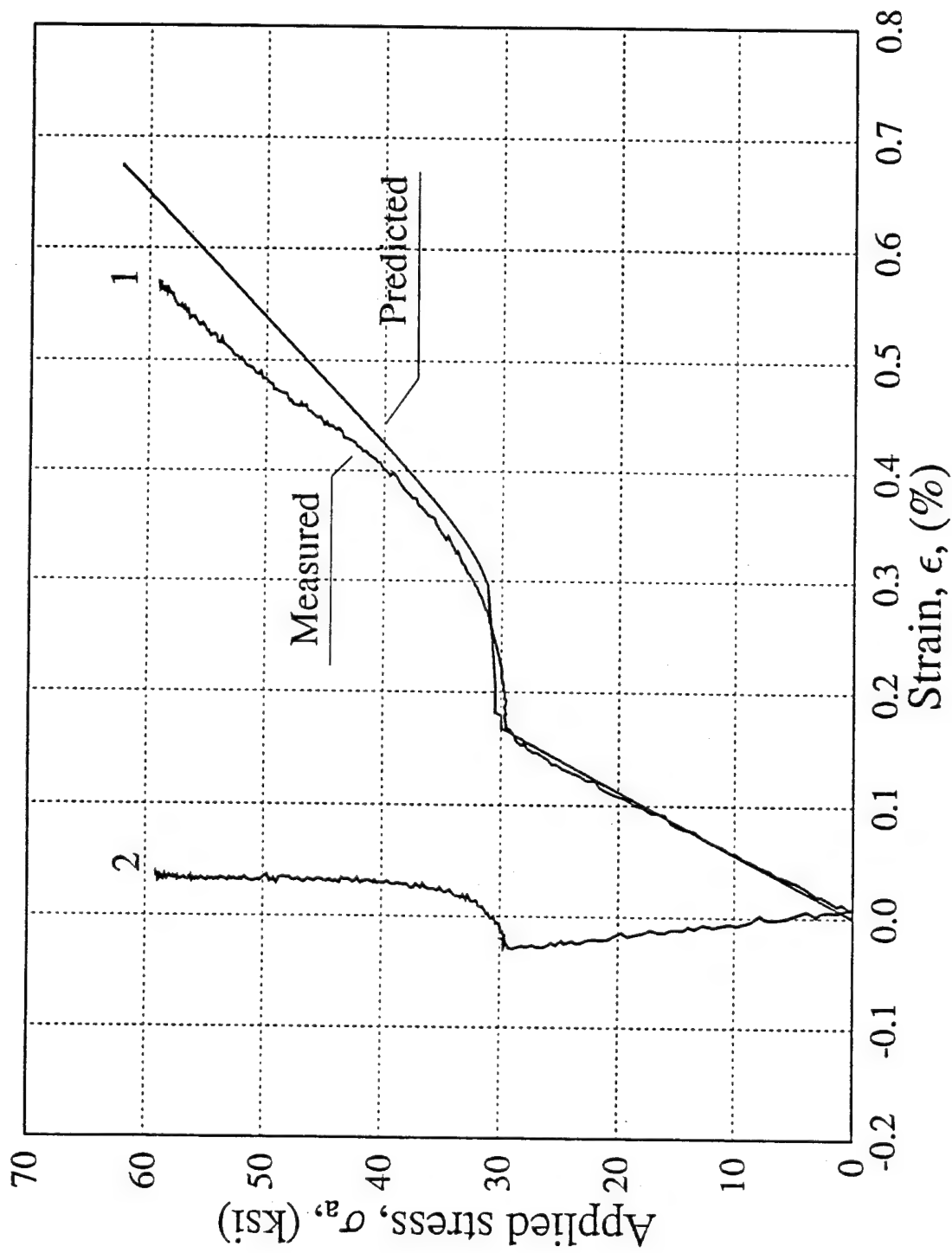
Fig. 32 Stress-Strain Curves for Unidirectional SiC/CAS Composite under Longitudinal Tensile Loading (1 - longitudinal, 2- transverse)

45

For the case of complete debonding, the transverse shear modulus G_{23}^1 is given by [28]:

$$\frac{G_{23}^1}{G_m} = \frac{(1 - V_f) \varphi}{(1 - V_f) \varphi + 4\chi(1 - v_m^2) V_f} \tag{20}$$

where

$$\varphi = (1 + v_m)[1 + 2(1 - v_m)Q](1 - V_f)^2 + [4R + (3 - 2v_m^2 - 2v_m v_{12f})Q](1 - V_f) V_f$$
$$+ 4(1 - v_m)(1 - v_{12f} v_{21f})(2 + V_f) V_f RQ$$

$$R = \frac{(1 + v_m) E_{1f}}{4(1 - v_{12f} v_{21f}) E_m}$$

$$Q = \frac{(1 + v_m) E_{2f}}{(1 - v_{12f} v_{21f}) E_m}$$

$$\chi = (1 - V_f)^2 + \frac{1}{1 + v_m}[(1 - v_m v_{12f})Q + 4(1 - v_m v_{12f})](1 - V_f) V_f R + \frac{1 - v_m}{E_m} E_{1f} V_f^2 Q$$

In the case of partial debonding along the fiber direction, it is assumed that the fiber-matrix interface around the circumference of the fiber is completely debonded. The transverse shear modulus is then calculated by linear interpolation of the moduli for the cases of perfect bonding and complete debonding, i.e.,

$$G_{23} = G_{23}^0 \frac{l - 2d}{l} + G_{23}^1 \frac{2d}{l}$$

or

$$\frac{G_{23}}{G_{23}^0} = \left(1 - \frac{G_{23}^1}{G_{23}^0}\right) \frac{2d}{l} \tag{21}$$

where the debond length d is calculated from eq. (17). The predicted shear modulus G_{23} is plotted versus applied strain and compared with the value obtained from wavespeed measurements of shear waves in Fig. 33. The agreement is as reasonable as can be expected.

46
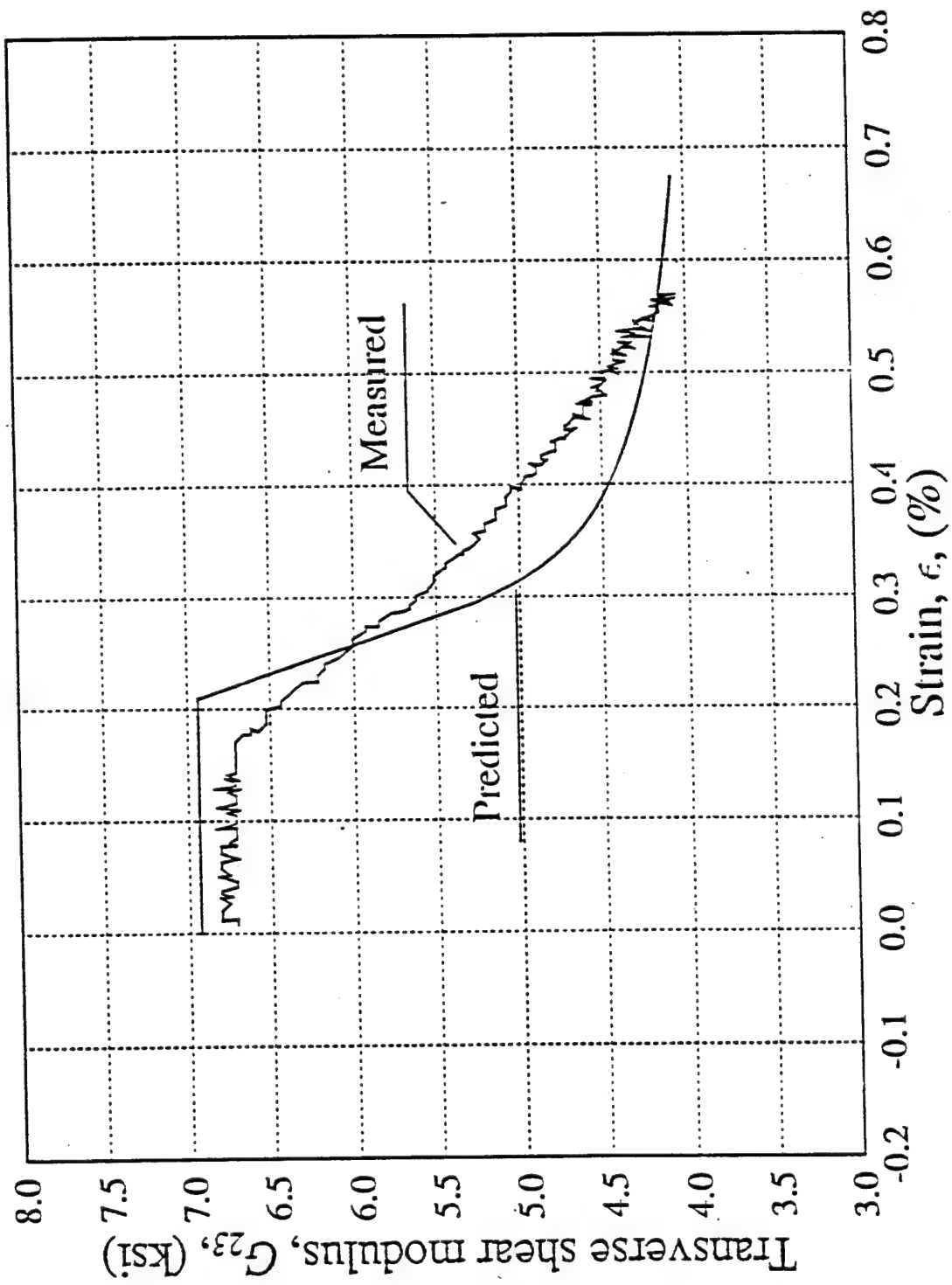
Fig. 33   Change in Transverse Shear Modulus due to Debonding during Loading

Conversely, the ultrasonically determined shear modulus G_{23} can be used in conjunction with the relation given above to calculate the debond length d as a function of applied average strain.

3.3 Numerical Studies of the Effects of Interphases in Unidirectional Composites [29]

A fiber with a reduced interphase stiffness contained in a unidirectionally fiber reinforced composite gives rise to higher stresses at its interphase as well as at the interphases of neighboring fibers. For a hexagonal array composite, detailed numerical results were presented. Three cases were investigated: (1) perfect composite, (2) perfect composite which contains a single fiber with lower interphase stiffness, (3) perfect composite which contains a single fiber with interphase cracks and lower interphase stiffness. Micromechanical stress distributions at the interfaces of the dissimilar fiber and its neighboring fibers were calculated by the use of the boundary element method for an hexagonal array composite subjected to either transverse tensile or compressive uniaxial loading.

The effects of fiber-matrix interphases on the micro- and macro-mechanical properties of unidirectionally fiber-reinforced composites were also studied for composites subjected to transverse shear loading. The interphases were modeled by the spring-layer model which accounts for continuity of tractions, but allows radial and circumferential displacement jumps across the interphase that are linearly related to the normal and tangential tractions. Numerical calculations in basic cells were carried out using the boundary element method. For the isothermal case the results display the effects of variation of interphase stiffness on the fields of stress and deformation and on the effective elastic constants for square array and hexagonal array composites with and without interphase failure.

The effects of fiber-matrix interphases and fiber volume ratio on the micro- and macro-thermomechanical behavior of unidirectionally fiber-reinforced square

48

and hexagonal array composites were also studied for the case of uniform temperature variation (cooling). Numerical calculations in basic cells were carried out using the boundary element method.

3.4 Cylinder Deformation Model

A new model was investigated to remedy the deficiencies of the shear lag model (see Appendix for details). The same cylindrical element between two matrix cracks was analyzed as before (Fig. 34). A form of the displacements in the fiber and matrix was assumed to satisfy axial symmetry and zero shear strain at the outer cylinder boundary. A set of governing equations was obtained by applying the principle of virtual work. These equations refer to a unit cell between two matrix cracks with a crack opening displacement (COD) and debonded regions at the ends (Fig. 35).

Considering the periodicity of matrix cracks, the governing equations can be integrated to yield the following nonlinear damage-strain relations:

$$
\left\{
\begin{array}{c}
(1 - f)\,\lambda_m\,COD_m \\
2\lambda_m\,l_d\,COD_i/R_f
\end{array}
\right\}
=
\begin{bmatrix}
b_{11} & b_{12} \\
b_{21} & b_{22}
\end{bmatrix}
\left\{
\begin{array}{c}
\bar{\varepsilon}_1 - \dfrac{\bar{\sigma}_1}{E_1} \\
\bar{\varepsilon}_2 + v_{12}\dfrac{\bar{\sigma}_1}{E_1}
\end{array}
\right\}
\tag{22}
$$

where

$$
b_{11} = 1 + \frac{f(v_f - v_m)}{1 - v_f v_m} + \frac{f(1 + v_f)(1 - v_m)}{1 - v_f v_m}\left(\frac{G_f}{G_m} - 1\right)
$$

$$
b_{12} = -\frac{(1 - f)(v_f - v_m)}{1 - v_f v_m}
$$

$$
b_{21} = \frac{f(v_f - v_m)}{1 - v_f v_m} - \frac{f v_m(1 + v_f)}{2(1 - v_f v_m)}\left(\frac{G_f}{G_m} - 1\right)
$$

$$
b_{22} = 1 - \frac{(1 - f)(v_f - v_m)}{1 - v_f v_m} - \frac{(1 - f)(1 + v_m)(1 - 2v_f)}{2(1 - v_f v_m)}\left(1 - \frac{G_m}{G_f}\right)
$$

cylinder displacements: $u(z)$, $w(z)$, $\kappa(z)$

cylinder stresses: N_1, N_2, S, M_1, M_2

cylinder strains: ϵ_1, ϵ_2, γ, q_1, q_2
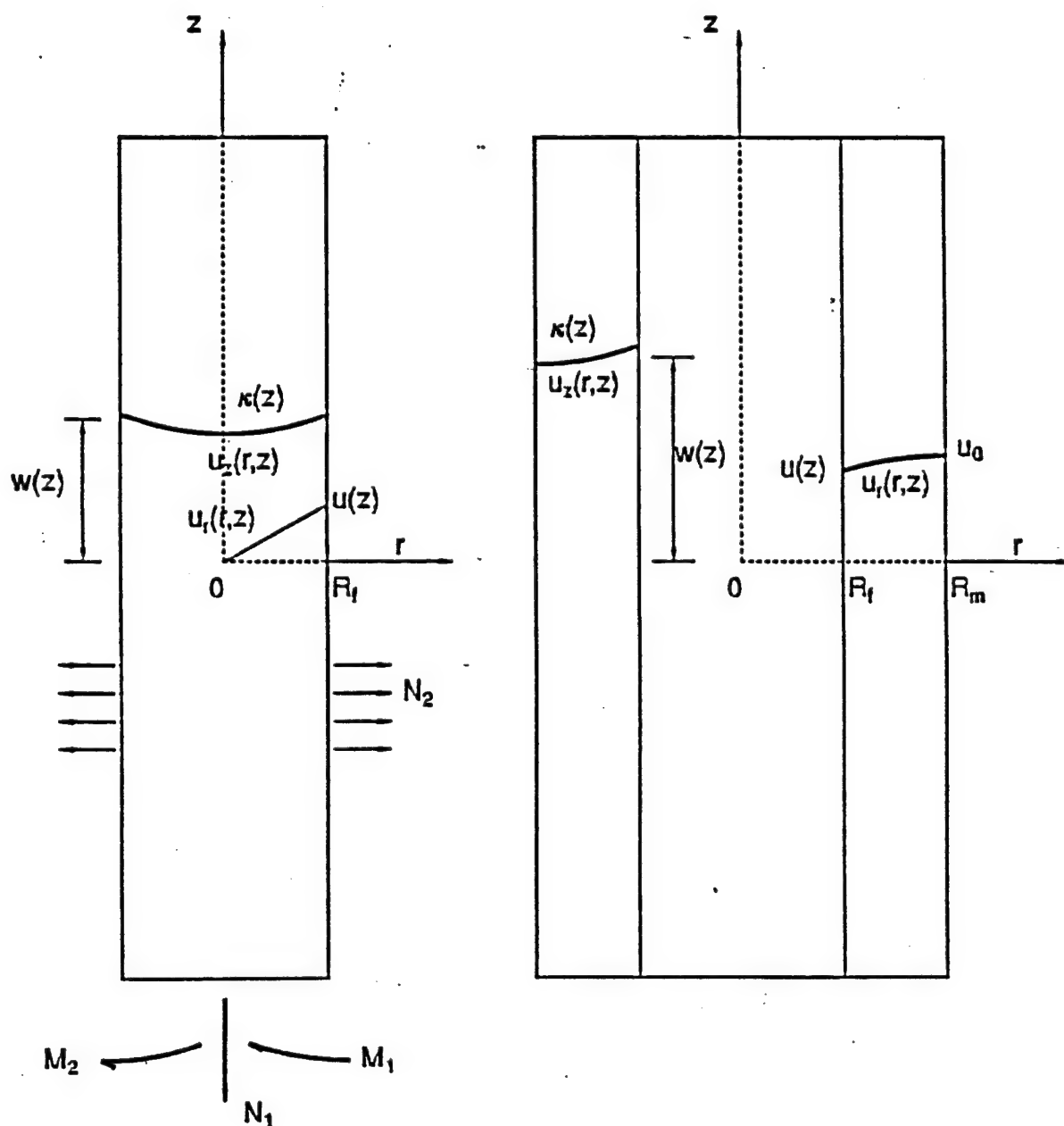
Fig. 34 Cylindrical Element of Fiber and Matrix and Assumed Form of Displacements
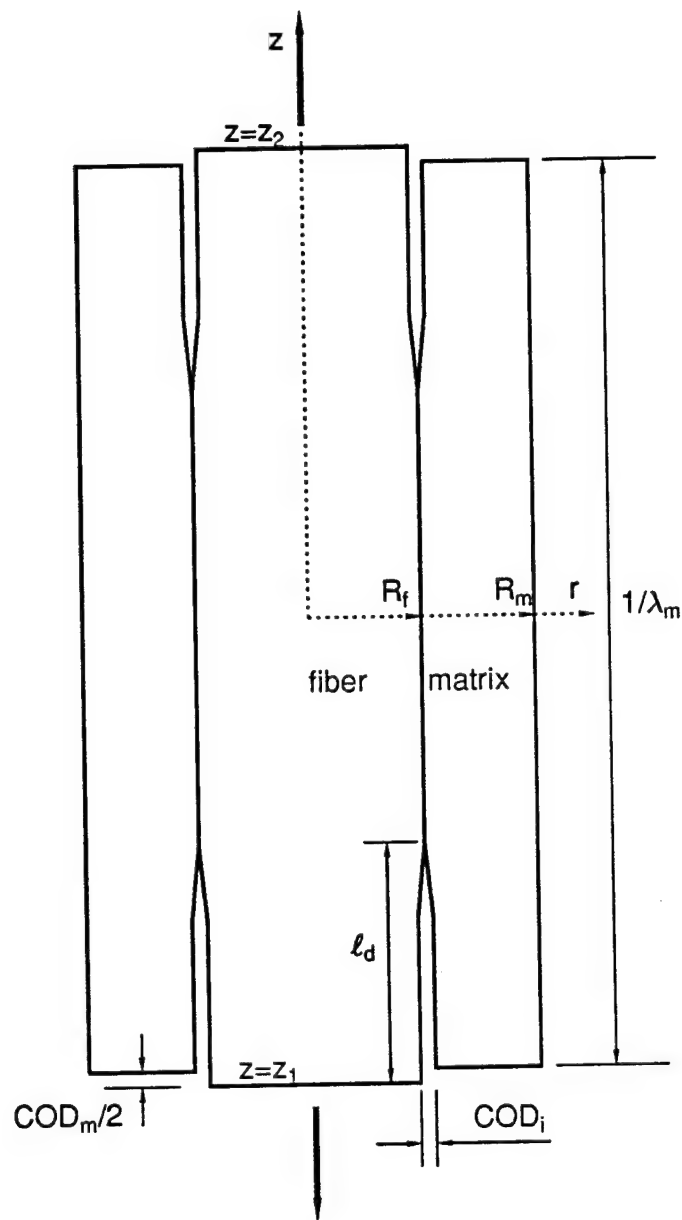
Fig. 35   Unit Cell Between Matrix Cracks Illustrating
COD and Debonding

E_1 $=$ longitudinal elastic modulus of undamaged composite.

ν_1 $=$ major elastic Poisson's ratio of composite.

$\overline{\sigma}_1$ $=$ average longitudinal stress in composite.

$\overline{\varepsilon}_1, \overline{\varepsilon}_2$ $=$ average longitudinal and transverse strains in composite, respectively.

$G_m, G_f =$ matrix and fiber shear moduli, respectively.

ν_m, ν_f $=$ matrix and fiber Poisson's ratios, respectively.

f $=$ fiber volume ratio.

$COD_m =$ matrix crack opening displacement.

COD_i $=$ interface crack opening displacement.

Relations (22) can be used to predict the transverse strain $\overline{\varepsilon}_2$ in terms of the longitudinal strain $\overline{\varepsilon}_1$. Assuming that the fiber and matrix remain in contact, i.e.,

$$COD_i = 0$$

then,

$$\overline{\varepsilon}_2 + \nu_{12} \frac{\overline{\sigma}_1}{E_1} = -\frac{b_{21}}{b_{22}} \left(\overline{\varepsilon}_1 - \frac{\overline{\sigma}_1}{E_1} \right)$$

(24)

or

$$\varepsilon_2^{nl} = -\nu_{12}^{nl} \; \varepsilon_1^{nl}$$

where

$$\varepsilon_2^{nl} = \overline{\varepsilon}_2 + \nu_{12} \frac{\overline{\sigma}_1}{E_1} = \text{nonlinear component of transverse strain}$$

$$\varepsilon_1^{nl} = \overline{\varepsilon}_1 - \frac{\overline{\sigma}_1}{E_1} = \text{nonlinear component of longitudinal strain}$$

$$\nu_{12}^{nl} = \frac{b_{21}}{b_{22}} = \text{"Poisson's ratio" relating nonlinear components of strain}$$

The nonlinear components of the strains are illustrated in Fig. 36. Substituting the known properties of the constituents and the composite and the
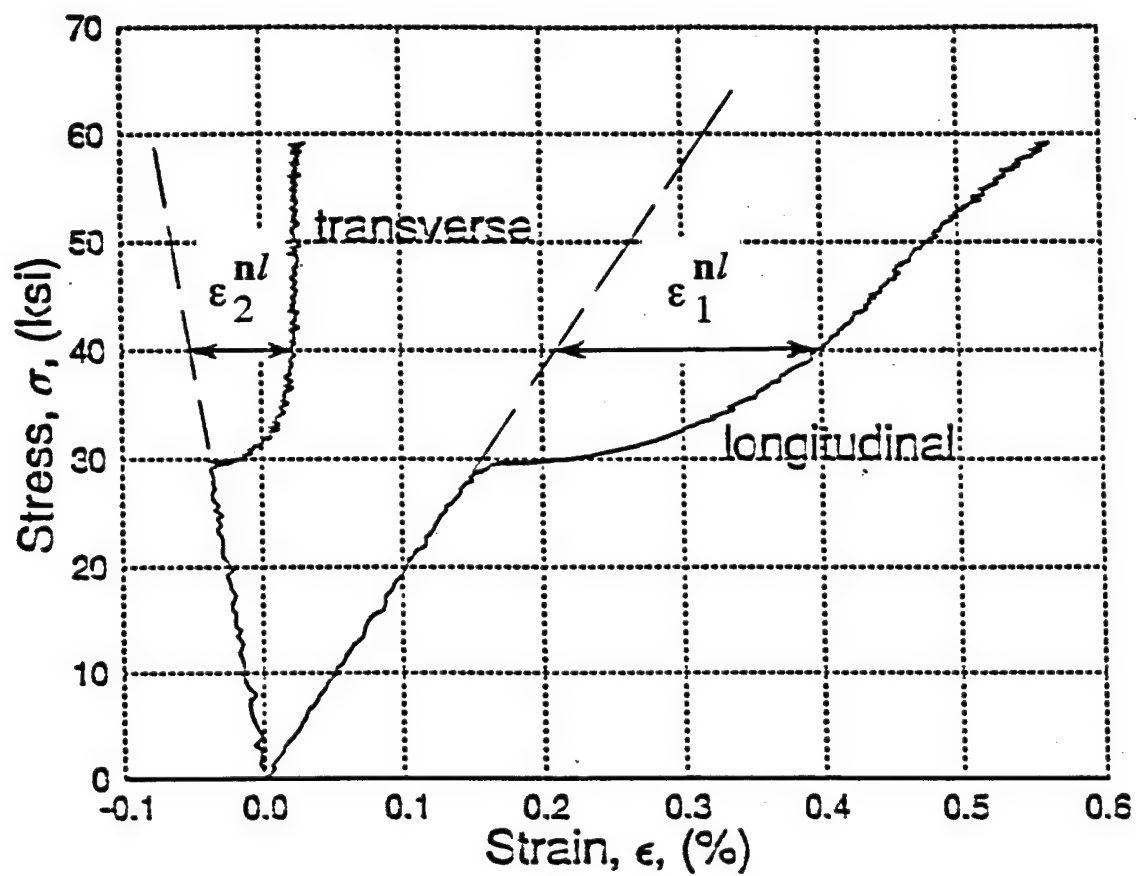
Fig. 36   Stress Strain Curves of Unidirectional SiC/CAS Composite
under Longitudinal Tension

measured $\overline{\sigma}_1 - \overline{\varepsilon}_1$ longitudinal stress-strain relationship in eq. (24), one obtains the transverse strain $\overline{\varepsilon}_2$. This predicted transverse strain agrees perfectly well with the one measured directly (Fig. 37).

The model development up to this point does not entail failure criteria. It simply relates a given state of damage (matrix cracking) to the average (macroscopic) stresses and strains in the composite. It makes use only of linear elasticity with the appropriate boundary and interface conditions.

Future work of this model will introduce failure criteria for matrix cracking and fiber/matrix debonding, residual stresses and interfacial friction. The hoped for result will be a comprehensive model capable of predicting damage evolution and the complete stress-strain curves to failure as a function of physical and experimentally measurable parameters.

4. FAILURE MECHANISMS AND DAMAGE EVOLUTION IN CROSSPLY LAMINATES [30].

The problem of crossply laminates has been studied extensively for polymer-matrix composites. The primary failure mechanism in these composites is transverse matrix cracking in the 90° layer reaching a limiting crack density. This is followed by longitudinal matrix cracking in the 0° layers, local delaminations at the intersections of matrix cracks and, finally, fiber fractures in the 0° layer leading to ultimate failure, Daniel et al. [31]. In the case of brittle-matrix composites the type, sequence and interaction of failure mechanisms are different and characteristic of the constituent material properties. Some experimental work on crossply ceramic-matrix composites has been reported by Sbaizero and Evans [32]. They tested symmetric [0/90]$_s$ SiC/LAS laminates in tension and bending. However, the observed failure modes were not easily explained. Subsequent work on crossply laminates dealt with a fracture mechanics model of a delamination crack formed at

54
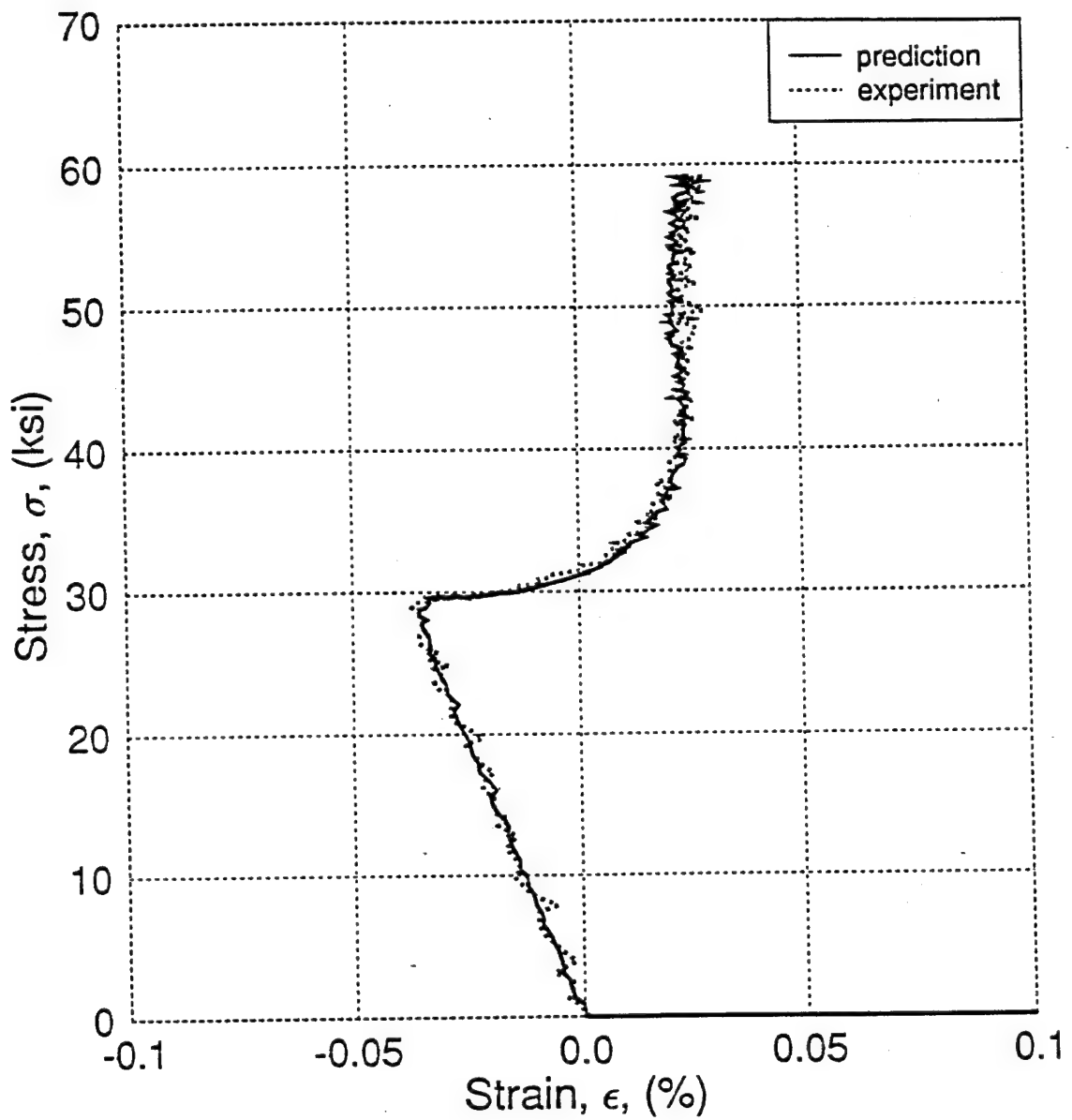
Fig. 37   Prediction of Transverse Strains of Unidirectional SiC/CAS
Composite under Longitudinal Tension

the tip of a notch cutting through 0° and 90° layers, see Sbaizero et al. [33] and Charalambides [34]. Mall and Kim [35] also conducted experimental investigations of failure mechanisms in SiC/CAS laminates. They observed that initial failure consisted of matrix microcracks occurring and growing in all plies in a random manner.

In the present work a systematic investigation was conducted of the failure mechanisms, their growth and interactions in a crossply SiC/CAS laminate under uniaxial tension [30]. It represents the first systematic experimental/analytical study of a crossply laminate with brittle matrix. Previous experimental work mentioned before reported random or other edge dominated failure mechanisms with no clear trends. The failure mechanisms observed and recorded in the present study are substantially different from those reported before and show a clear and systematic trend. The initial stages of failure in each layer are interpreted on the basis of the failure micromechanics of the unidirectional material under longitudinal and transverse loading. The interaction of failure mechanisms in the 0° and 90° layers and the later stages of damage are explained on the basis of classical lamination theory as well as on damage models available for crossply laminates. The various failure mechanisms and damage states were correlated with the overall mechanical behavior of the laminate. The main contribution of this work lies in the integration of the micromechanics of brittle matrix single layers and the macromechanics of a crossply laminate in predicting and interpreting the type and sequence of failure mechanisms and their interaction.

Crossply specimens were loaded under the microscope and the various failure mechanisms, their sequence, interaction and overall damage development were observed in real time and recorded.

The first stage of damage development consists of microcracks in the 90° layer, which then develop into transverse macrocracks (Fig. 38). These
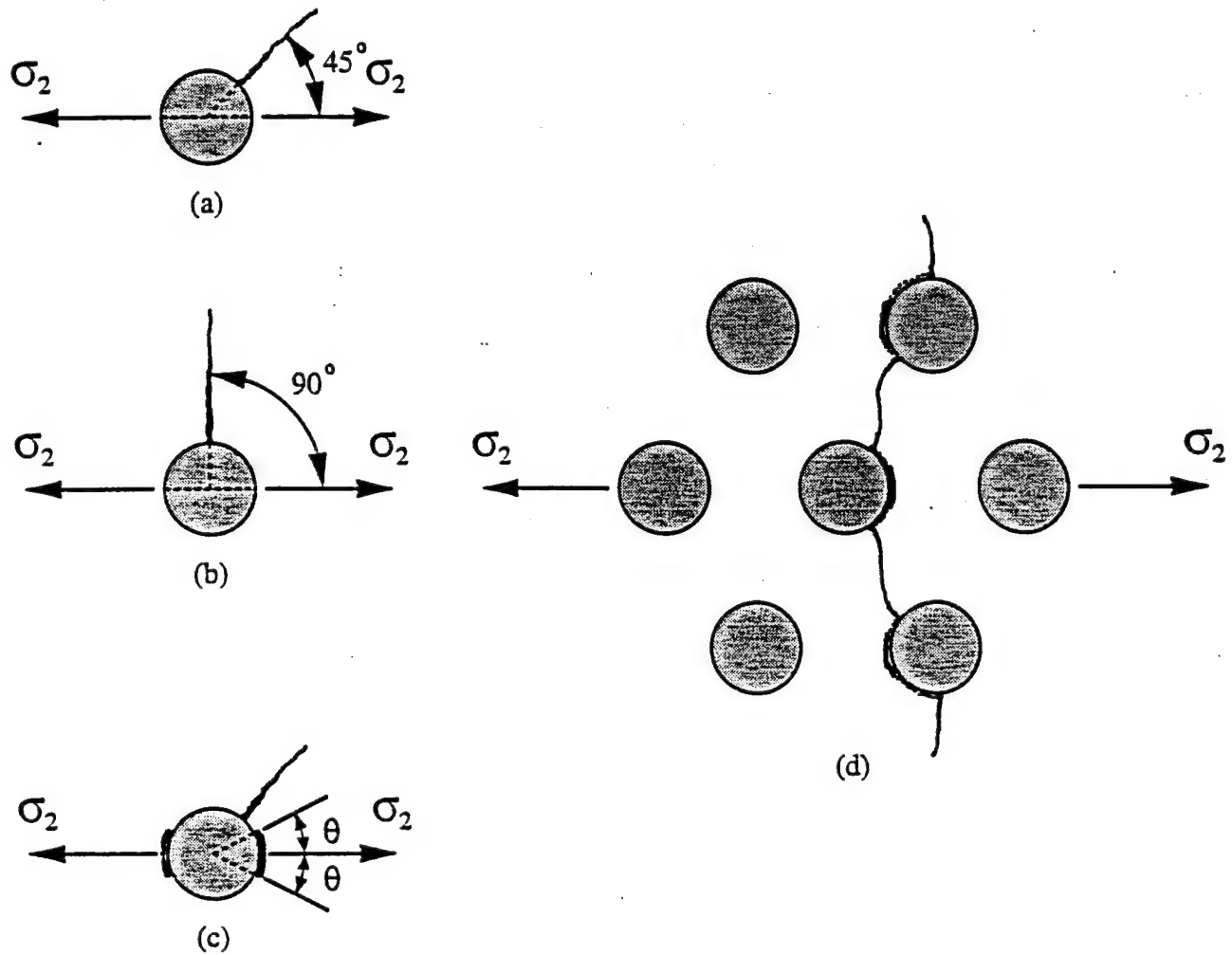
Fig. 38 Development of Failure Mechanisms in Transversely Loaded
Ceramic Matrix Composite
(a) Initial Radial Cracks Around Closely Packed Fibers
(b) Initial Radial Cracks Around Isolated Fibers
(c) Interfacial Cracks, and
(d) Interconnection of Radial and Interfacial Cracks and
Formation of Macrocracks

macrocracks increase in density up to a saturation limit, with a minimum crack spacing approximately equal to the 90° layer thickness. Thereafter, transverse matrix cracks are generated in the 0° layer (Fig. 39). These cracks also increase in density up to a minimum crack spacing of approximately eight fiber diameters. In the third stage of damage development there is an interconnection of the two sets of cracks. Several of the denser 0° layer cracks connect with each of the 90° layer cracks in a delta-like pattern (Fig. 40). This is finally followed by delaminations and additional cracking in the 90° layer prior to ultimate failure.

Damage development was correlated with the macroscopic stress-strain response of the unidirectional material under longitudinal and transverse loading and of the crossply laminate. It was noticed that first-ply failure in the 90° layer occurs at a higher layer stress than the transverse tensile strength of the unidirectional material. This may be attributed to the constraining effects of the 0° layer which tend to increase the in-situ transverse tensile strength of the 90° layer.

Following crack saturation in the 90° layer, cracking initiated and increased in the 0° layers at approximately the same strain levels where similar cracking was observed in the unidirectional material under longitudinal loading. However, the 0° layer stresses at the various stages of damage development, were higher than corresponding stress levels in the 0° unidirectional specimen for the same damage. This was explained as a stiffening or strengthening effect of the 0° layers caused by the attached 90° layer. Ultimate failure of the laminate clearly showed the synergistic effects of the 0° and 90° layers of the laminate.

Damage development in the 90° layer was compared with analytical predictions. A model developed previously for crossply graphite/epoxy composites was used to predict cracking in the 90° layer and stiffness degradation, both in the 90° layer and in the overall laminate. The predictions were in very good agreement with experimental observations.

Fig. 39   Matrix Cracking in 0°-Ply Following Saturation of Cracking in 90°-Ply
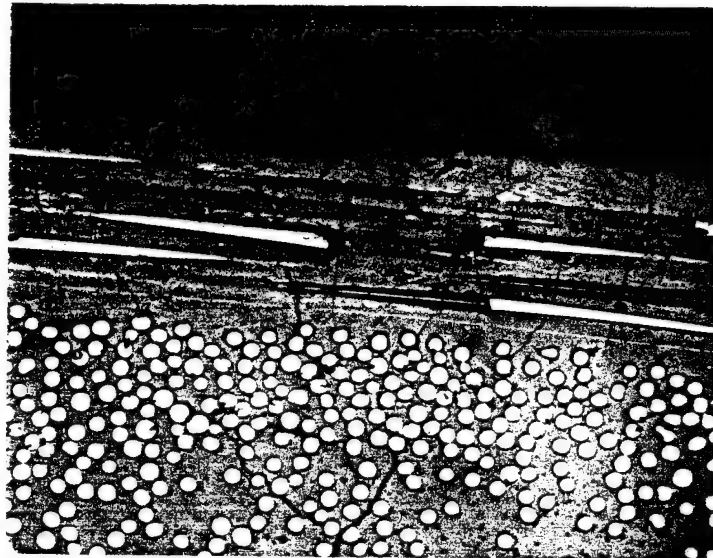
Fig. 40   Interconnection of 0°-Ply and 90°-Ply Macrocracks
(Formation of "Delta" Pattern)

The various failure mechanisms and the entire process of damage evolution were correlated with the macroscopic stress-strain curve of the crossply laminate as shown in Fig. 41. The effects of the various failure mechanisms on stiffness degradation is illustrated.

It was shown that the overall damage development is characterized by different scales at different stages. The relevant scales are fiber diameter and fiber spacing for failure initiation in the 90° layer; layer thickness for damage saturation in the 90° layer; and fiber diameter for matrix cracking in the 0° layer. Finally, there is a scale crossing phenomenon in the interaction between the damage in the 90° and 0° layers.

5. PUBLICATIONS AND PRESENTATIONS

Reprints of selected papers published or presented during the reporting period are included in the appendix.
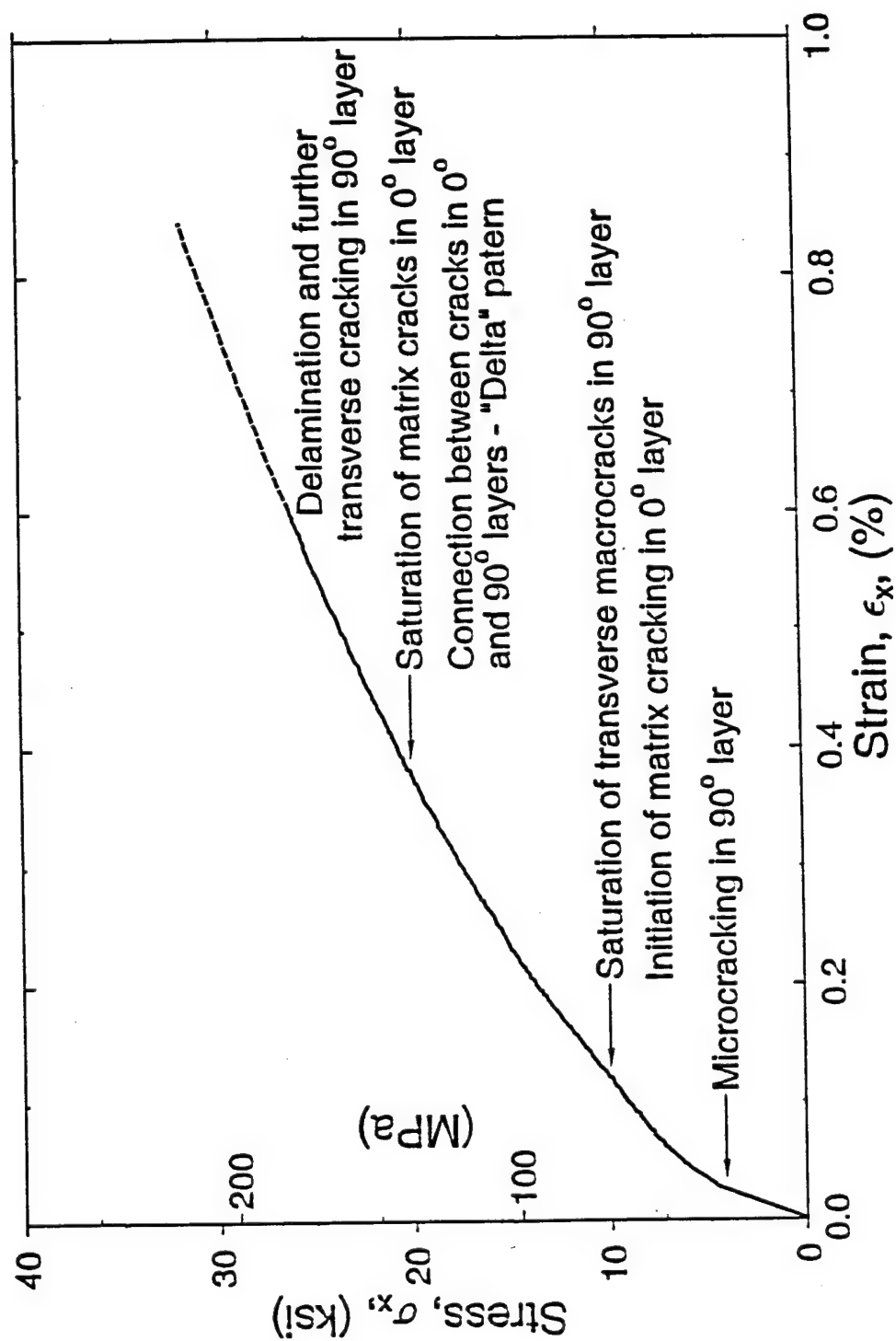
Fig. 41 Stress-Strain Behavior of [0/90₂]s Laminate with Corresponding Stages of Damage Development

REFERENCES

1. Aveston, J., Cooper, G. A. and Kelly, A., "The Properties of Fibre Composites," Conference Proceedings, National Physical Laboratory, IPC Science and Technology Press, Ltd., 1971, pp. 15-26.

2. Aveston, J. and Kelly, A., "Theory of Multiple Fracture of Fibrous Composites," *J. Materials Science,* Vol. 8, 1973, pp. 352-362.

3. Marshall, D. B. and Evans, A. G., "Failure Mechanisms in Ceramic-Fiber/Ceramic Matrix Composites," *J. American Ceramic Society,* Vol. 68, May 1985, pp. 225-231.

4. Marshall, D. B. and Evans, A. G., "Failure Mechanisms in Ceramic-Fiber/Ceramic-Matrix composites," *Ceram. Engng. Sci. Proc.,* Vol. 9, (7 -8), 1988, pp. 853-860.

5. Marshall, D. B., Cox, B. N. and Evans, A. G., "The Mechanics of Matrix Cracking in Brittle-Matrix Fiber Composites," *Acta Metall.,* Vol. 33, No. 11, 1985, pp. 2013-2021.

6. Budiansky, B., Hutchinson, J. W. and Evans, A. G., "Matrix Fracture in Fiber-Reinforced Ceramics," *J. Mech. Phys. Solids*, Vol. 34, (13), 1986, pp. 167-189.

7. Hsueh, C.-H., "Analytical Evaluation of Interfacial Shear Strength for Fiber-Reinforced Ceramic Composites," *J. American Ceramic Society,* Vol. 71, 1988, pp. 490-493.

8. Charalambides, P. G. and Evans, A. G., "Debonding Properties of Residually Stressed Brittle-Matrix Composites," *J. of Amer. Cer. Soc.,* Vol. 72, 1989, pp. 746-753.

9. McCartney, L. N., "New Theoretical Model of Stress Transfer Between Fibre and Matrix in a Unidirectionally Fibre-Reinforced Composite," *Proc. R. Soc. Lond.,* A425, 1989, pp. 215-244.

10. Daniel, I. M., Anastassopoulos, G. and Lee, J.-W., "Failure Mechanisms in Ceramic-Matrix Composites," *Proc. of SEM Spring Conf. on Experimental Mechanics,* May 29 - June 1, 1989, pp. 832-838.

11. Daniel, I. M., Anastassopoulos, G. and Lee, J.-W., "Experimental Micromechanics of Brittle-Matrix Composites," *Micromechanics: Experimental Techniques,* AMD-Vol. 102, ASME Winter Annual Meeting, San Francisco, CA, December 1989, pp. 133-146.

12. Lee, J.-W. and Daniel, I. M., "Deformation and Failure of Longitudinally Loaded Brittle-Matrix Composites," *Composite Materials: Testing and Design,* ASTM STP 1120, Amer. Soc. for Testing and Materials, Philadelphia, 1992, pp. 204-221.

13. Daniel, I. M., Anastassopoulos, G. and Lee, J.-W., "Failure Mechanisms and Interfacial Shear Strength in Brittle-Matrix Composites," AD-Vol. 29/AMD-Vol. 146, *Advances in Experimental Mechanics and Biomimetics,* ed. by W. F. Jones and J. M. Whitney, ASME 1992, Amer. Soc. of Mech. Eng., New York, NY, pp. 57-69.

14. Daniel, I. M., Anastassopoulos, G. and Lee, J.-W., "The Behavior of Ceramic Matrix Fiber Composites under Longitudinal Tension," *Composites Scie. and Tech.,* Vol. 46, No. 2, 1993, pp. 105-113.

15. Hutchinson, J. W. and Jenson, H. M., "Models of Fiber Debonding and Pullout in Brittle Composites with Friction," *Mech. of Mater.,* Vol. 9, 1990, pp. 139-163.

16. Zok, F. W. and Spearing, S. M., "Matrix Crack Spacing in Brittle Matrix Composites," *Acta Metall. Mater.,* Vol. 40, (8), 1992, pp. 2033-2043.

17. Weitsman, Y. and Zhu, H., "Multi-Fracture of Ceramic Composites," *J. Mech. Phys. Solids,* Vol. 41, (2), 1993, pp. 351-388.

18. Hashin, Z., "Analysis of Composite Materials - A Survey," *J. Appl. Mech.,* Vol. 50, 1983, pp. 481-505.

19. Benveniste, Y., "The Effective Mechanical Behavior of Composite Materials with Imperfect Contact between the Constituents," *Mech. of Mater.,* Vol. 4, 1985, pp. 197-208.

20. Achenbach, J. D. and Zhu H., "Effect of Interphases on Micro and Macromechanical Behavior of Hexagonal-Array Fiber Composites," *J. Appl. Mech.,* Vol. 57, 1990, pp. 956-963.

21. Wooh, S. C. and Daniel, I. M., "Real-Time Ultrasonic Investigation of Damage Development in Ceramic-Matrix Composite," Review of Progress in Quantitative Nondestructive Evaluation, Vol. 11B, Plenum Publ. Corp., New York, 1992, pp. 1523-1530.

22. Wooh, S. C. and Daniel, I. M., "Real-Time Ultrasonic Investigation of Fiber-Matrix Debonding in Ceramic-Matrix Composite," Review of Progress in Quantitative Nondestructive Evaluation, Vol. 12B, Plenum Publ. Corp., New York, 1993, pp. 1483-1490.

23. Wooh, S. C. and Daniel, I. M., "Real-Time Ultrasonic Monitoring of Fiber-Matrix Debonding in Ceramic-Matrix Composite," *Mechanics of Materials,* Vol. 17, 1994, pp. 379-388.

24. Luo, J. J., Wooh, S.-C. and Daniel, I. M., "Acoustic Emission Study of Failure Mechanisms in Ceramic Matrix Composite Under Longitudinal Tensile Loading," *J. of Comp. Materials, Vol. 29, 1995,* pp. 1946 - 1961.

25. Grande, D. H., Mandell, J. F., and Hong, K. C. C., "Fiber-Matrix Bond Strength Studies of Glass Ceramic and Metal Matrix Composites," *J. Mat. Scie.,* Vol. 23, 1988, pp. 311-328.

26. Eshelby, J. D., "The Determination of the Field of an Ellipsoidal Inclusion and Related Problems," *Proc. R. Soc. of London,* Vol. A (241), 1957, pp. 376-396.

27. Mori, T. and Tanaka, K., "Average Stress in Matrix and Average Elastic Energy of Materials with Misfitting Inclusions," *Acta Metall.*, Vol. 21, 1973, pp. 571-574.

28. Takahashi, K. and Chou, T.-W., "Transverse Elastic Moduli of Unidirectional Fiber Composites with Interfacial Debonding," *Metall. Trans. A,* Vol. 19A, 1988, pp. 129-135.

29. Choi, H. S. and Achenbach, J. D., "Stress States at Neighboring Fibers Induced by Single-Fiber Interphase Effects," *Int. J. Solids and Structures,* Vol. 32, No. 11. 1995, pp. 1555-1570.

30. Daniel, I. M. and Anastassopoulos, G., "Failure Mechanisms and Damage Evolution in Crossply Ceramic-Matrix Composites," to be published in the *Int. Journal of Solids and Structures,* Vol. 32, No. 3/4, 1995, pp. 341-355.

31. Daniel, I. M., Lee, J.-W. and Yaniv, G., "Damage Development and Property Degradation of Composite Materials," *Mech. of Comp. Mater.* (Ed. by G. J. Dvorak and N. Laws), ASME AMD, Vol. 92, 1988, pp. 149-160.

32. Sbaizero, O. and Evans, A. G., "Tensile and Shear Properties of Laminated Ceramic Matrix Composites," *J. Am. Cer. Soc.,* Vol. 69 (6), 1986, pp. 481-486.

33. Sbaizero, O., Charalambides, P. G. and Evans, A. G., "Delamination Cracking in a Laminated Ceramic-Matrix Composite," *J. Am. Cer. Soc.,* Vol. 73 (7), 1990, pp. 1936-1940.

34. Charalambides, P. G., "Steady-State Mechanics of Delamination Cracking in Laminated Ceramic-Matrix Composites," *J. of Amer. Cer. Soc.,* Vol. 74 (12), 1991, pp. 3066-3080.

35. Mall, S. and Kim, R. Y., "Failure Mechanisms in Laminates of Silicon Carbide Calcium-Aluminosilicate Ceramic Composite," *Composites,* Vol. 23, (4), 1992, pp. 215-222.

APPENDIX

Acoustic Emission Study of Failure Mechanisms in Ceramic Matrix Composite under Longitudinal Tensile Loading

JYI-JIIN LUO, SHI-CHANG WOOH AND ISAAC M. DANIEL
Robert R. McCormick School of Engineering and Applied Science
Northwestern University
2137 N. Sheridan Road
Evanston, IL 60208-3020

ABSTRACT: Acoustic emission (AE) measurements were correlated with macroscopic stress-strain behavior and direct microscopic observations of damage mechanisms in a unidirectional ceramic matrix composite under longitudinal tensile loading. Matrix crack initiation and the onset of AE events correspond to the proportional limit of the material. Both the crack density and cumulative AE counts vary linearly up to the point of crack saturation. Thereafter follows a "strain hardening" region corresponding mainly to fiber-matrix debonding and manifested by an increase of low to moderate amplitude AE activity and leveling off of high amplitude AE signals. At higher strains, beyond the "strain hardening" region, there are two characteristic parts in the AE output, one related to further damage (possibly debonding and fiber fracture) and the other clearly related to interfacial frictional sliding. Upon unloading further AE output related to sliding is observed. AE activity of low to intermediate amplitude continues in the last stages of loading and is believed to be associated with fiber fractures.

KEY WORDS: ceramic-matrix composites, failure mechanisms, damage, acoustic emission, cracking, debonding, SiC/CAS composite.

INTRODUCTION

THE BEHAVIOR OF brittle-matrix composite materials is intimately related to the deformation and failure micromechanisms including their exact sequence and interaction. These in turn are related to the properties of the constituents, matrix, fiber and interface/interphase, as well as the processing residual stresses. It is generally agreed that the possible failure mechanisms under longitudinal tensile loading are matrix cracking, fiber-matrix debonding and sliding, fiber fracture and pullout [1–10]. The relative magnitude, the exact sequence and quantita-

tive effect of these failure mechanisms on the overall behavior of the material vary from case to case. The randomness of fiber spacing and the statistical variability of constituent properties cause the various failure mechanisms to span certain ranges of applied strain during the loading process [11].

Matrix cracking and some fiber fractures have been observed directly by reflection light microscopy during loading [5–7]. However, optical observation of fiber matrix debonding is very difficult. Ultrasonic techniques were developed for monitoring of fiber matrix debonding in conjunction with an analytical model [9]. The need exists to complement and confirm previous observations and conclusions by different techniques.

The objective of this study was to apply acoustic emission (AE) techniques for detection and characterization of damage mechanisms and damage development in unidirectional ceramic matrix composites under longitudinal tension. Acoustic emission results were correlated with direct microscopic observations and the macroscopic stress-strain behavior of the material.

EXPERIMENTAL PROCEDURE

The material investigated was unidirectional SiC/CAS, calcium aluminosilicate glass ceramic reinforced with silicon carbide fibers (Nicalon). The specimen was obtained from Corning Glass Works in the form of a 3.12 mm (0.123 in.) thick, 16-ply unidirectional plate. The average fiber diameter is approximately 15 μm, and the fiber volume ratio of the composite is 0.40. The specimens were cut into 76 $\times$ 3.2 mm (3 $\times$ 0.124 in.) coupons and tabbed with glass/epoxy (Scotchply) for testing. The surface of the specimen was polished for microscopic observations.

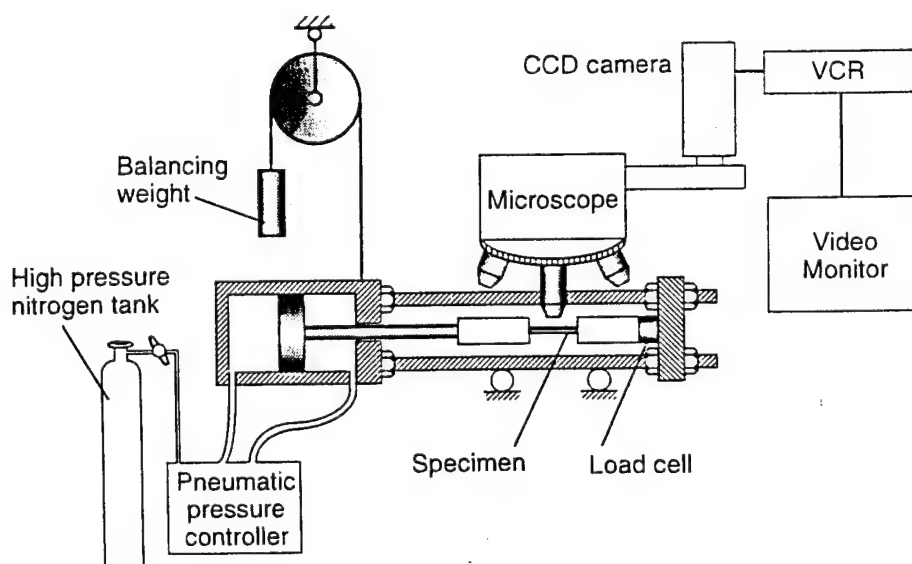Figure 1 illustrates schematically the loading fixture designed for loading spec-

Figure 1. *Setup for microscopic observation of failure mechanisms in composite specimens under load.*

imens under a reflection microscope [5–7]. Loading was applied and controlled by a pneumatic cylinder and recorded by a load cell. The specimen was instrumented with strain gages so that the stress-strain behavior was continuously recorded while the specimen was observed on the surface by a CCD camera and recorded on video tape. The matrix crack density at various applied stress levels was then easily determined from the video records after the test was finished by measuring the average spacing between matrix cracks.

Additional specimens were prepared and loaded in a servohydraulic testing machine (Instron). These specimens were instrumented with strain gages to record the stress-strain behavior, while the acoustic emission output was monitored concurrently with a 150 kHz AE sensor attached to the specimen (Figure 2). Acoustic emission data in the form of cumulative counts (hits) above a predetermined threshold were recorded and processed by a system incorporating a dedicated computer and a transient record analyzer (Locan-AT with TRA, Physical Acoustics Corp.). Some of the specimens were loaded up to failure in a continuous fashion while others were tested under a number of loading-unloading cycles with increasing maximum load.

RESULTS AND DISCUSSION

Monotonic Loading

Results of the macroscopic stress-strain behavior, matrix crack development and acoustic emission output were obtained, analyzed and correlated. Typical photomicrographs showing the development and multiplication of matrix cracking are shown in Figure 3. The crack density (number of cracks per unit length) was measured from such photomicrographs and, after normalizing it (by multiplying by five times the fiber diameter), it was plotted versus applied strain in Figure 4. It was found that matrix cracking occurred primarily in the 0.1–0.4% strain range. Superimposed in Figure 4 is a typical stress-strain curve to failure under longitudinal tensile loading. This curve displays several characteristic features which are related to the failure mechanisms and the failure process as will be discussed later. Figure 5 shows the acoustic emission output in the form of cumulative AE counts plotted versus applied strain. Superimposed for reference is the same stress-strain curve of Figure 4.

The various characteristics and measured parameters of the above results were correlated over five different regions of the loading history (Figure 6). In the initial region, the stress-strain curve is linear up to the proportional limit A ($\sigma = 97$ MPa, $\epsilon = 0.073\%$). In this region no apparent AE activity was recorded and no matrix cracking was observed. As the load is increased, the stress-strain curve becomes slightly nonlinear because of the stiffness degradation resulting from matrix cracking (region AB, $\sigma = 97$–213 MPa, $\epsilon = 0.073$–0.20%). Several initial microcracks of typical length equal to one to two interfiber distances were observed in this region. Acoustic emission output started in this region and increased linearly.

The characteristic "bend-over point" B, is followed by a region BC of reduced
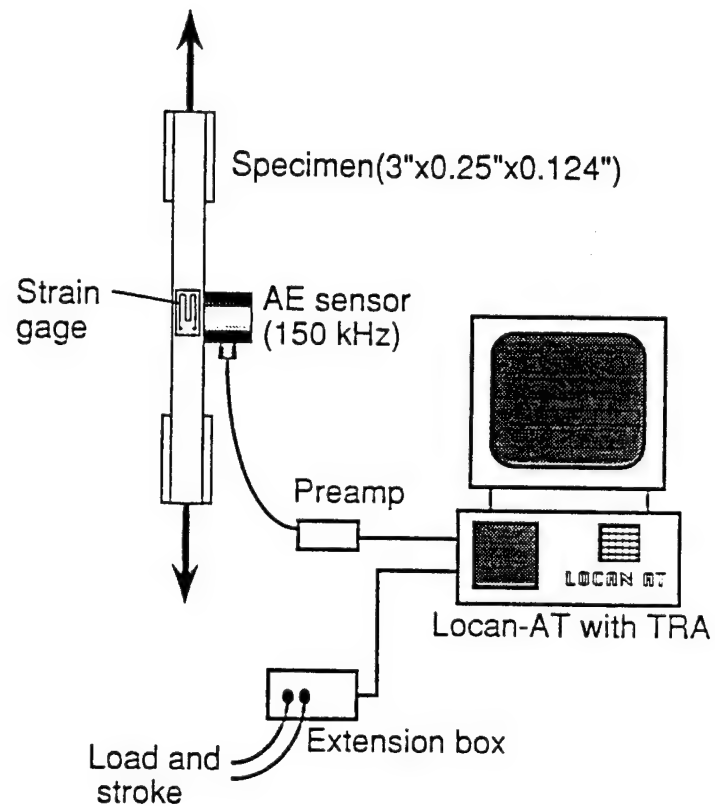
Figure 2. *Schematic diagram of acoustic emission monitoring under uniaxial tensile loading.*
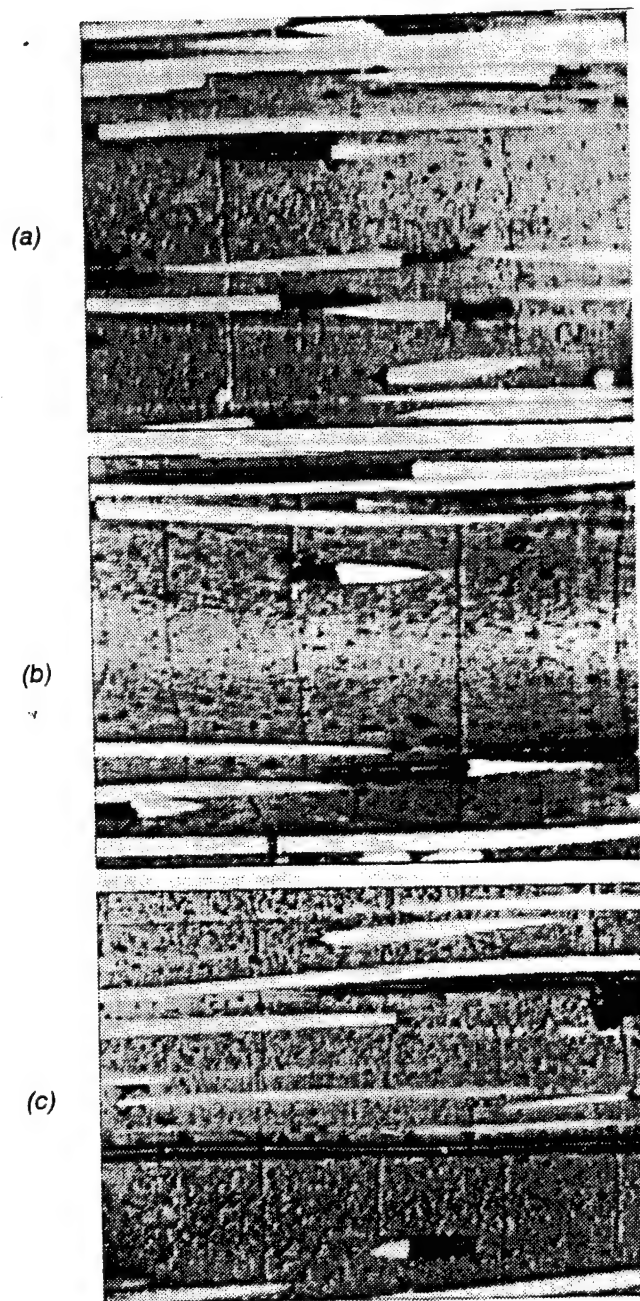
Figure 3. *Multiplication of transverse matrix cracking in unidirectional SiC/CAS composite under longitudinal tension. (a) σ = 25.7 ksi, ε = 0.15%, (b) σ = 28.3 ksi, ε = 23%, (c) σ = 32.3 ksi, ε = 0.31%.*
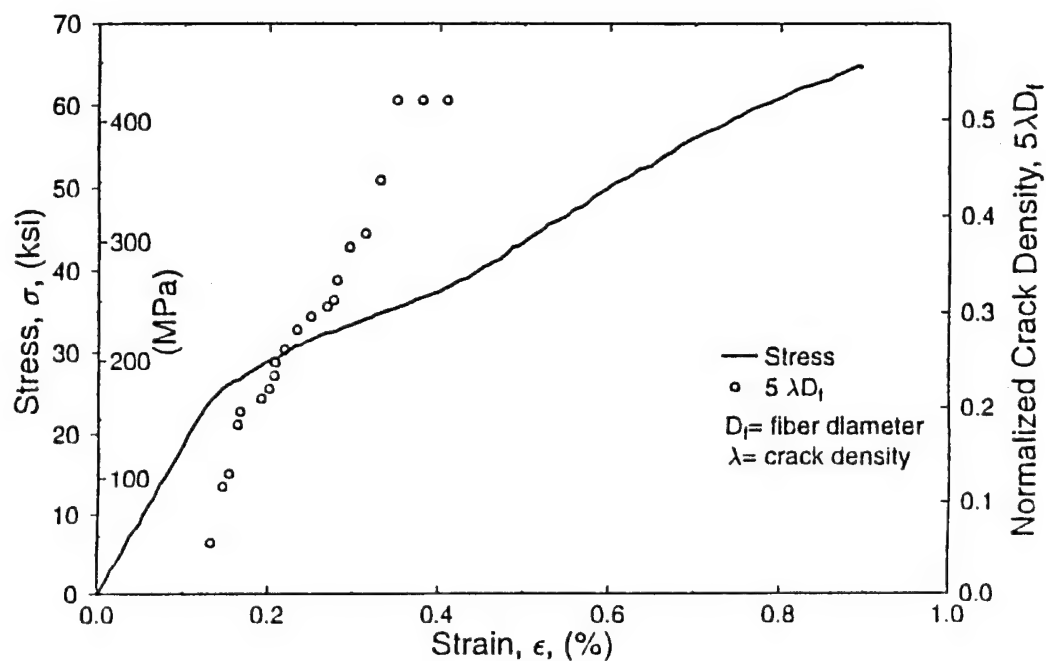
Figure 4. Stress and matrix crack density versus strain in unidirectional SiC/CAS composite under longitudinal tension.
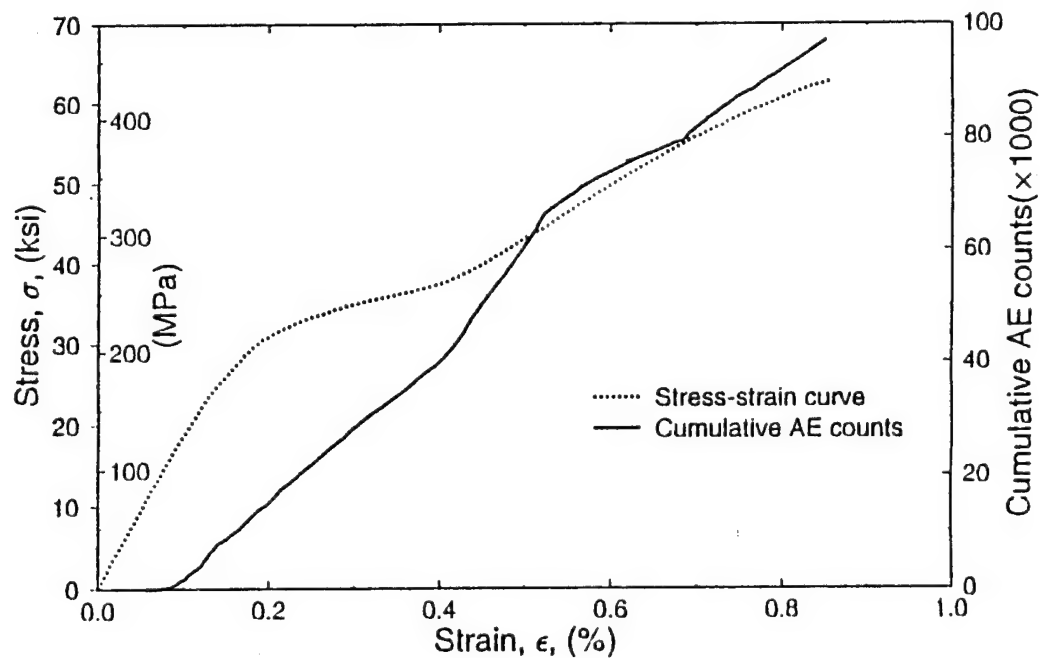
Figure 5. Stress and cumulative AE counts versus strain for unidirectional SiC/CAS composite under longitudinal tension.
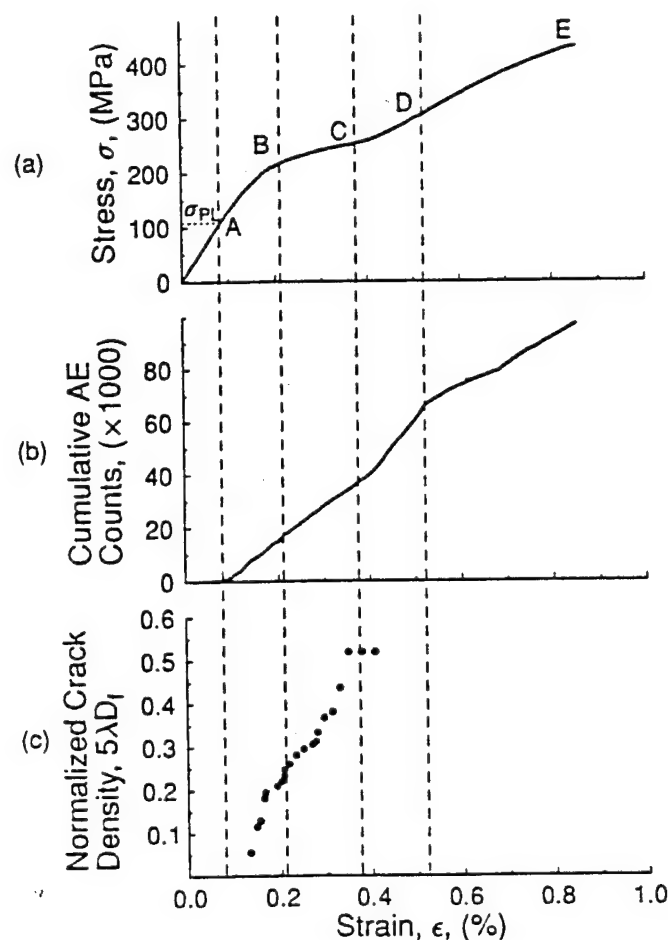
Figure 6. *Stress, cumulative AE counts, and matrix crack density versus strain for unidirectional SiC/CAS composite under longitudinal tension.*

but stabilized tangential stiffness (σ = 213–252 MPa, ϵ = 0.20–0.36%). In this region the matrix microcracks extend into macrocracks and increase in number throughout the gage section of the specimen. Both crack density and cumulative AE counts increase at a constant rate up to a point C where the matrix cracking is saturated (σ = 252 MPa, ϵ = 0.36%). The minimum crack spacing at this saturation point is approximately ten fiber diameters.

The following region CD (σ = 252–306 MPa, ϵ = 0.36–0.52%) is one of increasing tangential stiffness or a "strain hardening" region. Although matrix cracking appears to be saturated, increased AE output at a higher rate appears. It is believed that this AE activity is related to fiber-matrix debonding and/or sliding occurring in this region as indicated by ultrasonic measurements and analysis [7,9].

The terminal region DE (σ = 306–433 MPa, ϵ = 0.52–0.86%) is characterized by a gradually decreasing stiffness due to fiber fractures and pullout. AE activity continues at a reduced but stabilized rate.

The amplitude distribution of AE events and its relationship to the failure mechanisms were investigated. The variation of cumulative AE counts of various amplitude ranges with applied strain is shown in Figure 7, and histograms of AE
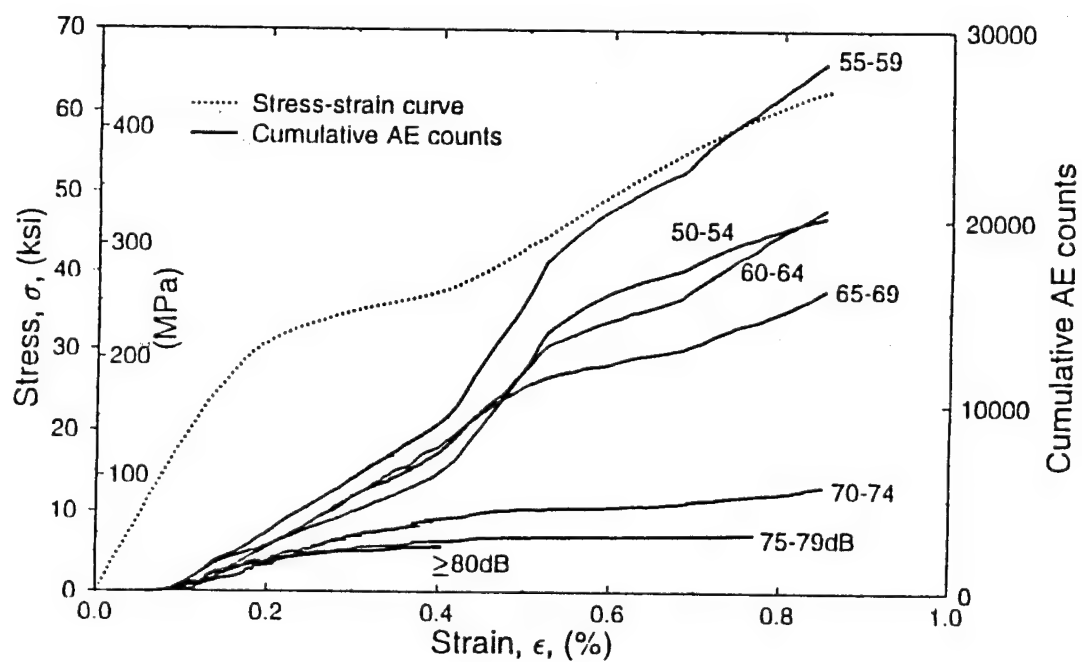
Figure 7. *Cumulative AE counts of various amplitude ranges for a unidirectional SiC/CAS composite under longitudinal tension.*
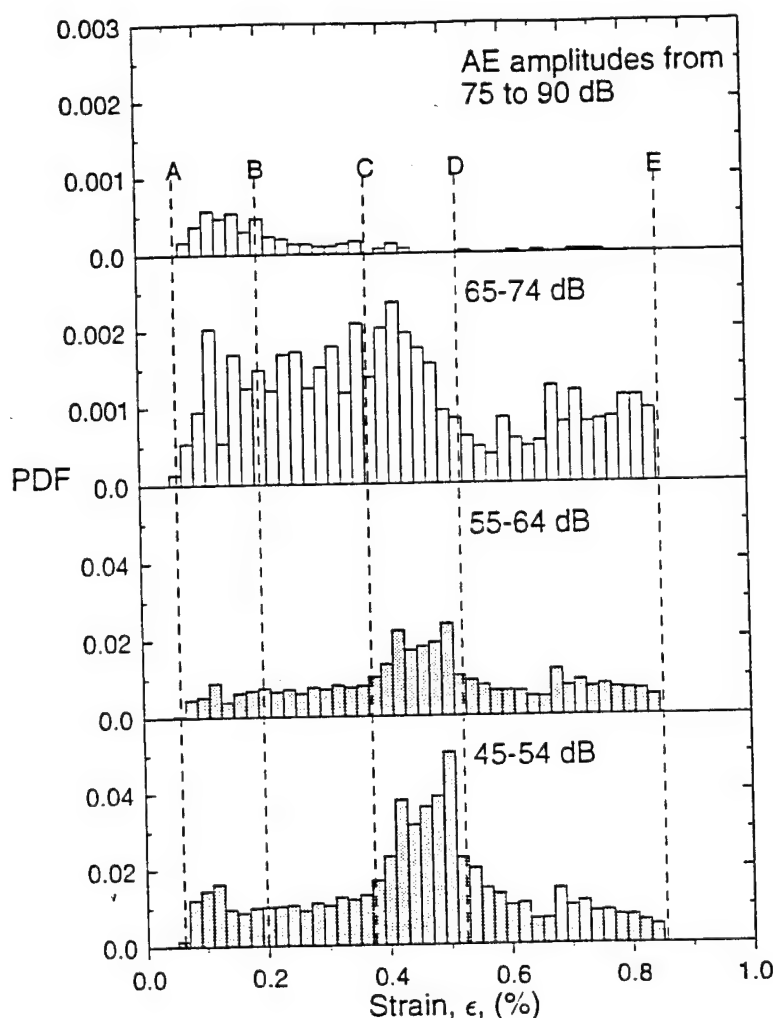
Figure 8. *Histograms of AE events for various amplitude ranges.*

events of various amplitude ranges are shown in Figure 8. It is seen that matrix cracking, which is the primary failure mechanism in region ABC, produces a broad band of AE activity. However, the highest amplitude signals (>75 dB) occur only in this region and cease at point C, the crack saturation level (Figure 6). Following crack saturation, middle to low amplitude events increase at increased rates over the "strain hardening" region CD. These results suggest that fiber-matrix debonding and sliding, the dominant failure mechanism in region CD, produce AE signals of lower amplitude but longer duration. In the final region DE the AE events of low to moderate amplitude are significantly fewer than in region CD, while high amplitude signals (70–74 dB). begin to appear again. This phenomenon could be explained by the fact that fiber fractures produce high amplitude signals of narrow pulse width but few in number.

Loading-Unloading

In addition to the continuous loading tests, loading-unloading tests were conducted. Figure 9 shows that the envelope of the loading-unloading stress-strain

curves matches the monotonic stress-strain curve. This implies that the loading-unloading process produces no significant additional damage in the material. Figures 10(a)–10(d) show cumulative AE count curves along with the corresponding stress-strain curves for the various loading-unloading loops. Figure 11 shows the records for all loops combined. It is noted that in the region below point C, or the first four loops of loading-unloading, no AE output is produced during unloading and reloading up to approximately the previous peak loading. This confirms the classical Kaiser effect and also implies that no significant debonding/sliding exists before saturation of matrix cracking. Any frictional sliding during unloading would produce additional AE counts.

In the "strain hardening" region CD where fiber-matrix debonding is believed to be dominant, the AE count rate increases during loading, but no activity is recorded during unloading (loops 4 and 5).

In regions beyond point D (loops 6,7 and final loading) a pronounced abrupt reduction in AE count rate occurs during loading. The AE output continues increasing at a slightly reduced rate during the initial stage of unloading. This AE activity during the last stage of loading and the initial stage of unloading (in loops 6 and 7) is attributed to frictional sliding in the debonded fiber-matrix interface. The characteristic rate change in AE counts in the loading curves of loop 7 and final loading step occurs at a strain equal to the peak strain reached in the previous loading. It seems that the two parts of AE output, the increasing rate part and the reduced constant rate one, demonstrate separate and independent Kaiser effects. The first part of the AE output is believed to be associated with further debonding and/or fiber fractures whereas the second part is primarily due to frictional sliding.
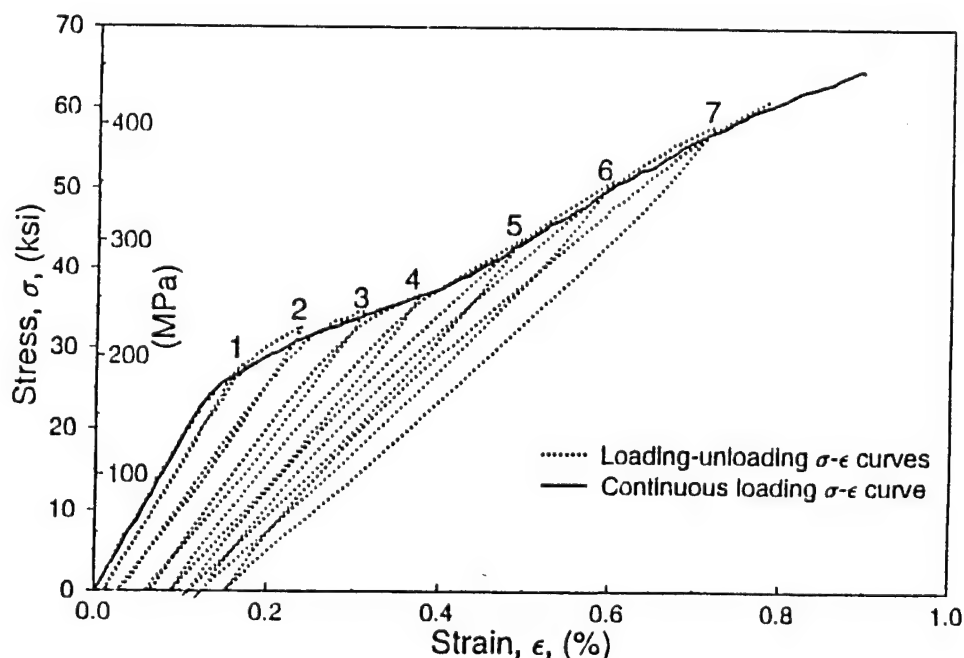
Figure 9. *Continuous loading and loading-unloading stress-strain curves for unidirectional SiC/CAS composite under uniaxial tension.*
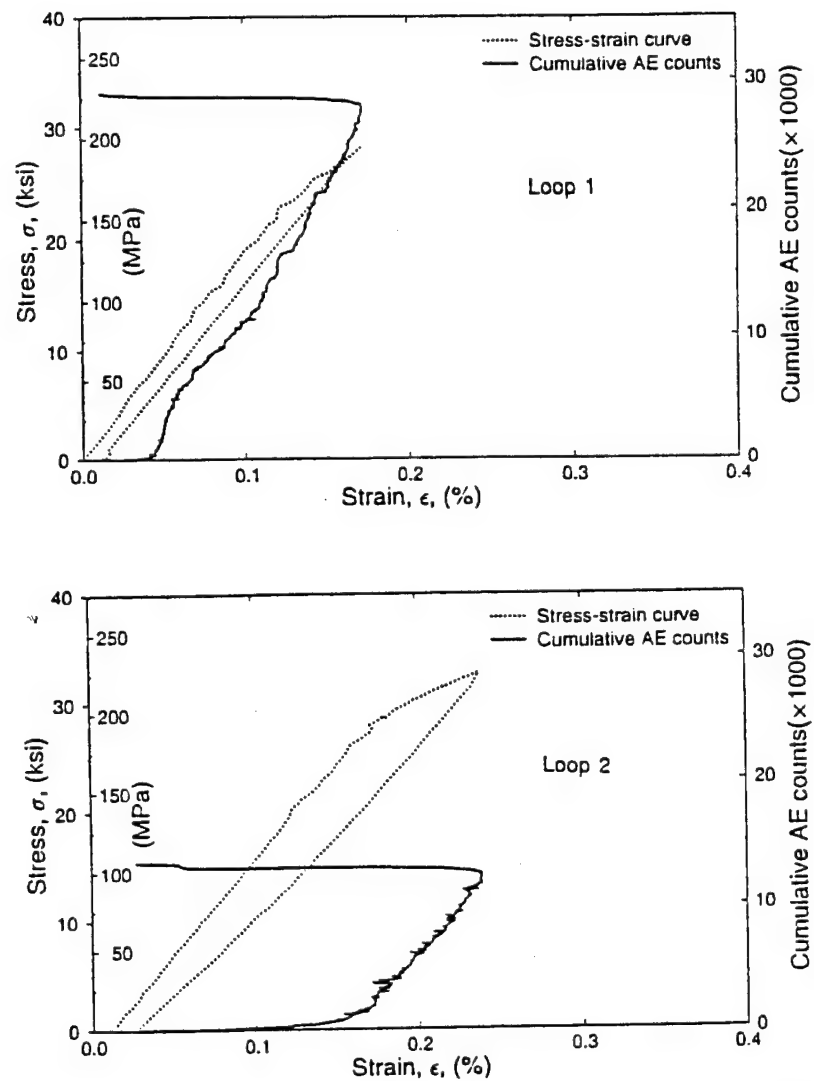
Figure 10. Stress and cumulative AE counts versus strain for loading and unloading of uni-directional SiC/CAS composite under longitudinal tension.

Figure 10 (continued). *Stress and cumulative AE counts versus strain for loading and unloading of unidirectional SiC/CAS composite under longitudinal tension.*
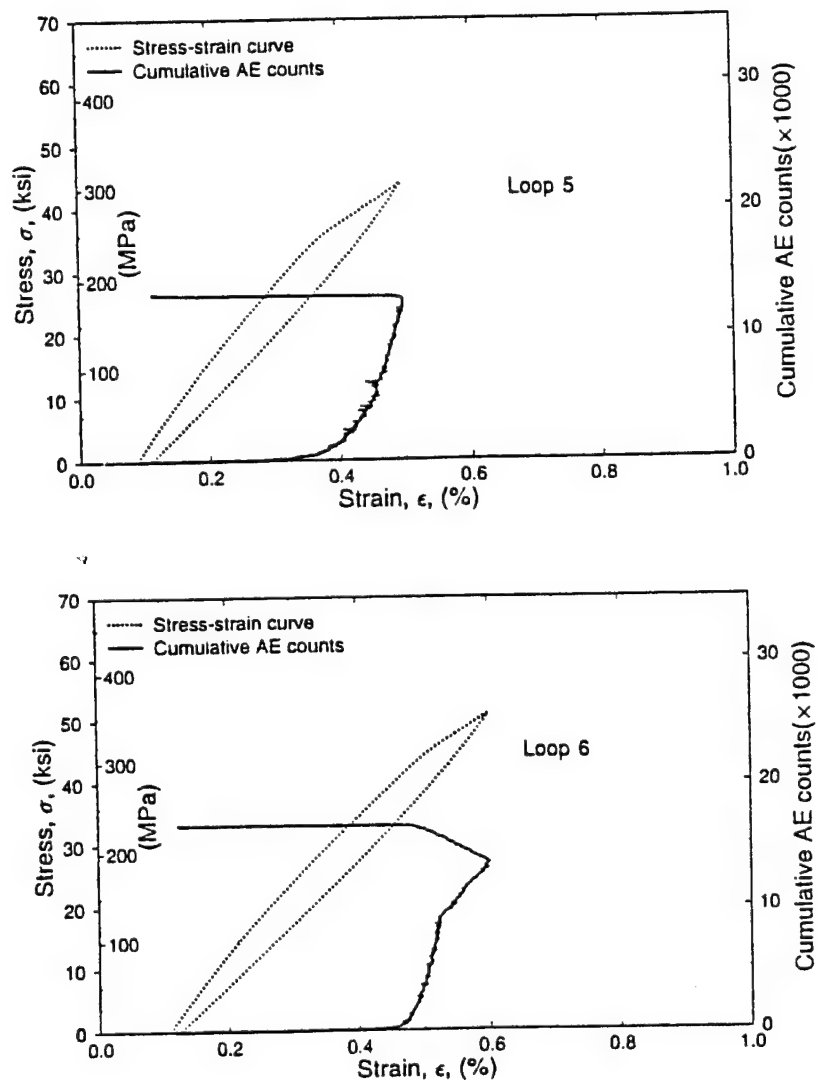
Figure 10 (continued). *Stress and cumulative AE counts versus strain for loading and unloading of unidirectional SiC/CAS composite under longitudinal tension.*

Figure 10 (continued). *Stress and cumulative AE counts versus strain for loading and unloading of unidirectional SiC/CAS composite under longitudinal tension.*
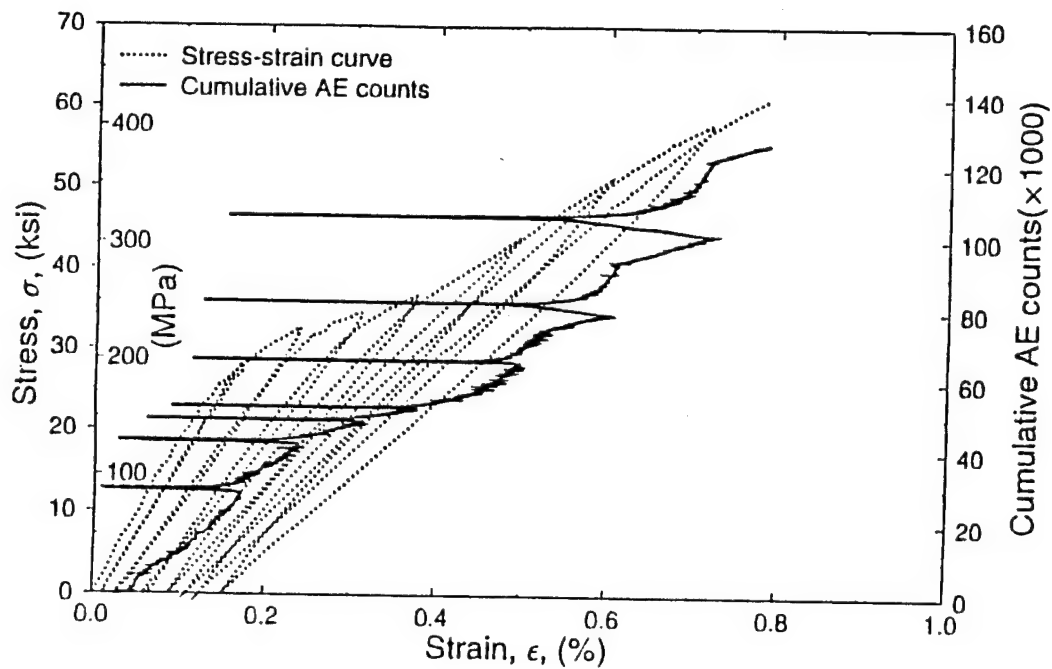
Figure 11. Stress and cumulative AE counts versus strain for loading and unloading of uni-directional SiC/CAS composite under longitudinal tension.

SUMMARY AND CONCLUSION

A correlation was made between macroscopic stress-strain behavior, acoustic emission measurements and direct microscopic observations of damage development in unidirectional SiC/CAS composites. Dominant damage mechanisms in different loading stages were identified by the correlation.

Under monotonic tensile loading matrix crack initiation and onset of AE events correspond to the proportional limit of the stress-strain curve. The matrix crack density and the cumulative AE counts vary linearly with strain through the nonlinear region between the proportinal limit and the beginning of the "strain hardening" region. At this point matrix cracking reaches a saturation level and the high amplitude AE activity levels off while the low to intermediate amplitude AE rate increases. The latter AE activity occurring over the "strain hardening" region is believed to be associated with fiber-matrix debonding.

In the case of loading-unloading cycles it is noted that the material demonstrates the Kaiser effect for loadings below the matrix crack saturation point. Beyond this point, increasing fiber-matrix debonding and fiber fractures produce changes in the AE rate and deviations from the Kaiser effect.

At higher strain levels beyond the "strain hardening" region an abrupt reduction is noticed in AE rate accompanied by further AE output during the initial stage of unloading. This characteristic behavior is attributed to frictional sliding during loading and unloading in the debonded fiber-matrix interfaces.

It was shown in this study that acoustic emission is a useful tool for studying the failure mechanisms of composite materials. For complete identification of failure mechanisms, all three kinds of damage should be observed: matrix crack-

ing, fiber-matrix debonding, and fiber fracture, of which the matrix cracking and fiber fracture are directly observable by the microscopic investigation. In the absence of reliable and practical methods for direct observation of debonding, AE is a good alternative method that provides indirect information about fiber-matrix debonding.

ACKNOWLEDGEMENTS

REFERENCES

1. Marshall, D. B. and A. G. Evans. 1985. "Failure Mechanisms in Ceramic-Fiber/Ceramic Matrix Composites," *J. Amer. Ceramic Society,* 68:225–231.

2. Marshall, D. B., B. N. Cox and A. G. Evans. 1985. "The Mechanics of Matrix Cracking in Brittle-Matrix Fiber Composites," *Acta Metall.,* 33(11):2013–2021.

3. Stang, H. and S. P. Shah. 1986. "Failure of Fiber-Reinforced Composites by Pull-out Fracture," *J. Materials Science,* 21:953–957.

4. Marshall, D. B. and A. G. Evans. 1988. "Failure Mechanisms in Ceramic Fiber/Ceramic-Matrix Composites," *Ceram. Engng. Sci. Proc.,* 9(7–8):853–860.

5. Daniel, I. M., G. Anastassopoulos and J.-W. Lee. 1989. "Failure Mechanisms in Ceramic-Matrix Composites," *Proc. of SEM Spring Conf. on Experimental Mechanics,* May 29–June 1:832–838.

6. Daniel, I. M., G. Anastassopoulos and J.-W. Lee. 1989. "Experimental Micromechanics of Brittle-Matrix Composites," *Micromechanics: Experimental Techniques,* AMD-Vol. 102, ASME Winter Annual Meeting, San Francisco, CA, December:133–146.

7. Daniel, I. M., G. Anastassopoulos and J.-W. Lee. 1993. "The Behavior of Ceramic Matrix Fiber Composites Under Longitudinal Loading," *Composites Scie. and Tech.,* 46:105–113.

8. Daniel, I. M., G. Anastassopoulos and J.-W. Lee. 1992. "Failure Mechanisms and Interfacial Shear Strength in Brittle-Matrix Composites," *AD-Vol. 29, AMD-Vol. 146,* W. F. Jones and J. M. Whitney, eds., New York: American Soc. of Mech. Engineers, pp. 57–69.

9. Wooh, S. C. and I. M. Daniel. 1994. "Real-Time Ultrasonic Monitoring of Fiber-Matrix Debonding in Ceramic Matrix Composite," *Mechanics of Materials,* 17:379–388.

10. Mall, S. and R. Y. Kim. 1992. "Failure Mechanisms in Laminates of Silicon Carbide Calcium-Aluminosilicate Ceramic Composite," *Composites,* 23(4):215–222.

11. Zok, F. W. and S. M. Spearing. 1992. "Matrix Crack Spacing in Brittle Matrix Composites," *Acta Metall. Mater.,* 40(8):2033–2043.

MECHANICS
OF
MATERIALS

Real-time ultrasonic monitoring of fiber–matrix debonding in ceramic-matrix composite

Shi-Chang Wooh and Isaac M. Daniel

Robert R. McCormick School of Engineering and Applied Science, Northwestern University, Evanston, IL 60208, USA

ELSEVIER

Real-time ultrasonic monitoring of fiber–matrix debonding in ceramic-matrix composite

Shi-Chang Wooh and Isaac M. Daniel

Robert R. McCormick School of Engineering and Applied Science, Northwestern University, Evanston, IL 60208, USA

Real-time ultrasonic techniques were developed for monitoring damage in a unidirectional ceramic-matrix composite under longitudinal tensile loading. Specifically, shear-wave transducers producing waves polarized in the transverse to the fiber direction were used in contact with the specimen to detect the initiation and propagation of fiber–matrix debonding, and to determine the transverse shear modulus and its degradation. The ultrasonically measured transverse shear modulus and its degradation was in reasonably good agreement with a prediction based on a modified shear lag model and interpolation between available solutions for fully bonded and fully unbonded fibers.

1. Introduction

Ceramic-matrix composites are receiving greater attention because of their potential use at high temperatures. Composites consisting of a ceramic matrix reinforced with high strength fibers have substantially higher strength, higher ultimate strains, better fracture toughness and ductility than comparable monolithic-matrix materials. These materials are attaining strengths of 1400 MPa (200 ksi) and ultimate strains of over 1%. Typical composites include silicon-carbide matrix reinforced with silicon-carbide fiber (SiC/SiC) and glass ceramics reinforced with silicon-carbide fibers, such as SiC/LAS (silicon carbide/lithium aluminosilicate) and SiC/CAS (silicon carbide/calcium aluminosilicate); see Brennan and Prewo (1982), and Prewo and Brennan (1982).

Correspondence to: Prof. I.M. Daniel, Theoretical and Applied Mechanics, Robert R. Mc Cormick School of Engineering and Applied Science, Northwestern University, Center for Quality Engineering and Failure Prevention, 327 Catalysis Building, 2137 North Sheridan Road, Evanston, IL 60208-3020, USA.

The macroscopic behavior of the material is intimately related to the constituent properties (fiber, matrix and interphase), the micromechanics of stress transfer between the constituents, and the failure mechanisms and their development under load. The micromechanics of stress transfer and fracture of brittle matrix composites has been studied analytically by many authors; e.g., Achenbach and Zhu (1989), Aveston et al. (1971), Aveston and Kelly (1973), Greszczuk (1969), Hsueh (1988), Lee and Daniel (1992), Marshall et al. (1985), McCartney (1989), Stang and Shah (1986). Although the various failure mechanisms are known, their relative magnitude, exact sequence and quantitative effect on overall behavior vary from case to case.

Failure mechanisms have been observed in real time by Marshall and Evans (1985) and Daniel et al. (1989a, 1989b, 1992), but the observations must be made under the microscope and are limited to the surface only. Furthermore, some mechanisms, such as fiber–matrix debonding, are very difficult to observe. There is a need to bridge the microscopic and macroscopic observations by means of nondestructive monitoring of internal damage. The ability to monitor damage

development during loading without interrupting the test is very important because the specimen must be loaded monotonically to failure at a controlled loading rate. Wooh and Daniel (1992) demonstrated that ultrasonic methods can be used to monitor damage evolution in real time. Ultrasonic measurements of attenuation and velocity of longitudinal and transverse waves were measured and correlated qualitatively with failure mechanisms.

Of the properties involved, the fiber–matrix bonding condition plays an important role on the mechanical behavior of the composite. For example, if the bonding is too weak, stresses are transferred poorly. On the other hand, if the bonding is very strong, the material behaves like a monolithic brittle one. Fiber–matrix debonding under stress is a sensitive indicator of material response and thus it is important to investigate it nondestructively.

This paper describes an ultrasonic technique for real-time monitoring of fiber–matrix debonding and a correlation between the ultrasonically measured transverse shear modulus and an analytical prediction.

2. Theoretical background

The material investigated was a unidirectional SiC/CAS composite, calcium aluminosilicate glass ceramic reinforced with silicon carbide fibers. Figure 1 illustrates a typical longitudinal stress–strain curve and corresponding failure mechanisms for this material. The curve shows four primary regions of interest. The initial region of the curve (A) is the linear elastic range where virtually no damage could be found. This linear region extends at least up to the level where the matrix stress or strain reaches the ultimate value of the matrix tensile strength or fracture strain. The initial longitudinal modulus of the composite is obtained by the rule of mixtures:

$$E_1 = E_f V_f + E_m V_m,\tag{1}$$

where E_f, E_m are the moduli of the fiber and
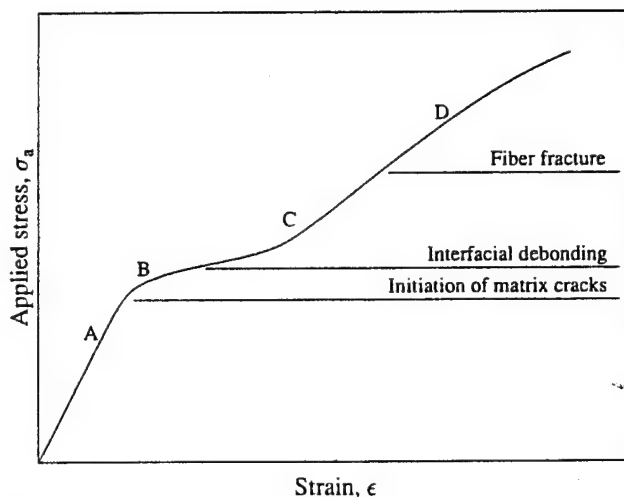
Fig. 1. Schematic illustration of stress–strain curve and failure mechanisms of unidirectional SiC/CAS composite.

matrix and V_f, V_m are the fiber and matrix volume ratios, respectively. Assuming the ultimate matrix strain to be lower than that of the fiber, the stress level at matrix crack initiation is given by the relationship

$$\sigma_1 = \frac{E_1}{E_m}(F_{mt} - \sigma_{rm}),\tag{2}$$

where F_{mt} is the matrix tensile strength and σ_{rm} is the axial residual stress in the matrix.

Following crack initiation and propagation across the specimen section, accompanied by fiber–matrix debonding, the curve tends to bend to a plateau or reduced stiffness region B corresponding to crack multiplication and further fiber–matrix debonding. In the middle of this region (C), matrix cracking becomes saturated while debonding continues. The curve enters region D as the interfacial debonding is saturated. Fiber fractures are observed somewhere in this range of stress and the material finally fails globally.

Figure 2 illustrates schematically a damaged material with matrix cracking and partial debonding near the crack tips. If the crack spacing (l) and debond length (d) are given, the transverse shear modulus G_{23} can be determined for the given applied stress by using a micromechanics approach based on Eshelby's equivalent inclusion method (see Eshelby, 1957; Mori and Tanaka,

1973; Takahashi and Chou, 1988). An isotropic matrix with transversely isotropic ellipsoidal inclusions is considered.

Assuming small displacements, the relationship between stress (σ_{ij}) and strain (ϵ_{ij}) tensors for a generally anisotropic material is expressed in the form

$$\sigma_{ij} = C_{ijkl}\epsilon_{kl}, \tag{3}$$

or

$$\epsilon_{ij} = S_{ijkl}\sigma_{kl}, \tag{4}$$

where C_{ijkl} is the stiffness tensor. The effective elastic compliances of the composite S_{ijkl} are obtained by considering the work done under the applied stress σ_{ij}:

$$S_{ijkl}\sigma_{ij}\sigma_{kl} = S_{ijkl}^{m}\sigma_{ij}\sigma_{kl} + V_{f}\sigma_{ij}\epsilon_{ij}^{*}, \tag{5}$$

where S_{ijkl}^{m} is the matrix elastic compliance and ϵ_{ij}^{*} is the solution of the following simultaneous equations:

$$C_{pqmn}^{m}\left[\epsilon_{mn} + (1 - V_{f})(T_{mnkl}\epsilon_{kl}^{*} - \epsilon_{mn}^{*})\right]$$
$$= C_{pqmn}^{f}\left[\epsilon_{mn} + (1 - V_{f})T_{mnkl}\epsilon_{kl}^{*} + V_{f}\epsilon_{mn}^{*}\right] \tag{6}$$

where C_{pqmn}^{m} and C_{pqmn}^{f} are the stiffnesses of the matrix and fiber, respectively, and T_{mnkl} is known as Eshelby's tensor.

For the case of perfect bonding between fiber and matrix, the transverse shear modulus G_{23}^{0} is obtained by substituting

$$\sigma_{23} = \sigma_{32} = 1,$$

all other $\sigma_{ij} = 0$, into Eq. (5):

$$\frac{G_{23}^{0}}{G_{m}} = \frac{G_{m}(1 - V_{f}) + G_{23f}(3 - 4\nu_{m} + V_{f})}{G_{m}[1 + (3 - 4\nu_{m})V_{f}] + G_{23f}(3 - 4\nu_{m})(1 - V_{f})}, \tag{7}$$

where ν_{m}, G_{m}, G_{23f} are the matrix Poisson's ratio, matrix shear modulus, and transverse shear modulus of the fiber, respectively. Subscripts 2 and 3 denote the transverse in-plane and transverse out-of-plane directions, respectively.

For the case of complete debonding, the transverse shear loading is replaced by the equivalent tension and compression at 45° with the direction of shear. Using the same equations as above for this case we obtain shear modulus G_{23}^{1} as:

$$\frac{G_{23}^{1}}{G_{m}} = \frac{(1 - V_{f})\phi}{(1 - V_{f})\phi + 4\chi(1 - \nu_{m}^{2})V_{f}}, \tag{8}$$
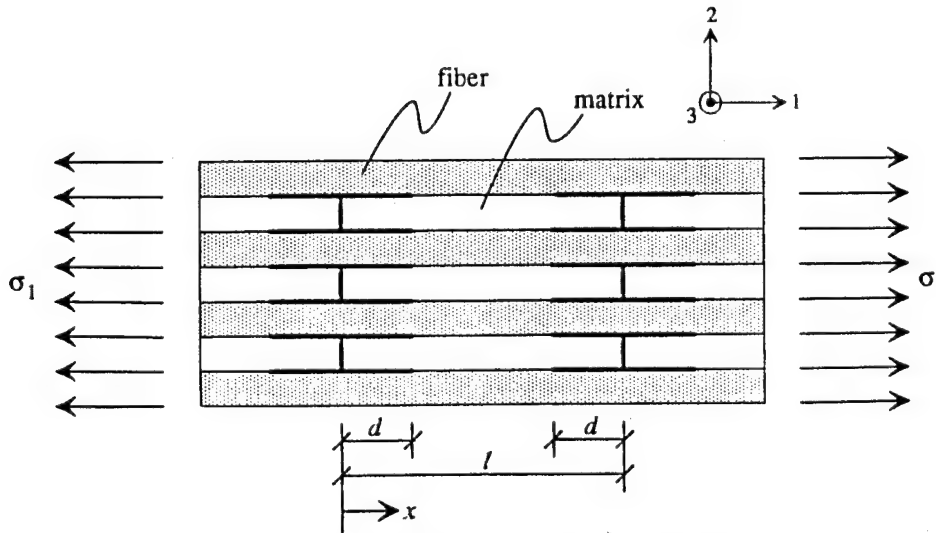
Fig. 2. Composite element with matrix cracking and partial debonding.

where

$$\phi = (1 + \nu_m)[1 + 2(1 - \nu_m)Q]$$
$$\times (1 - V_f)^2 + [4R + (3 - 2\nu_m^2 - 2\nu_m\nu_{12f})Q]$$
$$\times (1 - V_f)V_f + 4(1 - \nu_m)$$
$$\times (1 - \nu_{12f}\nu_{21f})(2 + V_f)V_f RQ,$$

$$R = \frac{(1 + \nu_m)E_{1f}}{4(1 - \nu_{12f}\nu_{21f})E_m},$$

$$Q = \frac{(1 + \nu_m)E_{2f}}{(1 - \nu_{12f}\nu_{21f})E_m},$$

$$\chi = (1 - V_f)^2 + \frac{1}{1 + \nu_m}$$
$$\times [(1 - \nu_m\nu_{12f})Q + 4(1 - \nu_m\nu_{12f})]$$
$$\times (1 - V_f)V_f R + \frac{1 - \nu_m}{E_m}E_{1f}V_f^2 Q.$$

In the case of partial debonding along the fiber direction, it is assumed that the fiber–matrix interface around the circumference of the fiber is completely debonded. The transverse shear modulus is then calculated by linear interpolation of the moduli for the cases of perfect bonding and complete debonding, i.e.,

$$G_{23} = G_{23}^0 \frac{l - 2d}{l} + G_{23}^1 \frac{2d}{l}, \tag{9}$$

or

$$\frac{G_{23}}{G_{23}^0} = 1 - \left(1 - \frac{G_{23}^1}{G_{23}^0}\right)a. \tag{10}$$

This approach is valid when the crack spacing is sufficiently smaller than the characteristic dimension of the ultrasonic sensor to be discussed below.

The ratio of debond length to crack spacing (d/l) is obtained from a modified shear lag analysis model proposed by Lee and Daniel (1992).

$$\frac{2d}{l} = 1 - \frac{1}{\beta}\log\frac{1 + \xi}{1 - \xi}, \tag{11}$$

where

$$\xi = \frac{2F_{is}}{M(\eta^2 - 1)}\frac{E_1}{E_m\sigma_1 + E_1\sigma_{rm}} \tag{12}$$

and

$$\eta = \frac{1}{\sqrt{V_f}},$$

$$\beta = \frac{Ml}{r_f},$$

$$M = \sqrt{H\left(\frac{1}{E_f} + \frac{1}{E_m(\eta^2 - 1)}\right)},$$

$$H = \frac{2}{\frac{1}{4G_f} + \frac{(3\eta + 1)(\eta - 1)}{3(\eta + 1)^2 G_m}},$$

in which r_f is the fiber radius, σ_1 is the applied stress, σ_{rm} is the axial residual stress in the matrix, F_{is} is the interfacial shear strength, and E_f, E_m, G_f, and G_m are the Young's moduli and shear moduli of the fiber and matrix, respectively.

Wooh and Daniel (1991) measured the five elastic constants of a transversely isotropic unidirectional laminate by means of ultrasonic wave propagation tests. Determination of G_{23} is experimentally much simpler than that of the other constants. For a plane wave, the displacements are given as

$$u_m = U_m \exp[kj(n_i x_i - ct)], \tag{13}$$

where k is the wave number, j is the unit imaginary number, n_i are the direction cosines of the normal to the wave front, U_m is the displacement amplitude, and c the wavespeed. Substituting Eqs. (3) and (13) into the equation of motion yields the eigenvalue equation and noting that a nontrivial solution exists when the determinant vanishes, the following determinantal equation is obtained

$$|C_{ijkl}n_l n_j - \rho c^2\delta_{ij}| = 0, \tag{14}$$

where δ_{ij} is the Kronecker delta and ρ is the density of the material. The stress–strain relationship for orthotropic materials is expressed in

terms of nine independent elastic constants, that is:

$$\begin{Bmatrix} \sigma_{11} \\ \sigma_{22} \\ \sigma_{33} \\ \sigma_{23} \\ \sigma_{31} \\ \sigma_{12} \end{Bmatrix} = \begin{bmatrix} C_{11} & C_{12} & C_{13} & 0 & 0 & 0 \\ C_{12} & C_{22} & C_{23} & 0 & 0 & 0 \\ C_{13} & C_{23} & C_{33} & 0 & 0 & 0 \\ 0 & 0 & 0 & C_{44} & 0 & 0 \\ 0 & 0 & 0 & 0 & C_{55} & 0 \\ 0 & 0 & 0 & 0 & 0 & C_{66} \end{bmatrix} \begin{Bmatrix} \epsilon_{11} \\ \epsilon_{22} \\ \epsilon_{33} \\ \gamma_{23} \\ \gamma_{31} \\ \gamma_{12} \end{Bmatrix}$$

(15)

where $[C_{ij}]$ is the stiffnes matrix, subscripts 1, 2, 3 denote the principal material axes, and γ_{ij} are the engineering shear strains. Then, Eq. (14) takes the form

$$\det \begin{vmatrix} \Gamma_{11} - \rho c^2 & \Gamma_{12} & \Gamma_{13} \\ \Gamma_{12} & \Gamma_{22} - \rho c^2 & \Gamma_{23} \\ \Gamma_{13} & \Gamma_{23} & \Gamma_{33} - \rho c^2 \end{vmatrix} = 0,$$

(16)

where the so-called Christoffel stiffnesses Γ_{ij} are given by

$$\begin{aligned}
\Gamma_{11} &= n_1^2 C_{11} + n_2^2 C_{66} + n_3^2 C_{55}, \\
\Gamma_{22} &= n_1^2 C_{66} + n_2^2 C_{22} + n_3^2 C_{44}, \\
\Gamma_{33} &= n_1^2 C_{55} + n_2^2 C_{44} + n_3^2 C_{33}, \\
\Gamma_{12} &= n_1 n_2 (C_{12} + C_{66}), \\
\Gamma_{23} &= n_2 n_3 (C_{23} + C_{44}), \\
\Gamma_{13} &= n_3 n_1 (C_{13} + C_{55}).
\end{aligned}$$

(17)

By setting the directional cosines for a wave motion traveling in the thickness direction x_3, i.e.,

$$n_1 = n_2 = 0 \quad \text{and} \quad n_3 = 1,$$

(18)

three distinct solutions for c are obtained. Of these, the solution of interest is the one related to the transverse shear modulus, that is

$$G_{23} = C_{44} = \rho c_{23}^2,$$

(19)
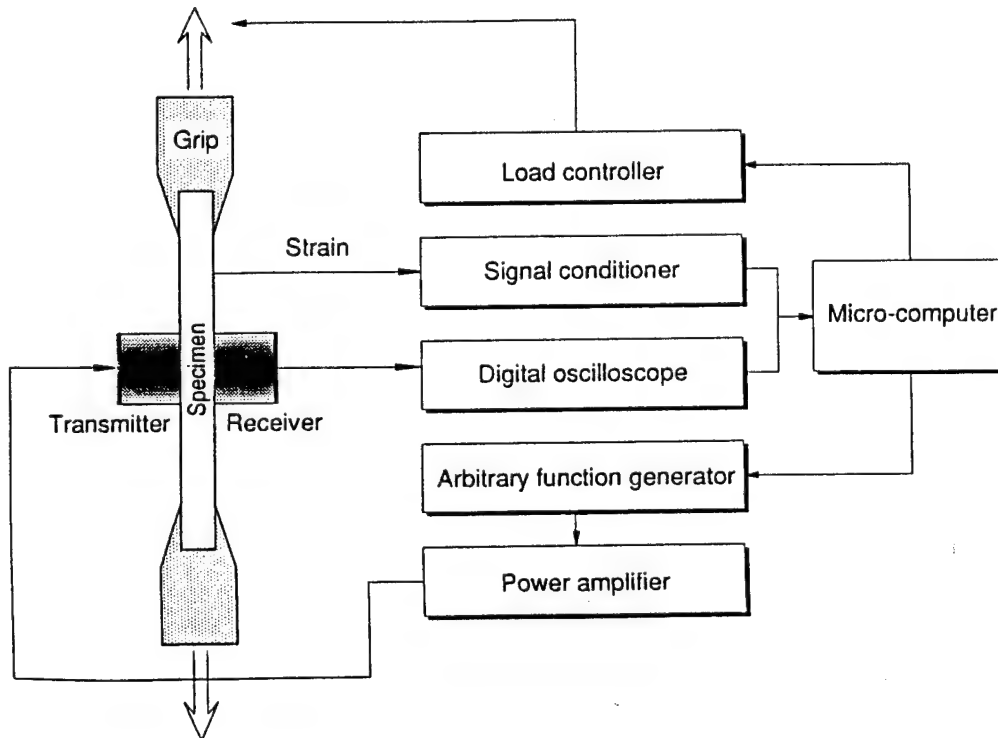
Fig. 3. Schematic block diagram of the ultrasonic system.

where c_{23} is the velocity of the shear wave polarized in the plane transverse to the fiber direction. Fiber–matrix debonding with a surface normal transverse to the wave propagation direction affects the transverse shear modulus degradation which is related to the corresponding wavespeed.

3. Experimental procedure

The material investigated was a unidirectional SiC/CAS, calcium-aluminosilicate glass ceramic reinforced with silicon-carbide fibers, manufactured by Corning Glass Works. The fiber is silicon-carbide yarn known as Nicalon (Nippon Carbon Co.) of 15 μm average diameter. The composite was obtained in the form of 16-ply, 3.048 mm (0.12 in) thick unidirectional plates.

Unidirectional coupons, 3.05 mm (0.12 in) thick, 17.27 mm (0.68 in) wide, and 15.24 cm (6 in) long, were prepared. They were tabbed with 2.54 cm (1 in) long glass/epoxy tabs and instrumented with strain gages on both sides. The specimens were loaded in a servohydraulic testing machine while applied' stress and strains (both longitudinal and transverse strains) were monitored and recorded. Meanwhile, a pair of ultrasonic shear wave transducers were tightly attached to the surfaces of the sample for ultrasonic characterization. These transducers were set up in through-transmission mode and they were aligned to generate a shear wave polarized perpendicular to the fiber direction. A microcomputer was used to control the entire process of load control and data acquisition. A 10 MHz toneburst signal generated by an arbitrary function generator (LeCroy 9100) excited the transmitter after passing through an RF power amplifier (ENI 325LA). Then, the transmitted multiple echoes were recorded by a digital oscilloscope (Tektronix RTD710) running at a sampling rate of 200 MHz (5 ns intervals). Figure 3 shows a schematic diagram of the ultrasonic test system used. As soon as all mechanical and ultrasonic measurements were completed, the specimen was immediately loaded to the next step and this procedure was repeated until global failure of the specimen.

4. Wavespeed measurements

Wavespeeds were measured from the wave traces of the transmitted and multiple echoes in the material as illustrated in Fig. 4. Figure 5 is a typical as-obtained waveform. The wavespeed is simply

$$c = 2h/\Delta t, \tag{20}$$

Fig. 4. Transmitted signals and multiple echoes for measurement of wavespeed and attenuation.

Fig. 5. Illustrative example of cepstrum analysis for measuring wavespeed: (a) as-obtained waveform; (b) magnitude spectrum; and (c) magnitude cepstrum.

for automated testing increases the chance of introducing errors.

An alternative approach is to determine the wavespeed based on ultrasonic interference spectroscopy (see Chang et al., 1974; Wooh and Daniel, 1991). In this method, the obtained waveforms $f(t)$ are expressed in the frequency domains as

$$F(\omega) = \int_{-\infty}^{\infty} f(\tau) \exp(-j\omega\tau) \, d\tau, \qquad (21)$$

by means of fast Fourier transform (FFT) (see Brigham, 1988). The relatively low periodicity of the echoes compared to the frequency of the ultrasonic wave produces well defined anti-resonance dips and peaks in the frequency spectrum as shown in Fig. 5b. The period of these dips or peaks directly gives the time interval Δt. One of the advantages of this method is that the dips appear even when the echoes interfere with each other, that is, this technique is useful even for very thin laminates. However, because of the many different situations, the algorithm of search for the local minima is computationally complex. The method of fails in a noisy environment, especially in a case when the specimen has severe internal damage and the signal-to-noise ratio becomes low.

To solve this problem, the so-called cepstrum analysis was used (see Childers et al., 1977; Wooh and Daniel, 1992). The above-mentioned spectrum is considered as another time series. Taking the FFT of the magnitude spectrum yields a spectrum of the spectrum called magnitude cepstrum which is back in the time domain:

$$g(t) = \int_{-\infty}^{\infty} |F(\omega)| \exp(-j\omega t) \, dt. \qquad (22)$$

The time in the cepstrum is called quefrency and since the interferences in the magnitude spectrum are periodic, the maximum amplitude occurs at the quefrency $t = \Delta t$ in the magnitude spectrum as illustrated in Fig. 5c. The algorithm for determining a time delay becomes much simpler because one needs to simply find a maximum amplitude and its absolute location in the que-

where Δt is the time interval between echoes and h is the specimen thickness. The time interval can be directly obtained in the time domain by measuring the time interval between two corresponding peaks of two consecutive echoes because the signal used is a single frequency toneburst. However, it is not desirable to measure the wavespeeds in this manner since it is sometimes difficult to locate the right peaks and the complex algorithm

frency domain. Wavespeeds are then calculated from Eq. (20).

A drawback of this method is that it is computation intensive because one needs to perform the Fourier transformation twice for each loading step. Fortunately, modern computers are capable of handling such a task in real time.

5. Attenuation measurements

Attenuation is another important parameter indicating damage in the material. Although we do not have an analytical solution for attenuation, it can be measured and correlated with the internal damage. In contrast to the transverse wavespeed, the attenuation is sensitive to matrix cracking as well. The amplitudes of the first three echoes in Fig. 4 are:

$$A_1 = \kappa A_0 T_{AB} T_{BC} \Omega,$$
$$A_2 = \kappa A_0 T_{AB} T_{BC} R_{BC} R_{BA} \Omega^3, \qquad (23)$$
$$A_3 = \kappa A_0 T_{AB} T_{BC} R_{BC}^2 R_{BA}^2 \Omega^5,$$

where κ is the sensitivity of the receiving transducer, A_0 the amplitude' of the incident signal, and $T_{AB}, T_{BC}, R_{BA}, R_{BC}$ are the transmission and reflection coefficients at the front and back surfaces of the specimen, respectively. The signal loss Ω is then expressed by solving the above equations:

$$\Omega = k_1 A_1 = k_2 \left(\frac{A_2}{A_1} \right)^{1/2}$$

$$= k_2 \left(\frac{A_3}{A_2} \right)^{1/2} = k_3 \left(\frac{A_3}{A_1} \right)^{1/2} = \dots. \qquad (24)$$

The attenuation can be expressed as the sum of the initial attenuation (α_0; no damage) and the attenuation due to damage (α_d):

$$a = \alpha_0 + \alpha_d. \qquad (25)$$

Therefore,

$$\alpha_d = \alpha - \alpha_0 = -\frac{20}{h} \log_{10} \left(\frac{\Omega}{\Omega_0} \right)$$

$$= -\frac{20}{h} \log_{10} q, \qquad (26)$$

where the relative signal loss q is

$$q = \frac{A_1}{(A_1)_0} = \left(\frac{A_2/A_1}{(A_2/A_1)_0} \right)^{1/2}$$

$$= \left(\frac{A_3/A_2}{(A_3/A_2)_0} \right)^{1/2} = \left(\frac{A_3/A_1}{(A_3/A_1)_0} \right)^{1/2}. \qquad (27)$$

Subscript zero means initial reference stage before loading. One can select any two echoes to calculate the attenuation, but it is more desirable to pick the echoes that correspond to the longest travel in order to minimize measurement errors.

Amplitudes of the individual wavelets were measured by introducing an imaginary gate on the waveforms and finding peak-to-peak values within the gate (Fig. 4). The location of the gate is recalculated by the wavespeed measurement so that the gate follows the corresponding wavelets.

6. Results and discussion

Some properties of the matrix and fiber constituents obtained from the literature and from tests are tabulated in Table 1 (Larsen and Adams, 1988). The unidirectional composite was mechanically characterized and the results are shown in Table 2.

As discussed before, the method used here is valid when the debond length is sufficiently smaller than the characteristic dimension of the ultrasonic transducer. In the present case, the diameter of the transducer used was 25.4 mm (1

Table 1
Constituent material properties

Property	CAS matrix	SiC fiber
Maximum use temperature, °C (°F)	1350 (2460)	1300 (2370)
Fiber diameter, μm	–	15
Density, g/cm³	2.8	2.6
Coefficient of thermal expansion, $10^{-6}/°C$ ($10^{-6}/°F$)	5.0 (2.8)	3.2 (1.8)
Elastic modulus, GPa (Msi)	98 (14.2)	170 (280)
Tensile strength, MPa (ksi)	124 (18) (flexural)	1930 (280)

Table 2
Measured properties of SiC/CAS unidirectional composite

Property	Value
Fiber volume ratio, V_f	0.39
Ply thickness, mm (in)	0.38 (0.015)
Longitudinal modulus, E_1, GPa (Msi)	125 (18.1)
Transverse modulus, E_2, GPa (Msi)	112 (16.2)
In-plane shear modulus, G_{12}, MPa (Msi)	52 (7.5)
Major Poisson's ratio, ν_{12}	0.18
Longitudinal tensile strength, F_{1t}, MPa (ksi)	393 (57)
Transverse tensile strength, F_{2t}, MPa (ksi)	55 (8)
Longitudinal ultimate tensile strain, ϵ_{1t}^u	0.0084
Transverse ultimate tensile strain, ϵ_{2t}^u	0.0005

Fig. 7. Change in normalized signal loss due to induced damage during loading with superimposed stress–strain curve.

in) which is approximately 160 times the measured minimum crack spacing (160 μm). Figure 6 shows the predicted and measured variation of the transverse shear modulus G_{23} due to induced debonding during loading. It shows qualitatively that the modulus is degraded as debonding grows. However, from the quantitative point view, the experimental curve shows some deviation from the prediction. The experimentally measured rate of degradation is more uniform than the predicted one. This disagreement could be attributed to the neglect of the frictional stress between the fiber and matrix. The friction prevents the sudden propagation of debonding immediately after initiation resulting in the less steep curve in this region. The agreement is better in the last part of
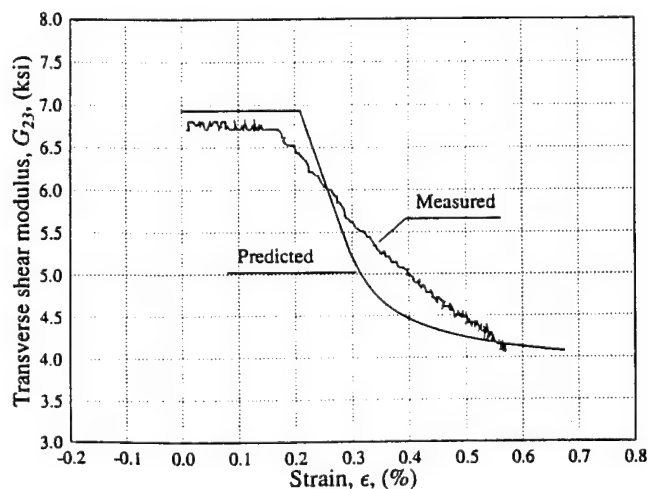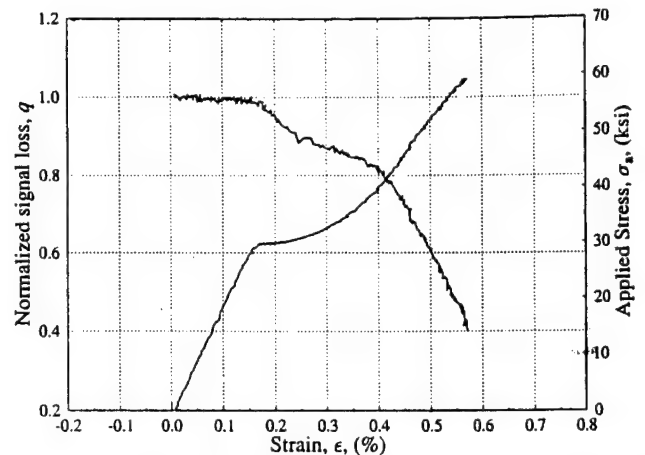
the curve corresponding to more extensive debonding.

Figure 7 shows the change in normalized ultrasonic signal loss due to induced damage during loading as a function of applied strain. The attenuation shows a good qualitative correlation with previously observed failure mechanisms and with the associated stress–strain curve. The point of initial change in signal loss coincides exactly with the proportional limit.

In summary, ultrasonic methods were developed for real-time monitoring of damage evolution in ceramic composites under tensile loading. The transverse shear modulus calculated from wavespeed measurements can be used as a sensitive indicator of fiber–matrix debonding. Ultrasonic attenuation shows good qualitative agreement with damage and the combination of attenuation and wavespeed would be a useful method to study failure mechanisms. Future studies should include the effects of residual stresses and the friction between fiber and matrix for a better prediction of material behavior.

Acknowledgement

Fig. 6. Change in transverse shear modulus due to debonding during loading.

References

Achenbach, J.D. and H. Zhu (1989), Effect of interfacial zone on mechanical behavior and failure of fiber-reinforced composites, *J. Mech. Phys. Solids 37(3)*, 381–393.

Aveston, J., G.A. Cooper and A. Kelly (1971), The properties of fiber composites, in: *Conf. Proc., National Physical Laboratory*, IPC Science and Technology Press Ltd., pp. 15–26.

Aveston, J. and A. Kelly (1973), Theory of multiple fracture of fibrous composites, *J. Mater. Sci. 8*, 352–362.

Brennan, J.J. and K.M. Prewo (1982), Silicon carbide fiber reinforced glass–ceramic matrix composites exhibiting high strength and toughness, *J. Mater. Sci. 17*, 2371–2383.

Brigham, E.O. (1988), *The Fast Fourier Transform and Its Applications*, Prentice Hall, Englewood Cliffs, New Jersey.

Chang, F.C., J.C. Couchman and B.G.W. Yee (1974), Ultrasonic resonance measurements of sound velocity in thin composite laminates, *J. Compos. Mater. 8*, 356.

Childers, D.G., D.P. Skinner, and R.C. Kemerait (1977), The cepstrum: a guide to processing, *Proc. of the IEEE 65(10)*, 1428–1443.

Daniel, I.M., G. Anastassopoulos and J.-W. Lee (1989a), Experimental micromechanics of brittle-matrix composites, in: *Micromechanics: Experimental Techniques*, AMD-Vol. 102, ASME Winter Annual Meeting, San Francisco, CA, pp. 133–146.

Daniel, I.M., G. Anastassopoulos and J.-W. Lee (1989b), Failure mechanisms in ceramic matrix composites, in: *Proc. SEM Spring Conf. on Experimental Mechanics*, pp. 832–838.

Daniel, I.M., G. Anastassopoulos and J.-W. Lee (1992), Failure mechanisms and interfacial shear strength in brittle-matrix composites, ASME Winter Annual Meeting, Anaheim, November 8–13, 1992.

Eshelby, J.D. (1957), The determination of the field of an ellipsoidal inclusion and related problems, *Proc. R. Soc., London A(241)*, 376–396.

Grande, D.H., J.F. Mandell and K.C.C. Hong (1988), Fiber–matrix bond strength studies of glass ceramic and metal matrix composites, *J. Mater. Sci. 23*, 311–328.

Greszczuk, L.B. (1969), Theoretical studies of the mechanics of the fiber–matrix interface in composites, in: *Interfaces in Composites*, ASTM STP 452, American Society for Testing and Materials, pp. 42–58.

Hsueh, C.-H. (1988), Analytical evaluation of interfacial shear strength for fiber-reinforced ceramic composites, *J. Am. Ceram. Soc. 71*, 490–493.

Larsen, D.C. and J. Adams (1988), Corning glass works, Private communication.

Lee, J.-W. and I.M. Daniel (1992), Deformation and failure of longitudinally loaded brittle-matrix composites, in: G.C. Grimes, ed., *Composite Materials: Testing and Design (Tenth Volume)*, ASTM STP 1120, American Society for Testing and Materials, pp. 204–221.

Marshall, D.B., B.N. Cox and A.G. Evans (1985), The mechanics of matrix cracking in brittle-matrix fiber composites, *Acta Metall. 33(11)*, 2013–2021.

Marshall, D.B. and A.G. Evans (1985), Failure mechanisms in ceramic-fiber/ceramic matrix composites, *J. Am. Ceram. Soc. 68*, 225–231.

McCartney, L.N. (1989), New theoretical model of stress transfer between fibre and matrix in a unidirectionally fiber-reinforced composite, in: *Proc. R. Soc. London A425*, 215–244.

Mori, T. and K. Tanaka (1973), Average stress in matrix and average elastic energy of materials with misfitting inclusions, *Acta Metall. 21*, 571.

Prewo, K.M. and J.J. Brennan (1982), Silicon carbide yarn reinforced glass matrix composites, *J. Mater. Sci. 17*, 1201–1206.

Stang H. and S.P. Shah (1986), Failure of fiber-reinforced composites by pull-out fracture, *J. Mater. Sci. 21*, 953–957.

Takahashi, K. and T.-W. Chou (1988), Transverse elastic moduli of unidirectional fiber composites with interfacial debonding, *Metall. Trans. 19A*, 129–135.

Wooh, S.C. and I.M. Daniel (1991), Mechanical characterization of a unidirectional composite by ultrasonic methods, *J. Acoust. Soc. Am. 90(6)*, 3248–3253.

Wooh, S.C. and I.M. Daniel (1992), Real-time ultrasonic investigation of damage development in ceramic-matrix composite, in: D.O. Thompson and D.E. Chimenti, eds., *Review of Progress in Quantitative Nondestructive Evaluation*, Vol. 11, Plenum Press, New York, pp. 1523–1530.

Pergamon

0020–7683(94)00199–5

STRESS STATES AT NEIGHBORING FIBERS INDUCED BY SINGLE-FIBER INTERPHASE DEFECTS

H. S. CHOI and J. D. ACHENBACH

Center for Quality Engineering and Failure Prevention, Northwestern University, Evanston,
IL 60208, U.S.A.

Abstract—A reduced interphase stiffness of a single fiber (the dissimilar fiber) in a unidirectionally reinforced composite gives rise to stress deviations in its own interphase, as well as in the interphases of neighboring fibers, relative to the stresses in a perfect composite. For transverse loading and an arbitrary cross-sectional distribution of the fibers, a general method is presented to calculate these stress deviations, based on solutions by the boundary element method of boundary integral equations for the dissimilar fiber and neighboring fibers. In this method nearest and next-nearest fibers are taken into account. The interphases are represented by the spring layer model. Detailed numerical results are presented for the special case of a hexagonal array composite. Results are compared for calculations taking into account nearest and next-nearest neighbors. Stresses at the matrix sides of the interphases and energy densities in the interphases have been calculated for the dissimilar fiber and for the next-nearest neighbors. These stresses have also been obtained for the case that the dissimilar fiber has interphase flaws.

INTRODUCTION

The overall mechanical properties and the strength of fiber-reinforced composites are significantly affected by the properties of very thin layers at the fiber–matrix interfaces, i.e. by fiber–matrix interphases. Several authors have investigated the effects of interphase compliance and interphase flaws on the effective elastic constants of the composite material. In these studies interphases have generally been represented by the spring-layer model. In this model the interphases are treated as very thin zones of unspecified thickness. The radial and tangential tractions are continuous across the interphase, but the displacements may be discontinuous between fiber and matrix due to the presence of the interphase. It has generally been assumed that the tractions are proportional to the corresponding displacement discontinuities. The proportionality constants characterize the stiffness of the interphase. This "spring-layer model" has been employed by many authors, e.g. Benveniste (1985), Steif and Hoysan (1987), Hashin (1990) and Achenbach and Zhu (1989). Benveniste (1985) calculated the effective modulus of a composite reinforced by spherical particles which are not well bonded to the matrix. Steif and Hoysan (1987) used an energy method for calculating the longitudinal stiffness of aligned short-fiber composites with imperfectly bonded interfaces. Hashin (1990, 1991) used the spring interphase model in his analysis of the thermoelastic behavior of a fiber reinforced composite as well as that of a particulate composite. He (1992) applied extremum principles of the theory of elasticity to composite bodies to obtain simple bounds for the effective elastic properties of two-phase materials with imperfect interfaces. Jasiuk *et al.* (1992) have investigated the effect of a sliding interface on the elastic properties of composites with randomly distributed circular and spherical rigid inclusions. Recently, Gosz *et al.* (1992) obtained the transverse constitutive response of a hexagonal array composite using a combined analytical and numerical method.

The effect of interphase flaws and radial matrix cracks on the overall mechanical properties has been studied by Achenbach and Zhu (1989, 1990) and Achenbach and Choi (1991). These investigations have been carried out for periodic arrays of the fibers, such as rectangular and hexagonal arrays, and it has been assumed that interface flaws and matrix cracks have the same periodic distribution as the fibers. By virtue of these geometrical

simplifications it was possible to consider a basic cell for detailed calculations of the fields of stress and deformation.

In this paper the more general case is considered of a single fiber which has either a smaller interphase stiffness, or whose interphase contains a defect. All the other fibers have the same interphase properties. The stress deviations in the interphases generated by the presence of the dissimilar fiber are calculated and relevant stresses and deformation energy densities in the interphases of the composite with the dissimilar fiber are compared with the corresponding quantities in the perfect composite. This work generalizes an earlier study by Zhu and Achenbach (1991). The approach used in this paper is applicable for linearly elastic behavior of the fibers and the matrix.

FORMULATION

Figure 1 shows a cross-sectional view of a unidirectionally reinforced fiber-composite in which all fibers are of the same radius a and have the same interphase properties, except one: the dissimilar fiber. This fiber has different interphase stiffness properties including the possibility that all or part of the interphase may have zero stiffness, i.e. the fiber may be completely or partially debonded. It is assumed that at a remote location the composite is subjected to uniform normal stresses $P\sigma_0$ and $Q\sigma_0$ in the x and y directions, respectively. The fibers are labelled by the index "q", where the index "0" is used to identify the dissimilar fiber, and where roughly speaking the larger the value of q, the larger the distance from the dissimilar fiber. The circumference of fiber q is denoted by Γ_q. A large contour Γ_∞ is the boundary of an area of interest of the cross section shown in Fig. 1. Inside Γ_∞ there are $N+1$ fibers. Thus $q = 0, 1, 2, \ldots, N$.

Following earlier papers by Achenbach and Zhu (1989, 1990), a very thin compliant interphase between fibers and matrix is modeled by a distribution of mechanical springs across a representative interface. This model implies that the tractions are continuous, but the displacements may be discontinuous across this interface. For linear behavior in the interphase, the relations between the relevant traction and displacement components may then be written as (at $r = a$)

$$-t_r^m = t_r^f = k_r(u_r^m - u_r^f) \quad \text{if} \quad -t_r^m = t_r^f > 0 \tag{1a}$$

$$-t_r^m = t_r^f \quad \text{and} \quad u_r^m = u_r^f \quad \text{if} \quad -t_r^m = t_r^f \leqslant 0 \tag{1b}$$

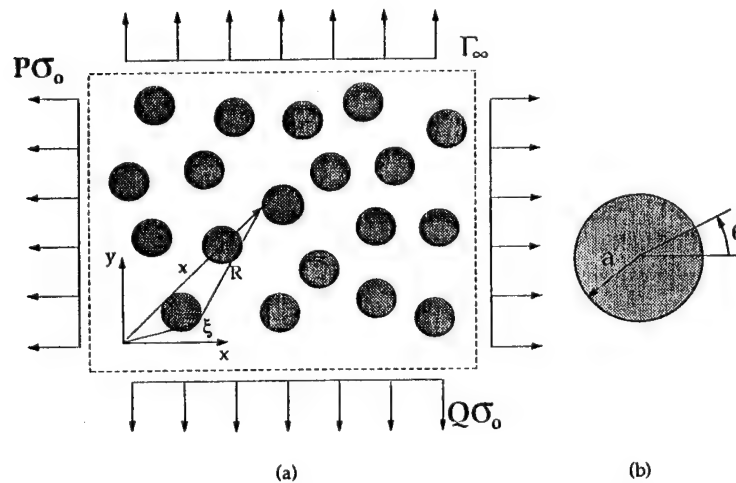$$-t_\theta^m = t_\theta^f = k_\theta(u_\theta^m - u_\theta^f) \tag{1c}$$

Fig. 1. (a) Cross-sectional view of the composite with a fiber with dissimilar interphase stiffness, (b) configuration of a fiber.

where t_r and t_θ are the interface tractions in the radial and circumferential directions, respectively. Here and in the sequel, quantities with upper index "m" and "f" are defined in the matrix and the fiber regions, respectively. The addition of eqn (1b) assures that the model will not allow a physically unrealistic radial overlap of the matrix and fiber materials across the interface. The constants k_r and k_θ are proportionality constants which define the mechanical properties of the interphase.

The conditions (1) include the case of perfect bonding ($k_r = k_\theta = \infty$) when the tractions and displacements are continuous and the case of total debonding ($k_r = k_\theta = 0$) when the tractions vanish. In the latter case, it should be noted that the pure sliding condition ($k_r = \infty, k_\theta = 0$) is assumed to exist on the interface when the radial stresses are compressive. If there exist interphase defects like open cracks, say over a region $-\theta_c < \theta < \theta_c < \pi/2$ and $-\theta_c + \pi < \theta < \theta_c + \pi$, then in the domain $0 \leqslant \theta \leqslant \pi/2$ the conditions (1) are valid for $r = a$, $\theta_c < \theta \leqslant \pi/2$, while for $r = a$ and $0 \leqslant \theta \leqslant \theta_c$, we should have interphase crack conditions defined by

$$t_r^m = t_r^f = t_\theta^m = t_\theta^f = 0. \tag{2}$$

It is also noted that for an interphase crack the ligament at the tip of the disbond undergoes a finite stretch when in tension, and consequently the tractions remain bounded. Hence the usual problems of violently oscillating singularities (see Williams, 1959) that are associated with crack-tip fields for a crack in a perfectly bonded interface, do not occur for the spring-layer model. This conclusion follows immediately from eqn (1) and the boundedness of the displacements.

For the generation of interphase cracks, as well as their propagation and arrest, it is feasible to use a critical stress, critical strain, or critical strain energy density criterion, because in the spring-layer model these quantities are well defined near the tip of an interphase crack. In this paper we will employ an energy density criterion, since it combines information on the tensile and shear stresses in the interphase. For the interphase model defined by eqns (1), the strain energy per unit interphase area is easy to calculate. We have

$$U = \frac{(t_r^f)^2}{2k_r} + \frac{(t_\theta^f)^2}{2k_\theta}. \tag{3}$$

It should be noted here that t_r^f is included in U only when t_r^f is positive (tension). It is assumed that compressive values of t_r^f do not affect the integrity of the interphase.

By substituting k into eqn (3) the normalized form of U, $\bar{U} = U\mu^m/(\sigma_0^2 a)$, becomes

$$\bar{U} = \frac{(t_r^f/\sigma_0)^2}{2k_r a/\mu^m} + \frac{(t_\theta^f/\sigma_0)^2}{2k_\theta a/\mu^m} \tag{4}$$

where μ^m is the shear modulus of the matrix material, and σ_0 is the applied stress. It is reasonable to assume that the interphase will break and form an interphase crack in a region of positive radial stress when

$$U \geqslant U^{cr}. \tag{5}$$

When $U = U^{cr}$, the applied stress σ_0 reaches a critical value σ_0^{cr} which can be related to U^{cr} by eqn (4) as

$$\sigma_0^{cr} = \left[\frac{\mu^m}{a} \frac{U^{cr}}{\bar{U}}\right]^{\frac{1}{2}} \tag{6}$$

An analysis of the initiation and propagation of matrix cracks must also be based on an appropriate criterion. For a perfect composite subjected to tensile stresses, numerical

results show, in agreement with physical intuition, see e.g. Achenbach and Zhu (1989, 1990), that the circumferential tensile stress at the fiber–matrix interphase is the largest tensile stress component in the matrix material. As a crack initiation criterion we choose

$$\sigma_\theta \geq \sigma^{cr} \tag{7}$$

where σ^{cr} is a critical stress of the matrix material for matrix crack initiation.

The displacement and traction components for the case that no dissimilar fiber is present (perfect composite) are denoted by $u_i^{fp}(x)$ and $t_i^{fp}(x)$ for the fibers, and $u_i^{mp}(x)$ and $t_i^{mp}(x)$ for the matrix material. The deviations of these quantities due to the presence of a dissimilar fiber are denoted by $\bar{u}_i^f(x)$, $\bar{t}_i^f(x)$, $\bar{u}_i^m(x)$ and $\bar{t}_i^m(x)$. The total displacement and traction fields in the presence of a dissimilar fiber may then be written as

$$u_i^f(x) = u_i^{fp}(x) + \bar{u}_i^f(x) \tag{8a}$$

$$u_i^m(x) = u_i^{mp}(x) + \bar{u}_i^m(x) \tag{8b}$$

$$t_i^f(x) = t_i^{fp}(x) + \bar{t}_i^f(x) \tag{8c}$$

$$t_i^m(x) = t_i^{mp}(x) + \bar{t}_i^m(x). \tag{8d}$$

The interface conditions corresponding to the case of a different interface constant are obtained by replacing in eqns (1a), (1b) and (1c) the total tractions t_r^m, t_θ^m, t_r^f, and t_θ^f by the superpositions (8c) and (8d). On the interphase $\Gamma_q(\neq \Gamma_0)$ we then have:

$$-\bar{t}_r^m = k_r(\bar{u}_r^m - \bar{u}_r^f) \tag{9a}$$

$$-\bar{t}_\theta^m = k_\theta(\bar{u}_\theta^m - \bar{u}_\theta^f) \tag{9b}$$

where (r, θ) is a local polar coordinate located at the center of each fiber and Γ_q represents the interfacial boundary of the fiber q. On the interphase Γ_0 we have:

$$-\bar{t}_r^m = -(k_r - \bar{k}_r)(u_r^{mp} - u_r^{fp}) + \bar{k}_r(\bar{u}_r^m - \bar{u}_r^f) \tag{9c}$$

$$-\bar{t}_\theta^m = -(k_\theta - \bar{k}_\theta)(u_\theta^{mp} - u_\theta^{fp}) + \bar{k}_\theta(\bar{u}_\theta^m - \bar{u}_\theta^f). \tag{9d}$$

In eqns (9c) and (9d), $\bar{k}_r$ and $\bar{k}_\theta$ are the interphase constants for the dissimilar fiber.

If the interphase Γ_0 contains an interphase crack in the range of $-\theta_c < \theta < \theta_c < \pi/2$ and $\pi - \theta_c < \theta < \pi + \theta_c$ then eqns (9c and 9d) become

$$-\bar{t}_r^m = -k_r(u_r^{mp} - u_r^{fp}) = t_r^{mp} \tag{9e}$$

$$-\bar{t}_\theta^m = -k_\theta(u_\theta^{mp} - u_\theta^{fp}) = t_\theta^{mp}. \tag{9f}$$

For all interphases Γ_q including Γ_0, the continuity of the tractions across the interphase Γ_q are satisfied by

$$-\bar{t}_r^m = \bar{t}_r^f \tag{10a}$$

$$-\bar{t}_\theta^m = \bar{t}_\theta^f. \tag{10b}$$

By appropriate coordinate transformations the interphase conditions (1a), (1b) and (1c) can be expressed in terms of Cartesian components of tractions and displacements

which will be used in the actual computations. The interphase conditions on the interphase Γ_q ($\neq \Gamma_0$) given by eqns (9a, 9b) may be rewritten as

$$aC_1 \cos \theta \frac{\bar{t}_x^m}{\mu^m} + aC_1 \sin \theta \frac{\bar{t}_y^m}{\mu^m} + \cos \theta(\bar{u}_x^m - \bar{u}_x^f) + \sin \theta(\bar{u}_y^m - \bar{u}_y^f) = 0 \qquad (11a)$$

$$-aC_2 \cos \theta \frac{\bar{t}_x^m}{\mu^m} + aC_2 \sin \theta \frac{\bar{t}_y^m}{\mu^m} \sin \theta(\bar{u}_x^m - \bar{u}_x^f) + \cos \theta(\bar{u}_y^m - \bar{u}_y^f) = 0 \qquad (11b)$$

where $\bar{t}_{x,y}^m/\mu^m$ has been introduced to enhance the accuracy of the solutions of the simultaneous equations in the numerical calculations using the BEM. The dimensionless compliant constants are defined as

$$C_1 \frac{1}{k_1} = \frac{\mu^m}{ak_r} \quad \text{and} \quad C_2 = \frac{1}{k_2} = \frac{\mu^m}{ak_\theta}. \qquad (12a,b)$$

Similarly the interphase conditions (9c, 9d) on the boundary of the dissimilar fiber, Γ_0, can be expressed as

$$a\bar{C}_1 \cos \theta \frac{\bar{t}_x^m}{\mu^m} + a\bar{C}_1 \sin \theta \frac{\bar{t}_y^m}{\mu^m} + \cos \theta(\bar{u}_x^m - \bar{u}_x^f) + \sin \theta(\bar{u}_y^m - \bar{u}_y^f)$$
$$+ a(\bar{C}_1 - C_1)\left(\cos \theta \frac{t_x^{mp}}{\mu^m} + \sin \theta \frac{t_y^{mp}}{\mu^m}\right) = 0 \quad (13a)$$

$$-a\bar{C}_2 \sin \theta \frac{\bar{t}_x^m}{\mu^m} + a\bar{C}_2 \cos \theta \frac{\bar{t}_y^m}{\mu^m} - \sin \theta(\bar{u}_x^m - \bar{u}_x^f) + \cos \theta(\bar{u}_y^m - \bar{u}_y^f)$$
$$- a(\bar{C}_2 - C_2)\left(\sin \theta \frac{t_x^{mp}}{\mu^m} - \cos \theta \frac{t_y^{mp}}{\mu^m}\right) = 0 \quad (13b)$$

where

$$\bar{C}_1 = \frac{1}{\bar{k}_1} = \frac{\mu^m}{a\bar{k}_r} \quad \text{and} \quad \bar{C}_2 = \frac{1}{\bar{k}_2} = \frac{\mu^m}{a\bar{k}_\theta}. \qquad (14a,b)$$

If the interphase of Γ_0 contains an interphase crack in the range of $-\theta_c < \theta < \theta_c < \pi/2$ and $\pi - \theta_c < \theta < \pi + \theta_c$ then eqns (13a, 13b) become

$$t_x^{mp} = -\bar{t}_x^m \quad \text{and} \quad t_y^{mp} = -\bar{t}_y^m. \qquad (15a,b)$$

If the dissimilar interphase Γ_0 has compressive radial tractions over one or more elements on Γ_0 then to prevent the interphase from overlapping, the eqns (13a, 13b) become

$$\bar{u}_x^m = \bar{u}_x^f \quad \text{and} \quad \bar{u}_y^m = \bar{u}_y^f \quad \text{on} \quad \Gamma_0 \quad \text{if } t_r^f < 0. \qquad (16a,b)$$

Continuity of tractions across the interphase Γ_q including Γ_0 is satisfied as

$$\bar{t}_x^m = -\bar{t}_x^f \quad \text{and} \quad \bar{t}_y^m = -\bar{t}_y^f \qquad (17a,b)$$

BIEs for unidirectional composite with one dissimilar fiber

In earlier papers, see e.g. Achenbach and Zhu (1989, 1990), a boundary integral equation has been derived for the displacements and tractions on the circumference of a fiber inside a basic cell of the composite. Here we write the analogous boundary integral equation for fiber q.

$$\frac{1}{2}u_i^m(\xi) = \int_{\Gamma+\Gamma_\infty} U_{ij}^m(x,\xi)t_j^m(x)\,\mathrm{d}\Gamma(x) - \int_{\Gamma+\Gamma_\infty} T_{ij}^m(x,\xi)u_j^m(x)\,\mathrm{d}\Gamma(x), \quad x\in\Gamma, \xi\in\Gamma_q \quad (18a)$$

where

$$\Gamma = \sum_{q=0}^{N} \Gamma_q \quad (18b)$$

and

$$U_{ij}^m(x,\xi) = \frac{1}{8\pi\mu^m(1-v^m)}\left[(3-4v^m)\ln\left(\frac{1}{R}\right)\delta_{ij} + \frac{\partial R}{\partial x_i}\frac{\partial R}{\partial x_j}\right] \quad (19a)$$

$$T_{ij}^m(x,\xi) = -\left[\lambda^m\frac{\partial}{\partial x_l}U_{il}^m(x,\xi)\delta_{jk} + \mu^m\frac{\partial}{\partial x_k}U_{ij}^m(x,\xi) + \mu^m\frac{\partial}{\partial x_j}U_{ik}^m(x,\xi)\right]n_k(x). \quad (19b)$$

A similar BIE for the solution $u_i^{mp}(\xi)$ in the matrix of the perfect composite can be written as

$$\frac{1}{2}u_i^{mp}(\xi) = \int_{\Gamma+\Gamma_\infty} U_{ij}^m(x,\xi)t_j^{mp}(x)\,\mathrm{d}\Gamma(x) - \int_{\Gamma+\Gamma_\infty} T_{ij}^m(x,\xi)u_j^{mp}(x)\,\mathrm{d}\Gamma(x), \quad x\in\Gamma, \xi\in\Gamma_q. \quad (20)$$

Subtracting eqn (20) from eqn (18) gives a BIE for $\bar{u}_i^m(\xi)$ as

$$\frac{1}{2}\bar{u}_i^m(\xi) = \int_\Gamma U_{ij}^m(x,\xi)\bar{t}_j^m(x)\,\mathrm{d}\Gamma(x) - \int_\Gamma T_{ij}^m(x,\xi)\bar{u}_j^m(x)\,\mathrm{d}\Gamma(x)$$

$$+ \int_{\Gamma_\infty} U_{ij}^m(x,\xi)\bar{t}_j^m(x)\,\mathrm{d}\Gamma(x) - \int_{\Gamma_\infty} T_{ij}^m(x,\xi)\bar{u}_j^m(x)\,\mathrm{d}\Gamma(x), \quad x\in\Gamma, \xi\in\Gamma_q. \quad (21)$$

Since the tractions $\bar{t}_i^m(x)$ corresponding to $\bar{u}_i^m(x)$ are self-equilibrating with respect to the center of fiber zero, it follows from Saint-Venant's principle that $\bar{u}_i^f(x)$, $\bar{u}_i^m(x)$, $\bar{t}_i^f(x)$ and $\bar{t}_i^m(x)$ decrease as the field point x moves away from the center of the dissimilar fiber. Hence, the contour can be appropriately chosen so far from the origin that the integrals over the contour Γ_∞ in eqn (21) come to vanish. As an additional approximation it may be assumed that only a small number of neighboring fibers need be included in Γ.

The corresponding BIE for the fiber q may be written as

$$\frac{1}{2}u_i^f(\xi) = \int_{\Gamma_q} U_{ij}^f(x,\xi)t_j^f(x)\,\mathrm{d}\Gamma(x) - \int_{\Gamma_q} T_{ij}^f(x,\xi)u_j^f(x)\,\mathrm{d}\Gamma(x), \quad x,\xi\in\Gamma_q. \quad (22)$$

Similarly, substituting eqn (8a) into eqn (22) yields

$$\tfrac{1}{2}\bar{u}_i^f(\xi) = \int_{\Gamma_q} U_{ij}^f(x,\xi)\bar{t}_j^f(x)\,d\Gamma(x) - \int_{\Gamma_q} T_{ij}^f(x,\xi)\bar{u}_j^f(x)\,d\Gamma(x)$$

$$-\tfrac{1}{2}u_i^{fp}(\xi) + \int_{\Gamma_q} U_{ij}^f(x,\xi)t_j^{fp}(x)\,d\Gamma(x) - \int_{\Gamma_q} T_{ij}^f(x,\xi)u_j^{fp}(x)\,d\Gamma(x), \quad x,\xi \in \Gamma_q. \quad (23)$$

But we know that the terms in the second line of eqn (23) vanish for all fibers in the composite without a dissimilar fiber, so we have

$$\tfrac{1}{2}\bar{u}_i^f(\xi) = \int_{\Gamma_q} U_{ij}^f(x,\xi)\bar{t}_j^f(x)\,d\Gamma(x) - \int_{\Gamma_q} T_{ij}^f(x,\xi)\bar{u}_j^f(x)\,d\Gamma(x), \quad x,\xi \in \Gamma_q. \quad (24)$$

For plane strain the circumferential stress σ_θ^m along the matrix side of the interphase may be calculated by

$$\sigma_\theta^m = -\frac{v^m}{1-v^m}\,t_r^m + \frac{2\mu^m}{a(1-v^m)}\left(u_r^m + \frac{\partial u_\theta^m}{\partial\theta}\right) \quad (25)$$

where $\partial u_\theta^m/\partial\theta$ will be obtained by a numerical differentiation method.

Example : hexagonal-array composite

Equations (1)–(25) are valid for any distribution of the fibers over the cross section. We will now, however, consider the special case of a hexagonal-array composite as shown in Fig. 2. For the case without a dissimilar fiber the interphase fields have been analysed by Achenbach and Zhu (1989, 1990).
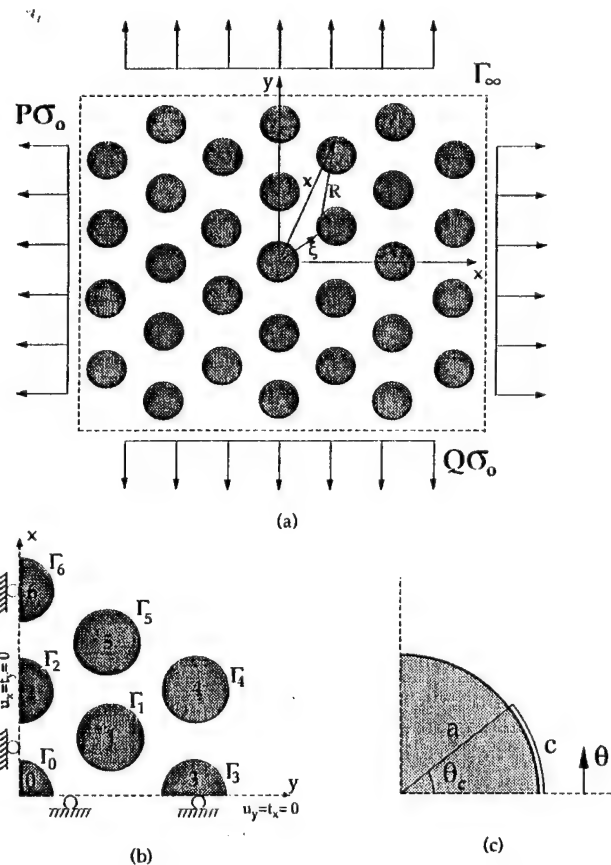

Fig. 2. Configuration for the hexagonal array : (a) the dissimilar fiber 0 has lower interphase stiffness. All other fibers have the same interphase stiffnesses, (b) shows the domain for numerical calculations, and (c) the dissimilar fiber 0 has interphase debonding.

The centers of the regular fibers are located at the following points

$$(x, y) = \left(\frac{\sqrt{3}}{2} bi, \frac{1}{2} bj\right) \quad |i|, |j| = 0, 1, 2, 3, \ldots \quad \text{and} \quad i+j = \text{even integer} \qquad (26)$$

where b is the distance between the centers of two adjacent fibers, and $|i|+|j| \neq 0$. A Cartesian coordinate system (x, y) has its origin at the center of the dissimilar fiber.

Because of symmetry with respect to the x- and y-axes we only need to consider the fibers in the first quadrant, as shown in Fig. 2. The nearest neighbors to the dissimilar fiber are denoted fibers 1 and 2, and the next nearest fibers are 3, 4, 5 and 6.

The symmetry conditions on the sides of the first quadrant make it possible to limit the boundary element calculations to that quadrant only. The fundamental solutions which satisfy the symmetry conditions $u_x = t_y = 0$ at $x = 0$ and $u_y = t_x = 0$ at $y = 0$ can be constructed from the full-space fundamental solutions given by eqns (19a)–(19b). For a load applied at (x, y) the construction is easily achieved by placing corresponding loads at the image points of (x, y) in the other three quadrants, as shown in Fig. 3. In terms of $U_{ij}(x, \xi)$ and $T_{ij}(x, \xi)$ given by eqns (19a)–(19b) (superscript "m" can be disregarded), the first quadrant fundamental solutions $U_{ij}^Q(x, \xi)$ and $T_{ij}^Q(x, \xi)$ may be written as

$$U_{ij}^Q(x, \xi) = U_{ij}(x, \xi) + \alpha U_{ij}(x, -\bar{\xi}) + \beta U_{ij}(x, -\xi) + \gamma U_{ij}(x, \bar{\xi}), \quad x, \xi \in \text{1st Quadrant} \quad (27a)$$

$$T_{ij}^Q(x, \xi) = T_{ij}(x, \xi) + \alpha T_{ij}(x, -\bar{\xi}) + \beta T_{ij}(x, -\xi) + \gamma T_{ij}(x, \bar{\xi}), \quad x, \xi \in \text{1st Quadrant} \quad (27b)$$

where the coefficients α, β and γ take values, $\alpha = \beta = -\gamma = -1$ for $i = 1$ and $-\alpha = \beta = \gamma = -1$ for $i = 2$ and $\bar{\xi}$ denotes the conjugate point of ξ.

More detailed expressions for $U_{ij}^Q(x, \xi)$ and $T_{ij}^Q(x, \xi)$ are given in the Appendix.

Boundary element method

Equations (18)–(24) have been solved numerically by an application of the boundary element method. The equations have been solved in the first quadrant shown in Figure 2(b) by using the fundamental solutions given by eqns (27a) and (27b). It has been assumed that the deviations in the fields of stress and deformation generated by the interphase properties of the dissimilar fiber 0 extend to the next nearest two fiber-layers only, i.e. to the fibers 1 and 2 in the first fiber-layer and to the fibers 3–6 in the second fiber-layer.
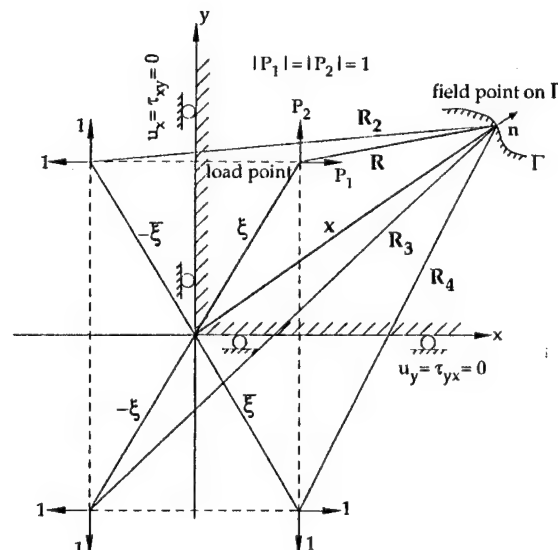

Fig. 3. Geometrical construction of the first quadrant fundamental solutions; $\xi = (\xi_1, \xi_2)$ and $\bar{\xi} = (\xi_1, -\xi_2)$.

The contours, Γ_0, Γ_1, Γ_2, Γ_3, Γ_4, Γ_5 and Γ_6, contain unknown deviations of the tractions and displacements. Along these contours, the integration is performed clockwise for the matrix side integration and counterclockwise for the fiber side. Suppose that the contours Γ_0, Γ_1, Γ_2, Γ_3, Γ_4, Γ_5 and Γ_6 are divided into N_0, N_1, N_2, N_3, N_4, N_5 and N_6 elements, respectively, where the fields are taken as constants over each element. We then have $8N_0$, $8N_1$, $8N_2$, $8N_3$, $8N_4$, $8N_5$ and $8N_6$ unknowns for the integrations over the contours Γ_0, Γ_1, Γ_2, Γ_3, Γ_4, Γ_5 and Γ_6, respectively (two traction and two displacement components on each side of a contour). Consequently we have a total of $8(N_0 + N_1 + N_2 + N_3 + N_4 + N_5 + N_6)$ unknowns. The same number of equations is needed. Equations (21) and (24) give $4(N_0 + N_1 + N_2 + N_3 + N_4 + N_5 + N_6)$ equations and the continuity of tractions, eqn (9), together with eqn (13) on the interface yields $4(N_0 + N_1 + N_2 + N_3 + N_4 + N_5 + N_6)$ equations. Hence the total number of equations is the same as the total number of unknowns. Thus the discretized system of eqns (21) and (24) can be solved numerically. When there are no interphase flaws, all interphases are equally divided, specifically in 120 or 60 elements, such that $4N_0 = N_1 = 2N_2 = 120$ and $2N_3 = N_4 = N_5 = 2N_6 = 60$. When Γ_0 contains a crack, the crack tip element and the element ahead of the crack tip element are further divided into smaller elements to give more accurate results. The number of elements near the crack tip is increased until a further increase does not change the numerical results. Numerical calculations have been carried out for FP/Al composites (see Takahashi and Chou, 1988) with the following properties:

$$\text{Aluminum matrix}: \mu^m = 25.61\,\text{GPa}, \nu^m = 0.345$$

$$\text{FP(Al}_2\text{O}_3\text{) fibers}: \mu^f = 157.9\,\text{GPa}, \nu^f = 0.2.$$

The perfect and the dissimilar interphase constants (k_r, k_θ) and $(\bar{k}_r, \bar{k}_\theta)$ were rendered dimensionless by division by μ^m/a, where a is the radius of the fibers. In the computations, the two interphase constants were taken equal in magnitude, and thus $k_r/(\mu^m/a) = k_\theta/(\mu^m/a) = k$. Similarly in the dissimilar interphase $\bar{k}_r/(\mu^m/a) = \bar{k}_\theta/(\mu^m/a) = \bar{k}$.

In the initial state of the calculation the radial interface stress $\sigma_r^m\ (= \sigma_r^f = t_r^f = -t_r^m)$ is computed under the assumption that eqn (1a) applies along the interface of the dissimilar fiber. If a negative radial stress value is obtained over one or more elements and the displacements display an overlap, eqn (1a) is replaced by eqn (1b) and the calculation is redone until the overlap disappears and all boundary conditions are satisfied. Values of $\bar{k} = 0.001, 0.1, 1, 10, 100$ and ∞ were considered for the interphase stiffness of the dissimilar fiber and $k = \infty$ for the neighboring fibers. The fiber volume ratio V_f was chosen as 0.2, 0.4, 0.6 or 0.8.

RESULTS

The approximation of including only the nearest and next-nearest neighbors in the BEM calculations would seem to be a reasonable one. The question does, however, arise whether sufficiently accurate results can be obtained by including only the nearest neighbors, i.e. fibers 1 and 2 in Fig. 2. Intuitively it is expected that this simpler approximation will be valid for smaller volume densities, V_f, of the fibers. Test calculations have been carried out for the case of uniaxial tension, for $V_f = 0.2$ and $V_f = 0.8$, and $\bar{k} = 10$ and $\bar{k} = 1$. The results are shown in Fig. 4. It is noted that the inclusion of the next-nearest neighboring fibers (solid lines) makes a small difference which becomes somewhat more pronounced for smaller values of $\bar{k}$ and larger values of V_f. The numerical results presented in the sequel have been carried out taking into account only the next nearest neighbors.

Figure 5 shows the stress fields σ_r/σ_0, $\sigma_{r\theta}/\sigma_0$, σ_θ/σ_0 at the matrix side of the interphase and the normalized strain energy density $\bar{U}$ in the interphase of the dissimilar fiber for the case of tension in the x direction. The radial stress in the region of tensile stresses decreases as the interphase stiffness, $\bar{k}$, of the dissimilar fiber decreases. The maximum value of the hoop stress, near $\theta = 75°$, does, however, increase as $\bar{k}$ decreases. Other calculations not

H. S. Choi and J. D. Achenbach
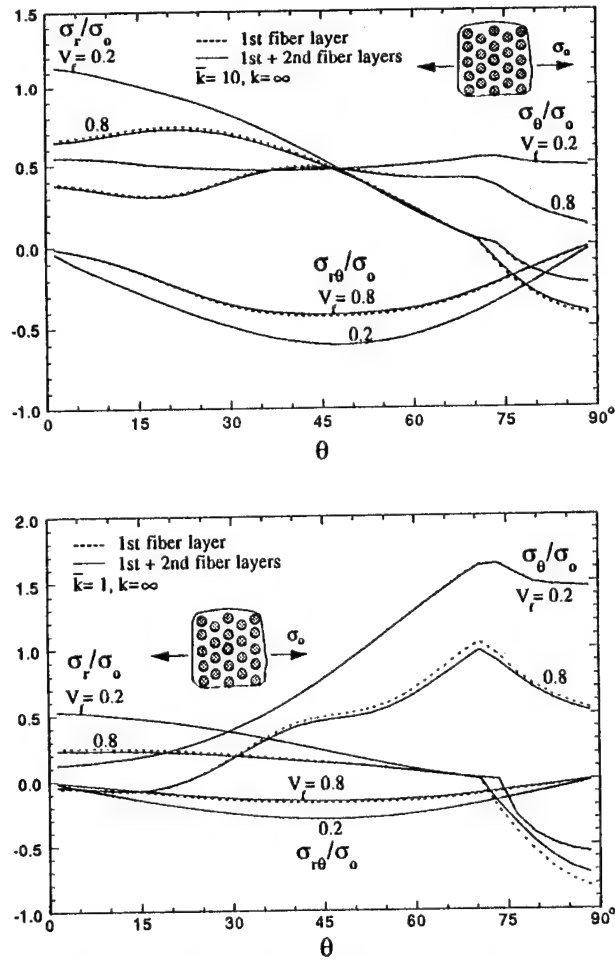
Fig. 4. Comparison of stress fields in the interphase of the dissimilar fiber obtained by considering only the first fiber layer (dashed lines) and considering both the first and second fiber layers (solid lines) for the selected values of V_f and $\bar{k}$.
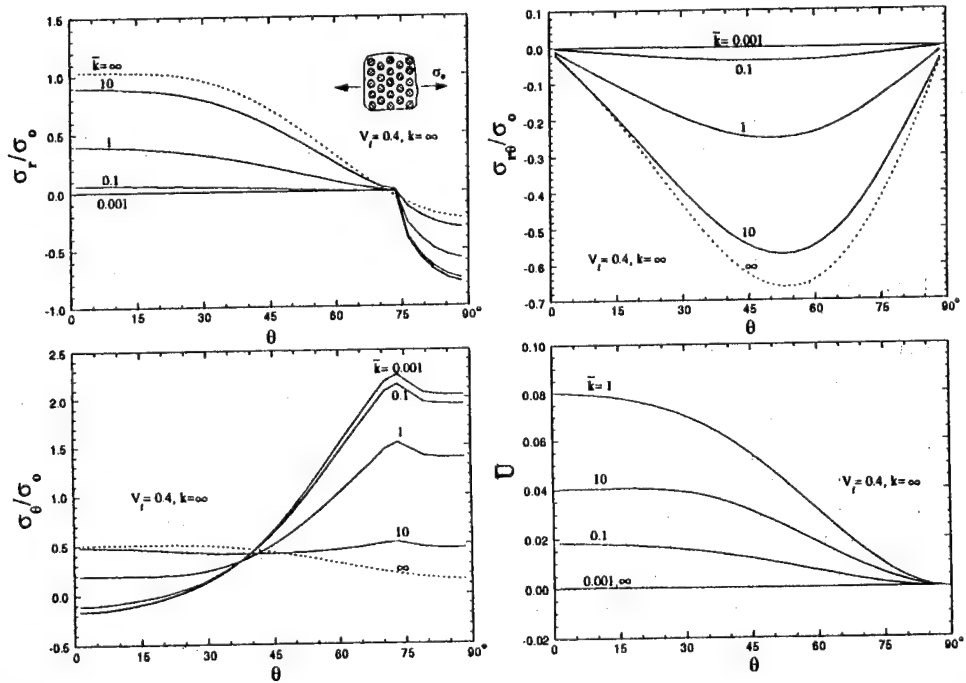
Fig. 5. σ_r/σ_0, $\sigma_{r\theta}/\sigma_0$, σ_θ/σ_0 at the matrix side of the interphase and U in the interphase of the dissimilar fiber 0, for various $\bar{k}$ with $k = \infty$ and $V_f = 0.4$, and for uniaxial tension in the x direction.
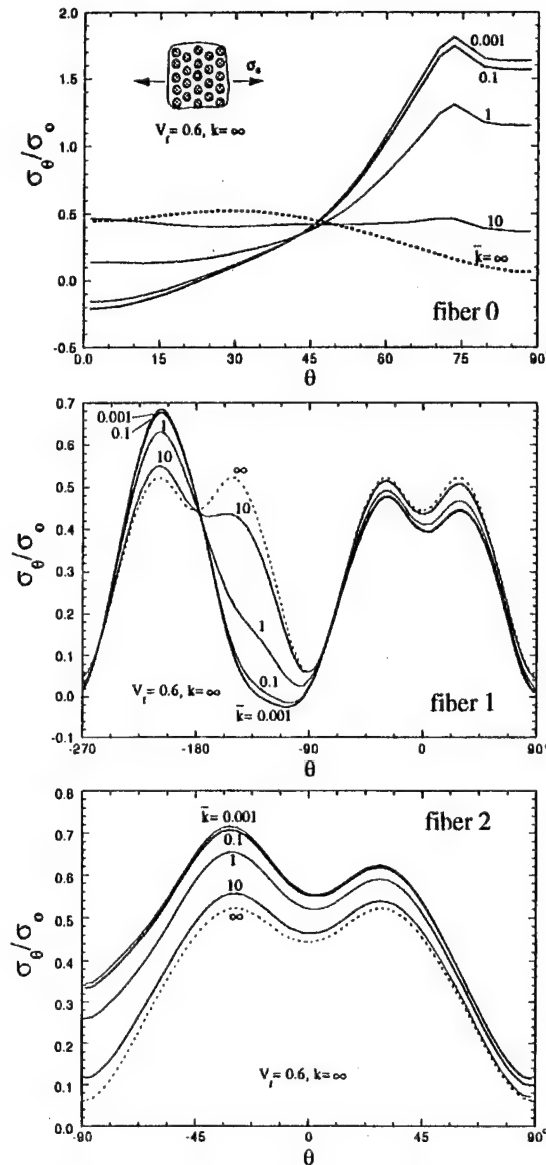
Fig. 6. σ_θ/σ_0 at the matrix side of the interphases of the dissimilar fiber 0 and the neighboring fibers
1 and 2, for various $\bar{k}$ with $k = \infty$ and $V_f = 0.6$, and for uniaxial tension in the x direction.

reported here show that the magnitudes of σ_r/σ_0, $\sigma_{r\theta}/\sigma_0$, σ_θ/σ_0 and U at the dissimilar
interphase are slightly less than those of σ_r/σ_0, $\sigma_{r\theta}/\sigma_0$, σ_θ/σ_0 and U at the interphases of the
perfect composite with the same interphase stiffness $(k = \bar{k})$ in all interphases. That differ-
ence becomes larger for lower interphase stiffness $\bar{k}$.

Figure 6 shows the hoop stresses along the matrix-side of the interphases of the three
fibers 0, 1 and 2 with $V_f = 0.6$ for various $\bar{k}$: $\bar{k} = \infty$, 10, 1, 0.1, 0.001. Comparison with the
results of Fig. 5 shows that the hoop stress σ_θ/σ_0 of the dissimilar fiber for $V_f = 0.6$ is slightly
smaller than that for $V_f = 0.4$. The hoop stresses of the neighboring fibers 1 and 2 slightly
increase as $\bar{k}$ decreases. The result shows that for low $\bar{k}$ the positive maximum hoop stress
$(\sigma_\theta)_{max}$ occurs near $\theta = 70°$ for the dissimilar fiber, near $\theta = -208°$ for the neighboring
fiber 1 and near $\theta = -30°$ for fiber 2.

Figure 7 shows the hoop stresses along the matrix side of the interphase of the dissimilar
fiber and the strain energy in the interphase for the case of uniaxial compression in the x
direction. When the composite is compressed in the x direction the maximum tensile hoop
stress occurs at $\theta = 0°$ for low $\bar{k}$ and at $\theta = 90°$ for high $\bar{k}$ (above 10). For the dissimilar

Fig. 7. σ_θ/σ_0 at the matrix side of the interphase and $\bar{U}$ in the interphase of the dissimilar fiber 0, for various $\bar{k}$ with $k = \infty$ and $V_f = 0.4$, for uniaxial compression in the x direction.
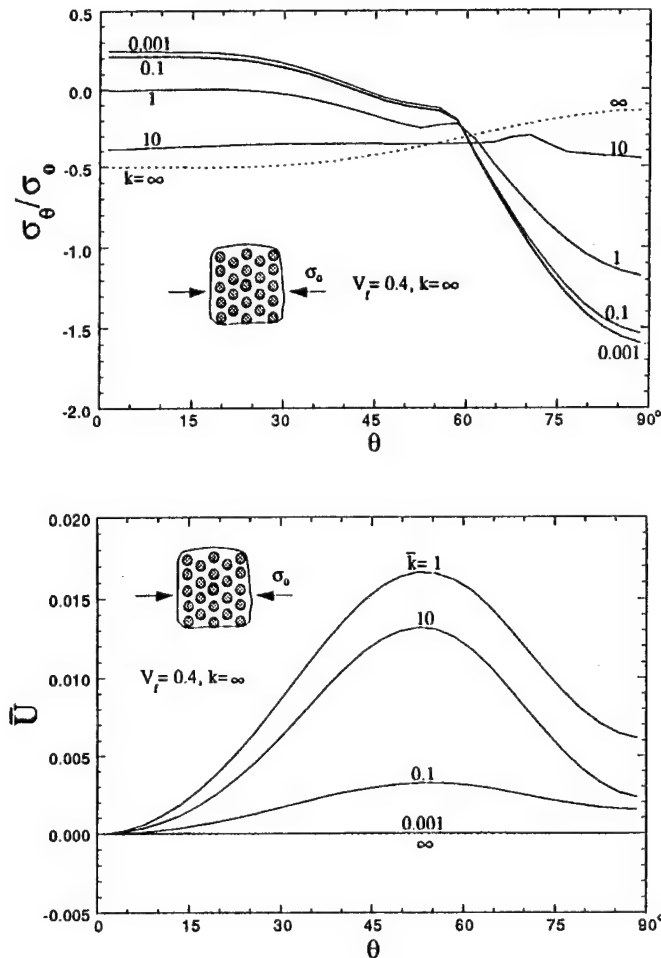
fiber the maximum strain energy $U_{\max}$ occurs near $\theta = 55°$ for $\bar{k} = 1$. The hoop stresses of the neighboring fibers 1 and 2 are compressive for any $\bar{k}$.

When the interphase of the dissimilar fiber contains interphase cracks as shown in Fig. 2(c), the behavior of σ_r/σ_0, $\sigma_{r\theta}/\sigma_0$, σ_θ/σ_0 and $\bar{U}$ depends greatly upon the interphase stiffness $\bar{k}$. Figure 8 shows σ_θ/σ_0 and $\bar{U}$ for various $\bar{k}$ along the matrix side of the interphase of the dissimilar fiber for an interphase crack of length $\bar{c} = c/0.05236a = 9$, for the case of an uniaxial tensile stress σ_0 in the x direction. The maximum hoop stress and energy density are obtained at the crack tip. The magnitude of the hoop stress increases with increasing values of $\bar{k}$. The results for σ_θ/σ_0 at the neighboring fibers 1 and 2 are also shown in Fig. 8. The overall behavior for the neighboring fibers is very similar to that displayed in Fig. 6.

Figure 9 shows σ_θ/σ_0 along the matrix side of the interphase of the dissimilar fiber and $\bar{U}$ in the interphase for $\bar{k} = 10$ and $\bar{k} = 1$, for various interphase crack lengths $\bar{c}$. The results show that for $\bar{k} = 10$ the positive maximum hoop stress occurs at the crack tip and increases as c increases. On the other hand for $\bar{k} = 1$ the positive maximum hoop stress occurs near $\theta = 75°$ for $\bar{c} < 18$. Results not displayed here show that for both $\bar{k} = 1$ and $\bar{k} = 10$ the stresses σ_θ along the interphases of the neighboring fibers 1 and 2 increase locally as $\bar{c}$ increases, but there is little difference between $\bar{k} = 1$ and $\bar{k} = 10$.

A stability condition is needed when interphase cracks are present. The strain energy criterion was introduced in the papers by Achenbach and Zhu (1989, 1990) to investigate the proclivity of an interphase crack to propagate. Figure 9 shows that $\bar{U}$ plotted versus θ shows maximums at the tips of the interphase cracks of the dissimilar fiber. For $\bar{k} = 1$, the
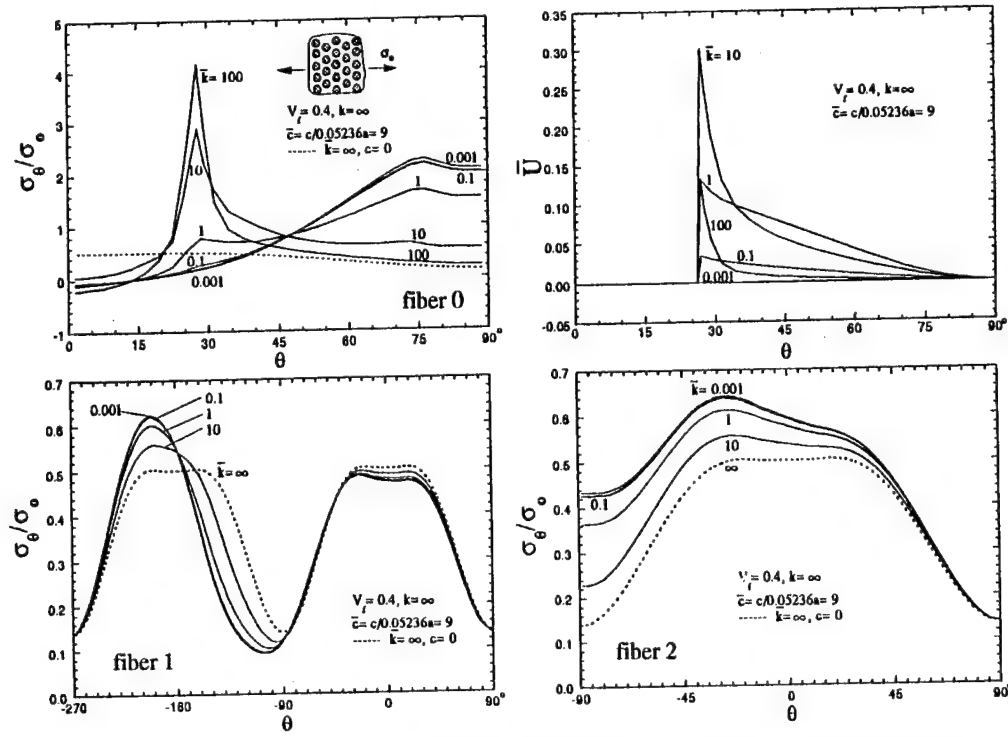
Fig. 8. σ_θ/σ_0 at the matrix sides of the interphases of the dissimilar fiber 0 and the neighboring fibers 1 and 2, and U in the interphase of fiber 0, for various $\bar{k}$ with $k = \infty$ and $V_f = 0.4$, and $\bar{c} = 9$, for uniaxial tension in the x direction.
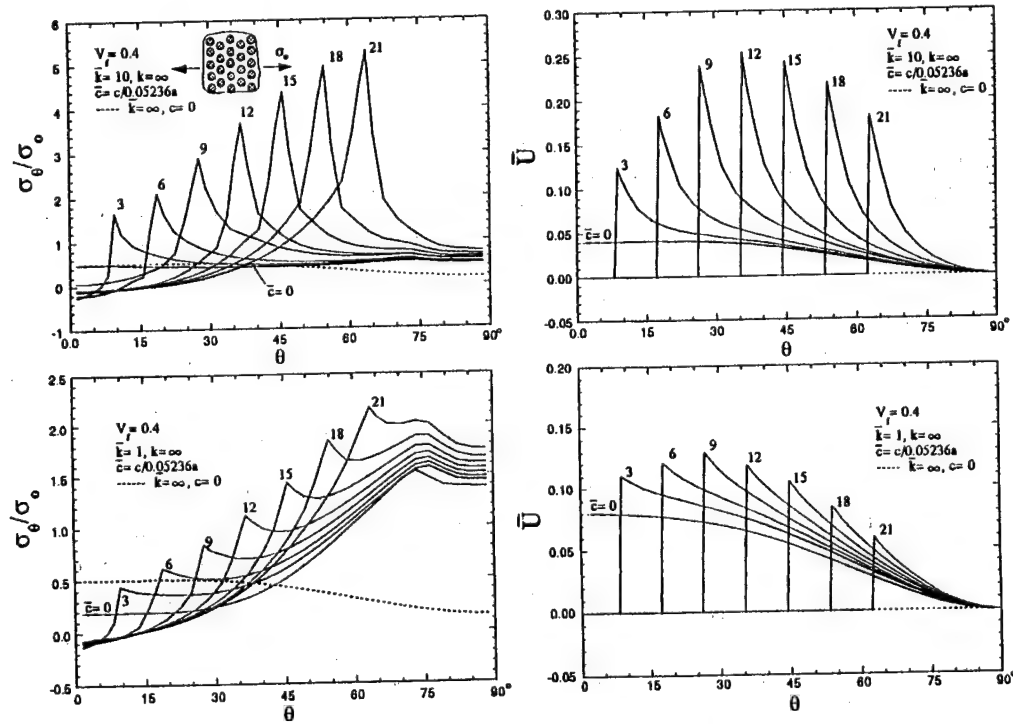
Fig. 9. σ_θ/σ_0 at the matrix side of the interphase and U in the interphase of the dissimilar fiber 0, for various $\bar{c}$ with $k = \infty$, $V_f = 0.4$ and $\bar{k} = 10$ and $\bar{k} = 1$, for uniaxial tension in the x direction.

maximum values first increase and then decrease as $\bar{c}$ increases. They become in fact smaller than for $\bar{c} = 0$, and hence the interface flaw will be arrested for that case.

CONCLUDING COMMENTS

A fiber whose interphase has a lower stiffness than the surrounding fibers, or whose interphase contains cracks, gives rise to higher fields of stress and deformation in its immediate vicinity. For the case of transverse loading, a numerical method based on the solution of boundary integral equations by the boundary element method has been developed to obtain the stresses at the matrix side of the interphases and the deformation energy density in the interphases, for the dissimilar fiber and its nearest neighbors. The example of a hexagonal array fiber composite has been discussed in some detail, and particular attention has been devoted to the hoop stresses and the deformation energy densities since critical values of these quantities may be associated with radial matrix cracking and interphase cracking, respectively.

REFERENCES

Achenbach, J. D. and Choi, H. S. (1991). Matrix cracking and interphase failure in fiber composites. In *Local Mechanics Concepts for Composite Material Systems* (Edited by J. N. Reddy and K. L. Reifsnider), pp. 149–163. IUTAM Symposium Blacksburg, VA, Springer–Verlag.

Achenbach, J., D. and Zhu, H. (1989). Effect of interfacial zone on mechanical behavior and failure of fiber-reinforced composites. *J. Mech. Phys. Solids* **37**, 381–393.

Achenbach, J. D. and Zhu, H. (1990). Effect of interphases on micro- and macro-mechanical behavior of hexagonal array fiber composites. *J. Appl. Mech.* **57**, 956–963.

Benveniste, Y. (1985) The effective mechanical behavior of composite materials with imperfect contact between the constituents. *Mech. Mater.* **4**, 197–208.

Gosz, M., Moran, B. and Achenbach, J. D. (1992). Load-dependent constitutive response of fiber composites with compliant interphases. *J. Mech. Phys. Solids* **40**, 1789–1803.

Hashin, Z. (1990). Thermoelastic properties of fiber composites with imperfect interface. *Mech. Mater.* **8**, 333–348.

Hashin, Z. (1991). Thermoelastic properties of particulate composites with imperfect interface. *J. Mech. Phys. Solids* **39**, 745–762.

Hashin, Z. (1992). Extremum principles for elastic heterogeneous media with imperfect interfaces and their application to bounding of effective moduli. *J. Mech. Phys. Solids* **40**, 767–780.

Jasiuk, I., Chen, J. and Thorpe, M. F. (1992). Elastic moduli of composites with rigid sliding inclusions. *J. Mech. Phys. Solids* **40**, 373–391.

Steif, P. and Hoysan, S. F. (1987). An energy method for calculating the stiffness of aligned short-fiber composites. *Mech. Mater.* **6**, 197–210

Takahashi, K. and Chou, T. W. (1988). Transverse elastic moduli of unidirectional fiber composites with interfacial debonding. *Metall. Trans. A*, **19A**, 129–135.

Williams, M. L. (1959). The stresses around a fault or crack in dissimilar media. *Bull. Seismol. Soc. Am.* **49**, 199–204.

Zhu, H. and Achenbach, J. D. (1991). Effect of fiber-matrix interphase defects on microlevel stress states at neighboring fibers. *J. Compos. Mater.* **25**, 224–238.

APPENDIX: FIRST QUADRANT FUNDAMENTAL SOLUTIONS

The components of the two-dimensional first quadrant fundamental displacement solutions may be written as

$$U^Q_{11}(x, \xi) = U_{11}(x, \xi) - U_{11}(x, -\bar{\xi}) - U_{11}(x, -\xi) + U_{11}(x, \bar{\xi})$$

$$= K\left[(3-4v)\ln\frac{R_2 R_3}{R R_4} + \left(\frac{\partial R}{\partial x_1}\right)_2^2 - \left(\frac{\partial R_2}{\partial x_1}\right)^2 - \left(\frac{\partial R_3}{\partial x_1}\right)^2 + \left(\frac{\partial R_4}{\partial x_1}\right)^2\right]$$

(A1)

where $K = 1/[8\pi\mu(1-v)]$. Also

$$U_{12}^Q(x,\xi) = U_{12}(x,\xi) - U_{12}(x,-\bar{\xi}) - U_{12}(x,-\xi) + U_{12}(x,\bar{\xi}) = K\left[\frac{\partial R}{\partial x_1}\frac{\partial R}{\partial x_2} - \frac{\partial R_2}{\partial x_1}\frac{\partial R_2}{\partial x_2} - \frac{\partial R_3}{\partial x_1}\frac{\partial R_3}{\partial x_2} + \frac{\partial R_4}{\partial x_1}\frac{\partial R_4}{\partial x_2}\right]$$

(A2)

$$U_{21}^Q(x,\xi) = U_{21}(x,\xi) + U_{21}(x,-\bar{\xi}) - U_{21}(x,-\xi) - U_{21}(x,\bar{\xi}) = K\left[\frac{\partial R}{\partial x_1}\frac{\partial R}{\partial x_2} + \frac{\partial R_2}{\partial x_1}\frac{\partial R_2}{\partial x_2} - \frac{\partial R_3}{\partial x_1}\frac{\partial R_3}{\partial x_2} - \frac{\partial R_4}{\partial x_1}\frac{\partial R_4}{\partial x_2}\right]$$

(A3)

and

$$U_{22}^Q(x,\xi) = U_{22}(x,\xi) + U_{22}(x,-\bar{\xi}) - U_{22}(x,-\xi) - U_{22}(x,\bar{\xi})$$

$$= K\left[(3-4v)\ln\frac{R_3 R_4}{R R_2} + \left(\frac{\partial R}{\partial x_2}\right)^2 + \left(\frac{\partial R_2}{\partial x_2}\right)^2 - \left(\frac{\partial R_3}{\partial x_2}\right)^2 - \left(\frac{\partial R_4}{\partial x_2}\right)^2\right]. \quad \text{(A4)}$$

Here, as shown in Fig. 2, R_2, R_3 and R_4 are the distances between the load point in the first quadrant and the image points in the second, third and fourth quadrants, respectively. Also, R is the distance between load point, ξ, and the field point, x. Thus,

$$R = |x-\xi|, \ R_2 = |x+\bar{\xi}|, \ R_3 = |x+\xi| \quad \text{and} \quad R_4 = |x-\bar{\xi}|. \quad \text{(A5)}$$

The first quadrant traction solutions may be expressed as

$$T_{11}^Q(x,\xi) = T_{11}(x,\xi) - T_{11}(x,-\bar{\xi}) - T_{11}(x,-\xi) + T_{11}(x,\bar{\xi})$$

$$= \frac{C}{R}\frac{\partial R}{\partial n}\left[(1-2v) + 2\left(\frac{\partial R}{\partial x_1}\right)^2\right] - \frac{C}{R_2}\frac{\partial R_2}{\partial n}\left[(1-2v) + 2\left(\frac{\partial R_2}{\partial x_1}\right)^2\right]$$

(A6)

$$- \frac{C}{R_3}\frac{\partial R_3}{\partial n}\left[(1-2v) + 2\left(\frac{\partial R_3}{\partial x_1}\right)^2\right] + \frac{C}{R_4}\frac{\partial R_4}{\partial n}\left[(1-2v) + 2\left(\frac{\partial R_4}{\partial x_1}\right)^2\right]$$

where $C = -2\mu K$. Also

$$T_{12}^Q(x,\xi) = T_{12}(x,\xi) - T_{12}(x,-\bar{\xi}) - T_{12}(x,-\xi) + T_{12}(x,\bar{\xi})$$

$$= \frac{C}{R}\left[2\frac{\partial R}{\partial n}\frac{\partial R}{\partial x_1}\frac{\partial R}{\partial x_2} + (1-2v)\left(n_1\frac{\partial R}{\partial x_2} - n_2\frac{\partial R}{\partial x_1}\right)\right]$$

$$- \frac{C}{R_2}\left[2\frac{\partial R_2}{\partial n}\frac{\partial R_2}{\partial x_1}\frac{\partial R_2}{\partial x_2} + (1-2v)\left(n_1\frac{\partial R_2}{\partial x_2} - n_2\frac{\partial R_2}{\partial x_1}\right)\right]$$

(A7)

$$- \frac{C}{R_3}\left[2\frac{\partial R_3}{\partial n}\frac{\partial R_3}{\partial x_1}\frac{\partial R_3}{\partial x_2} + (1-2v)\left(n_1\frac{\partial R_3}{\partial x_2} - n_2\frac{\partial R_3}{\partial x_1}\right)\right]$$

$$+ \frac{C}{R_4}\left[2\frac{\partial R_4}{\partial n}\frac{\partial R_4}{\partial x_1}\frac{\partial R_4}{\partial x_2} + (1-2v)\left(n_1\frac{\partial R_4}{\partial x_2} - n_2\frac{\partial R_4}{\partial x_1}\right)\right].$$

$$T_{21}^Q(x,\xi) = T_{21}(x,\xi) + T_{21}(x,-\bar{\xi}) - T_{21}(x,-\xi) - T_{21}(x,\bar{\xi})$$

$$= \frac{C}{R}\left[2\frac{\partial R}{\partial n}\frac{\partial R}{\partial x_1}\frac{\partial R}{\partial x_2} - (1-2v)\left(n_1\frac{\partial R}{\partial x_2} - n_2\frac{\partial R}{\partial x_1}\right)\right]$$

$$+ \frac{C}{R_2}\left[2\frac{\partial R_2}{\partial n}\frac{\partial R_2}{\partial x_1}\frac{\partial R_2}{\partial x_2} - (1-2v)\left(n_1\frac{\partial R_2}{\partial x_2} - n_2\frac{\partial R_2}{\partial x_1}\right)\right]$$

(A8)

$$- \frac{C}{R_3}\left[2\frac{\partial R_3}{\partial n}\frac{\partial R_3}{\partial x_1}\frac{\partial R_3}{\partial x_2} - (1-2v)\left(n_1\frac{\partial R_3}{\partial x_2} - n_2\frac{\partial R_3}{\partial x_1}\right)\right]$$

$$- \frac{C}{R_4}\left[2\frac{\partial R_4}{\partial n}\frac{\partial R_4}{\partial x_1}\frac{\partial R_4}{\partial x_2} - (1-2v)\left(n_1\frac{\partial R_4}{\partial x_2} - n_2\frac{\partial R_4}{\partial x_1}\right)\right]$$

and

$$T_{22}^Q(x, \xi) = T_{22}(x, \xi) + T_{22}(x, -\bar{\xi}) - T_{22}(x, -\xi) - T_{22}(x, \bar{\xi})$$

$$= \frac{C}{R} \frac{\partial R}{\partial n} \left[(1 - 2v) + 2 \left(\frac{\partial R}{\partial x_2} \right)^2 \right] + \frac{C}{R_2} \frac{\partial R_2}{\partial n} \left[(1 - 2v) + 2 \left(\frac{\partial R_2}{\partial x_2} \right)^2 \right] \qquad (A9)$$

$$- \frac{C}{R_3} \frac{\partial R_3}{\partial n} \left[(1 - 2v) + 2 \left(\frac{\partial R_3}{\partial x_2} \right)^2 \right] - \frac{C}{R_4} \frac{\partial R_4}{\partial n} \left[(1 - 2v) + 2 \left(\frac{\partial R_4}{\partial x_2} \right)^2 \right].$$

It can be verified that the first quadrant fundamental solutions satisfy the following boundary conditions on axes of symmetry:

$$U_{i1}(x, \xi) = T_{i2}(x, \xi) = 0, \quad x \in (x = 0, y \geqslant 0) \qquad (A10)$$

$$U_{i2}(x, \xi) = T_{i1}(x, \xi) = 0, \quad x \in (x \geqslant 0, y = 0). \qquad (A11)$$

Here the subscript i denotes the load direction and takes a value of 1 or 2, while the second subscript indicates the displacement or traction direction.

Cylinder Theory for Unidirectional Composite Materials

Jyi-Jiin Luo and Isaac M. Daniel

The theory discussed here is intended to provide an approximate solution of the multiple fracture problems of unidirectional fiber reinforced composite materials. The strategy is to assume a reasonable displacement field which is expected to be good enough for slowly varying traction boundary conditions on the lateral surface of a cylinder, then apply the variational principle to get the governing equations and necessary boundary conditions. All the field quantities(stresses, strains, and displacements) are expressed in terms of average quantities over the cross section of the cylinder. The unidirectional multiple fracture problem of a unidirectional composite is solved by patching the fiber and matrix cylinders together.

1   Basic Theory

For a hollow cylinder with inner radius R_i and outer radius R_o, the displacement field is assumed to take the following form

$$
\begin{aligned}
u_r(r,z) &= rf_1(z) + \frac{1}{r}f_2(z), & (1)\\
u_z(r,z) &= w(z) + g(r)\kappa(z). & (2)
\end{aligned}
$$

The radial displacement $u_r(r,z)$ is required to be constant at $r = R_o$, or

$$
u_r(R_o, z) = u_o.
$$

If we set the displacement at $r = R_i$ to $u(z)$, the radial displacement $u_r(r,z)$ can be written as

$$
u_r(r,z) = \frac{1}{R_o^2 - R_i^2}\left[\left(-r + \frac{R_o^2}{r}\right)R_i u(z) + \left(r - \frac{R_i^2}{r}\right)R_o u_o\right]. \qquad (3)
$$

1

Note that the radial displacement $u_r(r, z)$ is consistent with the Lamé solution of a pressurized cylinder.

For the axial displacement, we require w(z) to be equal to the average displacement of the cross section of the cylinder A, or

$$\int_A g(r)dA = 0. \tag{4}$$

The shear strain γ_{rz} at the outer diameter R_o is required to be zero,

$$\gamma_{rz}(R_o, z) = (u_{r,z} + u_{z,r})_{r=R_o} = 0.$$

Substituting the displacement fields (eqs. 2 and 3) into the above equation, we have

$$\left(\frac{dg(r)}{dr}\right)_{r=R_o} = 0. \tag{5}$$

Equations (4) and (5) are automatically satisfied if g(r) takes the following form

$$g(r) = \frac{1}{2}r^2 - R_o^2 \ln r - \alpha, \tag{6}$$

where α is defined by

$$\alpha = \frac{1}{A}\int_A (\frac{r^2}{2} - R_o^2 \ln r)dA, \tag{7}$$

in which the cross section area of the cylinder is given by $A = \pi|R_o^2 - R_i^2|$.

Putting $R_o = R_m$ and $R_i = R_f$ into the above displacement fields for matrix cylinder of a unidirectional composite element, we get

$$u_r(r, z) = \frac{1}{R_m^2 - R_f^2}\left[\left(-r + \frac{R_m^2}{r}\right)R_f u_m(z) + \left(r - \frac{R_f^2}{r}\right)R_m u_o\right], \tag{8}$$

$$u_z(r, z) = w_m(z) + g_m(r)\kappa_m(z), \tag{9}$$

where $g_m(r)$ is given by

$$g_m(r) = \frac{1}{2}r^2 - R_m^2 \ln r - \alpha_m, \tag{10}$$

$$\alpha_m = \frac{1}{A}\int_A (\frac{r^2}{2} - R_m^2 \ln r)dA. \tag{11}$$

2

The function $u_m(r)$ is interpreted as the radial displacement on the inner surface of the matrix. u_o is the radial displacement on the outer surface. The function $w_m(r)$ is the average axial displacement, and $\kappa_m(r)$ is interpreted as the curvature of axial displacement at large r.

In the fiber region, set $R_o = 0$, $R_i = R_f$, and $u_o = 0$, then eqs. (2) and (3) become

$$u_r(r,z) \;=\; \frac{r}{R_f} u_f(z), \tag{12}$$

$$u_z(r,z) \;=\; w_f(z) + g_f(r)\kappa(z), \tag{13}$$

where $g_f(r)$ is given by

$$g_f(r) \;=\; \frac{1}{2} r^2 - \alpha_f, \tag{14}$$

$$\alpha_f \;=\; \frac{1}{A} \int_A \frac{r^2}{2} dA = \frac{R_f^2}{4}. \tag{15}$$

The function $u_f(z)$ is interpreted as the radial displacement on the lateral surface of the fiber. The function $w_f(r)$ is the average axial displacement, and $\kappa_f(r)$ is interpreted as the curvature of the axial displacement at the center ($r = 0$) of the cross section of the fiber.

1.1 Cylinder Strains and Cylinder Stress Resultants

The strains in the hollow (matrix) cylinder can be found from the displacement fields given by eqs. (2) and (3)

$$\epsilon_r \;=\; u_{r,r} = \frac{1}{R_o^2 - R_i^2}\left[\left(-1 - \frac{R_o^2}{r^2}\right) R_i u(z) + \left(1 + \frac{R_i^2}{r^2}\right) R_o u_o\right], \tag{16}$$

$$\epsilon_\theta \;=\; \frac{u_r}{r} = \frac{1}{R_o^2 - R_i^2}\left[\left(-1 + \frac{R_o^2}{r^2}\right) R_i u(z) + \left(1 - \frac{R_i^2}{r^2}\right) R_o u_o\right], \tag{17}$$

$$\epsilon_z \;=\; u_{z,z} = \frac{dw(z)}{dz} + g(r)\frac{d\kappa(z)}{dz}, \tag{18}$$

$$\gamma_{rz} \;=\; u_{r,z} + u_{z,r} = \frac{dg(r)}{dr}\left[\kappa(z) - \frac{R_i}{R_o^2 - R_i^2}\frac{du(z)}{dz}\right]. \tag{19}$$

Define cylinder strains $\epsilon_1, \epsilon_2, \gamma, q_1$, and q_2 by

$$\epsilon_1 \;=\; \frac{1}{A} \int_A \epsilon_z dA, \tag{20}$$

3

$$\epsilon_2 = \frac{1}{A}\int_A \frac{\epsilon_r + \epsilon_\theta}{2}dA, \tag{21}$$

$$\gamma = \frac{1}{A}\int_A (\epsilon_r - \epsilon_\theta)dA, \tag{22}$$

$$q_1 = \frac{1}{I_1}\int_A \frac{dg(r)}{dr}\gamma_{rz}dA, \tag{23}$$

$$q_2 = \frac{1}{I_2}\int_A g(r)\epsilon_z dA, \tag{24}$$

where I_1 and I_2 are given by

$$I_1 = \int_A \left(\frac{dg(r)}{dr}\right)^2 dA, \qquad I_2 = \int_A [g(r)]^2 dA.$$

Substituting eqs. (16–19) into (20–24), we get the cylinder strain-displacement relations

$$\epsilon_1 = \frac{dw}{dz}, \tag{25}$$

$$\epsilon_2 = \frac{1}{R_o^2 - R_i^2}[R_o u_o - R_i u(z)], \tag{26}$$

$$\gamma = \frac{4}{m(R_o^2 - R_i^2)}[R_i u_o - R_o u(z)], \tag{27}$$

$$q_1 = \kappa(z) - \frac{R_i}{R_o^2 - R_i^2}\frac{du(z)}{dz}, \tag{28}$$

$$q_2 = \frac{d\kappa(z)}{dz}, \tag{29}$$

where m is defined by

$$\frac{1}{m} = \frac{R_o R_i}{A}\int_A \frac{1}{r^2}dA.$$

Define cylinder stress resultants $N_1, N_2, S, M_1,$ and M_2 by

$$N_1 = \int_A \sigma_z dA, \tag{30}$$

$$N_2 = \int_A \frac{\sigma_r + \sigma_\theta}{2}dA, \tag{31}$$

$$S = \int_A \frac{\sigma_r - \sigma_\theta}{2}dA, \tag{32}$$

$$M_1 = \int_A \frac{dg(r)}{dr}\tau_{rz}dA, \tag{33}$$

$$M_2 = \int_A g(r)\sigma_z dA. \tag{34}$$

4

Using linear elastic stress-strain relations between stresses in eqs. (30–34) and strains in eqs. (20–24), we obtain

$$N_1 = (\lambda + 2\mu)A\epsilon_1 + 2\lambda A\epsilon_2, \tag{35}$$

$$N_2 = 2(\lambda + \mu)A\epsilon_2 + \lambda A\epsilon_1, \tag{36}$$

$$S = \mu A\gamma, \tag{37}$$

$$M_1 = \mu I_1 q_1, \tag{38}$$

$$M_2 = (\lambda + 2\mu)I_2 q_2, \tag{39}$$

where λ and μ are Lamé's constants.

Substituting the cylinder strain-displacement relations (eqs. 25–29) into the cylinder stress-strain relations (eqs. 35–39), we get the cylinder stress-displacement relations

$$N_1 = (\lambda + 2\mu)A\frac{dw(z)}{dz} + \frac{2\lambda A}{R_o^2 - R_i^2}[R_o u_o - R_i u(z)], \tag{40}$$

$$N_2 = \frac{2(\lambda + \mu)A}{R_o^2 - R_i^2}[R_o u_o - R_i u(z)] + \lambda A\frac{dw(z)}{dz}, \tag{41}$$

$$S = \frac{2\pi\mu}{m}\left(R_i u_o - R_o u(z)\right), \tag{42}$$

$$M_1 = \mu I_1\left(\kappa(z) - \frac{R_i}{R_o^2 - R_i^2}\frac{du(z)}{dz}\right), \tag{43}$$

$$M_2 = (\lambda + 2\mu)I_2\frac{d\kappa(z)}{dz}. \tag{44}$$

The strain energy per unit length of the cylinder U_c is defined as

$$U_c = \int_A U\,dA \tag{45}$$

$$= \frac{1}{2}\int_A \left[\lambda(\epsilon_r + \epsilon_\theta + \epsilon_z)^2 + 2\mu(\epsilon_r^2 + \epsilon_\theta^2 + \epsilon_z^2 + \frac{\gamma_{rz}^2}{2})\right]dA. \tag{46}$$

Using the cylinder strain definitions (eqs. 20–24) and the cylinder stress-strain relations (eqs. 35–39), U_c can be simplified to

$$U_c = \frac{1}{2}\left\{\lambda A(\epsilon_1 + 2\epsilon_2)^2 + 2\mu A(\epsilon_1^2 + 2\epsilon_2^2) + m^2\mu A\gamma^2 + \mu I_1 q_1^2\right.$$
$$\left. + (\lambda + 2\mu)I_2 q_2^2\right\} \tag{47}$$

$$= \frac{1}{2}\left(N_1\epsilon_1 + 2N_2\epsilon_2 + m^2 S\gamma + M_1 q_1 + M_2 q_2\right). \tag{48}$$

5

The equations discussed in this section can be applied to the matrix region if R_o is replaced by R_m, and R_i by R_f. For the fiber region, R_o and u_o are replaced by zero, and R_i replaced by R_f.

2 Principle of Virtual Work

From eq. (47), we have

$$
\begin{aligned}
\delta U_c &= \lambda A(\epsilon_1 + 2\epsilon_2)(\delta\epsilon_1 + 2\delta\epsilon_2) + \mu A(2\epsilon_1\delta\epsilon_1 + 4\epsilon_2\delta\epsilon_2) \\
&\quad + m^2 \mu A \gamma \delta\gamma + \mu I_1 q_1 \delta q_1 + (\lambda + 2\mu) I_2 q_2 \delta q_2.
\end{aligned}
\tag{49}
$$

Using the cylinder stress-strain relations (eqs. 35–39), eq. (49) becomes

$$
\delta U_c = N_1 \delta\epsilon_1 + 2N_2 \delta\epsilon_2 + m^2 S \delta\gamma + M_1 \delta q_1 + M_2 \delta q_2.
\tag{50}
$$

Now consider the independent virtual displacements $\delta u(z), \delta w(z), \delta\kappa(z)$, and δu_o from an equilibrium state. Using the cylinder strain-displacement relations (eqs. 25–29), the variation of strain energy δU_c can be expressed as

$$
\begin{aligned}
\delta U_c &= \frac{R_i}{R_o^2 - R_i^2}\left(-2N_2 + \frac{dM_1}{dz} - 2mSR_o/R_i\right)\delta u(z) - \frac{dN_1}{dz}\delta w(z) \\
&\quad + \left(M_1 - \frac{dM_2}{dz}\right)\delta\kappa(z) + \frac{R_i}{R_o^2 - R_i^2}\left(2N_2 R_o/R_i + 2mS\right)\delta u_o \\
&\quad + \frac{d}{dz}\left(-\frac{R_i}{R_o^2 - R_i^2}M_1 \delta u(z) + N_1 \delta w(z) + M_2 \delta\kappa(z)\right).
\end{aligned}
\tag{51}
$$

The virtual work δW is

$$
\begin{aligned}
\delta W &= \int_S (T_r \delta u_r + T_z \delta u_z)dS \tag{52}\\
&= \int_{z_1}^{z_2} T_r(R_o, z)\delta u_o 2\pi R_o dz + \int_{z_1}^{z_2} T_r(R_i, z)\delta u(z)2\pi R_i dz \\
&\quad + \int_{z_1}^{z_2} T_z(R_i, z)[\delta w(z) + g(R_i)\delta\kappa(z)]2\pi R_i dz \\
&\quad + \int_A T_r(r, z_1)\frac{R_i R_o}{R_o^2 - R_i^2}\left[\left(-r + \frac{R_o^2}{r}\right)\frac{\delta u(z_1)}{R_o} + \left(r - \frac{R_i^2}{r}\right)\frac{\delta u_o}{R_i}\right]dA \\
&\quad + \int_A T_r(r, z_2)\frac{R_i R_o}{R_o^2 - R_i^2}\left[\left(-r + \frac{R_o^2}{r}\right)\frac{\delta u(z_2)}{R_o} + \left(r - \frac{R_i^2}{r}\right)\frac{\delta u_o}{R_i}\right]dA
\end{aligned}
$$

6

$$+ \int_A T_z(r, z_1)[\delta w(z_1) + g(r)\delta\kappa(z_1)]dA$$
$$+ \int_A T_z(r, z_2)[\delta w(z_2) + g(r)\delta\kappa(z_2)]dA. \tag{53}$$

The principle of virtual work requires that

$$\delta U - \delta W = \int_{z_1}^{z_2} \delta U_c dz - \delta W = 0. \tag{54}$$

Since $\delta u(z), \delta w(z), \delta\kappa(z)$ are arbitrary in the domain (z_1, z_2), from eqs. (51), (53) and (54), we conclude that the equations of equilibrium in the $z_1 < z < z_2$ domain are

$$\frac{R_i}{R_o^2 - R_i^2}\left(-2N_2 + \frac{dM_1}{dz} - 2mSR_o/R_i\right) = 2\pi R_i T_r(R_i, z), \tag{55}$$

$$-\frac{dN_1}{dz} = 2\pi R_i T_z(R_i, z), \tag{56}$$

$$-\frac{dM_2}{dz} + M_1 = 2\pi R_i g(R_i) T_z(R_i, z). \tag{57}$$

At $z = z_1$, we have

$$M_1(z_1) = -\int_A \frac{dg(r)}{dr} T_r(r, z_1)dA \quad \text{or} \quad \delta u(z_1) = 0, \tag{58}$$

$$N_1(z_1) = -\int_A T_z(r, z_1)dA \quad \text{or} \quad \delta w(z_1) = 0, \tag{59}$$

$$M_2(z_1) = -\int_A g(r) T_z(r, z_1)dA \quad \text{or} \quad \delta\kappa(z_1) = 0. \tag{60}$$

The boundary conditions at z_2 are similar. From δu_o we have the constant displacement condition

$$\int_{z_1}^{z_2}\left(N_2 + mSR_i/R_o\right)dz = A\int_{z_1}^{z_2} T_r(R_o, z)dz$$
$$+\frac{1}{2}\int_A\left(r - \frac{R_i^2}{r}\right)\left(T_r(r, z_1) + T_r(r, z_2)\right)dA \quad \text{or} \quad \delta u_o = 0, \tag{61}$$

which implies that we can either specify u_o or determine u_o from given tractions on the surface.

Substituting the cylinder stress-displacement relations (40–44) into eqs. (55–57), we can get the equilibrium equations in terms of displacements. In the matrix region, these equations are

$$\frac{\pi R_f \mu_m I_{1m}}{2A_m^2} u_m''(z) + \lambda_m w_m'(z) - \frac{\mu_m I_{1m}}{2A_m}\kappa_m'(z) - \frac{2\pi R_f}{A_m}\left[\lambda_m + \mu_m(1 + \frac{R_m^2}{R_f^2})\right]u_m(z)$$

7

$$= -T_{rm}(R_f, z) - \frac{2\pi R_m u_o(\lambda_m + 2\mu_m)}{A_m}, \tag{62}$$

$$\frac{(\lambda_m + 2\mu_m)A_m}{2\pi R_f} w_m''(z) - \lambda_m u_m'(z) = -T_{zm}(R_f, z), \tag{63}$$

$$\frac{A_m(\lambda_m + 2\mu_m)I_{2m}}{\pi R_f I_{1m}} \kappa_m''(z) + \mu_m u_m'(z) - \frac{A_m \mu_m}{\pi R_f} \kappa_m(z) = -T_{zm}(R_f, z), \tag{64}$$

where $A_m = \pi(R_m^2 - R_f^2)$ is the matrix cylinder cross-sectional area.

Similarly, the constant displacement condition (eq. 61) becomes

$$-\frac{2(\lambda_m + 2\mu_m)f}{R_f(1 - f)(z_2 - z_1)} \int_{z_1}^{z_2} u_m(z)dz + \lambda_m \frac{w_m(z_2) - w_m(z_1)}{z_2 - z_1} =$$

$$-\frac{\lambda_m + \mu_m(1 + f)}{1 - f} \frac{2u_o}{R_m} + \frac{1}{z_2 - z_1} \int_{z_1}^{z_2} T_{rm}(R_m, z)dz$$

$$+\frac{1}{2A_m(z_2 - z_1)} \int_{A_m} \left(r - \frac{R_f^2}{r}\right)\Big(T_{rm}(r, z_1) + T_{rm}(r, z_2)\Big)dA_m \tag{65}$$

Applying the same procedure in the fiber region, we have

$$\frac{\mu_f R_f}{4} u_f''(z) - \lambda_f w_f'(z) + \frac{\mu_f R_f^2}{4} \kappa_f'(z) - \frac{2(\lambda_f + \mu_f)}{R_f} u_f(z) = -T_{rf}(R_f, z), \tag{66}$$

$$(\lambda_f + 2\mu_f)\frac{R_f}{2} w_f''(z) + \lambda_f u_f'(z) = -T_{zf}(R_f, z), \tag{67}$$

$$(\lambda_f + 2\mu_f)\frac{R_f^3}{24} \kappa_f''(z) - \mu_f u_f'(z) - \mu_f R_f \kappa_f(z) = -T_{rf}(R_f, z). \tag{68}$$

The above equations can be rewritten as

$$\frac{c_1}{4} u_m''(\xi) + 2(a_m - 1)w_m'(\xi) - v_m'(\xi) - (2 + \frac{4fa_m}{1 - f})u_m(\xi)$$

$$= -\frac{R_f T_{rm}(\xi)}{\mu_m} - \frac{4a_m R_f}{1 - f}\left(\frac{u_o}{R_m}\right) \tag{69}$$

$$\frac{(1 - f)a_m}{f} w_m''(\xi) - 2(a_m - 1)u_m'(\xi) = -\frac{R_f T_{zm}(\xi)}{\mu_m}, \tag{70}$$

$$\frac{c_2 a_m(1 - f)}{3c_1^2 f} v_m''(\xi) + u_m'(\xi) - \frac{4}{c_1} v_m(\xi) = -\frac{R_f T_{zm}(\xi)}{\mu_m}, \tag{71}$$

8

where

$$f = R_f^2/R_m^2, \quad a_m = \frac{1 - \nu_m}{1 - 2\nu_m}, \quad c_1 = \frac{2\pi I_{1m}}{A_m^2}, \quad c_2 = \frac{48\pi^2 I_{2m}}{A_m^3},$$

$$\xi = z/R_f, \quad v_m(\xi) = \frac{I_{1m}}{2A_m}\kappa_m(z) = \mu_m(R_f)\kappa_m(z),$$

$$T_{rm}(\xi) = T_{rm}(R_f, z), \quad T_{zm}(\xi) = T_{zm}(R_f, z).$$

The constant displacement condition (eq. 65) becomes

$$-\frac{4(a_m - 1)f}{(1 - f)}\overline{u}_m + 2(a_m - 1)\frac{w_m(\xi_2) - w_m(\xi_1)}{\xi_2 - \xi_1} =$$

$$-2R_f\left(\frac{2a_m}{1 - f} - 1\right)\left(\frac{u_o}{R_m}\right) + \frac{R_f}{\mu_m(\xi_2 - \xi_1)}\int_{\xi_1}^{\xi_2} T_{rm}(R_m, z)d\xi$$

$$+\frac{R_f}{2\mu_m(\xi_2 - \xi_1)A_m}\int_A \left(\frac{r}{R_f} - \frac{R_f}{r}\right)\Big(T_{rm}(r, z_1) + T_{rm}(r, z_2)\Big)dA, \qquad (72)$$

where

$$\overline{u}_m = \frac{1}{\xi_2 - \xi_1}\int_{\xi_1}^{\xi_2} u_m(\xi)d\xi.$$

The traction terms in the above equation are zero if we consider the symmetry of the multiple crack problem of unidirectional composite materials.

Similarly, in the fiber region, we have

$$\frac{1}{4}u_f''(\xi) - 2(a_f - 1)w_f'(\xi) + v_f'(\xi) - (4a_f - 2)u_f(\xi) \quad = \quad -\frac{R_f T_{rf}(\xi)}{\mu_f}, \qquad (73)$$

$$a_f w_f''(\xi) + 2(a_f - 1)u_f'(\xi) \quad = \quad -\frac{R_f T_{zf}(\xi)}{\mu_f}, \qquad (74)$$

$$\frac{a_f}{3}v_f''(\xi) - u_f'(\xi) - 4v_f(\xi) \quad = \quad -\frac{R_f T_{zf}(\xi)}{\mu_f}, \qquad (75)$$

where

$$a_f = \frac{1 - \nu_f}{1 - 2\nu_f}, \qquad v_f(\xi) = \frac{R_f^2}{4}\kappa_f(z) = \mu_f(R_f)\kappa_f(z),$$

$$T_{rf}(\xi) = T_{rf}(R_f, z), \qquad T_{zf}(\xi) = T_{zf}(R_f, z).$$

9

3 Multiple fracture of unidirectional composite

The above theory can be applied to the multiple fracture problem of unidirectional composites. The following interfacial conditions are discussed:

1. Perfect bonding:

$$u_{rf}(R_f, z) = u_{rm}(R_f, z), \qquad u_{zm}(R_f, z) = u_{zm}(R_f, z),$$

or

$$u_f(z) = u_m(z), \qquad w_f(z) + v_f(z) = w_m(z) + v_m(z).$$

2. Constant friction:

$$u_{rf}(R_f, z) = u_{rm}(R_f, z), \qquad T_{zf}(R_f, z) = \pm\tau_o,$$

or

$$u_f(z) = u_m(z), \qquad T_{zf}(\xi) = \pm\tau_o.$$

3. Coulomb friction:

$$u_{rf}(R_f, z) = u_{rm}(R_f, z), \qquad T_{zf}(R_f, z) = \pm\mu T_{rf}(R_f, z),$$

or

$$u_f(z) = u_m(z), \qquad T_{zf}(\xi) = \pm\mu T_{rf}(\xi).$$

4. Noncontacting, or traction free interfaces:

$$T_{rf}(R_m, z) = 0, \qquad T_{rm}(R_f, z) = 0$$

or

$$T_{rf}(\xi) = 0, \qquad T_{zf}(\xi) = 0.$$

The continuity of tractions requires that

$$T_{rf}(R_f, z) = -T_{rm}(R_f, z), \qquad T_{zf}(R_f, z) = -T_{zm}(R_f, z),$$

or

$$T_{rf}(\xi) = -T_{rm}(\xi), \qquad T_{zf}(\xi) = -T_{zm}(\xi).$$

10

Consider any two of the above four cases connected together at z_1, which could include fiber-matrix debonding. The boundary conditions at the ends z_0 and z_2 specify either the cylinder displacements or the cylinder stress resultants, that is, at $\xi = \xi_0$ and $\xi = \xi_2$, we have

$$u_f \quad \text{or} \quad M_{1f} \quad \text{specified,}$$

$$u_m \quad \text{or} \quad M_{1m} \quad \text{specified,}$$

$$w_f \quad \text{or} \quad N_{1f} \quad \text{specified,}$$

$$w_m \quad \text{or} \quad N_{1m} \quad \text{specified,}$$

$$v_f \quad \text{or} \quad M_{2f} \quad \text{specified,}$$

$$v_m \quad \text{or} \quad M_{2m} \quad \text{specified.}$$

The continuity conditions at z_1 specify the continuity of cylinder displacements and cylinder stress resultants, that is,

$$u_f(\xi_1-) = u_f(\xi_1+), \qquad w_f(\xi_1-) = w_f(\xi_1+), \qquad v_f(\xi_1-) = v_f(\xi_1+),$$

$$u_m(\xi_1-) = u_m(\xi_1+), \qquad w_m(\xi_1-) = w_m(\xi_1+), \qquad v_m(\xi_1-) = v_m(\xi_1+),$$

$$M_{1f}(\xi_1-) = M_{1m}(\xi_1+), \quad N_{1f}(\xi_1-) = N_{1m}(\xi_1+), \quad M_{2f}(\xi_1-) = M_{2m}(\xi_1+),$$

$$M_{1f}(\xi_1-) = M_{1m}(\xi_1+), \quad N_{1f}(\xi_1-) = N_{1m}(\xi_1+), \quad M_{2f}(\xi_1-) = M_{2m}(\xi_1+).$$

4 Crack Opening Displacements and Stress-Strain Relations

Now we derive an important result from the cylinder model. Rewriting the equations of equilibrium (55–57) in the fiber region, we have

$$-\frac{1}{R_f}\left(-2N_{2f} + \frac{dM_{1f}}{dz}\right) = 2\pi R_f T_{rf}(R_f, z), \tag{76}$$

$$-\frac{dN_{1f}}{dz} = 2\pi R_f T_{zf}(R_f, z), \tag{77}$$

$$-\frac{dM_{2f}}{dz} + M_{1f} = 2\pi R_f g_f(R_f) T_{zf}(R_f, z), \tag{78}$$

11

and in the matrix region,

$$\frac{R_f}{R_m^2 - R_f^2}\left(-2N_{2m} + \frac{dM_{1m}}{dz} - 2mS_m\frac{R_m}{R_f}\right) = 2\pi R_f T_{rm}(R_f, z), \qquad (79)$$

$$-\frac{dN_{1m}}{dz} = 2\pi R_f T_{zm}(R_f, z), \qquad (80)$$

$$-\frac{dM_{2m}}{dz} + M_{1m} = 2\pi R_f g_m(R_f)T_{zm}(R_f, z). \qquad (81)$$

The constant displacement condition (eq. 61) gives

$$\int_{z_1}^{z_2}\left(N_{2m} + mS_m R_f/R_m\right)dz = A_m \int_{z_1}^{z_2} T_{rm}(R_m, z)dz$$
$$+\frac{1}{2}\int_{A_m}\left(r - \frac{R_f^2}{r}\right)\left(T_{rm}(r, z_1) + T_{rm}(r, z_2)\right)dA. \qquad (82)$$

Now we focus our attention to the global behavior of the representative element by considering average properties over $[z_1, z_2]$. Integrating eqs. (77) and (80) over $[z_1, z_2]$ with the weight function $(z - z_1)$, one gets

$$\int_{z_1}^{z_2} N_{1f}(z)dz = (z_2 - z_1)N_{1f}(z_2) + 2\pi R_f \int_{z_1}^{z_2} (z - z_1)T_{zf}(R_f, z)dz \qquad (83)$$

$$\int_{z_1}^{z_2} N_{1m}(z)dz = (z_2 - z_1)N_{1m}(z_2) + 2\pi R_f \int_{z_1}^{z_2} (z - z_1)T_{zm}(R_f, z)dz. \qquad (84)$$

Integrating eq. (76) over $[z_1, z_2]$, one gets

$$\int_{z_1}^{z_2} N_{2f}(z)dz = \frac{1}{2}M_{1f}(z)\Big|_{z_1}^{z_2} + \pi R_f^2 \int_{z_1}^{z_2} T_{rf}(R_f, z)dz. \qquad (85)$$

Integrating eq. (79) over $[z_1, z_2]$, and using eq. (82), one gets

$$\int_{z_1}^{z_2} N_{2m}(z)dz = \frac{1}{2}\int_{A_m}\left[T_{rm}(r, z_1) + T_{rm}(r, z_2)\right]rdA$$
$$+ \int_{z_1}^{z_2}\left[\pi R_f^2 T_{rm}(R_f, z) + \pi R_m^2 T_{rm}(R_m, z)\right]dz, \qquad (86)$$

$$\int_{z_1}^{z_2} S_m(z)dz = -\frac{R_f R_m}{2m}\int_{A_m}\left[T_{rm}(r, z_1) + T_{rm}(r, z_2)\right]\frac{1}{r}dA$$
$$-\frac{\pi R_f R_m}{m}\int_{z_1}^{z_2}\left[T_{rm}(R_f, z) + T_{rm}(R_m, z)\right]dz \qquad (87)$$

12

Consider now a representative composite element with matrix cracks at $z = z_1$ and $z = z_2$. Due to symmetry, the following boundary conditions are required:

$$T_{rf}(r, z_1) = T_{rm}(r, z_2) = 0, \tag{88}$$

and

$$\int_{z_1}^{z_2} T_{rm}(R_m, z)dz = 0, \tag{89}$$

which states the fact that there is no global stress acting on the lateral surface of the composite. Note that the constant displacement at the matrix outer surface is automatically satisfied in that displacement assumption. The continuity of stresses at the interface requires

$$T_{rf}(R_f, z) = -T_{rm}(R_f, z), \tag{90}$$
$$T_{zf}(R_f, z) = -T_{zm}(R_f, z). \tag{91}$$

Debonding, sliding and/or sticking could happen at the interface. These conditions usually would require further elaboration, but intentionally leaving out these conditions would imply that the results are applicable to all of them. Applying the above boundary conditions (eqs. 90 and 91) to eqs. (83–87), one gets

$$\frac{1}{z_2 - z_1} \int_{z_1}^{z_2} N_{1f}(z)dz = N_{1f}(z_2) + A_f Q, \tag{92}$$

$$\frac{1}{z_2 - z_1} \int_{z_1}^{z_2} N_{1m}(z)dz = N_{1m}(z_2) - A_f Q, \tag{93}$$

$$\frac{1}{z_2 - z_1} \int_{z_1}^{z_2} N_{2f}(z)dz = A_f P, \tag{94}$$

$$\frac{1}{z_2 - z_1} \int_{z_1}^{z_2} N_{2m}(z)dz = -A_f P, \tag{95}$$

$$\frac{1}{z_2 - z_1} \int_{z_1}^{z_2} S_m(z)dz = \frac{\pi R_m R_f}{m} P. \tag{96}$$

where the average interface radial traction P, and the normalized first moment of interface longitudinal traction Q are given by

$$P = \frac{1}{z_2 - z_1} \int_{z_1}^{z_2} T_{rf}(R_f, z)dz = -\frac{1}{z_2 - z_1} \int_{z_1}^{z_2} T_{rm}(R_f, z)dz, \tag{97}$$

$$Q = \frac{2}{R_f} \int_{z_1}^{z_2} \frac{z - z_1}{z_2 - z_1} T_{zf}(R_f, z)dz = -\frac{2}{R_f} \int_{z_1}^{z_2} \frac{z - z_1}{z_2 - z_1} T_{zm}(R_f, z)dz. \tag{98}$$

13

Our intention is to derive average stress and strain relations by integrating field quantities over the z-axis. The average strains are calculated by integrating the cylinder stress-strain relations over $[z_1, z_2]$, for example,

$$
\begin{aligned}
\bar{\epsilon}_{1f} &= \frac{1}{z_2 - z_1} \int_{z_1}^{z_2} \epsilon_{1f} dz \\
&= \frac{1}{z_2 - z_1} \int_{z_1}^{z_2} \frac{1}{E_f A_f} (N_{1f} - 2\nu_f N_{2f}) dz.
\end{aligned}
$$

Substituting eqs. (92 and 94) into the above equation, one gets

$$
E_f \bar{\epsilon}_{1f} = \frac{N_{1f}(z_2)}{A_f} - 2\nu_f P + Q. \tag{99}
$$

Following the same procedure, one gets the other average strain components:

$$
E_f \bar{\epsilon}_{2f} = -\nu_f \frac{N_{1f}(z_2)}{A_f} + (1 - \nu_f)P - \nu_f Q, \tag{100}
$$

$$
E_m \bar{\epsilon}_{1m} = \frac{N_{1m}(z_2)}{A_m} + \frac{2f\nu_m}{1 - f}P - \frac{f}{1 - f}Q, \tag{101}
$$

$$
E_m \bar{\epsilon}_{2m} = -\nu_m \frac{N_{1m}(z_2)}{A_m} - \frac{f(1 - \nu_m)}{1 - f}P + \frac{f\nu_m}{1 - f}Q, \tag{102}
$$

$$
\mu_m \bar{\gamma}_m = \frac{\pi R_m R_f}{m A_m}P, \tag{103}
$$

where all quantities with overbar represent their averages over $[z_1, z_2]$.

When the matrix has lower strength and suitable stiffness, the matrix cracks will develop first, and parallel matrix cracks could occur. Consider the problem with matrix cracks at z_1 and z_2, see fig. 1. The interface may have debonding and/or sliding. The composite longitudinal strain $\bar{\epsilon}_1$ is the same as the average fiber longitudinal strain $\bar{\epsilon}_{1f}$, or, using eq. (99),

$$
\bar{\epsilon}_1 = \bar{\epsilon}_{1f} = \frac{N_{1f}(z_2)}{E_f A_f} - \frac{2\nu_f}{E_f}P + \frac{1}{E_f}Q. \tag{104}
$$

The composite transverse strain $\bar{\epsilon}_2$ is given by

$$
\bar{\epsilon}_2 = \frac{u_m(R_m, z)}{R_m} = \frac{u_o}{R_m}. \tag{105}
$$

14

Integrating the cylinder strains-displacement relations (26) and (27) for the matrix cylinder, the above equation can be rewritten as

$$\bar{\epsilon}_2 = \bar{\epsilon}_{2m} - \frac{mfA_m}{2\pi(1-f)R_m R_f}\bar{\gamma}_m. \tag{106}$$

Substituting eqs. (102) and (103) into the above equation, we have

$$\bar{\epsilon}_2 = -\frac{\nu_m N_{1m}(z_2)}{E_m A_m} - \frac{2f}{(1-f)E_m}P + \frac{f\nu_m}{(1-f)E_m}Q. \tag{107}$$

The average matrix crack opening displacement COD_m is defined by

$$\begin{aligned}
COD_m &= [w_f(z_2) - w_f(z_1)] - [w_m(z_2) - w_m(z_1)] \\
&= (z_2 - z_1)(\bar{\epsilon}_{1f} - \bar{\epsilon}_{1m}).
\end{aligned}$$

We define the number of matrix cracks per unit length, or the matrix crack density, λ_m by

$$\lambda_m = \frac{1}{z_2 - z_1}. \tag{108}$$

Combining eqs. (99), (101) and (108), one can express the normalized matrix crack density $\lambda_m COD_m$ by

$$\begin{aligned}
\lambda_m COD_m &= \bar{\epsilon}_{1f} - \bar{\epsilon}_{1m} \\
&= \frac{N_{1f}(z_2)}{E_f A_f} - \frac{N_{1m}(z_2)}{E_m A_m} \\
&\quad - \left[\frac{\nu_f}{E_f} + \frac{f\nu_m}{(1-f)E_m}\right]2P + \left[\frac{1}{E_f} + \frac{f}{(1-f)E_m}\right]Q.
\end{aligned} \tag{109}$$

The average gap between the fiber surface and the inner matrix surface is given by

$$\bar{u}_m - \bar{u}_f = 2\lambda_m \ell_d COD_i, \tag{110}$$

where the average displacement $\bar{u}_f$ and $\bar{u}_m$ are given by

$$\bar{u}_f = \frac{1}{z_2 - z_1}\int_{z_1}^{z_2} u_f(z)dz, \tag{111}$$

$$\bar{u}_m = \frac{1}{z_2 - z_1}\int_{z_1}^{z_2} u_m(z)dz, \tag{112}$$

15

COD_i is the average interface crack opening in the debonded region, and ℓ_d is the debonded length.

Integrating the strain-displacement relations (25–27) for both the fiber and matrix region, one can rewrite the average gap in eq. (110) as

$$\frac{2\lambda_m \ell_d \text{COD}_i}{R_f} = \bar{\epsilon}_{2m} - \bar{\epsilon}_{2f} - \frac{mA_m}{2\pi(1-f)R_m R_f}\overline{\gamma}_m. \tag{113}$$

Using eqs. (100), (102) and (103), the above equation can be written as

$$\frac{2\lambda_m \ell_d \text{COD}_i}{R_f} = \frac{\nu_f N_{1f}(z_2)}{E_f A_f} - \frac{\nu_m N_{1m}(z_2)}{E_m A_m}$$
$$- \left[\frac{1-\nu_f}{E_f} + \frac{1+f+(1-f)\nu_m}{(1-f)E_m}\right]P + \left[\frac{\nu_f}{E_f} + \frac{f\nu_m}{(1-f)E_m}\right]Q. \tag{114}$$

Rearranging eqs. (104), (107), (109) and (114) in matrix form, we have

$$\left\{\begin{array}{c} \bar{\epsilon}_1 \\ \bar{\epsilon}_2 \end{array}\right\} = \left[\begin{array}{cc} \frac{1}{E_f} & 0 \\ 0 & -\frac{\nu_m}{E_m} \end{array}\right] \left\{\begin{array}{c} \frac{N_{1f}(z_2)}{A_f} \\ \frac{N_{1m}(z_2)}{A_m} \end{array}\right\} + \left[\begin{array}{cc} -\frac{2\nu_f}{E_f} & \frac{1}{E_f} \\ -\frac{2f}{(1-f)E_m} & \frac{f\nu_m}{(1-f)E_m} \end{array}\right] \left\{\begin{array}{c} P \\ Q \end{array}\right\}, \tag{115}$$

and

$$\left\{\begin{array}{c} \lambda_m \text{COD}_m \\ 2\lambda_m \ell_d \text{COD}_i/R_f \end{array}\right\} = \left[\begin{array}{cc} \frac{1}{E_f} & -\frac{1}{E_m} \\ \frac{\nu_f}{E_f} & -\frac{\nu_m}{E_m} \end{array}\right] \left\{\begin{array}{c} \frac{N_{1f}(z_2)}{E_f} \\ \frac{N_{1m}(z_2)}{E_m} \end{array}\right\}$$
$$+ \left[\begin{array}{cc} -\frac{\nu_f}{E_f} - \frac{f\nu_m}{(1-f)E_m} & \frac{1}{E_f} + \frac{f}{(1-f)E_m} \\ -\frac{1-\nu_f}{E_f} - \frac{1+f+(1-f)\nu_m}{(1-f)E_m} & \frac{\nu_f}{E_f} + \frac{f\nu_m}{(1-f)E_m} \end{array}\right] \left\{\begin{array}{c} P \\ Q \end{array}\right\}. \tag{116}$$

Eliminating P and Q from eqs. (115) and (116), after complex algebraic operations, one gets the following results

$$\left\{\begin{array}{c} (1-f)\lambda_m \text{COD}_m \\ 2\lambda_m \ell_d \text{COD}_i/R_f \end{array}\right\} = \left[\begin{array}{cc} b_{11} & b_{12} \\ b_{21} & b_{22} \end{array}\right] \left\{\begin{array}{c} \bar{\epsilon}_1 - \frac{\bar{\sigma}_1}{E_1} \\ \bar{\epsilon}_2 + \nu_{12}\frac{\bar{\sigma}_1}{E_1} \end{array}\right\}, \tag{117}$$

where

$$b_{11} = 1 + \frac{f(\nu_f - \nu_m)}{1 - \nu_f \nu_m} + \frac{f(1+\nu_f)(1-\nu_m)}{1 - \nu_f \nu_m}\left(\frac{\mu_f}{\mu_m} - 1\right), \tag{118}$$

$$b_{12} = -\frac{(1-f)(\nu_f - \nu_m)}{1 - \nu_f \nu_m}, \tag{119}$$

16

$$b_{21} = \frac{f(\nu_f - \nu_m)}{1 - \nu_f \nu_m} - \frac{f \nu_m (1 + \nu_f)}{2(1 - \nu_f \nu_m)} \left(\frac{\mu_f}{\mu_m} - 1 \right), \tag{120}$$

$$\begin{aligned} b_{22} &= 1 - \frac{(1 - f)(\nu_f - \nu_m)}{1 - \nu_f \nu_m} \\ &\quad - \frac{(1 - f)(1 + \nu_m)(1 - 2\nu_f)}{2(1 - \nu_f \nu_m)} \left(1 - \frac{\mu_m}{\mu_f} \right). \end{aligned} \tag{121}$$

The parameters $b_{ij}(i, j = 1, 2)$ are the elastic properties of the composites, and depend only on the constituent elastic constants and fiber volume ratio; $\bar{\sigma}_1$ is the composite longitudinal stress given by

$$\bar{\sigma}_1 = \frac{N_{1f} + N_{1m}}{A_f + A_m}. \tag{122}$$

Note that $N_{1m}(z_2)$ is zero because of the presence of matrix cracks; E_1 is the undamaged composite Young's modulus given by

$$E_1 = f E_f + (1 - f) E_m + \frac{4f(1 - f)(\nu_f - \nu_m)^2 \mu_m}{1 + f(1 - 2\nu_m) + (1 - f)(1 - 2\nu_f)\mu_m/\mu_f}, \tag{123}$$

and ν_{12} is Poisson's ratio given by

$$\nu_{12} = f \nu_f + (1 - f)\nu_m + \frac{f(1 - f)(\nu_f - \nu_m)[1 - 2\nu_m - (1 - 2\nu_f)\mu_m/\mu_f]}{1 + f(1 - 2\nu_m) + (1 - f)(1 - 2\nu_f)\mu_m/\mu_f}. \tag{124}$$

5   Results and Discussion

Introducing the experimentally determined constituent and composite properties in eq. (117), we obtain results for the total crack opening per unit length $\lambda_m \text{COD}_m$ and for $2\lambda_m \ell_d \text{COD}_i / R_f$, which are plotted versus applied strain ϵ_1 in Fig. 2 and 3. which are the results from two different batches of SiC/CAS. They both show that interfacial debonding happens a little bit after matrix cracks start. Fiber breaks are ignored in the calculation. Since fibers only break under higher loading (mostly after matrix crack saturation), these results are believed to be acceptible for lower strains, and can be used only for reference under higher strain.
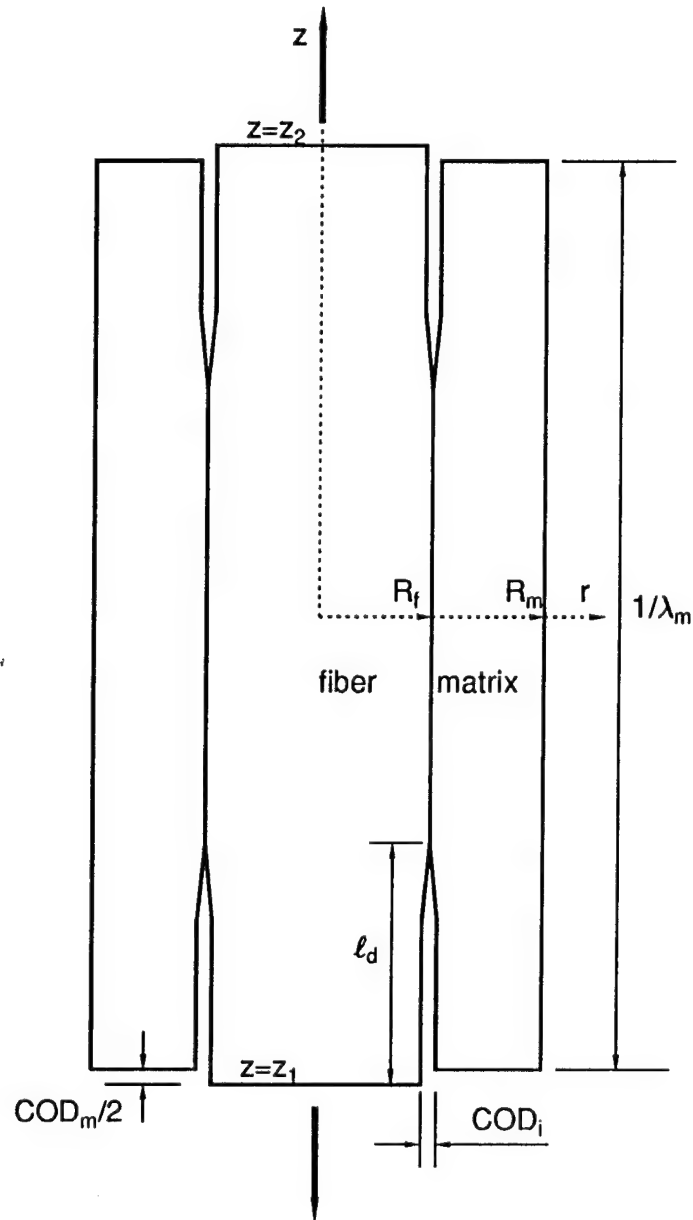
17

Fig. 1: Unit Cell Between Matrix Cracks Illustrating Matrix Crack Opening Displacement COD_m and Interface Debonding Crack Opening Displacement COD_i.

18

Fig. 2: Stress Strain Curves and Predicted Crack Opening Displacements COD_m and COD_i of Unidirectional SiC/CAS Composite under Longitudinal Tension.

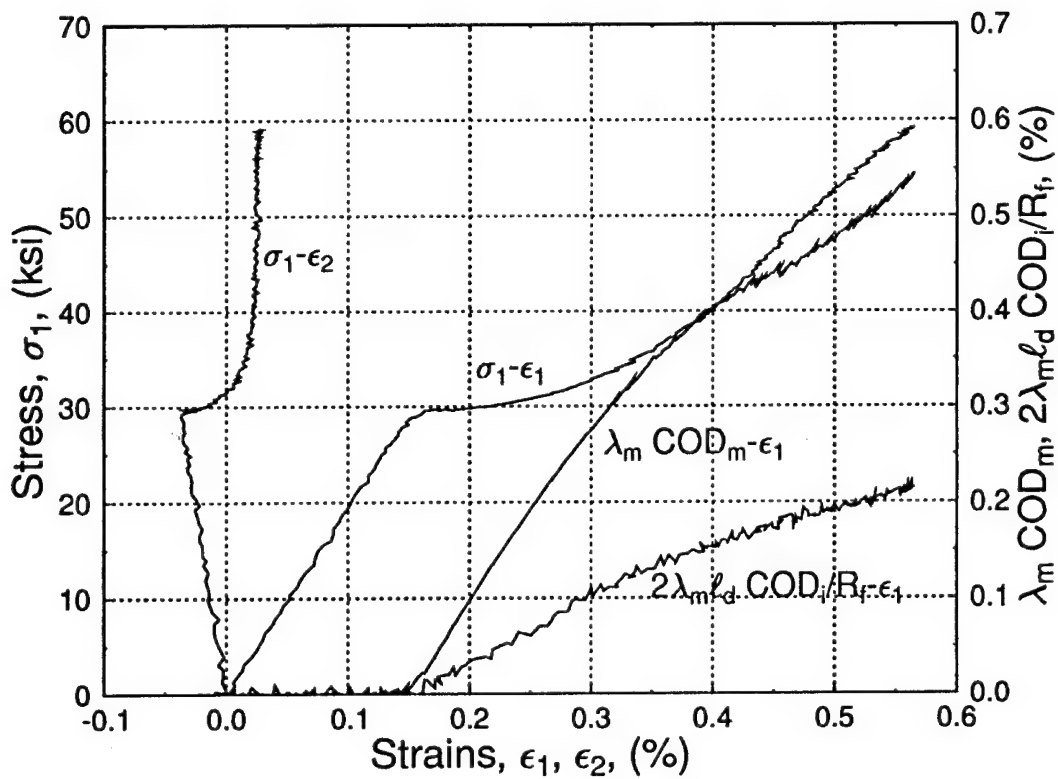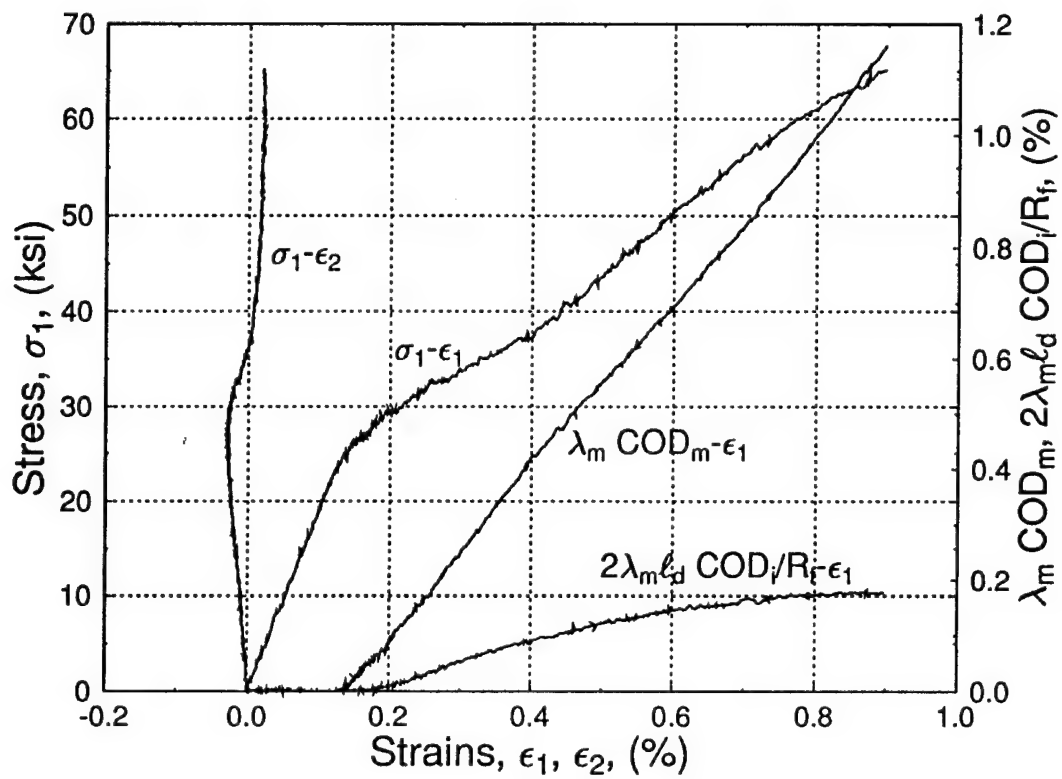19

Fig. 3: Stress Strain Curves and Predicted Crack Opening Displacements COD_m and COD_i of Unidirectional SiC/CAS Composite under Longitudinal Tension.

FAILURE MECHANISMS AND DAMAGE EVOLUTION IN CROSSPLY CERAMIC-MATRIX COMPOSITES

I. M. DANIEL and G. ANASTASSOPOULOS

McCormick School of Engineering and Applied Science, Northwestern University, Evanston,
IL 60208, U.S.A.

Abstract—Failure mechanisms were studied under the microscope in a crossply silicon carbide/glass-ceramic composite under axial tensile loading. Failure initiation takes place in the 90° layer. It takes the form of radial matrix cracks around the fibers, followed by interfacial cracks, which in turn coalesce into transverse macrocracks. These transverse macrocracks in the 90° layer reach a characteristic saturation crack density with a minimum crack spacing of the order of the layer thickness. Subsequently, transverse matrix cracks are generated in the 0° layer, increasing in density up to a minimum crack spacing of the order of eight fiber diameters. This stage of failure is accompanied by fiber–matrix debonding and some fiber-failures in the 0° layer. In the third stage of damage development, the macrocracks of the 90° layer branch off and connect with the 0° layer cracks in a characteristic "delta" pattern. This is finally followed by delamination and additional cracking in the 90° layer prior to ultimate failure. The various failure mechanisms and their interactions were discussed and compared with predictions of prior experimental and analytical studies of unidirectional and crossply composites.

1. INTRODUCTION

The newer generation of advanced composites designed to meet high temperature performance requirements includes ceramic-matrix composites. Ceramic composites display appreciable ductility and have higher fracture toughness and better fatigue endurance than comparable monolithic ceramics. Promising reinforcements include carbon, silicon carbide (SiC) and mullite fibers. Matrices used successfully include glass, glass-ceramic, carbon, silicon carbide, silicon nitride and aluminum oxide. Composites consisting of glass-ceramic matrices, such as lithium aluminosilicate (LAS), calcium aluminosilicate (CAS) and magnesium aluminosilicate (MAS) reinforced with silicon carbide yarn or monofilament have been developed; see Prewo and Brennan (1982), Brennan and Prewo (1982), Larsen and Adams (1989). These materials can be fabricated in both unidirectional and multidirectional laminate form, and can attain strengths of 1000 MPa (140 ksi) and ultimate strains of over 1%. Fracture toughness, as determined by a notched beam method, is more than five times that of the monolithic ceramic, Brennan and Prewo (1982).

The micromechanics of stress transfer and fracture have been studied experimentally and analytically by many investigators for the case of unidirectional composites, starting with the pioneering work by Aveston *et al.* (1971) and Aveston and Kelly (1973). Fundamental approaches used include shear lag or stress transfer models and fracture mechanics with stress or energy fracture criteria. Failure mechanisms in a SiC/LAS unidirectional composite under longitudinal loading have been observed and analyzed by Marshall and Evans (1985, 1988) and Marshall *et al.* (1985). Further analytical studies were described by Budiansky et al. (1986), Hsueh (1988), Charalambides and Evans (1989), McCartney (1989), Hutchinson and Jenson (1990), Zok and Spearing (1992) and Weitsman and Zhu (1993). The authors have reported both experimental and analytical investigations of a longitudinally and transversely loaded unidirectional SiC/CAS composite; see Daniel *et al.* (1989a,b, 1992, 1993) and Lee and Daniel (1992). Most studies to date on the behavior of composites under transverse loading are analytical, such as those by Hashin (1983), Benveniste (1985) and Achenbach and Zhu (1990).

The problem of crossply laminates has been studied extensively for polymer-matrix composites. The primary failure mechanism in these composites is transverse matrix cracking in the 90° layer reaching a limiting crack density. This is followed by longitudinal matrix cracking in the 0° layers, local delaminations at the intersections of matrix cracks and, finally, fiber fractures in the 0° layer leading to ultimate failure, Daniel *et al.* (1988). In the case of brittle-matrix composites the type, sequence and interaction of failure mechanisms are different and characteristic of the constituent material properties. Some experimental work on crossply ceramic-matrix composites has been reported by Sbaizero and Evans (1986). They tested symmetric [0/90]$_s$ SiC/LAS laminates in tension and bending. However, the observed failure modes were not easily explained. The initial delamination failure observed would only be possible near free edges in the case of a material with very low interlaminar shear strength. The orientation of the transverse ply cracks could only be explained by assuming compressive residual stresses in the 90° layers. Subsequent work on crossply laminates dealt with a fracture mechanics model of a delamination crack formed at the tip of a notch cutting through 0° and 90° layers, see Sbaizero *et al.* (1990) and Charalambides (1991). Mall and Kim (1992) also conducted experimental investigations of failure mechanisms in SiC/CAS laminates. They observed that initial failure consisted of matrix microcracks occurring and growing in all plies in a random manner.

This paper deals with a systematic investigation of the failure mechanisms, their growth and interactions in a crossply SiC/CAS laminate under uniaxial tension. It represents the first systematic experimental/analytical study of a crossply laminate with brittle matrix. Previous experimental work mentioned before reported random or other edge-dominated failure mechanisms with no clear trends. The failure mechanisms observed and recorded in the present study are substantially different from those reported before and show a clear and systematic trend. The initial stages of failure in each layer are interpreted on the basis of the failure micromechanics of the unidirectional material under longitudinal and transverse loading. The interaction of failure mechanisms in the 0° and 90° layers and the later stages of damage are explained on the basis of classical lamination theory as well as on damage models available for crossply laminates. The various failure mechanisms and damage states were correlated with the overall mechanical behavior of the laminate. The main contribution of this paper lies in the integration of the micromechanics of brittle matrix single layers and the macromechanics of a crossply laminate in predicting and interpreting the type and sequence of failure mechanisms and their interaction.

2. EXPERIMENTAL PROCEDURE

The material investigated was SiC/CAS, calcium aluminosilicate glass-ceramic reinforced with silicon carbide fibers, manufactured by Corning Glass Works. The fiber is silicon carbide yarn known as Nicalon (Nippon Carbon Co.). This fiber is available in continuous length tows with an average diameter of 15 μm. The composite material for this study was obtained in the form of unidirectional and [0/90]$_{2s}$ and [0/90$_2$]$_s$ crossply laminates.

The unidirectional material was characterized first to obtain average physical and mechanical properties. Unidirectional specimens instrumented with strain gages were tested under longitudinal and transverse tensile loading in a servohydraulic testing machine.

The macroscopic response of the crossply laminates was measured by testing specimens under axial tension. The specimens were 15.2 cm (6 in.) long and 1.27 cm (0.5 in.) wide. They were tabbed with 3.81 cm (1.5 in.) long crossply glass/epoxy tabs. These specimens were tested in a servohydraulic testing machine (Instron) using an extensometer to monitor strain to failure.

Failure mechanisms were monitored by testing smaller crossply coupons under the microscope with a specially designed fixture. The specimens were 76 mm (3 in.) long and 12.7 mm (0.5 in.) wide coupons. Potting epoxy was cast around these coupons to help in subsequent polishing and loading of the specimen. One edge of the specimen was polished for microscopic observations.
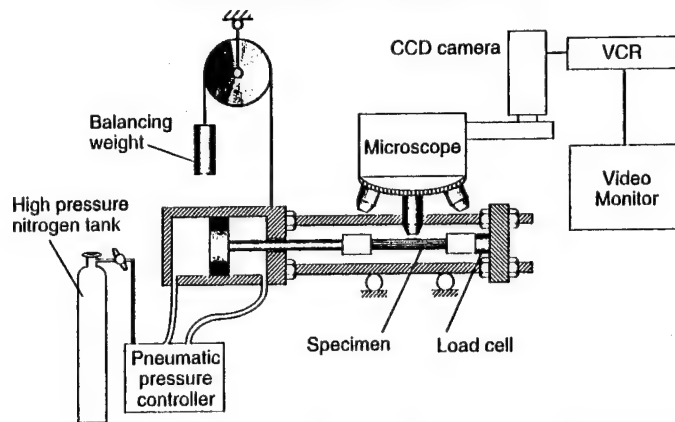
Fig. 1. Setup for microscopic observation of failure mechanisms in composite specimens under load.

A special loading fixture was designed and built for loading the specimens under the microscope (Fig. 1) ; see Daniel *et al.* (1989a,b). Load was applied and controlled by means of a pneumatic cylinder. The specimen with the grips attached was mounted onto a reaction frame attached to one end of the pneumatic cylinder. One end of the specimen was connected to the moving piston while the other end was reacted at the other end of the reaction frame through a strain gage load cell. The entire assembly, including air cylinder, reaction frame, specimen with grips and load cell, was suspended with a counterweight from a movable upright frame. Thus, any part of the loaded specimen could be moved to the stage of the microscope without any weight or force exerted on the microscope.

Two types of tests were conducted, continuous and intermittent loading tests. In the first type, loading is applied continuously to failure. A specific area of the specimen is observed through the microscope and recorded by a video camera. This type of loading yields a continuous stress–strain curve not affected by stress relaxation, as is the case during intermittent loading. However, only one small area of the specimen is being monitored and many interesting phenomena occurring outside the field of view are missed.

In the second type of test, loading is applied in steps. The stress and strain in the specimen are recorded in the beginning and at the end of each loading step. Photo-micrographs are taken at different areas of the specimen while the strain is held constant. One problem in this type of testing is stress relaxation during the holding period, which becomes more pronounced as damage progresses.

3. RESULTS

Material characterization
Some basic properties of the matrix and fiber constituents obtained from the literature and from previous tests are tabulated in Table 1.

Table 1. Constituent material properties

Property	CAS matrix†	SiC fiber‡
Maximum use temperature, °C (°F)	1350 (2460)	1300 (2370)
Fiber diameter (μm)	—	15
Density (g cm^{-3})	2.8	2.6
Coefficient of thermal expansion, $10^{-6\circ}\text{C}^{-1}$ ($10^{-6\circ}\text{F}^{-1}$)	5.0 (2.8)	3.2 (1.8)–4.9 (2.7)
Elastic modulus, GPa (10^6 psi)	98 (14.2)	170 (24.6)
Tensile strength, MPa (ksi)	124 (18) (flexural)	1930 (280)

† Larsen and Adams (1989).
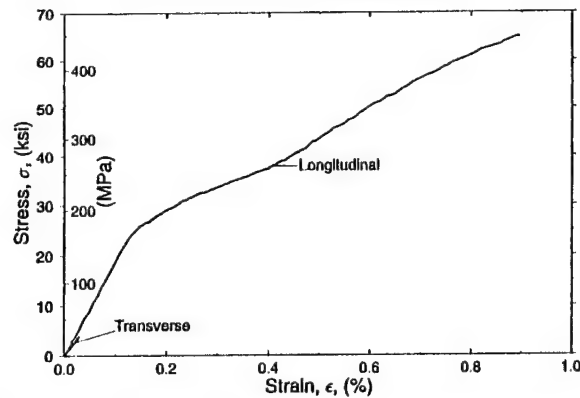‡ Prewo and Brennan (1982), Daniel *et al.* (1989).

Fig. 2. Stress–strain curves to failure of unidirectional SiC/CAS composite under longitudinal and transverse tension.

Examination of photomicrographs of transverse cross-sections showed that the fiber diameter ranges between 8 and 20 μm, with a median value of 15 μm. The fiber distribution is nonuniform with an average fiber volume ratio of $V_f = 0.39$. A low degree of porosity was measured ($V_v = 0.01$).

Typical stress–strain curves to failure of the unidirectional composite under longitudinal and transverse tension are shown in Fig. 2. Basic properties obtained from such macromechanical tests of the unidirectional SiC/CAS composite are tabulated in Table 2.

Damage initiation and development in 90° layer

The first stage of damage development, consisting of microcracking in the 90° layers, was studied by testing $[0/90]_{2s}$ crossply laminates under the microscope; see Daniel *et al.* (1989a,b). The first microcracks originated at the fiber–matrix interface and were nearly normal to the interface, which indicates that failure is caused by the circumferential tensile stress in the matrix. The randomness of the fiber packing makes it difficult to draw conclusions. However, some general patterns can be identified.

When the fibers are closely packed, usually in a near hexagonal array, radial cracks initiate at approximately 45° from the loading axis. An analysis for a closely packed hexagonal array of fibers showed that for a low stiffness interphase, the peak circumferential stress is the critical one and it occurs near the 45° location, Achenbach and Zhu (1990). This of course leads to radial cracking at this location, as observed experimentally.

When fibers are farther apart and are surrounded by a relatively large volume of matrix, radial cracks occur at approximately 90° from the loading axis. For a low stiffness

Table 2. Measured properties of SiC/CAS unidirectional composite

| Property	Value
Fiber volume ratio, V_f	0.39
Ply thickness, t, mm (in.)	0.38 (0.015)
Longitudinal modulus, E_1, GPa (Msi)	127 (18.4)
Transverse modulus, E_2, GPa (Msi)	112 (16.2)
In-plane shear modulus, G_{12}, GPa (Msi)	52 (7.5)
Out-of-plane shear modulus, G_{23}, GPa (Msi)	32 (4.7)
Major Poisson's ratio, ν_{12}	0.18
Longitudinal tensile strength, F_{1t}, MPa (ksi)	448 (65)
Transverse tensile strength, F_{2t}, MPa (ksi)	28 (4)
Longitudinal ultimate tensile strain, ε_{1t}^u	9×10^{-3}
Transverse ultimate tensile strain, ε_{2t}^u	2.5×10^{-4}
Longitudinal coefficient of thermal expansion, α_1, $\mu\varepsilon^\circ K^{-1}$ ($\mu\varepsilon^\circ F^{-1}$)	4.05 (2.25)
Transverse coefficient of thermal expansion, α_2, $\mu\varepsilon^\circ K^{-1}$ ($\mu\varepsilon^\circ F^{-1}$)	4.23 (2.35)
Out-of-plane coefficient of thermal expansion, α_3, $\mu\varepsilon^\circ K^{-1}$ ($\mu\varepsilon^\circ F^{-1}$)	4.32 (2.40)
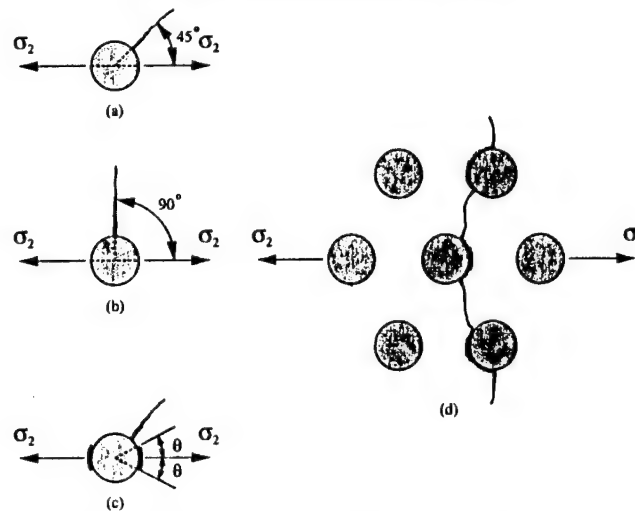
Fig. 3. Development of failure mechanisms in transversely loaded ceramic matrix composite.
(a) Initial radial cracks around closely-packed fibers. (b) Initial radial cracks around isolated fibers.
(c) Interfacial cracks. (d) Interconnection of radial and interfacial cracks and formation of macrocracks.

interphase the circumferential stress at the 90° location becomes critical, resulting in the observed radial cracks, Daniel et al. (1989).

As the load increases, a new failure mechanism develops, consisting of interface cracks in the area along the loading axis over an arc 2θ about the 0° point with $\theta < 45°$. These interface cracks are not immediately connected with the radial cracks developed earlier. Additional radial cracks may develop at this stage of damage development, and then, radial and interfacial cracks are connected to form a long continuous crack in the transverse layer. The various failure mechanisms and their sequence are illustrated schematically in Fig. 3.

The influence of these failure mechanisms on the stress–strain behavior of the $[0/90]_{2s}$ crossply laminate is shown in Fig. 4. The laminate behaves linearly up to an applied stress of 27.6 MPa (4 ksi) when the first radial cracks appear in the matrix. This causes a sudden drop in stiffness (secant modulus). At a higher applied stress, 32.4 MPa (4.7 ksi), interfacial cracking occurs causing another sudden, but smaller drop in stiffness. The interconnection of radial and interfacial cracks starts at a higher stress (36.6 MPa; 5.3 ksi) and progresses more gradually to the formation of continuous macrocracks, resulting in similarly gradual reduction in laminate stiffness. Similar stiffness reductions have been predicted by Zhu and Achenbach (1991) for a transversely loaded composite of the same properties, undergoing the same failure process.

The stiffness reductions illustrated in Fig. 4 are more pronounced in this test due to creep effects. The loading was applied intermittently over a relatively long period (more
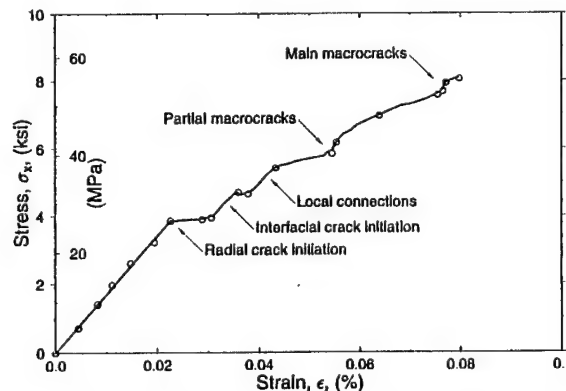

Fig. 4. Stress–strain curve of $[0/90]_{2s}$ crossply laminate with corresponding stages of damage development in transverse layer.
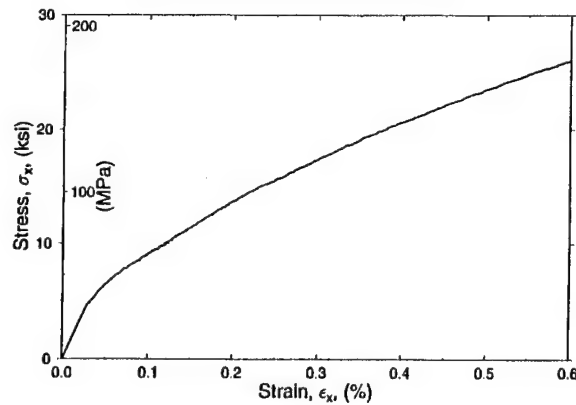
Fig. 5. Stress–strain curve of $[0/90_2]_s$ SiC/CAS crossply laminate under uniaxial tension.

than 30 min) to allow for photomicrographic recording of the various stages of damage development. The first continuous (across the 90° layer) macrocracks were formed at an applied stress of approximately 40 MPa (5.8 ksi), which corresponds to an axial stress of $\sigma_2 = 38$ MPa (5.5 ksi) in the 90° layer. The *in situ* lamina strength is comparable to the value measured by Mall and Kim (1992) and is higher than the transverse tensile strength $F_{2t} = 28$ (4 ksi) measured from a 90° transverse tensile test. Continued loading increases the number of macrocracks up to a saturation density, corresponding to a minimum macrocrack spacing of the order of the 90° layer thickness.

Figure 5 shows a stress–strain curve for a $[0/90_2]_s$ crossply laminate under uniaxial tension. Microcracking in the 90° layer (layer 2) started at an applied strain of approximately 0.025%. Transverse macrocracks reached a minimum crack spacing of 0.65 mm (0.0255 in.), comparable to the layer thickness of 0.68 mm (0.027 in.), at an applied stress of approximately 69 MPa (10 ksi), corresponding to a strain of approximately 0.12%.

The initial modulus in the linear region is

$$\bar{E}_x = 117\,\text{GPa} \ (16.9\,\text{Msi}),$$

which agrees with the calculated laminate modulus. The reduced secant modulus at the point of crack saturation ($\bar{\sigma}_x = 69$ MPa, $\bar{\varepsilon}_x = 0.12\%$) is

$$\bar{E}'_x = 58\,\text{GPa} \ (8.3\,\text{Msi}).$$

At this stage of damage development, corresponding to the proportional limit of the stress–strain response of the 0° layer (Fig. 2), no appreciable damage has occurred in the 0° layer (layer 1). Simple lamination analysis gives the following axial moduli and average axial stresses in the two layers:

$$E_1 = 127\,\text{GPa} \ (18.4\,\text{Msi})$$

$$E'_2 = 22.8\,\text{GPa} \ (3.3\,\text{Msi})$$

$$\sigma_{1x} = 152\,\text{MPa} \ (22\,\text{ksi})$$

$$\sigma_{2x} = 27.6\,\text{MPa} \ (4.0\,\text{ksi}),$$

where $E_1 =$ initial modulus of 0° layer, $E'_2 =$ degraded modulus of 90° layer, σ_{1x}, $\sigma_{2x} =$ average axial (x-direction) stresses in layers 1 and 2, respectively.

Damage initiation and development in 0° layer

Prior investigations have shown that, in a unidirectional SiC/CAS composite under longitudinal tension, transverse matrix cracking starts at an applied strain of approximately 0.1%, see Daniel *et al.* (1993). This value is slightly below the proportional limit of the
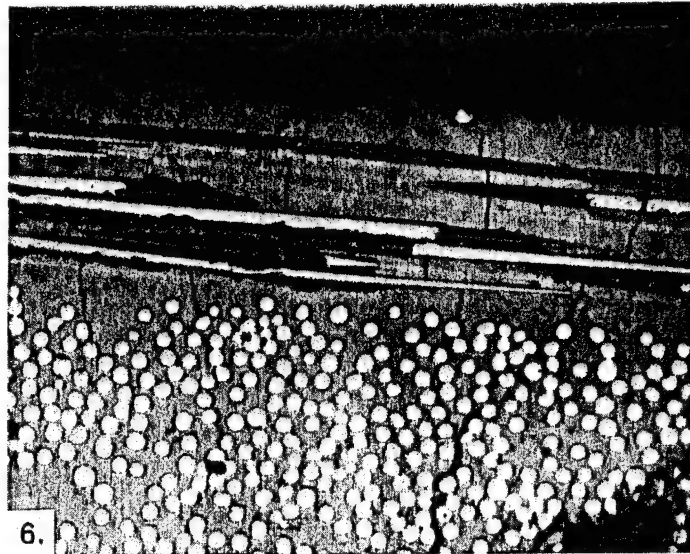
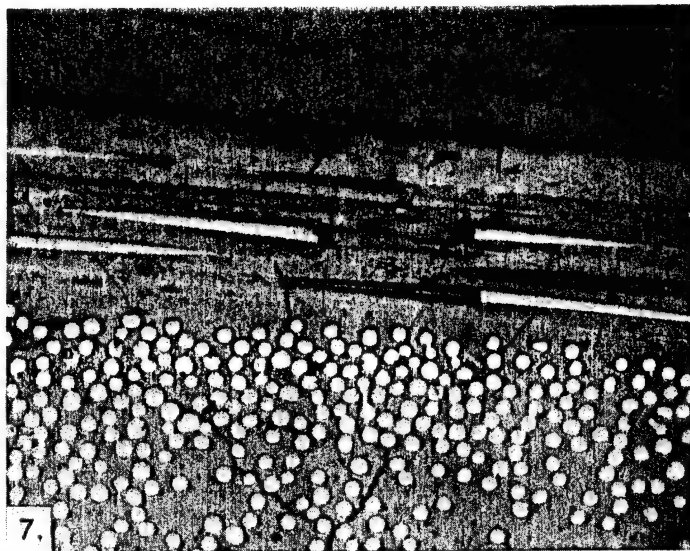Fig. 6. Matrix cracking in 0°-ply following saturation of cracking in 90°-ply.

Fig. 7. Interconnection of 0°-ply and 90°-ply macrocracks (formation of "delta" pattern).
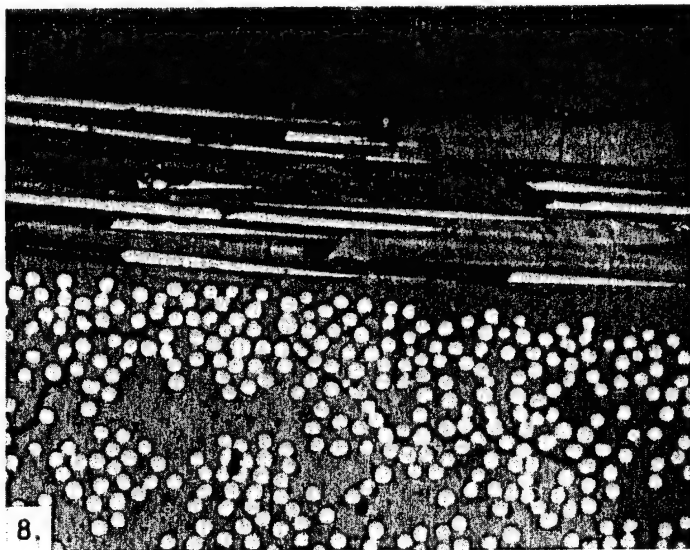
Fig. 8. Longitudinal cracking in 90°-ply.
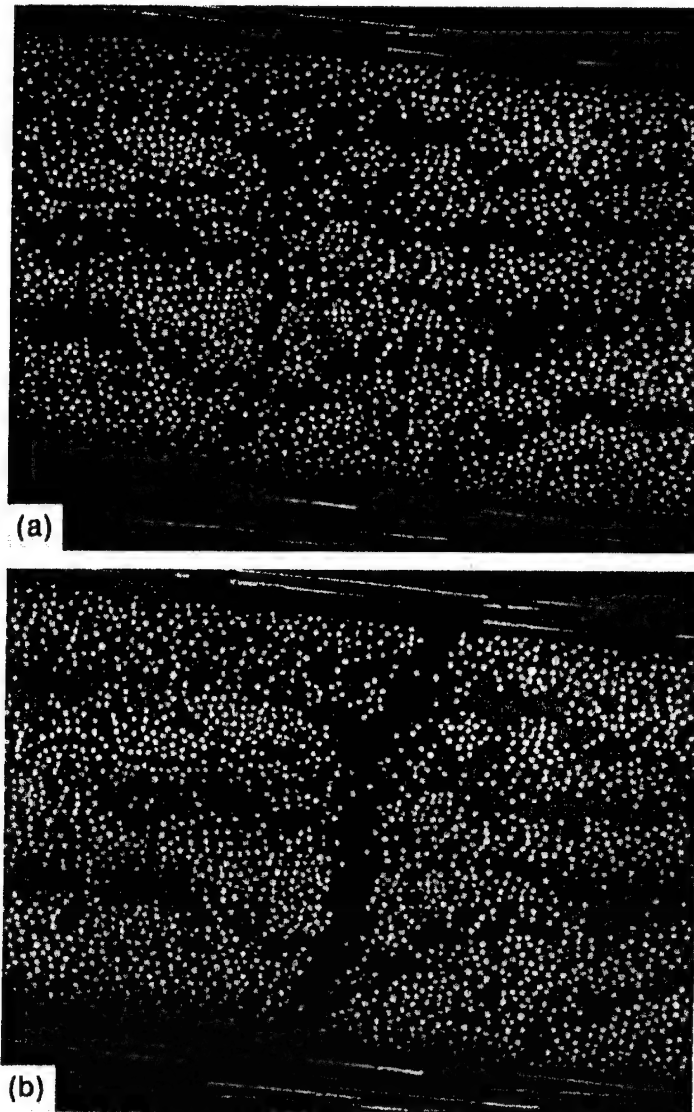
I. M. Daniel and G. Anastassopoulos

Fig. 9. Final stages of damage consisting of fiber fractures and debonding in 0° layer and crack opening in 90° layer. (a) $\bar{\sigma}_x = 199$ MPa (28.9 ksi), (b) $\bar{\sigma}_x = 210$ MPa (30.4 ksi).

longitudinal stress–strain curve of Fig. 2. Thus, damage in this layer starts near the saturation point of cracking in the 90° layer.

The initial failure in the 0° layer consists of transverse matrix cracks increasing in density with applied stress up to a minimum crack spacing of approx. 120 μm (0.0047 in.) at a stress of 138 MPa (20 ksi) and a strain of 0.37%, as shown in Fig. 6. This is close to the minimum crack spacing observed before in a unidirectional specimen under longitudinal loading and corresponds to eight fiber diameters, Daniel *et al.* (1992).

At this stage of damage development ($\bar{\sigma}_x = 138$ MPa, $\bar{\varepsilon}_x = 0.37\%$) the reduced secant modulus is

$$\bar{E}'_x = 37.3\,\text{GPa (5.4 Msi)}.$$

Assuming no increase in the average axial stress carried by the damaged 90° layer, the following axial moduli and average axial stresses are obtained in each of the two layers:

$$E'_1 = 97\,\text{GPa (14.0 Msi)}$$
$$E'_2 = 7.5\,\text{GPa (1.08 Msi)}$$
$$\sigma_{1x} = 359\,\text{MPa (52 ksi)}$$
$$\sigma_{2x} = 27.6\,\text{MPa (4.0 ksi)}.$$

The further reduction in the layer 2 modulus, while its average axial stress remains constant, is attributed to the increased opening displacements in layer 2 macrocracks, following crack formation and multiplication in layer 1.

One important observation is that the *in situ* reduced axial modulus E'_1 of layer 1 is appreciably higher than the corresponding modulus of the unidirectional material at the same stage of damage development, i.e. saturation of matrix cracks at a strain of $\varepsilon_1 = 0.37\%$ (see Fig. 2). This could be attributed to the fact that large segments of layer 2 remain adhered to layer 1 and bridge the matrix cracks in layer 1, thereby increasing its effective *in situ* stiffness.

At the same point of damage development, there is evidence that extensive fiber–matrix debonding occurs in this layer near and after matrix crack saturation, see Luo *et al.* (1994), Wooh and Daniel (1994). As in the case of the unidirectional material under longitudinal loading, isolated fiber breaks were observed before saturation of transverse matrix cracking in the 0° layers.

Damage interaction between 0° and 90° layers

As the applied stress is increased above 138 MPa (20 ksi), the matrix cracks in the 0° layer begin to propagate into the 90° layer and connect with the macrocracks already developed in that layer. Because of the difference in crack spacings in the two layers, several cracks in the 0° layer connect with each crack in the 90° layer forming a "delta-like" pattern in the 90° layer near the interface (Fig. 7). Each macrocrack in the 90° layer corresponds to five to six transverse cracks in the 0° layer.

With increasing load, axial (in the loading direction) cracks are generated in the 90° layer near the interface with the 0° layer (Fig. 8). These cracks (or delaminations) may be due to high interlaminar shear stresses developed at the tips of the transverse macrocracks in layer 2, and/or high interlaminar normal and shear stresses existing near the edges of crossply laminates (edge effect). Additional transverse cracks also appear in layer 2.

In the final stages of damage development extensive fiber–matrix debonding in layer 1 is accompanied by fiber fractures and sliding. This is manifested by large crack openings in layer 1 and even larger (more than five times larger) crack openings in layer 2 (Fig. 9).
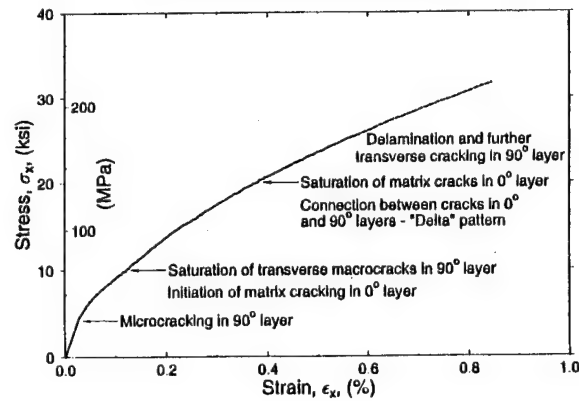
Fig. 10. Stress–strain behavior of $[0/90_2]_s$ laminate with corresponding stages of damage development.

The various failure mechanisms and the entire process of damage evolution are correlated with the macroscopic stress–strain curve of the $[0/90_2]_s$ laminate in Fig. 10. The effects of the various failure mechanisms on stiffness degradation are illustrated.

Ultimate failure occurred at an applied stress of over 220 MPa (32 ksi), which corresponds to an *in situ* longitudinal strength of over 607 MPa (88 ksi) in the 0° layer. This is much higher than any measured longitudinal strength of the unidirectional material and clearly shows the synergistic effect of the 0° and 90° layers of the laminate.

4. ANALYTICAL PREDICTIONS

The formation of transverse macrocracks in the 90° layer of a crossply laminate has been discussed by several investigators, including Reifsnider *et al.* (1983), Talreja (1985), Hashin (1985), Ogin *et al.* (1985), Laws and Dvorak (1988) and Lee and Daniel (1990). The analyses above were aimed primarily at polymer matrix composites, but since they are linear they can be applied to ceramic matrix composites as well. The analytical model described by Lee and Daniel (1990) was used here to explain the observed phenomena. This model was shown to give accurate predictions of stiffness degradation and crack spacing in the 90° layer.

Under axial loading the state of stress in each layer is essentially uniaxial. The first transverse macrocracks in layer 2 occur when the axial (x-axis) stress in that layer reaches the strength of the layer, i.e. the transverse tensile strength, F_{2t}, of the unidirectional material (Fig. 11). As discussed before, the *in situ* transverse strength of the layer is somewhat higher than the value measured by testing an unsupported unidirectional layer. The applied laminate stress $\bar{\sigma}_x$ at crack initiation in layer 2 is
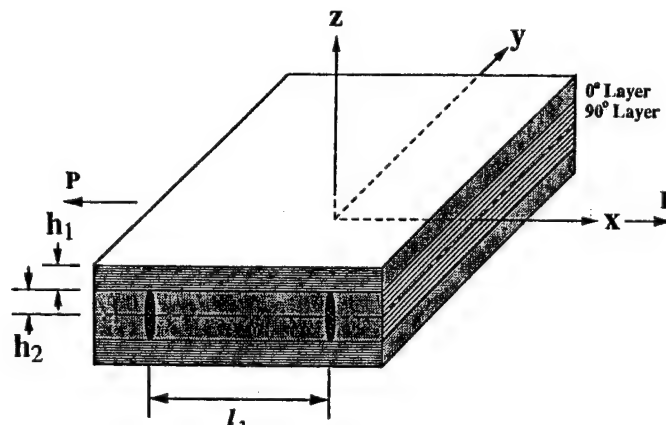

Fig. 11. Element of cracked crossply laminate under axial loading.

$$\bar{\sigma}_x = \frac{\bar{E}_x}{E_2}(F_{2t} - \sigma_{2x}^r), \tag{1}$$

where

$$\bar{E}_x = \frac{E_1 h_1 + E_2 h_2}{h_1 + h_2} = \text{axial modulus of undamaged laminate,}$$

$E_1, E_2 = $ longitudinal and transverse moduli of undamaged unidirectional material, respectively,

$F_{2t} = $ transverse (to the fibers) tensile strength of unidirectional material,

$\sigma_{2x}^r = $ residual axial stress in 90° layer.

The above residual stress is approximately equal to 7 MPa (1 ksi) for a 1100°C (2000°F) temperature difference between processing and room temperature. Substituting the known material properties and the value $F_{2t} = 38$ MPa (5.5 ksi) for the transverse tensile strength in eqn (1), we obtain a stress of

$$\bar{\sigma}_x = 28.8 \, \text{MPa} \, (4.2 \, \text{ksi}),$$

which agrees with the experimental observation of initiation of transverse macrocracks in the 90° layer (Fig. 5).

An element of the laminate with the 90° layer cracked under axial loading is shown in Fig. 11. Of particular significance to damage development in the laminate are the stress distributions in the layers and the stiffness reductions. The stress distributions in the layers between two transverse cracks in the 90° layer are given by Lee and Daniel (1990)

$$\sigma_{1x} = \frac{E_1}{\bar{E}_x}\left[1 + \frac{E_2 h_2 \cosh \alpha\left(\frac{l_2}{2} - x\right)}{E_1 h_1 \cosh \alpha \frac{l_2}{2}}\right]\bar{\sigma}_x + \left[1 - \frac{\cosh \alpha\left(\frac{l_2}{2} - x\right)}{\cosh \alpha \frac{l_2}{2}}\right]\sigma_{1x}^r \tag{2}$$

$$\sigma_{2x} = \left[1 - \frac{\cosh \alpha\left(\frac{l_2}{2} - x\right)}{\cosh \alpha \frac{l_2}{2}}\right]\left(\frac{E_2}{\bar{E}_x}\bar{\sigma}_x + \sigma_{2x}^r\right) \tag{3}$$

$$\tau_i = -\alpha h_2\left(\frac{E_2}{\bar{E}_x}\bar{\sigma}_x + \sigma_{2x}^r\right)\frac{\sinh \alpha\left(\frac{l_2}{2} - x\right)}{\cosh \alpha \frac{l_2}{2}}, \tag{4}$$

where $\sigma_{1x}, \sigma_{2x} = $ average (through the thickness) axial stresses in 0° and 90° layers, respectively, $\tau_i = $ interlaminar shear stress at interface between 0° and 90° layers,

$$\alpha = \left[\frac{(h_1 + h_2)\bar{E}_x}{h_1 h_2 E_1 E_2} \cdot \frac{3G_{12}G_{23}}{h_1 G_{23} + h_2 G_{12}}\right]^{1/2}, \tag{5}$$

$G_{12}, G_{23} = $ in-plane and out-of-plane shear moduli of undamaged unidirectional material, $\sigma_{1x}^r = $ axial residual stress in 0° layer (calculated as -13 MPa), $l_2 = $ crack spacing in 90° layer.

This crack spacing decreases with load up to a minimum characteristic value. Experimentally, a minimum crack spacing of 0.65 mm (0.0255 in.) was observed at an applied stress of $\bar{\sigma}_x = 69$ MPa (10 ksi), as mentioned before. The predicted crack spacing at this stress can be obtained by setting $\bar{\sigma}_x = 69$ MPa (10 ksi), $\sigma_{2x} = F_{2t} = 38$ MPa (5.5 ksi) and $x = l_2/2$ (midpoint between cracks) in eqn (3). Then, from eqn (3) we obtain

$$l_2 = \frac{2}{\alpha} \cosh^{-1} \eta \qquad (6)$$

where

$$\eta = \left[1 - \frac{F_{2t}}{\dfrac{E_2}{\bar{E}_x} \bar{\sigma}_x + \sigma_{2x}^r} \right]^{-1}.$$

For the numerical values above we obtain

$$(l_2)_{min} = 0.68 \text{ mm } (0.027 \text{ in.}).$$

Expressions for the reduced axial stiffness E_2' of the 90° layer and $\bar{E}_x'$ of the laminate are given as a function of crack spacing as follows, Lee and Daniel (1990):

$$\bar{E}_2' = \frac{(1-\beta)(E_2 \bar{\sigma}_x + \bar{E}_x \sigma_{2x}^r)}{\left(1 + \dfrac{E_2 h_2}{E_1 h_1} \beta \right) \bar{\sigma}_x + \dfrac{\bar{E}_x}{E_1}(1-\beta)\sigma_{1x}^r} \qquad (7)$$

and

$$\bar{E}_x' = \bar{E}_x \left[1 + \frac{E_2 h_2}{E_1 h_1} \beta + \frac{\sigma_{1x}^r}{\bar{\sigma}_x} \frac{\bar{E}_x}{E_1}(1-\beta) \right]^{-1}, \qquad (8)$$

where

$$\beta = \frac{2}{\alpha l_2} \tanh \left(\frac{\alpha l_2}{2} \right).$$

At the applied stress level of 69 MPa (10 ksi), where transverse crack saturation was noticed, but before any substantial damage occurred in the 0° layer, the 90° layer and laminate moduli are calculated as
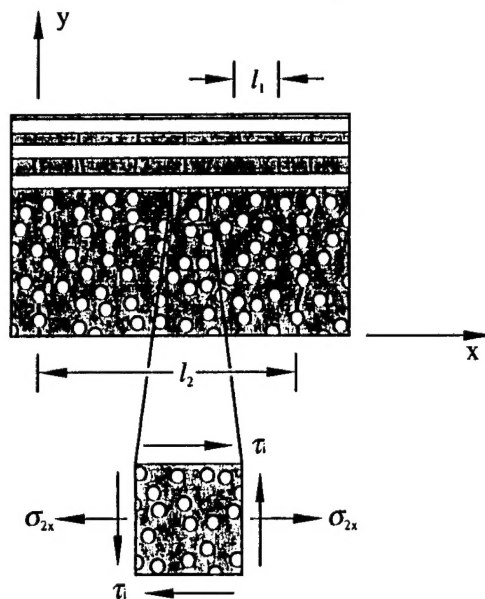
$$E_2' = 19 \text{ GPa } (2.8 \text{ Msi})$$

$$\bar{E}_x' = 55 \text{ GPa } (8.0 \text{ Msi}),$$

which are in good agreement with the experimental values of $E_2' = 22.8$ GPa (3.3 Msi) and $\bar{E}_x' = 58$ GPa (8.3 Msi) mentioned before.

The average stress carried by the 0° layer then, is

$$\sigma_{1x} \cong \sigma_{1x}^r + \frac{E_1}{\bar{E}_x'} \bar{\sigma}_x = 146 \text{ MPa } (21.1 \text{ ksi}).$$

The stress necessary to initiate transverse matrix cracking in the 0° layer is

$$l_2 \cong 6l_1$$

Fig. 12. Element of laminate with both layers cracked up to their saturation levels.

$$\sigma_{1x} = \frac{E_1}{E_m} (F_{mt} - \sigma^r_{mx}) - \sigma^r_{1x}$$

where E_m = matrix modulus, F_{mt} = matrix tensile strength, σ^r_{mx} = axial micro-residual stress in matrix of 0° layer.

Neglecting the counteracting residual stresses, tensile micro-residual stress σ^r_{mx} and compressive macro-residual stress σ^r_{1x}, we obtain the value

$$\sigma_{1x} \cong 154 \text{ MPa (22.3 ksi)}.$$

This shows that crack initiation takes place in the 0° layer at a slightly higher load level than that at which crack saturation occurs in the 90° layer. This also corresponds to the observed proportional limit of the longitudinal stress–strain curve (Fig. 2).

Cracking continues in the 0° layer up to a saturation crack density where $(l_1)_{min} = 0.120$ mm (0.0047 in.), which is one-sixth to one-fifth of $(l_2)_{min}$. An element of the laminate with both layers cracked up to their saturation levels is shown in Fig. 12. A subelement of the 90° layer at the interface with the 0° layer is subjected primarily to the normal axial stress σ_{2x} and interlaminar shear stress τ_i. These stresses result in a tensile principal stress at an angle that would explain the formation of branch cracks in the observed "delta" pattern.

5. SUMMARY AND CONCLUSIONS

The behavior of crossply ceramic-matrix composites under axial tensile loading was studied. The material investigated was SiC/CAS, calcium aluminosilicate glass-ceramic reinforced with silicon carbide (Nicalon) fibers. Specimens were loaded under the microscope and the various failure mechanisms, their sequence, interaction and overall damage development were observed in real time and recorded.

The first stage of damage development consists of microcracks in the 90° layer, which then develop into transverse macrocracks. These macrocracks increase in density up to a saturation limit, with a minimum crack spacing approximately equal to the 90° layer thickness. Thereafter, transverse matrix cracks are generated in the 0° layer. These cracks

also increase in density up to a minimum crack spacing of approximately eight fiber diameters. In the third stage of damage development there is an interconnection of the two sets of cracks. Several of the denser 0° layer cracks connect with each of the 90° layer cracks in a delta-like pattern. This is finally followed by delaminations and additional cracking in the 90° layer prior to ultimate failure.

Damage development was correlated with the macroscopic stress–strain response of the unidirectional material under longitudinal and transverse loading and of the crossply laminate. It was noticed that first-ply failure in the 90° layer occurs at a higher layer stress than the transverse tensile strength of the unidirectional material. This may be attributed to the constraining effects of the 0° layer which tend to increase the *in situ* transverse tensile strength of the 90° layer.

Following crack saturation in the 90° layer, cracking initiated and increased in the 0° layers at approximately the same strain levels where similar cracking was observed in the unidirectional material under longitudinal loading. However, the 0° layer stresses at the various stages of damage development, were higher than corresponding stress levels in the 0° unidirectional specimen for the same damage. This was explained as a stiffening or strengthening effect of the 0° layers caused by the attached 90° layer. Ultimate failure of the laminate clearly showed the synergistic effects of the 0° and 90° layers of the laminate.

Damage development in the 90° layer was compared with analytical predictions. A model developed previously for crossply graphite/epoxy composites was used to predict cracking in the 90° layer and stiffness degradation, both in the 90° layer and in the overall laminate. The predictions were in very good agreement with experimental observations.

It was shown that the overall damage development is characterized by different scales at different stages. The relevant scales are fiber diameter and fiber spacing for failure initiation in the 90° layer; layer thickness for damage saturation in the 90° layer; and fiber diameter for matrix cracking in the 0° layer. Finally, there is a scale crossing phenomenon in the interaction between the damage in the 90° and 0° layers.

REFERENCES

Achenbach, J. D. and Zhu, H. (1990). Effect of interphases on micro and macromechanical behavior of hexagonal-array fiber composites. *J. Appl. Mech.* **57,** 956–963.
Aveston, J. and Kelly, A. (1973). Theory of multiple fracture of fibrous composites. *J. Mater. Sci.* **8,** 352–362.
Aveston, J., Cooper, G. A. and Kelly, A. (1971). The properties of fibre composites. *Conf. Proc., National Physical Laboratory*, pp. 15–26. IPC Science and Technology Press, Surrey, U.K.
Benveniste, Y. (1985). The effective mechanical behavior of composite materials with imperfect contact between the constituents. *Mech. Mater.* **4,** 197–208.
Brennan, J. J. and Prewo, K. M. (1982). Silicon carbide fibre reinforced glass-ceramic matrix composites exhibiting high strength and toughness. *J. Mater. Sci.* **17,** 2371–2383.
Budiansky, B., Hutchinson, J. W. and Evans, A. G. (1986). Matrix fracture in fiber-reinforced ceramics. *J. Mech. Phys. Solids* **34** (13), 167–189.
Charalambides, P. G. (1991). Steady-state mechanics of delamination cracking in laminated ceramic-matrix composites. *J. Am. Ceram. Soc.* **74** (12), 3066–80.
Charalambides, P. G. and Evans, A. G. (1989). Debonding properties of residually stressed brittle-matrix composites. *J. Am. Ceram. Soc.* **72,** 746–53.
Daniel, I. M., Anastassopoulos, G. and Lee, J.-W. (1989a). Failure mechanisms in ceramic-matrix composites. *Proc. SEM Spring Conf. Experimental Mechanics,* 29 May–1 June, 1989, 832–838.
Daniel, I. M., Anastassopoulos, G. and Lee, J.-W. (1989b). Experimental micromechanics of brittle-matrix composites. *Micromechanics: Experimental Techniques,* Vol. AMD **102,** pp. 133–146. ASME Winter Annual Meeting, San Francisco, CA.
Daniel, I. M., Anastassopoulos, G. and Lee, J.-W. (1992). Failure mechanisms and interfacial shear strength in brittle-matrix composites. *Advances in Experimental Mechanics and Biomimetics,* Vol. AD 29/AMD 146, (Edited by W. F. Jones and J. M. Whitney), pp. 57–69. ASME.
Daniel I. M., Lee, J.-W. and Anastassopoulos, G. (1993). The behavior of ceramic matrix fiber composites under longitudinal loading. *Compos. Sci. Technol.* **46,** 105–113.
Daniel, I. M., Lee, J.-W. and Yaniv, G. (1988). Damage development and property degradation of composite materials. In *Mechanics of Composite Materials* (Edited by G. J. Dvorak and N. Laws), Vol. AMD92, 149–160. ASME.
Hashin, Z. (1983). Analysis of composite materials—a survey. *J. Appl. Mech.* **50,** 481–505.

Hashin, Z. (1985). Analysis of cracked laminates; a variational approach. *Mech. Mater.* **4**, 121–136.

Hsueh, C.-H. (1988). Analytical evaluation of interfacial shear strength for fiber-reinforced ceramic composites. *J. Am. Ceram. Soc.* **71**, 490–493.

Hutchinson, J. W. and Jenson, H. M. (1990). Models of fiber debonding and pullout in brittle composites with friction. *Mech. Mater.* **9**, 139–163.

Larsen, D. C. and Adams, J. (1989). Corning glass works. Private communication.

Laws, N. and Dvorak, G. J. (1988). Progressive transverse cracking in composite laminates. *J. Compos. Mater.* **22**, 900–916.

Lee, J.-W and Daniel, I. M. (1990). Progressive transverse cracking of crossply composite laminates. *J. Compos. Mater.* **24**, 1225–1243.

Lee, J.-W. and Daniel, I. M. (1992). Deformation and failure of longitudinally loaded brittle-matrix composites. In *Composite Materials: Testing and Design*, Vol. ASTM, STP 1120 (Edited by Glenn C. Grimes), pp. 204–221. American Society for Testing and Materials, Philadelphia.

Luo, J.-J., Wooh, S.-C. and Daniel, I. M. (1994). Acoustic emission study of failure mechanisms in ceramic matrix composite under longitudinal tensile loading. *Review of Progress in QNDE*, Vol. **13** (Edited by D. O. Thompson and D. E. Chimenti), pp. 469–476. Plenum Press, New York.

Mall, S. and Kim, R. Y. (1992). Failure mechanisms in laminates of silicon carbide calcium–aluminosilicate ceramic composite. *Composites* **23** (4), 215–222.

Marshall, D. B. and Evans, A. G. (1985). Failure mechanisms in ceramic-fiber/ceramic-matrix composites. *J. Am. Ceram. Soc.* **68**, 225–231.

Marshall, D. B. and Evans, A. G. (1988). Failure mechanisms in ceramic-fiber/ceramic-matrix composites. *Ceram. Engng Sci. Proc.* **9** (7–8), 853–860.

Marshall, D. B., Cox, B. N. and Evans, A. G. (1985). The mechanics of matrix cracking in brittle-matrix fiber composites. *Acta Metall.* **33** (11), 2013–2021.

McCartney, L. N. (1989). New theoretical model of stress transfer between fibre and matrix in a unidirectionally fibre-reinforced composite. *Proc. R. Soc. Lond. Ser.* **A425**, 215–244.

Ogin, S. L., Smith, P. A. and Beaumont, P. W. R. (1985). Matrix cracking and stiffness reduction during the fatigue of a [0/90] GFRP laminate. *Compos. Sci. Technol.* **22**, 23–31.

Prewo, K. M. and Brennan, J. J. (1982). Silicon carbide yarn reinforced glass matrix composites. *J. Mater. Sci.* **17**, 1201–1206.

Reifsnider, K. L., Henneke, E. G., Stinchcomb, W. W. and Duke, J. C. (1983). Damage mechanisms and NDE of composite laminates. *Mechanics of Composite Materials; Recent Advances* (*Proc. IUTAM Symp. Mechanics of Composite Materials*) (Edited by Z. Hashin and C. T. Herakovich), pp. 399–420. Pergamon Press, New York.

Sbaizero, O. and Evans, A. G. (1986). Tensile and shear properties of laminated ceramic matrix composites. *J. Am. Ceram. Soc.* **69**(6), 481–486.

Sbaizero, O., Charalambides, P. G. and Evans, A. G. (1990). Delamination cracking in a laminated ceramic-matrix composite. *J. Am. Ceram. Soc.* **73** (7), 1936–1940.

Stang, H. and Shah, S. P. (1986). Failure of fiber-reinforced composites by pull-out fracture. *J. Mater. Sci.* **21**, 953–957.

Talreja, R. (1985). Transverse cracking and stiffness reduction in composite laminates. *J. Compos. Mater.* **19**, 355–375.

Weitsman, Y. and Zhu, H. (1993). Multi-fracture of ceramic composites. *J. Mech. Phys. Solids* **41** (2), 351–388.

Wooh, S.-C. and Daniel, I. M. (1994). Real-time ultrasonic monitoring of fiber-matrix debonding in ceramic matrix composite. *Mech. Mater.* **17**, 379–388.

Zhu, H. and Achenbach, J. D. (1991). Radial matrix cracking and interphase failure in transversely loaded fiber composites. *Mech. Mater.* **11**, 347–356.

Zok, F. W. and Spearing, S. M. (1992). Matrix crack spacing in brittle matrix composites. *Acta Metall. Mater.* **40** (8), 2033–2043.